Quantitative estimation of vegetation traits and temporal dynamics using 3-D radiative transfer models, high-resolution hyperspectral images and satellite imagery

Alberto Hornero Luque

Submitted to Swansea University in fulfilment of the requirements for the degree of Doctor of Philosophy.

2021

Abstract

Large-scale monitoring of vegetation dynamics by remote sensing is key to detecting early signs of vegetation decline. Spectral-based indicators of physiological plant traits (PTs) have the potential to quantify variations in photosynthetic pigments, chlorophyll fluorescence emission, and structural changes of vegetation as a function of stress. However, the specific response of PTs to disease-induced decline in heterogeneous canopies remains largely unknown, which is critical for the early detection of irreversible damage at different scales. Four specific objectives were defined in this research: i) to assess the feasibility of modelling the incidence and severity of *Phytophthora cinnamomi* and *Xylella fastidiosa* based on PTs and biophysical properties of vegetation; ii) to assess non-visual early indicators, iii) to retrieve PT using radiative transfer models (RTM), high-resolution imagery and satellite observations; and iv) to establish the basis for scaling up PTs at different spatial resolutions using RTM for their retrieval in different vegetation covers. This thesis integrates different approaches combining field data, air- and space-borne imagery, and physical and empirical models that allow the retrieval of indicators and the evaluation of each component's contribution to understanding temporal variations of disease-induced symptoms in heterogeneous canopies. Furthermore, the effects associated with the understory are introduced, showing not only their impact but also providing a comprehensive model to account for it. Consequently, a new methodology has been established to detect vegetation health processes and the influence of biotic and abiotic factors, considering different components of the canopy and their impact on the aggregated signal. It is expected that, using the presented methods, existing remote sensors and future developments, the ability to detect and assess vegetation health globally will have a substantial impact not only on socio-economic factors, but also on the preservation of our ecosystem as a whole.

Declaration

This work has not previously been accepted in substance for any degree and is not being concurrently submitted in candidature for any degree.

The candidate confirms that the work submitted is his own and that appropriate credit has been given where reference has been made to the work of others.

The candidate gives consent for his thesis, if accepted, to be available for photocopying and inter-library loan, and for the title and summary to be made available to outside organisations.

This copy has been supplied on the understanding that it is copyright material and that no quotation from the thesis may be published without proper acknowledgement.

The right of Alberto Hornero Luque to be identified as the author of this work has been asserted by him in accordance with the Copyright, Designs and Patents Act 1988.

Authorship Statement

Paper 1: Hornero, A., Hernández-Clemente, R., North, P.R.J., Beck, P.S.A., Boscia, D., Navas-Cortes, J.A., Zarco-Tejada, P.J., Monitoring the incidence of *Xylella fastidiosa* infection in olive orchards using ground-based evaluations, airborne imaging spectroscopy and Sentinel-2 time series through 3-D radiative transfer modelling, Remote Sensing of Environment, 236, 111480. 2020. DOI: 10.1016/j.rse.2019.111480

Located in Chapter 2.

Alberto Hornero (AH)	Swansea University
Rocío Hernández-Clemente (RHC)	Swansea University
Peter R. J. North (PN)	Swansea University
Pieter S. A. Beck (PB)	European Commission
Donato Boscia (DB)	Consiglio Nazionale delle Ricerche
Juan Antonio Navas-Cortes (JNC)	Spanish National Research Council
Pablo J. Zarco-Tejada (PZT)	University of Melbourne

AH and PZT conceived the idea. AH, DB, JNC and PZT collected field data. RHC, PN, PB and PZT provided background information. AH performed the sensor calibration and pre-processing chain. AH, PN and RHC developed the method and analysed the data. AH wrote the manuscript; all authors helped to review and updating the manuscript.

All authors approved the final manuscript before publication.

Paper 2: Hornero, A., North, P.R.J., Zarco-Tejada, P.J., Rascher, U., Martín, M.P., Migliavacca, M., Hernández-Clemente, R., Assessing the influence of the understory in the interpretation of chlorophyll fluorescence retrieved from heterogeneous canopies through 3-D radiative transfer modelling, Remote Sensing of Environment, 253, 112195. 2021. DOI: 10.1016/j.rse.2020.112195

Located in Chapter 3.

Alberto Hornero (AH)	Swansea University
Peter R. J. North (PN)	Swansea University
Pablo J. Zarco-Tejada (PZT)	University of Melbourne
Uwe Rascher (UR)	Forschungszentrum Jülich
M. Pilar Martín (PM)	Spanish National Research Council
Mirco Migliavacca (MM)	Max Planck Institute
Rocío Hernández-Clemente (RHC)	Swansea University

AH, PN and RHC conceived the idea. PN and AH developed the model. PM and MM collected field data and provided background information. UR designed the airborne hyperspectral campaigns and developed the sensor calibration and pre-processing chain. AH, PZT and RHC designed the methodology and analysed the data. AH wrote the manuscript, and all authors contributed to the process of reviewing and updating the manuscript.

All authors approved the final manuscript before publication.

Paper 3: A. Hornero, P.J. Zarco-Tejada, J.L. Quero, P.R.J. North, F.J. Ruiz-Gómez, R. Sánchez-Cuesta, R. Hernández-Clemente, Modelling hyperspectral- and thermal-based plant traits for the early detection of *Phytophthora*-induced symptoms in oak decline, *Under Review (minor changes)*.

Located in Chapter 4.

Alberto Hornero (AH)	Swansea University
Pablo J. Zarco-Tejada (PZT)	University of Melbourne
Jose L. Quero (JQ)	University of Cordoba
Peter R. J. North (PN)	Swansea University
Francisco J. Ruiz-Gómez (FRG)	University of Cordoba
Rafael Sánchez-Cuesta (RSC)	University of Cordoba
Rocío Hernández-Clemente (RHC)	Swansea University

AH, PZT and RHC conceived the idea and designed the airborne campaign and data analysis. AH, JQ, FRG, RSC and RHC collected field data. PZT, PN, JQ and RHC provided background information. AH performed the sensor calibration, pre-processing chain. AH wrote the manuscript; all authors helped to review and updating the manuscript.

All authors approved the final manuscript before publication.

Table of Contents

Acknowledgements

This work was supported by research fellowship DTC GEO 29 "Detection of global photosynthesis and forest health from space" from the Science Doctoral Training Centre (Swansea University, United Kingdom). Data collection was partially supported by the European Union's Horizon 2020 research and innovation programme through grant agreements POnTE (635646) and XF-ACTORS (727987); the SynerTGE (CGL2015-G9095-R), QUERCUSAT (CGL2013-40790-R) and ESPECTRAMED (CGL2018-86161-R) projects from the Spanish Research Agency (MINECO/FEDER, UE); and ESA-FLEX Sense 2018 Project (ESA Contract No. ESA RFP/3-15477/18/NL/NA).

Firstly, I would like to acknowledge my supervisors Prof. Pablo J. Zarco-Tejada and Prof. Peter R.J. North, for their guidance, support and encouragement throughout this period. I also thank Pieter Beck, Sergio Cogliati, Alexander Damm, Abdelaziz Kallel, Mirco Migliavacca, Juan Antonio Navas, Patrick Rademske and Uwe Rascher for scientific discussions. I would like to thank Forschungszentrum Jülich GmbH (Germany) and QuantaLab-IAS-CSIC (Spain) laboratories for assistance and support provided during the airborne campaigns, as well as IPSP-CNR (Italy), Dipartimento di Scienze del Suolo (Università di Bari, Italy), SpecLab (CCHS-CSIC, Spain) and ERSAF (UCO, Spain) personnel for their support during the field campaigns. And last but not least, the most special mention goes to my wife, who has not only sacrificed her time for mine but has made me grow as a person, inspiring me at every moment and making me feel better in my low moments, filling me with happiness during this long journey and making me smile when I needed it the most.

Dedicated to my grandparents, you will always continue to be an example of sacrifice and determination; you will always be in my heart. To my parents (in-law as well), my sister, my friends, for being there and sharing good times. To my daughters, África and Iris, for showing me the value of precious little moments. To Rocío, for all your support in this long journey and for giving me the best of yourself. Thank you.

List of Tables

List of Figures

List of Abbreviations and Acronyms

AERONET	AErosol RObotic NETwork
Anth	Anthocyanins
AOD	Aerosol Optical Depth
ARVI	Atmospherically Resistant Vegetation Index
ATSAVI	Adjusted Transformed Soil-Adjusted Vegetation Index
BRF	Bidirectional Reflectance Factor
Cab	Chlorophyll a+b content
Car	Carotenoids
CARI	Chlorophyll Absorption in Reflectance Index
Cdm	Dry matter content
CI	Chlorophyll Index
Cw	Water content
CWL	Central Wavelength
DART	Discrete Anisotropic Radiative Transfer model
DI	Disease Incidence
DS	Disease Severity
EFSA	European Food Safety Authority
EPPO	European and Mediterranean Plant Protection Organization
ESA	European Space Agency
(fA)PAR	(Fraction of Absorbed) Photosynthetically Active Radiation
FC	Fractional Cover
Fi	FLuorescence quantum efficiency
FLD	Fraunhofer Line Depth
FLEX	FLuorescence Explorer
FLIGHT	Forest Light model
FWHM	Full-Width at Half-Maximum
GEMI	Global Environment Monitoring Index
GNDVI	Green Normalised Difference Vegetation Index
GnyLi	Gnyp and Li index
GPP	Gross Primary Productivity
HPLC	High-Precision Liquid Chromatography
HS	HyperSpectral
FOV	Field Of View
IFOV	Instantaneous Field Of View
IRECI	Inverted Red-Edge Chlorophyll Index

LAI	Leaf Area Index
LIC3	Lichtenthaler index 3
LiDAR	Light Detection And Ranging
LUT	LookUp Table
MAE	Mean Absolute Error
MCARI	Modified Chlorophyll Absorption Ratio Index
MCRT	Monte Carlo Ray Tracing
MERIS	Medium Resolution Imaging Spectrometer
ML	Machine Learning
MND	Middle-infrared Normalised Difference
MODIS	Moderate Resolution Imaging Spectroradiometer
MSAVI	Modified Soil-Adjusted Vegetation Index
MSI	Multispectral Instrument
MSR	Modified Simple Ratio
MTB	Mean Temporal Background
MTCI	MERIS Terrestrial Chlorophyll Index
NASA	National Aeronautics and Space Administration
NDI	Normalised Difference Index
nDSM	Normalised Digital Surface Model
NDVI	Normalised Difference Vegetation Index
NRMSE	Normalised Root Mean Square Error
OA	Overall Accuracy
OCO-2	Orbiting Carbon Observatory 2
OSAVI	Optimised Soil-Adjusted Vegetation Index
PB	Persistent Background
Pc	*Phytophthora cinnamomi*
PCA	Principal Component Analysis
PRI	Photochemical Reflectance Index
PSSRa	Pigment Specific Simple Ratio A
PT	Plant Trait
qPCR	Quantitative Polymerase Chain Reaction
RAMI	Radiative Transfer Model Intercomparison
RF	Random Forest
RMSE	Root Mean Square Error
ROMC	RAMI On-line Model Checker
RT(M)	Radiative Transfer (Modelling)
S2	Sentinel-2

S2REP	Sentinel-2 Red-Edge Position
SAA	Solar Azimuth Angle
SAIL	Scattering by Arbitrary Inclined Leaves
SAVI	Soil-Adjusted Vegetation Index
SIF	Sun-Induced chlorophyll Fluorescence
SMARTS	Simple Model of the Atmospheric Radiative Transfer of Sunshine
SVM	Support Vector Machine
SWIR	Short-wave Infrared
SZA	Solar Zenith Angle
TANSO	Thermal And Near-infrared Sensor for Observation
TBP	Temporal Background per Plot
TCARI	Transformed Chlorophyll Absorption Ratio Index
Tc-Ta	Canopy temperature minus air temperature
TOC	Top Of Canopy
TROPOMI	TROPOspheric Monitoring Instrument
V(IS-)NIR	Visible and Near-InfraRed
VHR	Very High Resolution
VI	Vegetation Index
VIF	Variance Inflation Factor
Xf	*Xylella fastidiosa*
ΔDI	Relative increase of Disease Incidence
ΔDS	Relative increase of Disease Severity

Chapter 1

Introduction

1.1. Biotic and abiotic stresses in plants

Over the last decade, plant diseases and environmental stress have increased worldwide due to the global impact of anthropogenic and climate change, affecting the distribution and survival of many species and threatening to undermine human wellbeing (Sturrock *et al.*, 2011). Stress in plants may be either physical or chemical, known as abiotic stress; or biological, like diseases, insects, or pests, known as biotic. The co-occurrence of biotic and abiotic stressors is associated with massive and rapid increases in plant mortality in crops (Carvajal-Yepes *et al.*, 2019) and forest species (Forzieri *et al.*, 2021) that threaten the survival of these species (Ennos, 2015).

The occurrence of extreme weather events causes enormous damage to plant productivity and ecosystem sustainability (Allen *et al.*, 2015; Pareek *et al.*, 2020). Global warming is predicted to significantly increase the frequency of droughts and floods. Other significant abiotic stresses driven by climate change include an increase in soil salinity, heat stress and a decrease of soil fertility (Pandey *et al.*, 2017). Among all abiotic stressors, the temperature has been documented as a potent driver of drought accelerating forest decline and tree mortality across the globe (Park Williams *et al.*, 2013).

Several pests, diseases, and other biotic agents have considerable impacts on the vegetation all over the world. For example, *Phytophthora* is a genus of some 150 species with a broad host range devastating natural forest

ecosystems in several countries of Europe, Oceania and the USA. Only in Australia, more than 40% of native plant species are susceptible to *Phytophthora* dieback (Shearer *et al.*, 2004). In Europe, *Phythopthora*-induced diseases are one of the main causes of tree mortality in Fagus, Castanea and Quercus genera. Specifically, in the case of oak decline, root rot caused by *Phytophthora cinnamomi* (*Pc*) is considered the main driver causing tree death (Colangelo *et al.*, 2018; Ruiz Gómez *et al.*, 2018). This invasive pathogen, regarded as one of the main invasive species in forest ecosystems in the northern hemisphere (Burgess *et al.*, 2017), triggers several non-specific symptoms in oak trees, including general defoliation, crown desiccation or discolouration of the crown when the decay is regressive, or sudden tree death, with brown foliage remaining attached to the crown. Another example is the massive effect caused by *Xylella fastidiosa* (*Xf*), a phytopathogenic bacterium with the ability to inhabit the xylem of more than 500 plant species and causing extensive damage to multiple plants worldwide (Almeida and Nunney, 2015). The first outbreak of *Xf* in Europe was detected in olive orchards in Puglia (southern Italy) in 2013, and it has recently been identified in France and Spain officially (EFSA, 2018) and even more recently in Israel (EPPO, 2019). According to the latest studies (Saponari *et al.*, 2017), olive stands can be infected for more than five months without visible symptoms. During this period, the bacterium can spread within the xylem tissue and theoretically cause water-related stress that can lead, among other impacts, to lower transpiration and photosynthetic rates. Symptoms then become visible, with a progressive increase in discolouration and defoliation of tree crowns within several months, and leading to tree death within a few years.

Pathogen-induced symptoms are often aggravated by biotic stressors (Manion and Lachance, 1992; Trumbore *et al.*, 2015). Furthermore, climate warming has also increased the expansion of several pests and diseases and increased the severity of the damage caused to vegetation, resulting in massive agricultural production losses (Savary *et al.*, 2019) and forest dieback (Seidl *et al.*, 2018). In forests, the interaction of biotic and abiotic factors is more

intense than in crops, as the application of treatments that minimise the effects of environmental stress factors is more complex. Forest decline is a product of this complex multifactorial syndrome that responds to the high heterogeneity of natural ecosystems (Hutchings *et al.*, 2000). Over the last decade, forest decline has increased worldwide due to the global impact of anthropogenic and climate change, affecting the distribution and survival of many species and threatening to undermine human wellbeing (Allen *et al.*, 2010). Tree mortality in conifers (Camarero *et al.*, 2015) and broadleaved species presents a severe risk to the stability of forest ecosystems (Macpherson *et al.*, 2017).

There is a high likelihood for a plant to recover successfully from the damage caused by biotic and climate-induced physiological stress if the stress is temporal, short-term, and mild. However, severe or prolonged stresses induce plant senescence and lead to an irreversible process of decline. These two temporal stages can potentially be monitored with different plant traits (PTs), allowing the assessment of the severity and incidence. PTs are defined as anato-biochemical and morpho-pheno-physiological characteristics of plants, measurable at the individual level without reference to the environment, which impact plant fitness through their effects on growth, reproduction and survival (Kattge *et al.*, 2011; Violle *et al.*, 2007). Early detection of alterations of different functional traits of the plant is therefore essential to assess and monitor the vegetation's health status.

1.2. Spectral plant trait alterations as indicators of plant health

Plant functional traits, such as biochemical composition, chlorophyll fluorescence, water content and vegetation structure, are strongly related to vegetation health status and how plants respond to environmental and biotic stressors (Ahrens *et al.*, 2020). In particular, pathogen- and climate-induced plant decline typically involve two general stages: i) an early stage of stress

pressure or predisposition, during which a plant puts more energy into fighting off the pathogen, altering different biochemical PTs — e.g. leaf pigments and water content, and altering the emission of chlorophyll fluorescence — with non-visible symptoms, and ii) an intermediate to an advanced stage with visual symptoms altering different vegetation structure PTs — e.g. Leaf Area Index (LAI) and Fractional Cover (FC) — which is not easily reversed. It is essential to identify and monitor both stages, but plant die-off control is more effective when management practices, such as culling or clearance of affected plants, are applied at an early stage.

Monitoring alterations in PTs caused by biotic and abiotic factors is crucial to assessing vegetation response, as well as to anticipate abnormal responses early enough to enable the implementation of effective management responses (Cunniffe *et al.*, 2016). Defoliation and yellowing are the most common symptoms of vegetation change; thus, LAI and chlorophyll concentration have been extensively studied (Hernández-Clemente *et al.*, 2019). Passive sensors collecting information in the visible and infrared are mainly used to study these variables. Both defoliation and discolouration — by means of chlorophyll degradation (Zarco-Tejada *et al.*, 2019) — produce a decrease in the infrared signal and an increase in red and blue regions. This effect can be enhanced by the combination of spectral bands known as vegetation indices (VIs). Fig. 1.1 shows physiological indicators used to quantify early-stage vegetation health from multi/hyperspectral and thermal data.

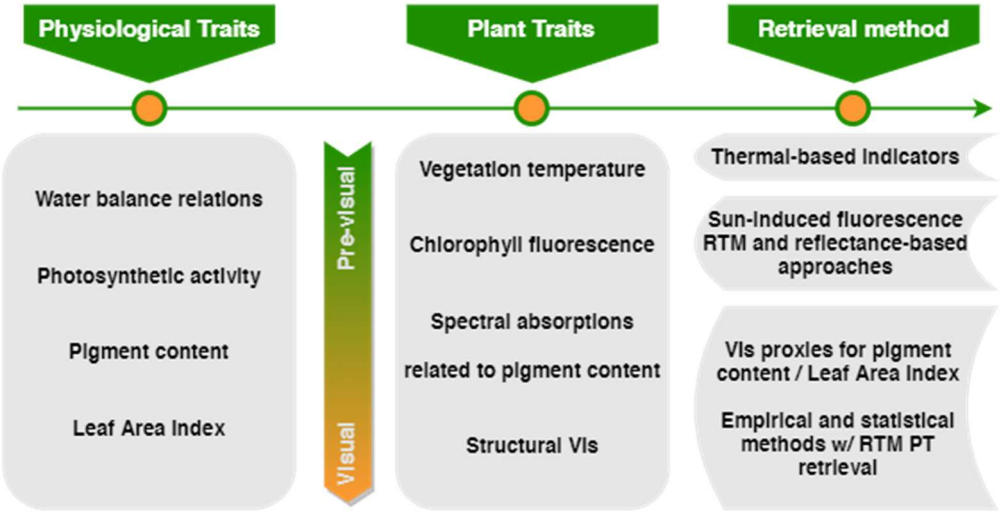

Figure 1.1 An overview of physiological indicators and plant traits characterisation.

Recent work has shown that early symptoms of *Xf* infection in olive trees are detectable through very high-resolution hyperspectral and thermal remote sensing images acquired from aerial platforms. These symptoms manifest as alterations in photoprotection mechanisms, reduced photosynthetic activity due to reduction and degradation processes of photosynthetic pigments, and decreased chlorophyll fluorescence emission and plant transpiration rates (Zarco-Tejada *et al.*, 2018a). Unfortunately, while airborne imaging spectroscopy allows for detecting early non-visible symptoms of *Xf* infection, such tree-level alterations cannot be directly detected by current satellite sensors due to their limited spectral and spatial resolutions. This raises the question of what alternatives we have if we are willing to cover larger areas or what kind of methodology would be appropriate when working with spatial resolutions where several environmental components are aggregated. Furthermore, unlike in homogeneous crops, the heterogeneity of discontinuous crop orchards and natural forest canopies in terms of species composition and structure and the differences between individuals due to microsite and ecophysiological conditions increase the spectral mixture, thus reducing the PTs' accuracy retrieved from the images.

1.3. Retrieval methods of physiological plant trait indicators

In recent years, several strategies have been implemented to retrieve PTs from spectral information: empirical relationships using different statistical regression methods, VIs, and radiative transfer models (RTMs). The empirical relationship is the classic approach to fit field data observations with spectral data or VIs. The main disadvantage of empirical relationships is their limited applicability at different spatial and temporal levels, but the advantage is that they can be easily used for a wide range of variables. The use of VIs as proxies for PTs is another relatively straightforward solution; however, the signal cannot be decoupled, and when working with lower spatial resolutions or looking at the physiological state of a particular component, one would be limited. RTMs are physically-based functions that simulate the light energy scattered or absorbed through different media. When the models are applied to the vegetation canopy, RTMs help to understand the interactions of radiation with vegetation and the atmosphere, accounting for variations in different geometries, illumination conditions, and scene components (e.g. canopy, understory, and soil). Thus, the use of RTM helps us better represent the high level of context dependency by allowing us to generalise the results to different environments.

1.3.1. Empirical relationships and VIs

Empirical methods can be parametric (e.g. linear models, generalised linear models, or non-linear models) or non-parametric (e.g. machine learning regression algorithms, random forest regressions, or neural networks) (Liu *et al.*, 2016). Typical parametric models to assess vegetation features from satellite passive optical observations include the use of VIs with linear and multiple regression models. In contrast, non-parametric approaches exploit the entire reflectance signal and are able to model non-linear relationships. Non-parametric approaches have been shown to work well with high-

dimensional and multicollinear hyperspectral data and have been shown to outperform linear parametric regression based on VIs (Verrelst *et al.*, 2015b).

The most widely used VI is the Normalised Difference Vegetation Index (NDVI). NDVI has been successfully applied for vegetation trend analysis (Beck *et al.*, 2011; Chen *et al.*, 2018; Fang *et al.*, 2018; Gillespie *et al.*, 2018) and for monitoring vegetation productivity, for instance, in olive groves (Brilli *et al.*, 2013; Noori and Panda, 2016). In addition to its strengths, the limitations of NDVI for vegetation monitoring have received significant attention in the literature (Montandon, 2009; Myneni *et al.*, 1991). These limitations stem from its sensitivity to soil and atmospheric characteristics, as well as its tendency to saturate in high biomass environments. Potential alternatives include the soil-adjusted vegetation index (SAVI) (Huete, 1988), the adjusted soil-transformed vegetation index (ATSAVI) (Baret and Guyot, 1991), the atmosphere-resistant vegetation index (ARVI) (Huete *et al.*, 1994), and the global environmental monitoring index (GEMI) (Pinty and Verstraete, 1992). For example, ARVI has a similar dynamic range to NDVI, but is on average four times less sensitive to atmospheric effects than NDVI (Kaufman and Tanre, 1992). However, the spectral mixture obtained with medium-resolution satellite observations inherently limits the extent to which VIs can extend field observations of plant functional traits to entire landscapes (Atzberger and Richter, 2012; Zurita-Milla *et al.*, 2015). Furthermore, the large contributions to canopy spectral reflectance produced by understory variation could have important implications for the applicability of VIs to the analysis of temporal change. The literature lacks studies focusing on the sensitivity of VIs to variations in both vegetation health and temporal evolution, including the contribution of changes in the understory that significantly affect the reflectance acquired by Sentinel-2 imagery.

1.3.2. Radiative transfer modelling in heterogeneous canopies

RTMs can overcome some of the typical limitations of strictly empirical approaches by minimising the dependence on field measurements and modelling the mixing of reflectance produced by different components' contribution at lower spatial resolution. These two factors are essential to improving the retrieval of vegetation biophysical parameters over time. In uniform vegetation canopies, 1-D RTMs such as SAIL (Verhoef, 1984) have been successfully used to monitor grass and crop stress (Bayat *et al.*, 2016; Martín *et al.*, 2007). However, modelling heterogeneous and discontinuous vegetation canopies requires complex 3-D RTM models that account for tree canopy structure and background effects. Previous studies have used 3-D models such as FLIGHT (North, 1996) to provide a three-dimensional representation of tree canopies to adequately characterise the spatial heterogeneity of the tree canopy (Hernández-Clemente *et al.*, 2012; Kötz *et al.*, 2004; Liu *et al.*, 2020; Roberts *et al.*, 2020) or even to perform spatial and spectral scaling of different biophysical variables (Bye *et al.*, 2017; Hernández-Clemente *et al.*, 2017). Still, none of these models includes the effects produced by the understory on spectral reflectance in open canopies. Understory variations are especially important in natural environments, with high impacts on analysing time series data over heterogeneous and sparse canopies (Assal *et al.*, 2016; Yang *et al.*, 2014). Yet, at the same time, the large number of parameters needed in even more complex 3-D models can limit inversion procedures (Hernández-Clemente *et al.*, 2014; Yáñez-Rausell *et al.*, 2015), and further research is required in order to understand the impact of structural components from medium (10–60 m/pixel) and high ($<$ 10 m/pixel) spatial resolution imagery.

In this context, models are essential to relate observed optical properties to biophysical and biochemical attributes of leaves and analyse the effect of heterogeneous canopy structures at different spatial resolutions (Wu and Li, 2009). Several methods have been proposed to estimate biochemical traits

from hyperspectral reflectance, including model scaling and inversion methods that couple leaf and canopy transfer models (Verrelst *et al.*, 2018). Other strategies include using proven linear spectral unmixing techniques to separate the spectral properties of forest floor and understory components (Markiet and Mõttus, 2020). Despite the progress made, this modelling approach does not yet include the contribution of fluorescence and the impact of multiple scattering between tree and understory components and the background layer.

Regarding sun-induced chlorophyll fluorescence (SIF) emission, recent studies have included its modelling at leaf (Kallel, 2020; Pedrós *et al.*, 2010; Vilfan *et al.*, 2018, 2016) and canopy levels in homogeneous (Atherton *et al.*, 2019; Romero *et al.*, 2020; Yang and van der Tol, 2018; Zeng *et al.*, 2019) and heterogeneous (Hernández-Clemente *et al.*, 2017; Liu *et al.*, 2019; Zhao *et al.*, 2016) canopies. In addition, previous studies have attempted to account for spatial heterogeneity using the first available model-based approaches (Zarco-Tejada *et al.*, 2013a). Airborne sensors such as HyPlant, the first fluorescence sensor specifically designed to support the FLEX mission that is aimed at validating SIF retrieval for a large canopy and different vegetation types (Rascher *et al.*, 2015), can provide valuable information with which to better model and understand the effect of SIF signals among mixed pixels.

The impact of background components on SIF could particularly affect seasonal analyses, in which the temporal variation of the understory fraction is high. Forest areas such as holm oak trees, or heterogeneously cultivated areas such as olive trees, have complex canopy structures and the distribution of the understory cover fraction depends mainly on topography, canopy positions, soil composition, and lighting conditions. Consequently, assuming an invariant and homogeneous soil effect as background could increase the uncertainty of biophysical parameters retrieved from high- and medium-resolution images (Tagliabue *et al.*, 2019). These previous studies have demonstrated the need to develop new modelling approaches that consider multiple

scattering, cross-shading of canopies, soil variation, and the background in the retrieval of SIF.

1.3.3. Current strategies to improve the retrieval of physiological indicators

There is extensive literature focused on developing quantitative methods to estimate vegetation canopy composition from images by applying empirical or physical RTM (Berjón *et al.*, 2013). Given that diseases generate changes in the specific composition of the tree canopy, the development of these methods opens a new pathway in the analysis of the evolution of new diseases. An emerging alternative method is the combined use of PTs retrieved using RTM and VIs with combinations in the visible, near-visible, and shortwave infrared spectral bands. In that context, an essential aspect in VI applicability is to make a proper selection of formulations that best represent the composition by formulating, testing and modifying a large number of VIs to describe the amount of biomass loss that occurs at very advanced disease stages (Castrignano *et al.*, 2020). Plant disease diagnosis has been demonstrated to require quantification of forest biomass and the physiological state of that biomass, based on functional PTs such as photosynthetic rate, water stress, anthocyanins chlorophyll a and b, and leaf carotenoid content (Hernández-Clemente *et al.*, 2019).

Recently, new possibilities have been developed using photon-vegetation interaction to detect plant physiological status, based on detecting SIF emission and thermal dissipation (Gonzalez-Dugo *et al.*, 2014; Mohammed *et al.*, 2019; Zarco-Tejada *et al.*, 2012). SIF, a faint glow produced by plant leaves, is a reliable indicator of photosynthetic activity in forest canopies and can, therefore, be used as a powerful non-invasive marker to monitor vegetation condition, resilience, and recovery.

Nonetheless, the contribution of different PT indicators remains largely unknown in forest species. Detecting the specific contribution of PT indicators

for the anticipation of forest decline processes is especially relevant to choosing the suitable sensors for assessing damage and monitoring the right indicators during the decline process.

1.4. Upscaling plant traits from remote sensing data for large-scale plant health monitoring

The retrieval of PT at larger scales is essential to extrapolating local information to a larger context. For operational plant health monitoring, the development of robust and accurate tools for the effective and timely diagnosis of plant health is still needed: first, to reduce the spread of diseases, and second, to increase the efficiency of plant management treatments, e.g. for reducing crop yield and forest biomass losses (Hernández-Clemente *et al.*, 2019; Sisterson *et al.*, 2010).

The plant spectral signature provides a powerful and reduced cost alternative to field measurements to quantify the biochemical composition and functionality of vegetation over large areas (Homolová *et al.*, 2013; Rocha *et al.*, 2019). Remote sensing is a fundamental tool for the spatio-temporal analysis of vegetation's physiological status using different PT indicators and allowing us to consider not only the effects of late stages of disease (e.g. defoliation or chlorosis) but also pre-visual early detection variables due to stomatal closure or reduced photosynthesis. Therefore, large-scale early detection of PTs is one of the most critical factors for plant health monitoring and management.

Unfortunately, retrieving PTs for large-scale monitoring in heterogeneous canopies is challenging due to spectral mixing effects produced by the structure of the vegetation canopy, shadows and understory. The development of techniques that facilitate the assessment and quantification of the vegetation condition in both time and space is a fundamental step in disease control. The use of spectral information collected from image time series allows the recording, analysis and detection of vegetation changes produced by various

factors such as environmental and seasonal changes or decay processes modifying the physiology, morphology and phenology of plants. The PTs' determination that characterises these changes can be retrieved from high-resolution hyperspectral airborne data or satellite imagery.

1.4.1. Use of high-resolution airborne data

The use of airborne sensors with high spatial and spectral resolution provide not only the desired timing but also the acquisition of an increased number of narrow and contiguous bands, which at the same time enables a better and more detailed description of the electromagnetic spectrum, and thus more accurate performance in the estimation of biochemical and biophysical parameters. Besides, the temporal resolution of airborne images can be used to establish trends in vegetation and detect any alteration caused by diseases or other abiotic agents. For this purpose, different statistical techniques adapted to time series analysis have been proposed so far (Paruelo *et al.*, 2005).

In heterogeneous vegetation canopies, high-resolution images ($<$ 10 m/px) are needed to distinguish the canopy and understory from the background (Wagner et al., 2018). Therefore, quantifying the contribution of each pixel helps to improve and understand the models used to quantify biophysical parameters from mixed pixels (Yu *et al.*, 2018). Additionally, the impact of the understory on canopy reflectance is particularly challenging for studying complex canopies comprising different plant architectures and physiology (Eriksson *et al.*, 2006). Therefore, it is essential to quantify the contribution of each component of the subpixel scene in mixed canopies characterised by a heterogeneous distribution of trees and understory when working with satellite imagery at medium (10–500 m/px) and low ($>$ 500 m/px) spatial resolutions. Furthermore, temporal changes in the physiological state and composition of the understory also have an effect on the relationships between satellite data and vegetation properties due to the impact of mixed pixels.

1.4.2. Use of satellite image data

Satellite missions such as Sentinel-2 are particularly relevant for operational vegetation monitoring. This mission's specific objective is to provide multispectral data with a high spatial and temporal resolution using two simultaneous satellites. The spectral bands of the multispectral instrument have been designed to study the land surface and offer a unique opportunity to monitor vegetation health. Another recent mission of high relevance, to be launched in 2023, is FLEX (FLuorescence EXplorer), which aims to gain a deeper understanding of how the photosynthesis process works by making global measurements of fluorescence and how photosynthesis affects the water and carbon cycles; measurements that will provide further insight into plant health and stress.

Sentinel-2 satellite imagery is freely available and combines moderate to high spatial resolution (60 to 10 m) in 13 spectral bands, with a revisit time of about five days. Thanks to their combination of spatial, spectral, and temporal resolution, Sentinel-2 data could, in theory, be used to help monitor disease propagation over entire regions at a frequency that cannot be achieved by other means. Studies prior to the launch and using simulated Sentinel-2 data products demonstrated the sensor's ability to measure biophysical variables such as chlorophyll content (Frampton *et al.*, 2013) and leaf area index (Herrmann *et al.*, 2010). The added value of Sentinel-2 red-edge bands consists of increased accuracy for estimating chlorophyll content (Zarco-Tejada *et al.*, 2019), FC of forest canopies, quantification of LAI (Korhonen *et al.*, 2011), and ground cover mapping (Forkuor *et al.*, 2018). Thus, Sentinel-2 data extend the possibility of using passive optical satellite data for vegetation monitoring, especially in heterogeneous and complex canopies (Lange *et al.*, 2017). The temporal resolution of Sentinel-2 can report trends in vegetation characteristics affected by infectious agents more accurately than other satellites such as Landsat (Rahimzadeh-Bajgiran *et al.*, 2018) or MODIS (Mura *et al.*, 2018). Recent studies have investigated the actual sensor capabilities to monitor temporal changes in vegetation

activity in different canopy types such as wetlands (Araya-López *et al.*, 2018; White *et al.*, 2017), grasslands (Hill, 2013) and forests (Castillo *et al.*, 2017; Zarco-Tejada *et al.*, 2018b).

Despite the great potential of Sentinel-2, its spatial resolution causes pixel mixing effects that make it difficult to separate the contribution of different components of the canopy scene, such as soil, shadows, and understory, especially in open vegetation canopies. The mixture of canopy components makes it difficult to scale up plant functional traits from pure canopy views to broader spatial scales. Besides, the understory and soil in heterogeneous vegetation canopies vary spatially and seasonally due to vegetation phenology and understory dynamics, which affects multi-temporal spectral datasets. While airborne imaging spectroscopy allows, for instance, the detection of early and even non-visible symptoms of *Xf* infection (Zarco-Tejada *et al.*, 2018a), such tree-level disturbances cannot be directly detected by current satellite sensors due to their limited spectral and spatial resolutions. A hypothesis, however, is that symptoms in the intermediate and advanced stages of the disease, which are visible in the form of leaf browning, wilting, chlorosis and leaf desiccation, should be observable in satellite images, such as the ones acquired by the Sentinel-2 satellite sensor, mainly due to spectral bands located in the red-edge region, which is sensitive to photosynthetic pigment absorption, and the feasibility of tracking structural changes due to the NIR bands. Satellite monitoring of these symptoms could support the tracking of outbreaks, providing spatial distribution related to its epidemiology and contributing to the assessment of vegetation health by environmental managers and other end-users. Also, this satellite's short revisit interval at moderate latitudes (up to 2–3 days) provides critical temporal information on short-term variation in vegetation condition over large areas.

1.5. Objectives and thesis structure

This thesis is focused on the quantitative estimation of vegetation traits and dynamics using high-resolution hyperspectral data and medium resolution satellite imagery, and radiative transfer modelling. Four specific objectives were defined and addressed in this research:

- Assessment of the ability of PT and biophysical properties of the vegetation to monitor incidence and severity disease levels in *Xf* and *Pc* affected areas
- Assessing non-visual early indicators using spectral vegetation indices from high-resolution imagery and satellite-based observation
- Developing and evaluating a methodology for PT retrieval using 3-D RTM and high-resolution hyperspectral and thermal images
- Establishing the basis for the scaling up of PTs at different spatial resolutions using RTM tailored to the spatial and spectral resolution of satellite imagery for the retrieval of vegetation traits over different vegetation canopy types

The methodology and developments carried out in the preparation of this thesis have had the main purpose of providing a valuable contribution to improve the understanding of vegetation dynamics and the early detection of diseases, improving an existing radiative transfer model to enhance its capabilities, which have not been contemplated to date in the monitoring of the physiological state of vegetation, and finally, paving the way for future studies that should focus on the decoupling of the signal at lower resolutions through the use of satellite by applying the proposed methodologies over large regions.

This thesis covers five chapters. The **first chapter** provides a general overview; the **last chapter** offers the synthesis and concluding remarks, discussing them in a broad context and showing their implications and future

practical applications; and the three middle chapters represent individual research projects (Fig. 1.2), two of which are published in Remote Sensing of Environment, with the third currently under review. The particular objectives for these chapters are as follows:

- **Chapter 2**: Determining whether satellite data could be used to monitor *Xf*-induced temporal changes is key to providing information on *Xf*'s epidemiology spread over large areas. Thus, the applicability of spectrum-based indicators for disease detection on a larger scale using satellite data is one of the questions initially raised in this work, with an additional research question focused on assessing the feasibility of modelling changes in this disease from multi-temporal Sentinel-2 imagery data using VI and RTM.

- **Chapter 3**: In order to better understand the SIF modelling from coarse spatial resolutions in heterogeneous canopies, the need arises to modify an existing RTM model by considering the separate contribution of tree canopy and background components. More specifically, this objective is based on analysing the contribution of SIF emitted by the understory in aggregated pixels using high spectral and spatial resolution images collected from a high-resolution hyperspectral system dedicated explicitly for this purpose. Likewise, this would help us to provide a deeper understanding of the impact of the variation in understory cover fraction on the total SIF calculated at different scales.

- **Chapter 4**: Implementing the retrieval and identification of the specific PTs that contribute most to recognising early symptoms of oak decline is the primary goal of the work in this chapter, providing continuity to the underlying objective of understanding the contribution of different PTs in the analysis of symptomatic and asymptomatic trees affected by biotic and abiotic stressors. Making use of the model developed in the previous chapter, we aim to build a PT

analytical approach for the detection and assessment of severity levels in the early detection of vegetation decline.

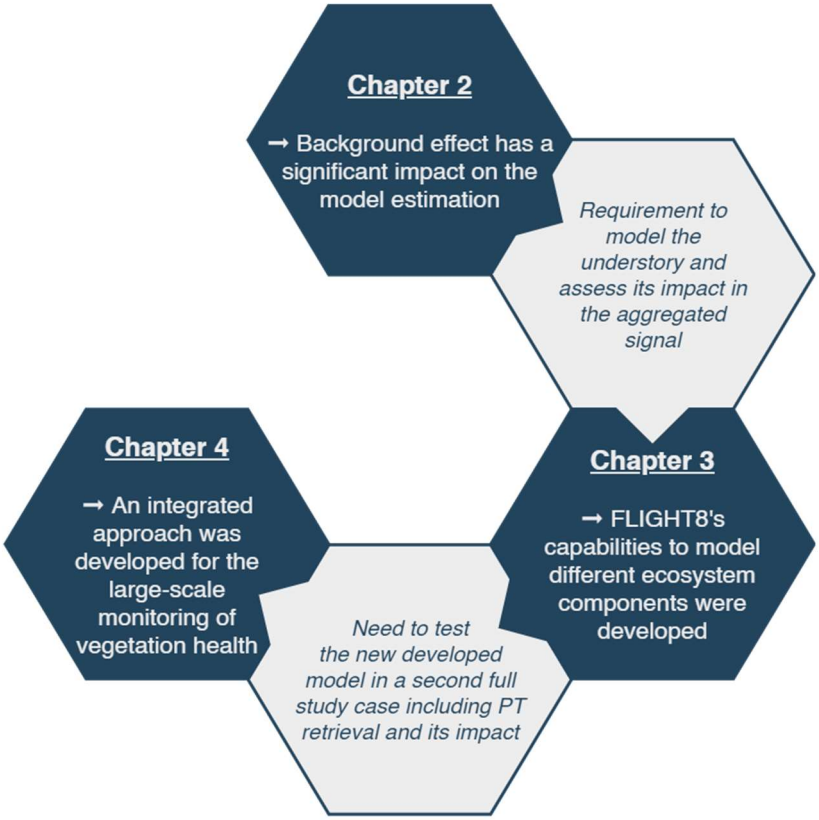

Figure 1.2 Flow between middle chapters highlighting the key connections motivating the research development.

In an effort to integrate the material published in various academic journals into a more traditional thesis structure, the chapters have been reformatted to give them coherence. For ease of reference, all figures and tables have been listed and combined at the beginning of this thesis, and the references have been incorporated and arranged at the end of it.

Chapter 2

Monitoring the incidence of *Xylella fastidiosa* infection in olive orchards using ground-based evaluations, airborne imaging spectroscopy and Sentinel-2 time series through 3-D radiative transfer modelling

Abstract

Outbreaks of *Xylella fastidiosa* (*Xf*) in Europe generate considerable economic and environmental damage, and this plant pest continues to spread. Detecting and monitoring the spatio-temporal dynamics of the disease symptoms caused by *Xf* at a large scale is key to curtailing its expansion and mitigating its impacts. Here, we combined 3-D radiative transfer modelling (3D-RTM), which accounts for the seasonal background variations, with passive optical satellite data to assess the spatio-temporal dynamics of *Xf* infections in olive orchards. We developed a 3D-RTM approach to predict *Xf* infection incidence in olive orchards, integrating airborne hyperspectral imagery and freely available Sentinel-2 satellite data with radiative transfer modelling and field observations. Sentinel-2A time series data collected over a two-year period were used to assess the temporal trends in *Xf*-infected olive orchards in the Apulia region of southern Italy. Hyperspectral images spanning the same two-year period were used for validation, along with field

surveys; their high resolution also enabled the extraction of soil spectrum variations required by the 3D-RTM to account for canopy background effect. Temporal changes were validated with more than 3000 trees from 16 orchards covering a range of disease severity (DS) and disease incidence (DI) levels. Among the wide range of structural and physiological vegetation indices evaluated from Sentinel-2 imagery, the temporal variation of the Atmospherically Resistant Vegetation Index (ARVI) and Optimized Soil-Adjusted Vegetation Index (OSAVI) showed superior performance for DS and DI estimation ($r^2_{VALUES}>0.7$, $p<0.001$). When seasonal understory changes were accounted for using modelling methods, the error of DI prediction was reduced 3-fold. Thus, we conclude that the retrieval of DI through model inversion and Sentinel-2 imagery can form the basis for operational vegetation damage monitoring worldwide. Our study highlights the value of interpreting temporal variations in model retrievals to detect anomalies in vegetation health.

2.1. Introduction

Xylella fastidiosa (*Xf*), a plant pathogenic bacterium that can live in the xylem of more than 300 plant species, causes severe damage to multiple crops around the world, including olive trees and stone fruits (Almeida and Nunney, 2015). The first outbreak of *Xf* in Europe was detected in olive orchards in Apulia (southern Italy) in 2013 (Saponari *et al.*, 2017), and the pathogen has now been officially identified in France and Spain (EFSA, 2018) and very recently (2019) in Israel (EPPO, 2019). According to Saponari *et al.* (2017), olive stands can be infected for more than five months without visible symptoms. During this period, the bacterium can spread within the xylem tissue and, theoretically, cause water-related stress that may lead to, among other things, lower transpiration and photosynthetic rates. Symptoms then start to become visible, with a progressive increase in discolouration and defoliation of the tree crowns within a few months, leading to tree death within a few years.

Accurate detection and diagnosis of *Xf* symptoms is critical for the operational monitoring of *Xf* spread and for the reduction of losses in crop yield (Sisterson *et al.*, 2010). Recent work showed that early symptoms of *Xf* infection in olive trees are detectable through very high-resolution hyperspectral and thermal remote sensing images acquired from airborne platforms: these symptoms manifest as alterations in photoprotective mechanisms, reduction in photosynthetic activity due to photosynthetic pigment reduction and degradation processes, and decreased chlorophyll fluorescence emission and plant transpiration rates (Zarco-Tejada *et al.*, 2018a). Unfortunately, while airborne imaging spectroscopy permits the detection of early and even non-visible symptoms of *Xf* infection, such tree-level alterations cannot be detected directly by current satellite sensors due to their limited spectral and spatial resolutions. However, we hypothesise that symptoms at intermediate to advanced stages of *Xf* disease, which are visible as leaf browning, wilting, chlorosis, and desiccation of leaves, should be observable in Sentinel-2 satellite data due in large part to the spectral bands located in the red-edge region, which is sensitive to photosynthetic pigment absorption. Satellite-based monitoring of such symptoms could support the monitoring of *Xf* spread over large areas, providing the spatial distribution related to the epidemiology of *Xf* and contributing to the assessment of vegetation health by environmental managers and other end-users. Furthermore, the short revisit interval (up to every 2–3 days) of this satellite at moderate latitudes provides key temporal information about short-term variation in vegetation status over large areas.

Sentinel-2 images from 2015 on are freely available and combine moderate-to-high spatial resolution (10 to 60 m) in 13 spectral bands, with a revisit time of five days. Given their combination of spatial, spectral, and temporal resolution, Sentinel-2 data could, in theory, be used to help monitor the spread of *Xf* over entire regions with a frequency not achievable by other means. Pre-launch studies using simulated Sentinel-2 data products demonstrated the potential of the sensor to measure biophysical variables such as chlorophyll content (Frampton *et al.*, 2013) and leaf area index (Herrmann

et al., 2011). The added value of the Sentinel-2's red-edge bands consists of increased accuracies for the estimation of chlorophyll content (Zarco-Tejada *et al.*, 2019), the fractional cover (FC) of forest canopies, the quantification of leaf area index (LAI) (Korhonen *et al.*, 2011), and land-cover mapping (Forkuor *et al.*, 2018). Sentinel-2 data thus widen the possibility of using passive optical satellite data for vegetation monitoring, particularly in non-homogeneous and complex canopies (Lange *et al.*, 2017). The temporal resolution of Sentinel-2 can report trends in vegetation characteristics affected by infective agents with higher accuracy than other satellites such as Landsat (Rahimzadeh-Bajgiran *et al.*, 2018) or MODIS (Mura *et al.*, 2018). Recent studies have investigated the actual capabilities of the sensor for monitoring temporal changes in vegetation activity in canopy types such as wetlands (Araya-López *et al.*, 2018; Whyte *et al.*, 2018), grasslands (Hill, 2013) and forests (Castillo *et al.*, 2017; Zarco-Tejada *et al.*, 2018b). To the extent of our knowledge, no prior studies have explored the applicability of Sentinel-2 to evaluation of the spectral variations produced by *Xf*-induced disease.

Despite the widespread interest in Sentinel-2, its spatial resolution causes mixed-pixel effects that make it challenging when attempting to separate the contribution of the different canopy-scene components such as soil, shadows, and understory, particularly in open vegetation canopies. This aspect is critical in the case of olive orchards, where planting densities are typically in the range of 200 to 2000 trees/ha and the canopy is rarely closed (Sibbett and Ferguson, 2005). The mixture of canopy-scene components hampers the scaling up of plant functional traits from views of pure tree crowns to broader spatial scales. Furthermore, the understory and soil in these landscapes vary spatially and seasonally as a result of vegetation phenology, agricultural practices, and soil–vegetation understory dynamics, impacting the multi-temporal spectral datasets.

Common approaches to assessing vegetation traits from passive optical satellite observations include the use of vegetation indices (VIs) and radiative transfer models (RTMs). The Normalized Difference Vegetation Index

(NDVI) has been widely applied for vegetation trend analysis (Beck *et al.*, 2011; Fang *et al.*, 2018; Gillespie *et al.*, 2018) and to monitor vegetation productivity in olive groves (Brilli *et al.*, 2013; Noori and Panda, 2016). In addition to its strengths, the limitations of NDVI for vegetation monitoring have received much attention in the literature (Montandon, 2009; Myneni *et al.*, 1991); these limitations stem from its sensitivity to soil and atmospheric features, and its tendency to saturate in high-biomass environments. Potential alternatives include the Soil-Adjusted Vegetation Index (SAVI) (Huete, 1988), Adjusted Transformed Soil-Adjusted Vegetation Index (ATSAVI) (Baret and Guyot, 1991), atmospherically resistant vegetation index (ARVI) (Huete *et al.*, 1994) and Global Environment Monitoring Index (GEMI) (Pinty and Verstraete, 1992). For instance, ARVI has a similar dynamic range to NDVI, but on average it has been demonstrated to be four times less sensitive to atmospheric effects compared to NDVI (Kaufman and Tanre, 1992). However, the spectral mixture obtained with medium-resolution satellite observations inherently limits the extent to which VIs can scale up field observations of plant functional traits to entire landscapes (Atzberger and Richter, 2012; Zurita-Milla *et al.*, 2015). In addition, the large contributions to the spectral reflectance of the canopy produced by variation in the understory could have important implications for the applicability of VIs to temporal change analysis. The literature lacks studies focused on the sensitivity of VIs to variations in both vegetation health and temporal change, including the contribution of changes in the understory that heavily affect the reflectance acquired by Sentinel-2 images.

RTMs can overcome some of these typical limitations of purely empirical approaches, minimising the dependence on field measurements and modelling the reflectance mixture produced by the contribution of different components at medium resolutions. These two factors are essential to improving the retrieval of biophysical vegetation parameters over time. For uniform canopies, 1-D RTMs such as SAIL (Verhoef, 1984) have been successfully used to monitor grass and crop stress (Bayat *et al.*, 2016; Martín *et al.*, 2007). However, modelling heterogeneous and discontinuous vegetation

canopies requires complex 3-D RTM models that account for tree canopy structure and background effects. Previous studies have used FLIGHT to provide a 3-D representation of tree canopies and perform the spatial and spectral scaling of different biophysical variables (Bye *et al.*, 2017; Hernández-Clemente *et al.*, 2017). Still, none of these models includes the effects produced by the understory on the spectral reflectance in open canopies. The variations in understory are especially important in natural environments, with high impacts on time-series data analysis over heterogeneous and sparse canopies (Assal *et al.*, 2016; Yang *et al.*, 2014). Other RTMs such as DART (Gastellu-Etchegorry *et al.*, 1996) have overcome these limitations and could particularly benefit the simulation of the canopy. By contrast, the large number of parameters needed in complex 3-D models limits the inversion procedures (Hernández-Clemente *et al.*, 2014; Yáñez-Rausell *et al.*, 2015).

Here, we investigate the suitability of Sentinel-2 satellite images for monitoring disease symptoms in *Xf*-infected olive orchards. Using field observations and multi-temporal remote sensing data, we assessed (i) the capability of physiological and structural VIs calculated from Sentinel-2 imagery to accurately evaluate DI and DS in olive orchards infected by *Xf* in southern Italy, and (ii) whether the application of a 3-D radiative transfer model to account for temporal changes in the soil and understory improves the prediction of *Xf*-disease incidence from Sentinel-2 time-series data.

2.2. Materials and methods

2.2.1. Study site and field data collection

The study was conducted in an olive-growing area (*Olea europaea* L.) in Apulia (southern Italy, 40°30′50″N, 18°01′50″E) where *Xf* was officially detected for the first time in October 2013 (Fig. 2.1). The phytosanitary

measures implemented have been unsuccessful in preventing the spread of *Xf* throughout southern Apulia. The area is characterised by a temperate climate with mild winters and a landscape dominated by olive orchards that favour the natural spread of *Xf* (Saponari *et al.*, 2017; Strona *et al.*, 2017). By 2015, the pathogen had spread to ca. 275,000 ha in the region, and it currently affects an area greater than 600,000 ha (labelled as 'Infected zone' in Fig. 2.1A).

Figure 2.1 Sentinel 2A scene of southern Italy (large inset, A) with an overlay (green box, B) in which airborne hyperspectral mosaics are shown. The three hyperspectral images were acquired from aircraft on 28 June 2016 with a micro-hyperspectral imager (red box, C) yielding 40-cm spatial resolution. The infected zone highlighted in the main map (A) outlines the area where *Xylella fastidiosa* has been observed as of March 2018 (Commission Implementing Decision (EU) 2018/927, 2018)

Field surveys were carried out in 16 olive orchards located in the *Xf*-infected zone in which qPCR analysis had confirmed its presence (Zarco-Tejada *et al.*, 2018a). During the surveys, disease severity (DS) and disease incidence

(DI) were assessed for 3300 olive trees. Seem (1984) defines DS as the quantity of disease that is affecting entities within a sampling unit; DI is a quantal measure, defined as the proportion or percentage of diseased entities within a sampling unit. DS thus accounts for disease severity, while DI only considers whether a tree is affected or not. DI is, therefore, quicker and easier to measure, and generally more accurate and reproducible than other quantitative measures, making it the commonly preferred measurement method for the detection and enumeration of disease propagation patterns (Horsfall and Cowling, 1978). Based on visual inspection, we assigned individual trees to one of the five DS categories available (Fig. 2.2) depending on the proportion of the crown affected by typical *Xf* symptoms including desiccation and discolouration of leaves and branches. DS ranged from 0, indicating the absence of symptoms, to 4, when most of the branches in the crown were dead (Table 2.1). DI was either 0 or 1, indicating non-symptomatic trees and symptomatic trees, respectively, where non-symptomatic trees corresponded to a DS of 0 and symptomatic trees to any other severity (DS>0; Fig. 2.2) From these assessments for each tree, we calculated the average DS and DI of all trees for each orchard (DSo and DIo, respectively).

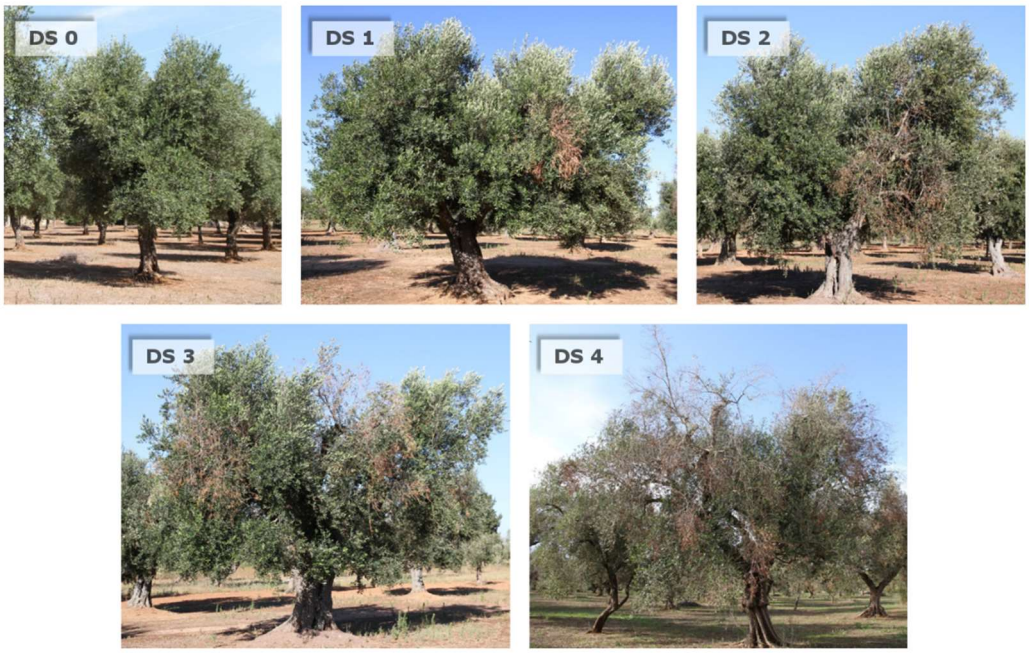

Figure 2.2 Examples of the five disease severity (DS) classes that olive trees (n=3300) were assigned to during a field survey in 2016 that was repeated in 2017. The classes related to the extent of severity of typical visual symptoms of *Xylella fastidiosa* ranging from apparently healthy trees (DS=0) to trees showing canopies with a prevalence of dead branches (DS = 4).

Table 2.1 *Xylella fastidiosa* evaluation criteria: crown-level severity and incidence assignment.

DS Level	Severity	Description	Desiccation	Incidence
0	Healthy	Symptomless	0%	No incidence
1	Initial severity	Few desiccated branches affecting a limited part of the canopy	$> 0 \leq 25\%$	Incidence
2	Medium severity	Desiccation affecting a large part of the canopy	$> 25 \leq 50\%$	Incidence
3	High severity	Canopy with desiccated branches uniformly distributed	$> 50 \leq 75\%$	Incidence
4	Very high severity	Severe tree decline	$> 75\%$	Incidence

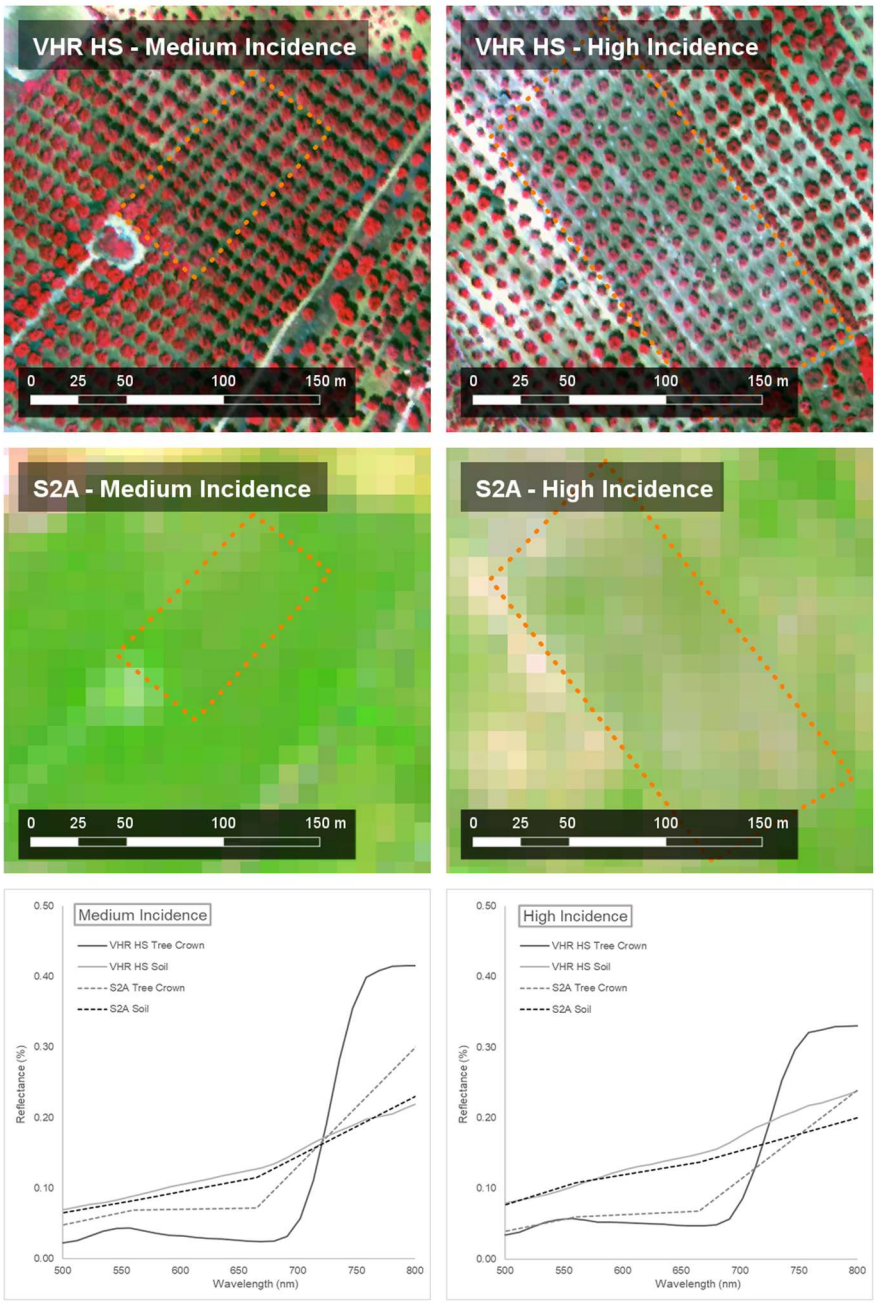

Figure 2.3 Example of olive orchards with medium (left panels) and high (right panels) incidence of *Xf*-related disease, viewed by an airborne high-resolution narrow-band hyperspectral camera (VHR HS, top row), by Sentinel-2A (S2A, middle row, RGB-composite of bands B3, B2 and B4) and through their spectral signatures captured by the VHR HS and S2A (bottom row).

The first field survey was conducted in June 2016 and observed 48.5% of the trees to be asymptomatic; when the survey was repeated in July 2017, this value was 15.2%. Symptomatic trees were identified in all sampled orchards in both years, with a minimum DIo of 25.0% and 63.9% in 2016 and 2017, respectively. These values reflect the fact that all of the olive orchards across a very large region, extending more than 50 km from our study sites, are infected to some degree (Fig. 2.1). Given the ubiquity of *Xf* in such area and the challenge of locating an area free of *Xf*, a direct comparison between *Xf*-infected and *Xf*-free orchards experiencing similar environmental conditions was not possible. The relative increase of *Xf* infection in the surveyed orchards, expressed as ΔDS and ΔDI, was measured based on the DSo and DIo observed between the 2016 and 2017 field surveys as:

$$\Delta DS = (DSo_{\text{year n+1}} - DSo_{\text{year n}}) / DSo_{\text{year n}} \quad (1)$$

$$\Delta DI = (DIo_{\text{year n+1}} - DIo_{\text{year n}}) / DIo_{\text{year n}} \quad (2)$$

where values above zero for ΔDS and ΔDI imply an aggravation of the visual symptoms, zero values correspond to orchards with no significant changes, and values below zero indicate a lessening of visual symptoms in an orchard.

2.2.2. Sentinel-2A imagery

A temporal dataset of Sentinel-2 images was used to analyse the feasibility of detecting the ΔDS and ΔDI of *Xf* infection using VI trends. The Multispectral Instrument (MSI), on board Sentinel-2A, acquires imagery at a 10-day interval under constant viewing conditions, which results in 4- to 6-day revisit times at mid-latitudes due to the swath overlap between neighbouring orbits. The MSI measures reflected radiance in 13 spectral bands from visible and near-infrared (VNIR) to short-wave infrared (SWIR), with images at 12 bits per channel and a spatial resolution of 10 m (Central Wavelength [CWL] at 496.6, 560.0, 664.5 and 835.1 nm with a bandwidth of 98, 45, 38 and 145

nm, respectively), 20 m (CWL at 703.9, 740.2, 782.5, 864.8, 1613.7 and 2202.4 nm with a bandwidth of 19, 18, 28, 33, 143 and 242 nm, respectively) and 60 m (CWL at 443.9, 945.0 and 1373.5 nm with a bandwidth of 27, 26 and 75 nm, respectively).

We used the multi-temporal Sentinel-2A data available for the first two complete years after its launch in 2015 to build a multi-temporal spectral dataset from the 86 cloud-free Sentinel-2A images (Level-1C, ortho-rectified imagery expressed in top-of-atmosphere reflectance) (Richter *et al.*, 2011) available from July 2015 to August 2017. From Level-1C, the images were atmospherically corrected to generate Level-2A (bottom-of-atmosphere – surface reflectance – provided with a pixel classification mask) with Sen2Cor (version 2.3.1). Using the scene classification from Level-2A, we then filtered the data that were affected by clouds or cirrus before calculating a suite of VIs.

We selected spectral VIs that are primarily sensitive to canopy structure or pigment concentration and compatible with the spectral bandset of Sentinel-2. The equations and references for each VI are shown in Table 2.2. More precisely, we calculated (i) conventional and corrected ratio and normalised indices derived from the near-infrared and red bands such as the Normalized Difference Vegetation Index (NDVI), Modified Simple Ratio (MSR), Green Normalized Difference Vegetation Index (GNDVI) and Renormalized Difference Vegetation Index (RDVI); (ii) conventional soil-adjusted indices such as the Adjusted Transformed Soil-Adjusted VI (ATSAVI), Optimized Soil-Adjusted Vegetation Index (OSAVI) and Modified Soil-Adjusted Vegetation Index (MSAVI), and corrected versions using SWIR bands such as $OSAVI_{1510}$; (iii) conventional and corrected chlorophyll VIs such as the Chlorophyll Index (CI), Normalized Difference Index (NDI), Medium Resolution Imaging Spectrometer (MERIS) Terrestrial Chlorophyll Index (MTCI), Pigment Specific Simple Ratio A (PSSRa), Sentinel-2 Red-Edge Position (S2REP), and Inverted Red-Edge Chlorophyll Index (IRECI); and (iv) chlorophyll indices formulated to minimise their sensitivity to structural effects

based on the Chlorophyll Absorption in Reflectance Index (CARI) and its transformations into Transformed Chlorophyll Absorption Ratio Index (TCARI) and Modified Chlorophyll Absorption Ratio Index (MCARI) normalised by OSAVI in the form $^{\mathrm{TCARI}}/_{\mathrm{OSAVI}}$ and MCARI_{1510} using SWIR bands, as formulated in Table 2.2. Finally, a smoothing algorithm based on Local Polynomial Regression Fitting (Cleveland *et al.*, 1992) was used to reduce atmospheric variability and fill gaps to produce daily time series of the indices.

Table 2.2 Vegetation indices derived from Sentinel-2 data included in this study and their formulations.

Vegetation index	Equation	Reference
Normalized Difference Vegetation Index	$\mathrm{NDVI} = (\mathrm{R}_{800} - \mathrm{R}_{670})/(\mathrm{R}_{800} + \mathrm{R}_{670})$	(Rouse *et al.*, 1974)
Chlorophyll Index	$\mathrm{CI} = \frac{\mathrm{R}_{750}}{\mathrm{R}_{710}}$	(Zarco-Tejada *et al.*, 2001)
Normalized Difference Index	$\mathrm{NDI} = (\mathrm{R}_{706} - \mathrm{R}_{664})/(\mathrm{R}_{704} + \mathrm{R}_{664})$	(Delegido *et al.*, 2011)
MERIS Terrestrial Chlorophyll Index	$\mathrm{MTCI} = (\mathrm{R}_{754} - \mathrm{R}_{709})/(\mathrm{R}_{709} - \mathrm{R}_{681})$	(Dash and Curran, 2007)
Modified Chlorophyll Absorption Ratio Index	$\mathrm{MCARI} = ((\mathrm{R}_{700} - \mathrm{R}_{670}) - 0.2(\mathrm{R}_{700} - \mathrm{R}_{550}))\left(\frac{\mathrm{R}_{700}}{\mathrm{R}_{670}}\right)$	(Haboudane *et al.*, 2004)
Green Normalized Difference Vegetation Index	$\mathrm{GNDVI} = (\mathrm{R}_{800} - \mathrm{R}_{550})/(\mathrm{R}_{800} + \mathrm{R}_{550})$	(Gitelson *et al.*, 1996)
Pigment Specific Simple Ratio A	$\mathrm{PSSRa} = \frac{\mathrm{R}_{800}}{\mathrm{R}_{680}}$	(Blackburn, 1998)
Sentinel-2 Red-Edge Position	$\mathrm{S2REP} = 705 + 35\frac{\frac{\mathrm{R}_{783} + \mathrm{R}_{665}}{2} - \mathrm{R}_{705}}{\mathrm{R}_{740} - \mathrm{R}_{705}}$	(Frampton *et al.*, 2013)
Inverted Red-Edge Chlorophyll Index	$\mathrm{IRECI} = (\mathrm{R}_{783} - \mathrm{R}_{665})/(\mathrm{R}_{705} + \mathrm{R}_{740})$	(Frampton *et al.*, 2013)
Renormalized Difference Vegetation Index	$\mathrm{RDVI} = (\mathrm{R}_{800} - \mathrm{R}_{670})/\sqrt{(\mathrm{R}_{800} + \mathrm{R}_{670})}$	(Roujean and Breon, 1995)
Modified Simple Ratio	$\mathrm{MSR} = \frac{\mathrm{R}_{800}/\mathrm{R}_{670} - 1}{(\mathrm{R}_{800}/\mathrm{R}_{670})^{0.5} + 1}$	(Chen, 1996)
Transformed Chlorophyll Absorption Ratio	$\mathrm{TCARI} = 3\left((\mathrm{R}_{700} - \mathrm{R}_{670}) - 0.2\,(\mathrm{R}_{700} - \mathrm{R}_{550})\frac{\mathrm{R}_{700}}{\mathrm{R}_{670}}\right)$	(Haboudane *et al.*, 2002)
Optimized Soil-Adjusted Vegetation Index	$\mathrm{OSAVI} = (1 + 0.16)\,\frac{\mathrm{R}_{800} - \mathrm{R}_{670}}{\mathrm{R}_{800} + \mathrm{R}_{670} + 0.16}$	(Rondeaux *et al.*, 1996)

Modified Soil-Adjusted Vegetation Index	$\text{MSAVI} = (1+\text{L})\dfrac{\text{R}_{800}-\text{R}_{670}}{\text{R}_{800}+\text{R}_{670}+\text{L}}$	(Qi *et al.*, 1994)
TCARI/OSAVI	$\text{TCARI/OSAVI} = \dfrac{\text{TCARI}}{\text{OSAVI}}$	(Haboudane *et al.*, 2002)
Modified Chlorophyll Absorption Ratio Index 1510	$\text{MCARI1510} = ((\text{R}_{700}-\text{R}_{1510}) -0.2(\text{R}_{700}-\text{R}_{550}))\left(\frac{\text{R}_{700}}{\text{R}_{1510}}\right)$	(Herrmann *et al.*, 2010)
Transformed Chlorophyll Absorption Ratio 1510	$\text{TCARI1510} = 3\left((\text{R}_{700}-\text{R}_{1510}) - 0.2\,(\text{R}_{700}-\text{R}_{550})\dfrac{\text{R}_{700}}{\text{R}_{1510}}\right)$	(Herrmann *et al.*, 2010)
Optimized Soil-Adjusted Vegetation Index 1510	$\text{OSAVI1510} = (1+0.16)\,\dfrac{\text{R}_{800}-\text{R}_{1510}}{\text{R}_{800}+\text{R}_{1510}+0.16}$	(Herrmann *et al.*, 2010)
Red Green Ratio Index	$\text{IRG} = \text{R}_{670}-\text{R}_{550}$	(Gamon and Surfus, 1999)
Perpendicular Vegetation Index	$\text{PVI} = \dfrac{\text{R}_{800}-\text{a}\cdot\text{R}_{670}-\text{b}}{\sqrt{\text{a}^2+1}}$	(Richardson and Wiegand, 1977)
Ratio Vegetation Index - Simple Ratio 800/670	$\text{RVI} = \dfrac{\text{R}_{800}}{\text{R}_{670}}$	(Pearson and Miller, 1972)
Adjusted Transformed Soil-Adjusted VI	$\text{ATSAVI} = \text{a}\cdot\dfrac{\text{R}_{800}-\text{a}\cdot\text{R}_{670}-\text{b}}{\text{a}\cdot\text{R}_{800}+\text{R}_{670}-\text{ab}+\text{x}(1+\text{a}^2)}$	(Baret and Guyot, 1991)
Atmospherically Resistant Vegetation Index	$\text{ARVI} = \dfrac{\text{R}_{800}-\text{R}_{670}-\text{y}(\text{R}_{670}-\text{R}_{450})}{\text{R}_{800}+\text{R}_{670}-\text{y}(\text{R}_{670}-\text{R}_{450})}$	(Bannari *et al.*, 1995)
Global Environment Monitoring Index	$\text{GEMI} = \text{n}(1-0.25\text{n})\dfrac{\text{R}_{670}-0.125}{1-\text{R}_{670}}$, $\text{n} = \dfrac{2({\text{R}_{800}}^2-{\text{R}_{670}}^2)+1.5\cdot\text{R}_{800}+0.5\cdot\text{R}_{670}}{\text{R}_{800}+\text{R}_{670}+0.5}$	(Pinty and Verstraete, 1992)
Difference Vegetation Index	$\text{DVI} = \text{g}\cdot\text{R}_{800}-\text{R}_{670}$	(Richardson and Wiegand, 1977)
Aerosol Free Vegetation Index 1600	$\text{AFRI1510} = \text{R}_{800}-0.66\dfrac{\text{R}_{1600}}{\text{R}_{800}+0.66\cdot\text{R}_{1600}}$	(Karnieli *et al.*, 2001)
Aerosol Free Vegetation Index 2100	$\text{AFRI2100} = \text{R}_{800}-0.5\dfrac{\text{R}_{2100}}{\text{R}_{800}+0.56\cdot\text{R}_{2100}}$	(Karnieli *et al.*, 2001)

For each of the 16 orchards, we used the daily dataset of VIs to calculate the values for June 2016 and July 2017, taking the means over 2-week intervals centred on the dates of the ground measurement collection to reduce random fluctuations in time-series data. We additionally calculated the

temporal rate of change for each VI in the form $VI_{year=n+1}$ / $VI_{year=n}$ in order to understand the temporal trajectory of VIs as a function of *Xf* infection. Finally, Pearson correlation analysis and p-values, adjusted with a Bonferroni correction to control false positives (Haynes, 2013), were used to determine the strength and statistical significance of the relationship between the in-situ measurements of *Xf* impact, i.e. ΔDI and ΔDS, and the rate of change of VIs derived from Sentinel-2 data.

2.2.3. Airborne hyperspectral images

For validation purposes, we collected very high-resolution images (Fig. 2.3) on 28th June 2016 and 3rd July 2017 using a micro-hyperspectral imager—Micro-Hyperspec VNIR model (Headwall Photonics Inc., Fitchburg, MA, USA)—on board a Cessna aircraft. Visible and near-infrared spectral regions (400–885 nm) were covered by operating the sensor with 260 bands and a radiometric resolution of 12 bits at a 1.865 nm CWL interval, yielding 6.4 nm full-width at half-maximum (FWHM) spectral resolution with a 25-µm slit. The acquisition frame-rate on board the aircraft was 50 frames per second with an integration time of 18 ms; with a focal length of 8 mm, an angular field of view (FOV) of 49.82° was produced (corresponding to an instantaneous FOV [IFOV] of 0.93 mrad). More platform and sensor configuration details can be found in Zarco-Tejada *et al.* (2013). The hyperspectral sensor was radiometrically calibrated in the laboratory with an integrating sphere (CSTM-USS-2000C Uniform Source System from Labsphere, North Sutton, NH, USA) by calculating coefficients derived from the calibrated light source at four illumination levels. The atmospheric correction was carried out using the total incoming irradiance simulated with the SMARTS model (Gueymard, 1995, 2001), which allowed the conversion of radiance values to reflectance. The model was fed with data from a weather station (WX510 from Vaisala, Vantaa, Finland) and a Microtops II Sunphotometer (Solar Light Co., Philadelphia, PA, USA). Hyperspectral imagery was orthorectified with PARGE (ReSe Applications Schläpfer, Wil, Switzerland) using

inputs from an inertial measurement unit (MTiG from Xsens, Enschede, Netherlands) installed on board and synchronized with the imager; image correction and data pre-processing are described in detail in Hernández-Clemente *et al.* (2012) and Zarco-Tejada *et al.* (2016).

The hyperspectral images had a ground resolution of 40 cm, allowing us to distinguish individual olive tree crowns from the background made up of soil and understory vegetation. We used the hyperspectral images to evaluate the contribution of the background to the relationship between ∆DI and the rate of change of VIs derived from the Sentinel-2 data. To do this, we calculated for each orchard the hyperspectral VIs separately for the background areas surrounding the trees – by defining each tree crown as the area within a 5-m radius from the centroid and then masking the crowns by image segmentation – and for the tree crowns only.

We also used the very high-resolution images as ground-truth for model parametrisation, detailed in the next section, following the methodology proposed by Zarco-Tejada *et al.* (2019) using scene components extracted from airborne hyperspectral images. Fig. 2.4 shows a strong correlation between VIs derived from Sentinel-2 and hyperspectral images over the 16 olive orchards in both 2016 (r^2=0.86, $p<0.001$ for NDVI and r^2=0.78, $p<0.001$ for OSAVI) and 2017 (r^2=0.68, $p<0.001$ for NDVI and r^2=0.66, $p<0.001$ for OSAVI). The consistency between the two datasets enabled the use of the high-resolution imagery as ground-truth for model parametrisation (Fig. 2.4).

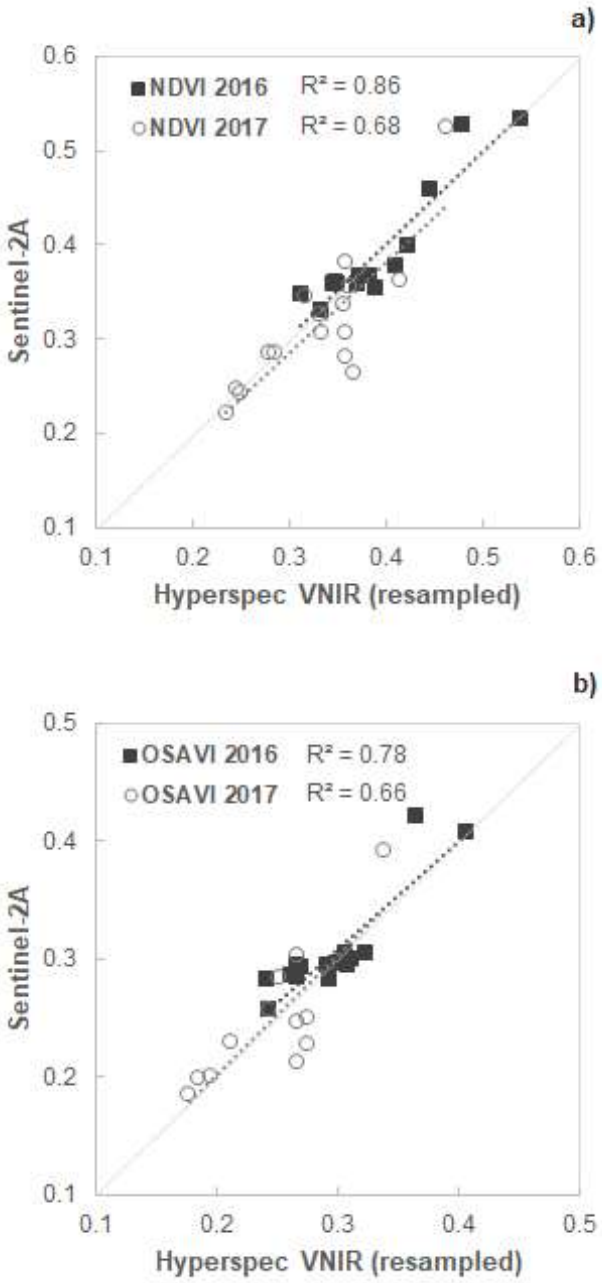

Figure 2.4 Comparison between Sentinel-2A and high-spatial-resolution aircraft (Hyperspec VNIR) imagery using the vegetation indices NDVI (a) and OSAVI (b) of 16 olive orchards surveyed in June 2016 and July 2017.

2.2.4. Model simulations

We used a coupled leaf-canopy radiative transfer model to analyse the sensitivity of different VIs to orchard-level changes in *Xf*-induced disease incidence through time and to evaluate the effects of the background and soil on symptom detection. The leaf optical properties were simulated with the PROSPECT-D model (Feret *et al.*, 2017), which requires seven variables: the leaf structure coefficient (N), chlorophyll content (C_{a+b}), carotenoid content (C_{x+c}), anthocyanin content (Anth), brown pigment content (C_{brown}), water equivalent thickness (C_w) and dry matter content (C_m). The PROSPECT leaf model was coupled to the 3-dimensional FLIGHT model (Hernández-Clemente *et al.*, 2017; North, 1996) to simulate the optical effects stemming from heterogeneous architecture of the olive tree crowns and orchards. FLIGHT uses Monte Carlo Ray Tracing (MCRT) techniques to simulate the radiative transfer within and between tree crowns and other canopy components. FLIGHT calculates directional reflectance of the canopy by accumulating photon energy in the observation direction as a function of different components defining the canopy structure (crown shape and size, tree height, position, density and distribution) (Table 2.3).

Table 2.3 Nominal values used in PROSPECT+FLIGHT simulation analysis.

Variable	Variable code	Nominal values
PROSPECT		
Structure coefficient	N	1.2
Chlorophyll a+b content	C_{a+b} (µg/cm^2)	10 – 80
Carotenoid content	C_{x+c} (µg/cm^2)	10
Anthocyanin content	Anth (µg/cm^2)	1.0
Brown pigment content	C_{brown} (arb. unit)	0.0
Water content	C_w (cm)	0.015
Dry matter	C_m (g/cm^2)	0.009
FLIGHT		
Mode of operation	MODE	r (reverse)
Dimension of model	FLAG	3 (3D Representation)
Solar zenith, view zenith (°)	θs, θv	39.27, 0.0
Solar azimuth, view azimuth (°)	Φs, Φv	103.87, 0.0
Number of wavebands	NO_WVBANDS	401
Image size	IM_SIZE	200 x 200
Number of photons traced	-	40000 (reverse mode, from image size)
Total LAI (LAI crown)	TOTAL_LAI	0.25 – 3.5
Leaf angle distribution	LAD [1–9]	0.015, 0.045, 0.074, 0.1,0.123, 0.143, 0.158, 0.168, 0.174
Fractional cover (%)	FRAC_COV	5 – 55

Using the described PROSPECT+FLIGHT modelling approach, we generated a lookup table (LUT) to investigate the temporal dynamics of *Xf*-induced disease incidence using VIs calculated from simulated spectra. We built a LUT with 7056 simulations using the input parameters described in Table 2.3. The nominal values used to generate the simulations were defined based on field measurements and hyperspectral imagery (Table 2.3) to mimic the orchards' architecture and the level of disease impact across the study area. The 40-cm spatial resolution hyperspectral images (Fig. 2.3 top) were used to distinguish the scene components (Fig. 2.5), facilitating the parametrisation of the FLIGHT model simulations. In particular, we quantified the fractional cover of each orchard (FCo) using NDVI calculated from

the high-resolution hyperspectral image. A threshold of NDVI > 0.3 was applied to distinguish tree crowns from background pixels during image segmentation according to Niblack's thresholding method (Niblack, 1986) and Sauvola's binarization techniques (Sauvola and Pietikäinen, 2000). Next, we applied a binary watershed analysis using the Euclidean distance map for each object to automatically separate trees with overlapping crowns, which enables one to rebuild the scene with the same features. The FCo values retrieved from the airborne sensor were related to the field observations (DSo and DIo), with a linear regression model (r^2=0.67, $p<0.05$) used as a proxy for DSo and DIo in the model simulation. The relationship between FCo and DSo was used to mimic the natural range of variation in FCo values for each DSo and used as input in the LUT. The initial LUT was then classified to set an approximate range of FCo per DSo and DIo (Table 2.4). For each class (DSo Level 0 to 4), we assumed a range of crown diameters and LAI per orchard to comply with the FCo defined for each level. We also assumed a decrease in the chlorophyll content values corresponding to the increase in DSo to mimic the typical discolouration observed in *Xf*-infected olive trees.

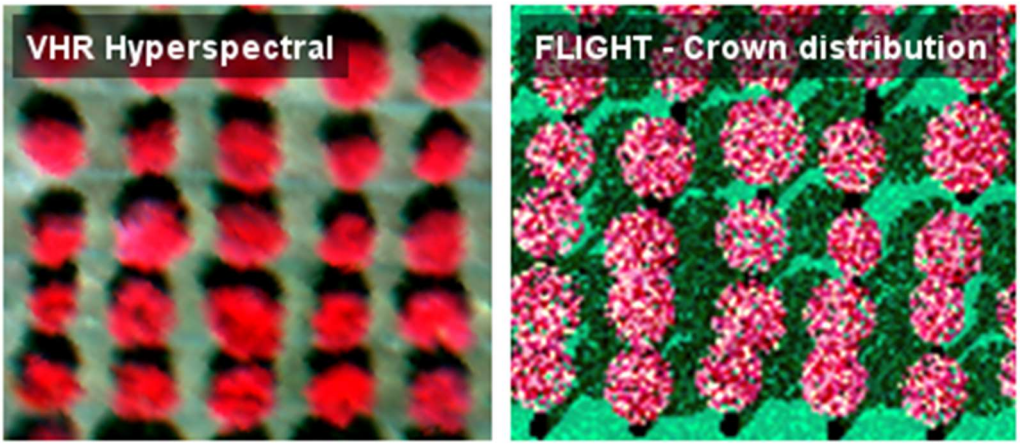

Figure 2.5 Overview of an olive grove acquired with a 40-cm hyperspectral sensor enabling the identification of single trees (left panel) and a 3-D scene generated with FLIGHT Monte Carlo simulation mimicking crown distribution (right panel).

Table 2.4 Classification criteria in the model inversion, including disease severity (DSo) and fractional cover (FCo) at orchard level, leaf area index at both crown (LAICROWN) and scene level (LAISCENE), and chlorophyll content (Ca+b).

DSo Level	Description	FCo (%)	LAI_{CROWN}	C_{a+b}	LAI_{SCENE}
0	Healthy	45 – 55	2 – 3.5	65 – 80	0.9 – 1.925
1	Initial severity	25 – 45	1.5 – 2	50 – 65	0.375 – 0.9
2	Medium severity	20 – 25	0.75 – 1.5	35 – 50	0.15 – 0.375
3	High severity	10 – 20	0.5 – 0.75	20 – 35	0.05 – 0.15
4	Very high severity	5 – 10	0.25 – 0.5	10 – 20	0.0125 – 0.05

To define the synthetic dataset associated with the change, we established a pool of combinations of change describing the positive increase rate of severity ($c = \sum_{k=1}^{5} k$) between orchards classified at different levels for the years *n* and *n+1* (*year* $n_{L4}\rightarrow$ *year* $n+1_{L4}$, *year* $n_{L3}\rightarrow$ *year* $n+1_{L3}$, *year* $n_{L3}\rightarrow$ *year* $n+1_{L4}$, …, *year* $n_{L0}\rightarrow$ *year* $n+1_{L4}$). The rate of change between simulations for years *n* and *n+1* was used for the final retrieval of ΔDI and ΔDS.

Three different approaches were evaluated to account for the canopy background in the simulations: (i) a more complex solution that included the background spectral reflectance variation recorded by the hyperspectral images between 2016 and 2017 for each plot, named here as the "temporal background per plot" (TBP); (ii) a simpler approach considering a "persistent spectral reflectance for the background" (PB) using a bare-soil spectrum extracted from the hyperspectral imagery collected in 2016; and (iii) a compromise alternative that computed the average of the background's spectral reflectance recorded for all plots during 2016 and 2017, named here as the "mean temporal background scheme" (MTB). The performance of the model under each strategy was evaluated based on the Root Mean Square Error (RMSE) between the DI increase estimated from the retrieved Sentinel-2 data and the field-observed DI scored for each of the 16 orchards evaluated.

2.3. Results

In this section we present results from empirical approaches to detect variations in DI of *Xf*-infected olive orchards using physiological and structural VIs calculated from Sentinel-2 imagery. Then, we report results using a 3-D radiative transfer model to predict temporal changes of *Xf*-induced disease incidence that accounts for the soil and understory variations affecting the temporal trends.

2.3.1. Temporal trends of DS and DI and vegetation indices

Both DI and DS caused by *Xf* increased between 2016 and 2017 in all of the surveyed olive orchards (Fig. 2.6). DS and DI were significantly correlated with each other (r^2=0.84, $p<0.05$), as were the temporal change rates ΔDS and ΔDI (r^2=0.79, $p<0.05$). Orchards where incidence had already reached 100% in 2016 continued to see an increase in symptom severity (e.g. Fig. 2.6, orchards A5 and A4), and orchards with a low initial incidence and severity (e.g. C20 to B3), showed a strong increase in both one year later, as reflected by high ΔDI and ΔDS, respectively.

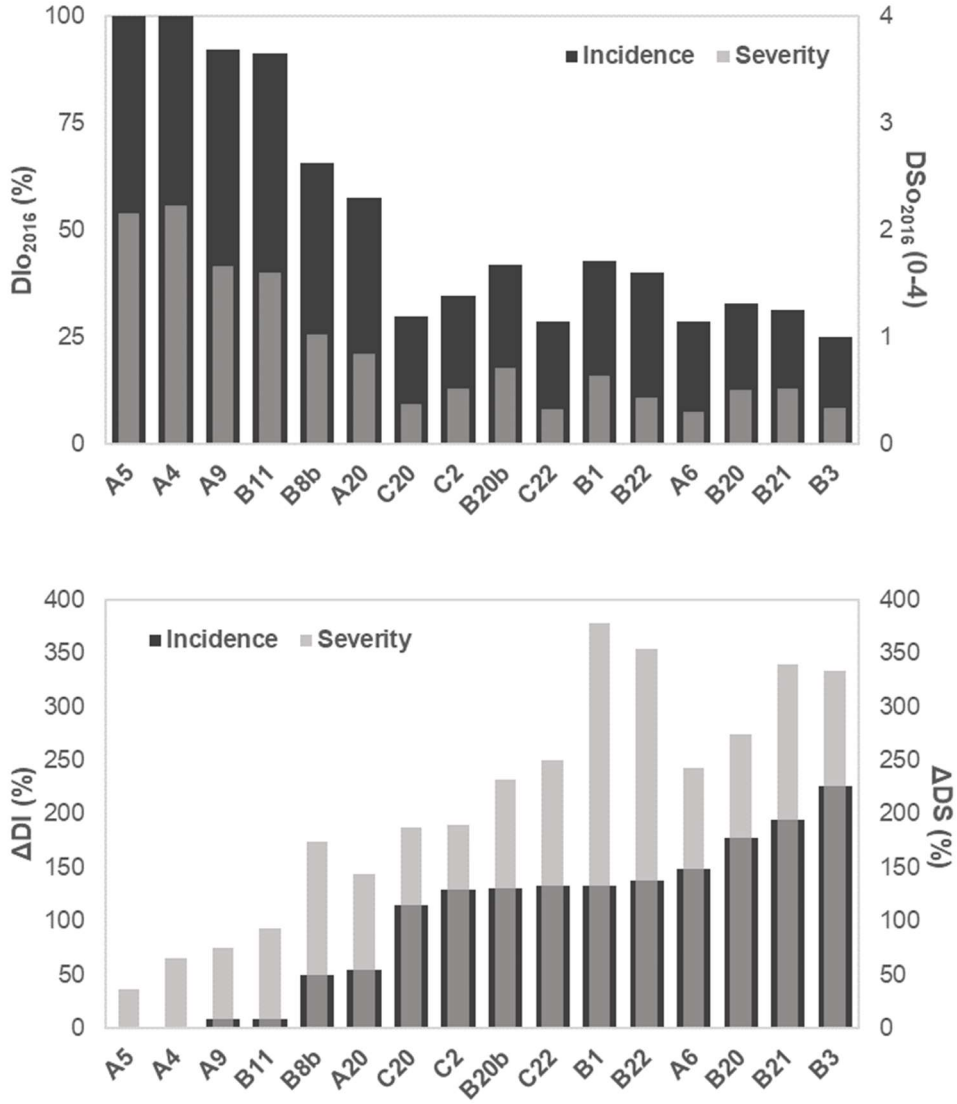

Figure 2.6 Temporal evolution of DIo and DSo between 2016 and 2017. (Top) DS and DI in 2016; (bottom) ΔDI and ΔDS between 2016 and 2017. X-axis labels refer to the 16 olive orchards surveyed.

The rate of change in 17 out of the 26 Sentinel-2 VIs correlated significantly ($p<0.001$) with both ΔDS and ΔDI, and six of them showed a coefficient of determination (r^2) exceeding 0.57 (Fig. 2.7). The indices ARVI and OSAVI produced the highest coefficients of determination with ΔDI ($r^2=0.75$ and $r^2=0.76$, respectively; $p<0.001$) (Fig. 2.8). Other VIs such as ATSAVI and NDVI yielded similar results ($r^2=0.72$ and $r^2=0.71$, respectively),

outperforming RDVI (r^2=0.65) and MSR (r^2=0.61). The relationships between these VIs and ΔDS yielded similar results (r^2_{ARVI}=0.74, r^2_{OSAVI}=0.71, r^2_{ATSAVI}=0.72, r^2_{NDVI}=0.71, r^2_{RDVI}=0.57, r^2_{MSR}=0.6; p<0.001 in all cases). Surprisingly, however, greater ΔDI values were associated with smaller reductions in the VIs (Fig. 2.8), whether considering entire orchards (Fig. 2.8), the background cover only (Fig. 2.9a), or tree crowns only (Fig. 2.9b). Furthermore, VIs calculated from the background area around each tree, made up of soil and understory vegetation and excluding tree crowns, displayed a similar pattern in which orchards with greater ΔDI showed smaller VI reductions (Fig. 2.9).

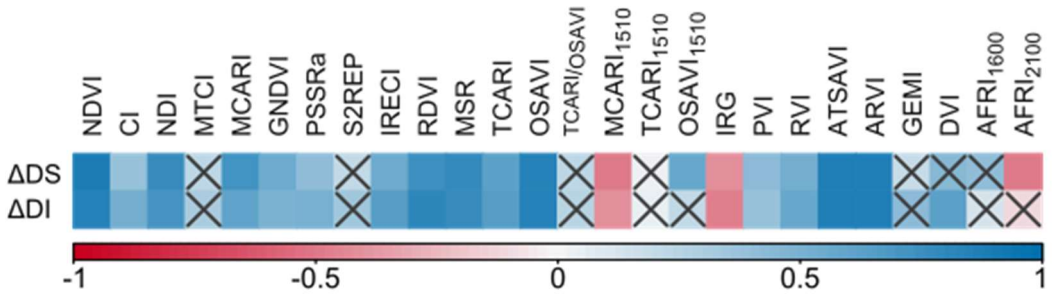

Figure 2.7 Relationship between increases in severity (ΔDS) and incidence (ΔDI) and temporal rate of change in Sentinel-2 vegetation indices selected for this study. Correlation coefficients range from −1 to 1. Cross (X) symbols indicate non-significant relationships (p-value ≥ 0.001).

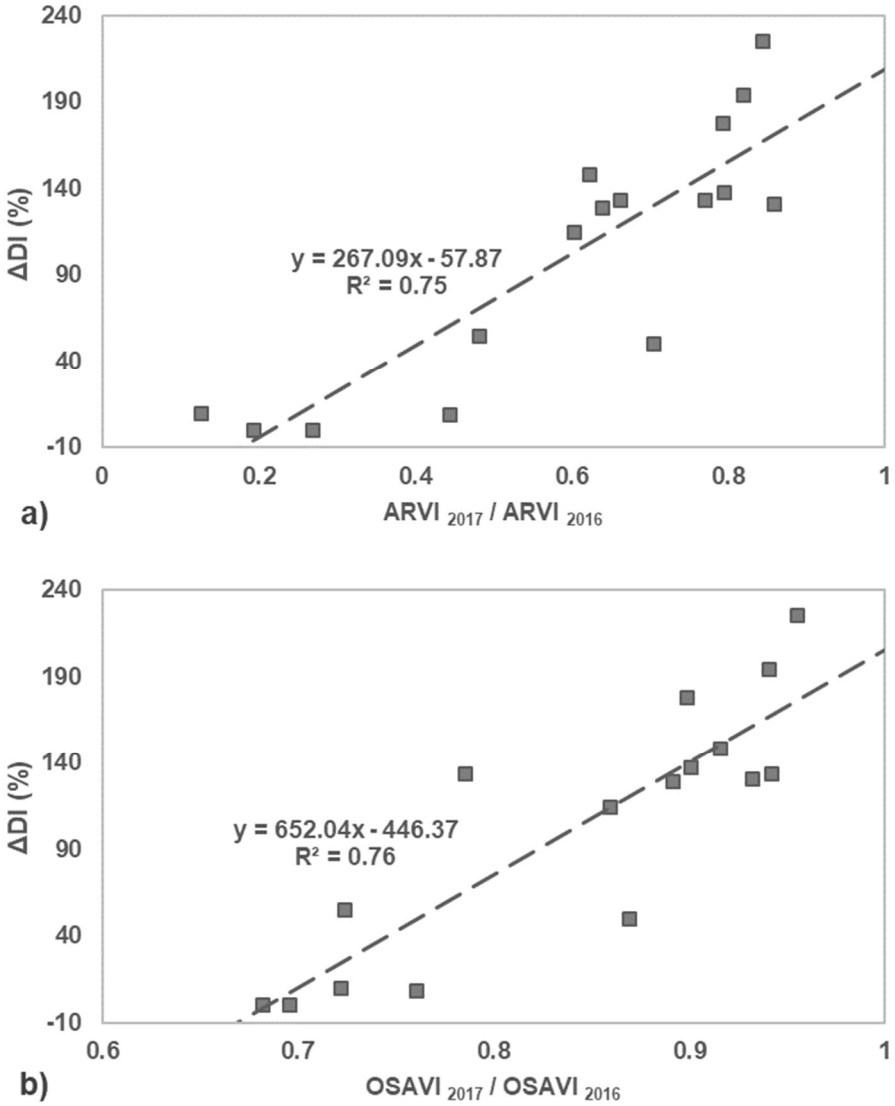

Figure 2.8 Relationship between *Xf* incidence increase (ΔDI) and the rate of change of the vegetation indices ARVI (a) and OSAVI (b). Rate of change was calculated from Sentinel-2 images taken in 2016 and 2017.

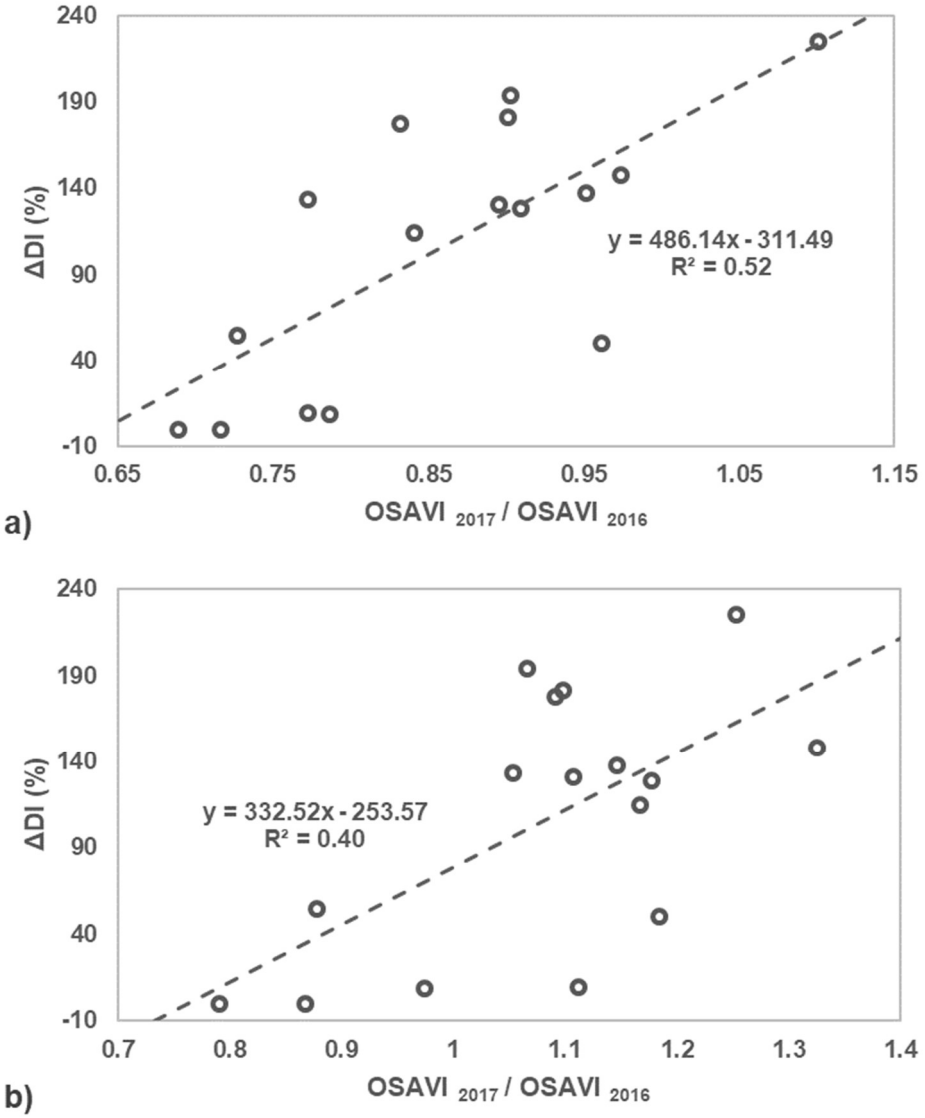

Figure 2.9 Relationship between *Xf* incidence increase (ΔDI) and the rate of change of the vegetation index OSAVI with the background around a tree, determined by assuming a radius of 5 m around the centroid of each tree and masking the tree crowns by segmentation (a); and taking only tree crowns (b). Rate of change was calculated from hyperspectral imagery in 2016 and 2017 due to its resolution sufficient to discriminate between background and trees.

The analysis of the temporal changes observed by Sentinel-2A ARVI and OSAVI revealed distinct patterns in orchards with medium and high DI over the last two years (Fig. 2.10). Orchards with high DI had a lower ARVI and

OSAVI than those with medium DI. The differences between medium and high DI were more substantial during the summer, when the VIs tended to be lower than in winter, and much less variable than in spring, when infection symptoms develop more rapidly and potentially depend on local-scale environmental conditions as well as on the physiological status of individual trees.

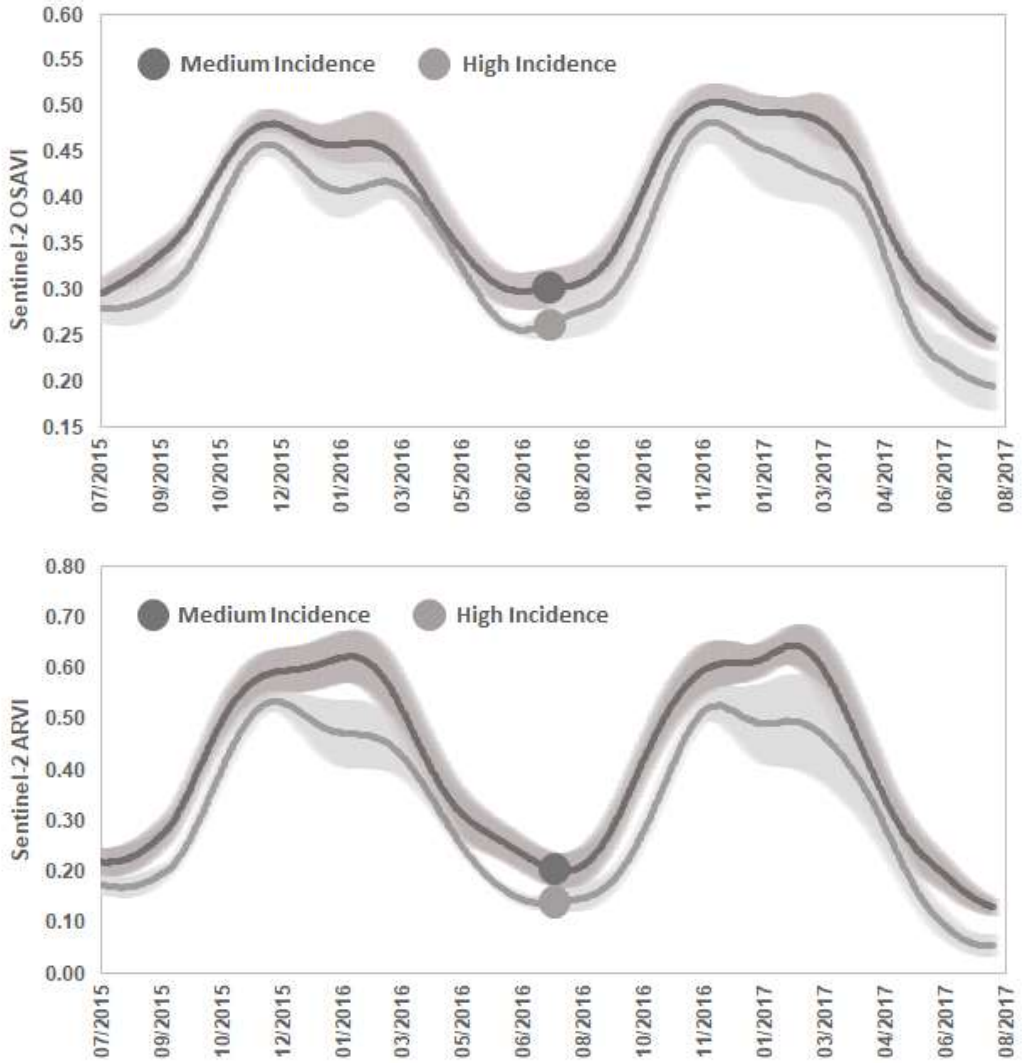

Figure 2.10 Daily mean OSAVI (top) and ARVI (bottom) two-year time series of orchards with medium and high *Xf* incidence as evaluated in the field on 28 June 2016 (dots indicate the timing of the field survey). Lines represent the mean of medium-incidence (DIo_{2016}<50%; n=10) and high-incidence (DIo_{2016}>50%; n=6) orchards, and bands extend two standard deviations around them.

2.3.2. Modelling changes in vegetation trends with S2A

The results of the radiative transfer modelling approach, which was proposed to evaluate the sensitivity of VIs to track the temporal evolution of *Xf* disease, are displayed in Fig. 2.11. The FLIGHT model simulations obtained using a synthetic multi-temporal dataset, built with inputs within the typical range of variation observed in olive groves affected by *Xf* in two consecutive years for OSAVI (Fig. 2.11a) and ARVI (Fig. 2.11b), showed a direct relationship between ΔDI and the rate of change between two consecutive years. The simulated VIs generated using the MTB approach were significantly related to ΔDI for OSAVI, ARVI and NDVI, and yielded similar accuracy to the empirical relationship with OSAVI (r^2=0.74) but somewhat lower accuracy with ARVI (r^2=0.49) and higher with NDVI (r^2=0.68) (data not shown). In any case, the linear responses of the simulated VIs matched the empirical relationships very closely.

ΔDI estimated through model inversion using two different VIs (ARVI and OSAVI) corresponded well with the field observations of the ΔDI temporal change (Fig. 2.12). The complexity in accounting for the background in the models had an effect on the goodness-of-fit, introducing a bias in the DI change estimates (Fig. 2.12); when the year-to-year evolution of the background was considered independently for each of the orchards (TBP approach), the model simulations were entirely corrected for background effects and, therefore, the accuracy of ΔDI retrievals using OSAVI and ARVI was significantly higher ($RMSE_{OSAVI}$=43% and $RMSE_{ARVI}$=44%; $NRMSE_{OSAVI}$=0.19 and $NRMSE_{ARVI}$=0.20) (Fig. 2.12a, b). Model performance decreased when instead the mean background reflectance time series from all orchards (MTB approach) was used as a model input ($RMSE_{OSAVI}$=50% and $RMSE_{ARVI}$=84%; $NRMSE_{OSAVI}$=0.22 and $NRMSE_{ARVI}$=0.36) (Fig. 2.12 c, d). Finally, when model simulations did not account for the temporal changes in background reflectance at all (PB approach), the fitted models degraded significantly, leading to even larger errors (RMSE≥140%; NRMSE>0.6) (Fig. 2.12e, f).

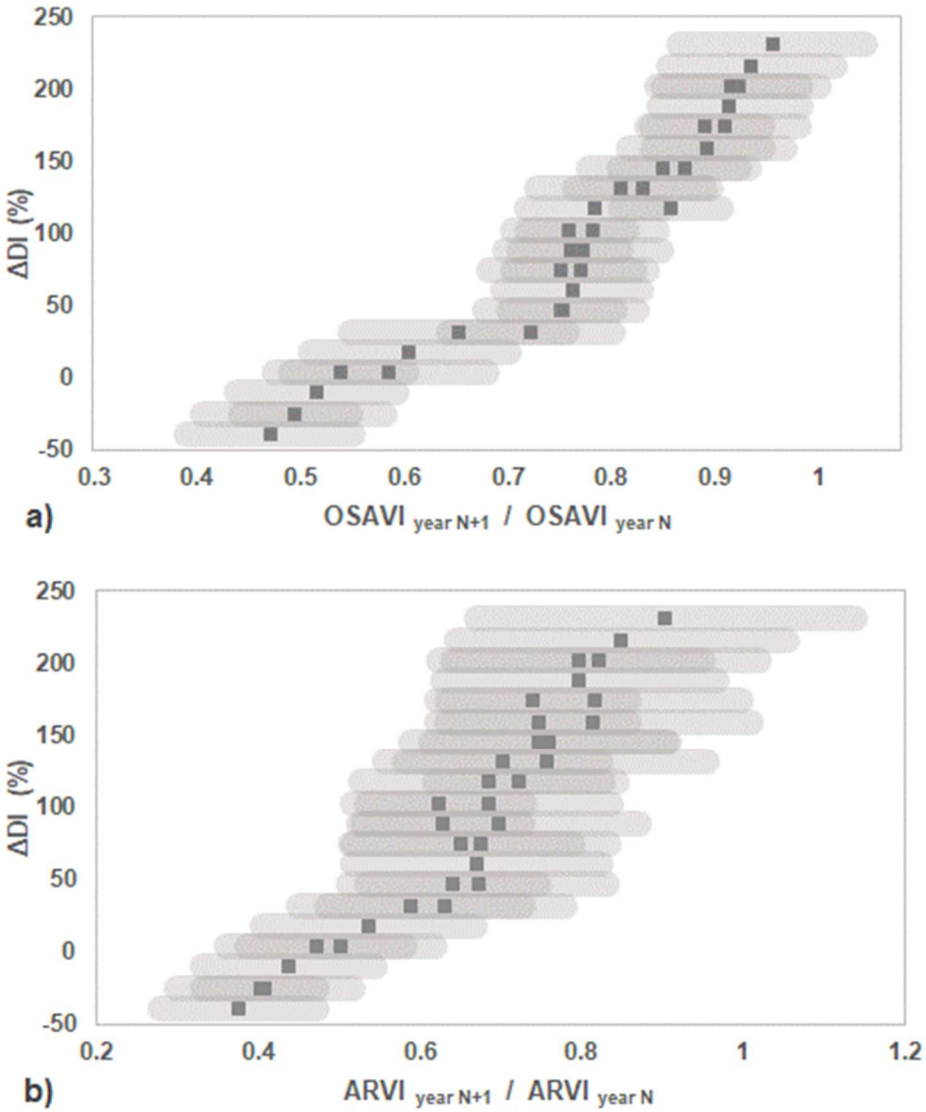

Figure 2.11 Simulations of the disease incidence increase (ΔDI) with OSAVI (a) and ARVI (b), generated by PROSPECT+FLIGHT and using the average spectral reflectance measured in parts of the orchards not covered by olive tree crowns to represent the background in the model (MTB approach). Bands surrounding the points show the variability in results for the same ΔDI, and the points themselves are the average values within those simulations.

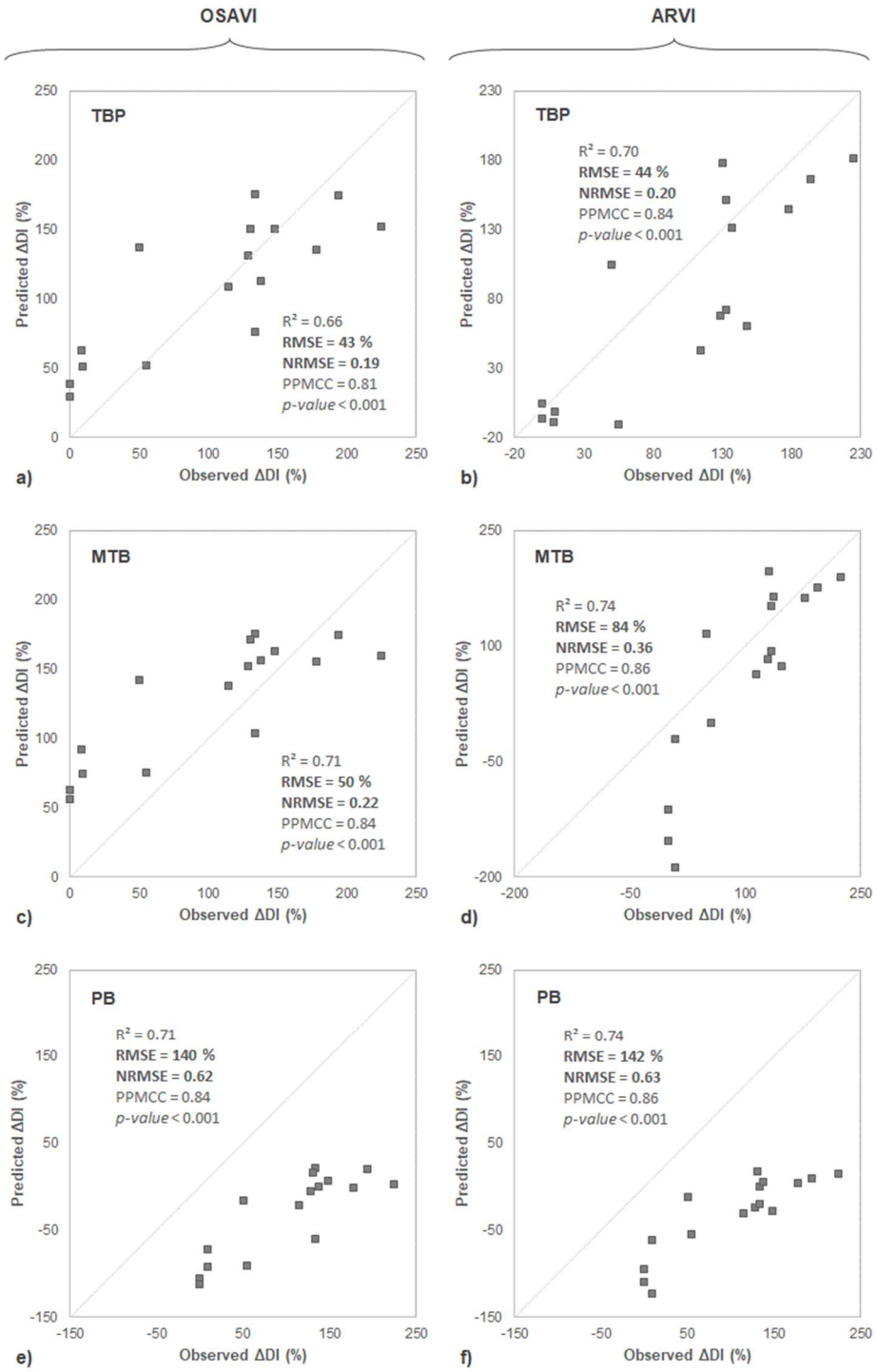

Figure 2.12 Estimated versus measured Xf incidence increase (ΔDI) using OSAVI (left) and ARVI (right) vegetation indices. Graphs show PROSPECT+FLIGHT inversions calculated using TBP (a, b), MTB (c, d) and PB (e, f); see text for details.

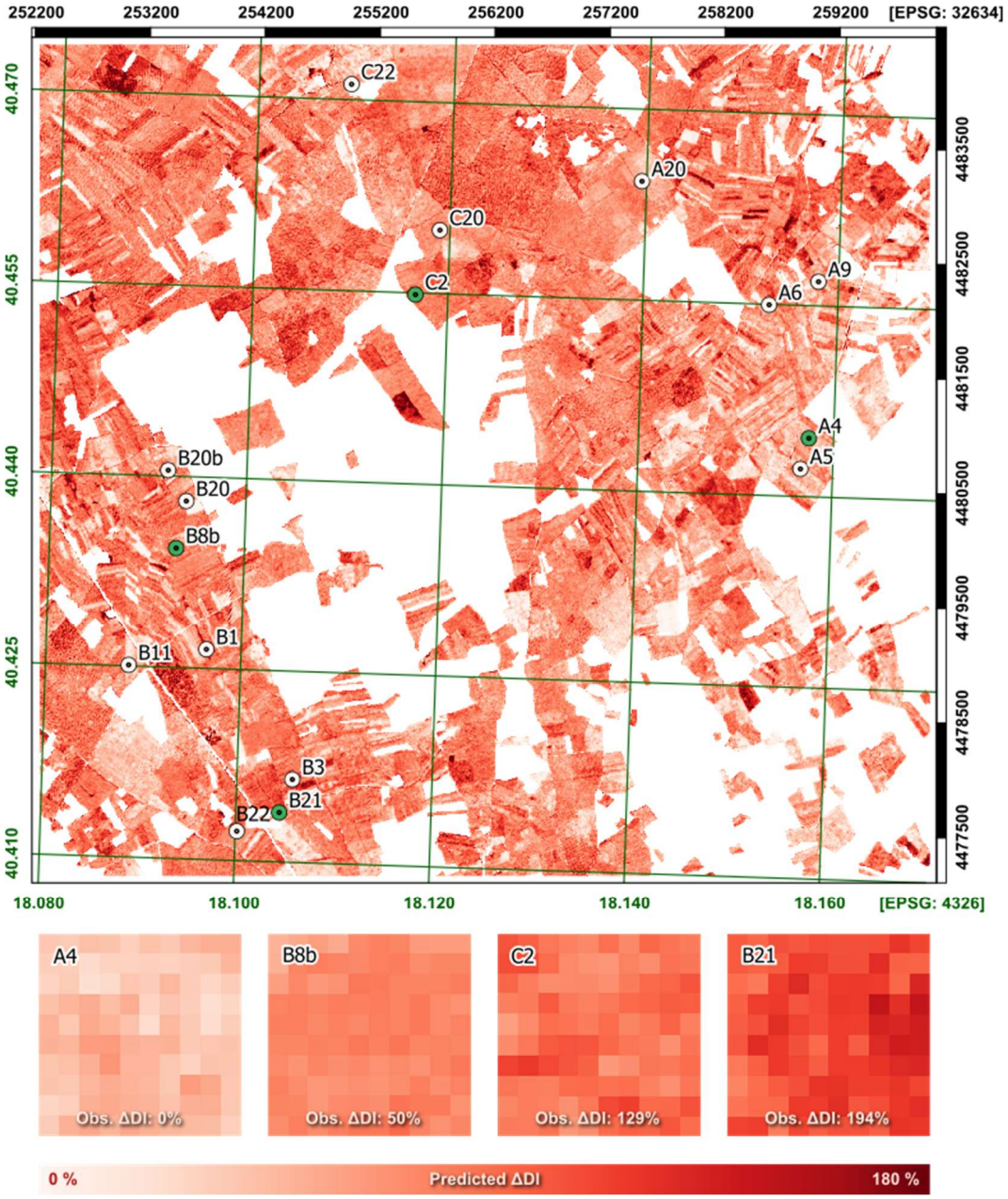

Figure 2.13 *Xf*-disease incidence increase (ΔDI) map generated from Sentinel-2A data of 29th June 2016 and 24th June 2017 using a lookup table (LUT) generated by inverting a PROSPECT+FLIGHT model that considered the temporal changes in background reflectance across all orchards (MTB approach; see text for details). Dots in the map indicate the individual olive orchards that were surveyed in the field. Bottom panels show incidence increases over different areas (green dots) where olive orchards were surveyed, representing a range of predicted ΔDI values. The observed incidence increase for each selected orchard is also indicated. The map has been masked with a layer of olive groves for Puglia extracted from

the Puglia Land Cover 2011 (InnovaPuglia Spa - Servizio Territorio e Ambiente, 2013).

Applying model-inversion methodology with OSAVI and the MTB model (Fig. 2.11a, Fig. 2.12c) to entire Sentinel-2A scenes generated a map of the predicted yearly increase in *Xf*-induced disease incidence between June 2016 and 2017 (Fig. 2.13). Looking in detail at four of the surveyed olive orchards (bottom panels in Fig. 2.13), representing a range of predicted ΔDI values, we can confirm that predictions of low to high percentages (0 to 180%) of *Xf*-disease incidence increase corresponded with the field observation records, which reported ΔDI from 0 to 194% for those fields. Furthermore, predicted maps generated with the model show enough spatial resolution to provide operational monitoring at the orchard level.

2.4. Discussion

The first research aim of this study was to determine whether satellite data could be used to monitor temporal changes of *Xf*-induced DI and DS, and to provide insights into the epidemiology of *Xf* spread over large areas. Non-visual symptoms of *Xf* infection can be detected using very high-resolution hyperspectral images and radiative transfer models (Zarco-Tejada *et al.*, 2018a), providing an innovative tool for the early detection of infected olive trees on a local scale. However, since *Xf* has spread rapidly in southern Italy over the last few years, affecting entire olive orchards, tracking more conspicuous damage (such as DI and DS) across large areas could help measure, forecast, and mitigate the impact of *Xf* on the landscape and on socio-economic sectors depending on it (Luvisi *et al.*, 2017; White *et al.*, 2017). The fast spread of *Xf* was reflected in our field observations: DI and DS increased considerably between 2016 and 2017, and ∆DI and ∆DS were linearly related. Indeed, the widespread increase of *Xf* infections in the last three years in

southern Apulia (Girelli *et al.*, 2017) has posed a risk to the olive trees and to this economic sector in the region.

Under natural conditions, biotic and abiotic factors jointly affect the development of vegetation diseases over different spatial and temporal scales. The interaction may cause a progressive loss in chlorophyll and biomass, producing irreversible changes in the vegetation. Both alterations are detectable and quantifiable through VIs calculated from Sentinel-2 data (Zarco-Tejada *et al.*, 2019). However, the relationships between VIs (OSAVI or NDVI) and DS or DI were poor when considering data from 2016 and 2017 together ($r^2<0.22$, $p<0.05$) (Fig. A1, Appendix A.), indicating that the VIs reflect orchard characteristics other than *Xf* symptoms and that such characteristics vary considerably between years. Hence, a precise disease assessment requires a quantitative estimation of the temporal evolution of the disease (ΔDI and ΔDS) rather than a mere quantification of DI and DS at one specific time (Nutter *et al.*, 2006). Indeed, the availability of frequent multispectral data from Sentinel-2 offers the opportunity to assess both spatial and temporal variation in VIs to monitor *Xf* infections in olive orchards over time.

When working with multi-temporal data acquired over non-closed canopies, one of the main challenges is to decouple the spectral reflectance changes produced by alterations in the vegetation condition from those produced by atmospheric and background factors. Here, the seasonal variation of VIs showed the highest variability in winter and early spring. In these periods, cloudy days are more frequent, increasing the residual noise in the data and the need for temporal interpolation. The sensitivity of different VIs to soil background and atmospheric effects were previously analysed in efforts to improve the accuracy of the retrieval of LAI and absorbed photosynthetically active radiation (APAR) (Baret and Guyot, 1991; Haboudane *et al.*, 2004; Huete *et al.*, 1985) and chlorophyll (Haboudane *et al.*, 2008; Zhang *et al.*, 2008). The variation in FC of a forest under decline also affects the performance of some VIs with higher sensitivity to canopy structure changes

(Hernández-Clemente *et al.*, 2011). The best-performing VIs in our study, OSAVI and ARVI, tend to be relatively robust to background and atmospheric effects (Kaufman and Tanre, 1992; Rondeaux *et al.*, 1996). Empirical and modelling results agreed regarding the accuracy of OSAVI as the best-performing index to track ΔDI. By contrast, the performance of ARVI with regard to the field observations was not entirely confirmed by model simulations. This may be related to the fact that ARVI is a vegetation index that minimises the atmospheric effects on the reflectance, conditions that were not included in the modelling, which assumed stable conditions for both years.

The overall robustness shown by modified VIs such as OSAVI or ARVI is in disagreement with some other studies, in which traditional indices yielded better performance. For instance, Frampton *et al.* (2013) reported that LAI and chlorophyll could be extracted from Sentinel-2 NDVI images for crops as well as from novel indices such as S2REP and MTCI. Differences in the homogeneity of crop versus olive orchard canopies might explain this apparent contradiction: in the latter case, the confounding effects produced by the structural heterogeneity of the orchards invalidated VIs with high sensitivity to soil effects and atmospheric conditions.

The contribution of the background seems to affect not only the spectral reflectance of the canopy measured by Sentinel-2 but also the spectral reflectance retrieved from the diseased crowns using hyperspectral images. Both sensors, with different spatial and spectral resolutions, showed a significant and similar relationship, with greater ΔDI leading to smaller VI reductions. This counterintuitive result is unlikely to be driven by weather patterns in the two years, as the sampled orchards experienced very similar meteorological conditions. Instead, it might reflect the impact of the background on the crown spectral response because olive tree crowns generally display low crown transmittance and LAI (Gómez Calero *et al.*, 2011), and defoliation increases with DS. As a result, the background has a particularly large contribution to temporal VI trends once the *Xf* disease symptoms

increase, even when using self-corrected (Kaufman and Tanre, 1992) and soil-adjusted (Rondeaux *et al.*, 1996) VIs and considering only tree crowns. Simultaneously, the increase in *Xf* infection was associated with a decrease in FC of the trees and an increase in the FC of the background, further increasing the dominance of the understory in the signal at orchard-level resolution. This inverse effect, i.e. an increase in the greenness of the background when the health of *Xf*-infected trees decreases, could be due to orchard management if diseased orchards are abandoned and no longer mowed or ploughed, leaving low-stature vegetation to reoccupy the soil. It may also be partly ecologically driven if diseased trees leave more nutrients and water available to the understory (Peltzer and Köchy, 2001).

This pattern further emphasises the relevance of incorporating 3-D RTMs when analysing VIs to explicitly incorporate background effects if the impact of *Xf* on spectral characteristics of olive groves is to be modelled with considerable precision (Meggio *et al.*, 2008; Richardson and Wiegand, 1977). This conclusion links to our second research question, which focused on the feasibility of modelling changes in DI from multi-temporal Sentinel-2 image data using VIs and radiative transfer models. In fact, the background effect has a significant impact on the model estimation against in-situ measurements: there was an improvement in the retrieval of ΔDI of 33.5% when accounting for the background effects, and a further 9.5% improvement when its heterogeneity was also considered. These results have critical implications in the use of VIs to assess the temporal evolution of the disease due to the non-homogeneous background effects across orchards affected by *Xf*, which alter the spectral signature of the canopy obtained with Sentinel-2 image data. The simulation approach demonstrated the benefit of using a 3-D radiative transfer model accounting for such effects, which is critical when monitoring the future spread of *Xf* infections and understanding its epidemiology (Fuente *et al.*, 2018). Therefore, this study takes one step further via modelling methods to properly account for the changes observed in canopy monitoring studies, enabling the retrieval of vegetation trends

associated with *Xf* infections and improving the understanding of the dynamics of the understory.

The proposed methodology based on the use of RTM and Sentinel-2 imagery offers the advantage of using free satellite data over any other remote sensing product limited by the availability of hyperspectral images. However, the applicability of these methods within a systematic detection system may be limited by the computational time required for model inversion, notwithstanding this limitation can be overcome in combination with data-driven machine learning algorithms based on multi-output methods emulating the functioning of RTM (Rivera *et al.*, 2015). The result of mapping disease-incidence dynamics using radiative transfer modelling illustrates the potential of the Sentinel-2 sensor to assess olive groves' health dynamics. The challenge of mapping disease infections has been thus far mainly addressed using environmental data and probabilistic models (Hay *et al.*, 2006) and rarely approached in quantitative terms. Remote sensing that combines physical methods and VIs makes it possible to map the DI dynamics of *Xf* based on the main biophysical changes it causes at the landscape scale. The dense time series provided by Sentinel-2 satellites make continuous mapping feasible and bring new opportunities for monitoring diseases incidence worldwide. Future work should consider methods to disentangle direct plant-level effects of *Xf* infection from those that manifest themselves in other components of the landscape because of changes in either vegetation composition or management.

2.5. Conclusions

This study demonstrates that Sentinel-2 data enables the detection of changes associated with temporal variations of *Xf*-induced symptoms at the orchard level. The use of satellite imagery to monitoring large-scale dynamics is key to combat *Xf* infections. Our work took advantage of a two-year dataset collected in the *Xf*-infected area in southern Italy, integrating

Sentinel-2 satellite images and high-resolution hyperspectral imagery, field observations and radiative transfer modelling. The temporal rate of change of disease incidence (DI) and disease severity (DS) was evaluated using different VIs and showed that the monitoring of *Xf*-infected orchards required the use of self-corrected and soil-adjusted VIs. Among the Sentinel-2 VI assessments, the best performance was observed for those that minimised the atmospheric and background effects such as ARVI, OSAVI and ATSAVI. These VIs performed better than traditional VIs such as NDVI, RDVI and MSR. However, the confounding effects of the understory had a considerable impact on the VIs obtained from Sentinel-2 over *Xf*-infected olive orchards due to the discontinuous canopy that characterises this crop. This study demonstrated that 3-D RTM and field observations properly explained the temporal variations experienced by both the tree canopy and the background, a critical aspect to accurately predicting ΔDI and ΔDS. Applying a temporal trend analysis supported by the 3-D RTM demonstrated that ARVI and OSAVI can be used to monitor orchard-level changes in DI and DS, yielding Normalised Root Mean Square Error (NRMSE) values below 0.22 and 0.36, respectively, for the two years of analysis. Overall, these results suggest that Sentinel-2 time-series imagery can provide useful spatio-temporal indicators to monitor the damage caused by *Xf* infections across large areas.

Chapter 3

Assessing the influence of the understory in the interpretation of chlorophyll fluorescence retrieved from heterogeneous canopies through 3-D radiative transfer modelling

Abstract

A major international effort has been made to monitor sun-induced chlorophyll fluorescence (SIF) from space as a proxy for the photosynthetic activity of terrestrial vegetation. However, the effect of spatial heterogeneity on the SIF retrievals from canopy radiance derived from images with medium and low spatial resolution remains uncharacterised. In images from forest and agricultural landscapes, the background comprises a mixture of soil and understory and can generate confounding effects that limit the interpretation of the SIF at the canopy level. This paper aims to improve the understanding of SIF from coarse spatial resolutions in heterogeneous canopies by considering the separated contribution of tree crowns, understory and background components, using a modified version of the FluorFLIGHT radiative transfer model (RTM). The new model is compared with others through the RAMI model intercomparison framework and is validated with airborne data. The airborne campaign includes high-resolution data collected over a tree-grass ecosystem with the HyPlant imaging spectrometer within the FLuorescence EXplorer (FLEX) preparatory missions. Field data measurements

were collected from plots with a varying fraction of tree and understory vegetation cover. The relationship between airborne SIF calculated from pure tree crowns and aggregated pixels shows the effect of the understory at different resolutions. For a pixel size smaller than the mean crown size, the impact of the background was low ($R^2 > 0.99$; NRMSE < 0.01). By contrast, for a pixel size larger than the crown size, the goodness of fit decreased ($R^2 < 0.6$; NRMSE > 0.2). This study demonstrates that using a 3D RTM model improves the calculation of SIF significantly ($R^2 = 0.83$, RMSE = 0.03 mW m^{-2} sr^{-1} nm^{-1}) when the specific contribution of the soil and understory layers are accounted for, in comparison with the SIF calculated from mixed pixels that considers only one layer as background ($R^2 = 0.4$, RMSE = 0.28 mW m^{-2} sr^{-1} nm^{-1}). These results demonstrate the need to account for the contribution of SIF emitted by the understory in the quantification of SIF within tree crowns and within the canopy from aggregated pixels in heterogeneous forest canopies.

3.1. Introduction

International efforts have been carried out to monitor fluorescence from space in global studies using different sensors (Köhler *et al.*, 2018; Mohammed *et al.*, 2019) and modelling approaches (Verrelst *et al.*, 2015a). One of the main challenges of the global low-resolution (over 60 m/pixel) sun-induced fluorescence (SIF) maps resides in the impact of the background components when quantifying SIF from large pixels aggregating different scene components. The first SIF global maps (Frankenberg *et al.*, 2011; Joiner *et al.*, 2011) were derived from the thermal and near-infrared *sensor* for observation (TANSO) onboard the greenhouse gases observing satellite (GOSAT) (Guanter *et al.*, 2012). A recent study has focused on downscaling SIF using the Global Ozone Monitoring Instrument 2 (GOME-2) and producing a daily corrected SIF global dataset with a spatial resolution of 0.05°(Duveiller *et al.*, 2020). The most recent SIF products based on the Orbiting Carbon Observatory 2 (OCO-2) launched in 2014 and the TROPOspheric

Monitoring Instrument (TROPOMI) in 2018 provide a footprint of 1.3 × 2.25 km and 3.5 × 7 km at nadir respectively. OCO-2 and TROPOMI SIF products have the potential to provide GPP estimations for homogeneous vegetation type covers (Köhler *et al.*, 2018; Li *et al.*, 2018). Although these global maps were important achievements, questions were raised regarding the interpretation of the SIF quantified from mixed pixels that aggregate vegetation, soil and shadow components (Xinchen Lu *et al.*, 2018). In the coming years, new possibilities of improving the spatial resolution of SIF global maps open up with the upcoming launch of the ESA Fluorescence Explorer (FLEX) satellite in 2022, designed to measure the instantaneous chlorophyll fluorescence signal with a very high spectral-resolution (0.1 nm) imaging spectrometer and a spatial resolution of 300 m. This will provide a completely new opportunity to assess the dynamics of actual photosynthesis through SIF, which offers a major advance over current capabilities that can only detect potential photosynthesis as derived through passive reflectance monitored by conventional Earth-resources satellites. The spatial resolution of FLEX is not, however, sufficient to understand the confounding effects of background components that affect the quantification of vegetation SIF at the pixel level. Recent initiatives, such as the FlexSense campaign (Siegmann *et al.*, 2019) for collecting airborne measurements at very fine resolution during the FLEX-Sentinel Tandem experiment, will contribute to the understanding and interpretation of SIF from aggregated pixels. Previous studies have attempted to interpret the SIF signal quantified at different scales, which is an important issue due to the effects of fractional vegetation cover and structure, and background (Zarco-Tejada *et al.*, 2013b).

In heterogeneous forest and agricultural canopies, high-resolution images are required to enable the crowns and understory to be delineated from the background (Wagner *et al.*, 2018). The quantification of the contribution of each pixel helps to understand and to improve the models used to quantify biophysical parameters from mixed pixels (Yu *et al.*, 2018). The estimation of some of these parameters, such as the fraction of green vegetation cover (FC), leaf area index (LAI), or the fraction of absorbed photosynthetically

active radiation (fAPAR), have critical implications in the estimation of Gross Primary Productivity (GPP) at the regional or global scale (Lin *et al.*, 2018; Tagliabue *et al.*, 2019). In fact, the impact of the understory on canopy reflectance is particularly challenging for studying complex canopies comprising different plant architectures and physiology (Eriksson *et al.*, 2006). Recent studies have demonstrated that SIF-GPP relationships not only are significantly affected by vegetation type (Li *et al.*, 2018; Sun *et al.*, 2018) but even vary within the same kind of vegetation (Migliavacca *et al.*, 2017). These studies concluded that finer resolution SIF observations were required to improve the accuracy of the models. However, it remains unclear how the covariation between SIF and GPP is affected by mixed vegetation from landscape to global scales (Sun *et al.*, 2017), although it has been shown that the canopy structure plays a dominant role in the SIF-GPP relationship (Dechant *et al.*, 2020; Duveiller *et al.*, 2020). Therefore, it is critical to quantify the contribution of each sub-pixel scene component in mixed canopies that are characterised by a heterogeneous distribution of trees and understory when working with satellite images at medium and low spatial resolutions.

Furthermore, temporal changes in the physiological condition and composition of the understory also affect the relationships between satellite data and vegetation properties, due to mixed pixel effects. This is especially the case at medium and low spatial resolutions, which alter temporal relationships, as demonstrated by Hornero *et al.* (2020). In that study, Sentinel-2 data was used to show an inverse relationship between vegetation indices and the increase in the disease incidence quantified from trees affected by *Xylella fastidiosa* (*Xf*) infection due to understory effects. The results demonstrated that the decrease in tree density, caused by the disease, produced an increase in the understory fraction, resulting in a controversial increase in the Normalized Difference Vegetation Index (NDVI) in the affected fields.

In this context, models are essential to relate observed optical properties to leaf biophysical and biochemical attributes and to analyse the effect of

heterogeneous canopy structures at different spatial resolutions (Wu and Li, 2009). Several methods have been proposed to calculate biochemical traits from hyperspectral reflectance, including scaling-up and model inversion methods that couple leaf and canopy transfer models (Verrelst *et al.*, 2018). For instance, recent studies (Melendo-Vega *et al.*, 2018) have used a coupled model strategy (1D PROSAIL + 3D FLIGHT) including the contribution of the grass background to improve the simulation of the spectral properties for multi-layered tree-grass ecosystems. Other strategies include the use of linear spectral unmixing techniques tested to separate the spectral properties of forest floor and overstory components (Markiet and Mõttus, 2020). Despite the progress achieved, this modelling approach does not yet include the contribution of fluorescence and the impact of the multiple scattering produced between tree and understory components and the background layer.

In recent modelling studies, the chlorophyll fluorescence emission has been included at the leaf (Kallel, 2020; Pedrós *et al.*, 2010; Vilfan *et al.*, 2018, 2016) and canopy level in homogeneous (Atherton *et al.*, 2019; Romero *et al.*, 2020; Yang and van der Tol, 2018; Zeng *et al.*, 2019) and heterogeneous forest canopies (Hernández-Clemente *et al.*, 2017; Liu *et al.*, 2019; Zhao *et al.*, 2016). Furthermore, previous studies have attempted to account for spatial heterogeneity using the first available model-based approximations (Zarco-Tejada *et al.*, 2013b). A more complex three-dimensional canopy radiative transfer model (RTM) – FluorFLIGHT (Hernández-Clemente *et al.*, 2017) – was developed to parameterise the canopy structure to estimate SIF from heterogeneous forest canopies. The model is based on the combination of FLUSPECT (Vilfan *et al.*, 2016) with the 3D ray-tracing model FLIGHT (North, 1996) to simulate multiple scattering within the canopy including the contribution of the gap and shadows between the tree crowns. Modelling results with FluorFLIGHT showed that the variability in the percentage of sunlit and shaded vegetation and soil affects the absolute values of total SIF from aggregated pixels and therefore, the interpretation of SIF from coarse resolution images.

Despite the extensive work conducted with FLIGHT (Bye *et al.*, 2017; Hernández-Clemente *et al.*, 2017; Montesano *et al.*, 2015; Zarco-Tejada *et al.*, 2019, 2018a), strategies that simulate SIF in heterogeneous canopies and consider the effects of different background components, such as soil type or understory fraction, have been limited by difficulties in simulating complex canopy structures and vertical heterogeneity. To simulate SIF of complex multi-scale plant architectures, another 3D ray-tracing approach, the Discrete Anisotropic Radiative Transfer (DART) model (Gastellu-Etchegorry *et al.*, 1996), has been proposed. This model has been recently used with data collected from a hand-held spectroradiometer to demonstrate that SIF is greatly influenced by canopy structure and understory vegetation (Liu *et al.*, 2019). However, further research is still necessary to understand the impact of structural components on the retrieval of SIF from medium ($10 - 60$ m/pixel) to high ($0.3 - 10$ m/pixel) spatial resolution satellite images. Airborne sensors such as HyPlant, the first fluorescence sensor designed to support the FLEX mission and dedicated to validating the retrieval of SIF for a large canopy and different vegetation types (Rascher *et al.*, 2015), can provide valuable information with which to model and understand better the effect of SIF signals among mixed pixels.

The impact of background components on SIF might particularly affect seasonal analyses, where the temporal variation of the understory fraction is high. Forest canopies, in particular, exhibit a complex canopy structure and the distribution of the understory cover fraction mainly depends on topography, sunfleck positions, soil composition and illumination conditions (Tagliabue *et al.*, 2019). Consequently, assuming an invariant and homogeneous effect of the soil as background might increase the uncertainty of biophysical parameters retrieved from high- and medium-resolution imagery (Hornero *et al.*, 2020; Meng *et al.*, 2018). These previous studies have demonstrated the need to develop new modelling approaches that consider the multiple scattering, mutual shading of the crowns, variation in the soil, and shading of the background in SIF retrieval.

In this study, we propose a modification of the 3D RTM FluorFLIGHT model to simulate canopy reflectance and SIF in heterogeneous canopies, including the effects of different background components, such as the soil and the understory cover fraction. In particular, we aim to i) analyse the contribution of SIF emitted by the understory in aggregated pixels using high spectral and spatial resolution imagery collected from the airborne hyperspectral HyPlant system, ii) study the impact of the variation in the understory cover fraction on the total SIF calculated at different scales. We compare this modified model with others from the Radiation Transfer Model Intercomparison (RAMI-3) exercise under the RAMI On-line Model Checker framework (ROMC) (Widlowski *et al.*, 2008, 2007) and validate it with field and airborne data.

3.2. Material and methods

3.2.1. Study site and ground data collection

The study was carried out in a Mediterranean tree-grass ecosystem (locally known as *dehesa*) located in Majadas de Tiétar (western Spain, 39°56′20″N, 5°46′28″W) (Fig. 3.1). The *dehesa* is a unique and practically endemic agrosilvopastoral system of the Iberian Peninsula, formed mainly by holm and cork oaks, with a lower stratum of grasses and shrubs, and generally shows extensive livestock use. These two strata, trees and understory, mainly define the vegetation structure in the study area. The tree layer covers approximately 20% of the surface and is predominantly composed of holm oak (*Quercus ilex* L. subsp. *ballota*) (Bogdanovich *et al.*, 2021). The understory grass layer is highly dynamic and is dominated by species of the three main functional plant forms of grasses, forbs and legumes (Migliavacca *et al.*, 2017).

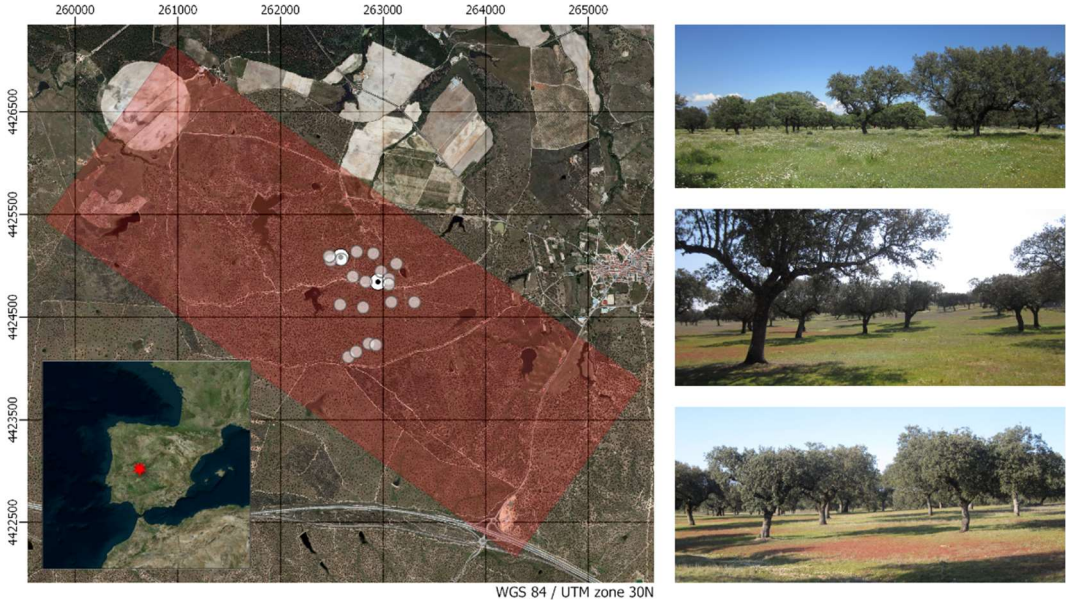

Figure 3.1 Location of the study site selected for the quantification of SIF through high-resolution hyperspectral imaging (left). The red shaded area represents the image coverage. The grey dots represent the 25 × 25 m plots that were sampled to obtain the biochemical and structural variables of the understory, and the white dotted circles represent the radiometric towers with FloX instruments attached measuring up- and down-welling radiance. The images on the right show the heterogeneity of the landscape and the understory within the area of study.

Field measurements were taken on 24 June 2018 simultaneously with the airborne campaign described in section 2.2 to perform the image processing and model parametrisation. In particular, total incoming radiance was required for the SIF and the reflectance calculation for both empirical and simulated data. Solar irradiance data were measured at the time of image acquisition with a SIF-enabled high-resolution spectroradiometer instrument (FloX, JB Hyperspectral Devices, Düsseldorf, Germany) mounted and levelled on a 9-metre tower above the tree canopy. Two FloX boxes were installed over two trees (Fig. 3.1) during the flight, and another one was also used to collect spectral data from the understory in 15 plots (transects) between these trees. Each FloX equipment consists of two sealed and isolated spectroradiometers, FULL and FLUO (Table 3.1). Total incoming radiation was also simulated by the SMARTS model (National Renewable

Energy Laboratory, United States Department of Energy) (Gueymard, 1995, 2001), using aerosol optical depth measured at 550 nm from the AERONET (Holben *et al.*, 1998) station over Majadas (Spain), located at a central point in the study area. A comparison between solar irradiance from different sources is presented in Fig. B1 (Appendix B.).

Table 3.1 FloX specification. FULL and FLUO spectroradiometers used for the field data collection.

OPTIC	FULL	FLUO
Spectrometer-based model	FLAME VIS-NIR	QE Pro
Wavelength range (nm)	400 – 950	650 – 800
Spectral resolution (nm)	1.5	0.3
Signal-to-noise ratio	250	1000
Field of view (deg) (down- / up-welling radiance)	180 / 25	180 / 25

Biochemical and structural variables of the understory to enter into the model were obtained by destructive sampling of the grass layer in nineteen plots of 25 × 25 m located within the study area (Fig. 3.1). Two 25 × 25 cm grass samples were collected on each plot in areas visually identified to be representative of the variability in each plot; if the plot contained trees, one of the samples was acquired below the canopy to take into account the potential variability induced by the tree crowns (Melendo-Vega *et al.*, 2018; Mendiguren *et al.*, 2015). The understory leaf area index (LAI) was also measured by destructive sampling. All rooted plants within each 25 × 25 cm quadrant were collected using clippers and stored in sealed plastic bags. These were weighed in the field and then transported in a cooler to the laboratory, where subsamples were selected, and green and dry fractions were manually separated. Subsample fractions were scanned in an Epson Perfection V30 colour scanner (Epson American Inc., Long Beach, CA, USA). The leaf area was calculated automatically from the scanned images using the unsupervised classification algorithm ISOCLUS implemented in PCI Geomatica (PCI Geomatics, Richmond Hill, Ontario, Canada). ISOCLUS is based (with minor modifications) on the ISODATA method

described in Tou *et al.* (1974). To measure the chlorophyll a (Ca), b (Cb), a+b (Cab) and total carotenoids (Cca) pigment concentration, a parallel grass sample (pigment quadrant) was taken adjacent to the quadrant where biophysical and structural variables previously described were sampled. In each pigment quadrant, the green fraction of the standing vegetation was sampled, weighed and frozen in dry ice in the field (for further details see Gonzalez-Cascon and Martin, 2018). The pigment concentrations in the homogenised grass sample were spectrophotometrically analysed in four replicates per sample using 80% (v/v) acetone as a solvent (Gonzalez-Cascon *et al.*, 2017). Percentage of dry mass was determined as well in three replicates per sample. All samples were then placed in an oven for 48h at a constant temperature of 60 ºC to obtain their dry weight. Pigment concentrations per mass were determined in the green grass fraction material and calculated at 65 ºC. Pigment content per total leaf area (µg/cm^2) was calculated combining pigment concentrations per mass determined from the pigment quadrant and parameters obtained from the contiguous quadrant as:

$$\mathrm{C_{ab,leaf,grass}} = \frac{1000\ C_{ab,dmass,g}\ W_{d,s,v}}{A_{leaf,}} \qquad (1)$$

Where $\mathrm{C_{ab,dmass,g}}$ (%) is the concentration of chlorophyll a + b per unit of dry mass of green grass measured in the pigment quadrant and $\mathrm{W_{d,s,v}}$ (g) and $\mathrm{A_{leaf,s}}$ (cm^2) are the dry weight and leaf surface area respectively of the green fraction of a subsample collected in the contiguous quadrant.

To characterise the tree canopy, leaf properties were measured for 19 individuals by destructive sampling using a Li-Cor 1800-12 integrating sphere (Li-Cor, Lincoln, NE, USA) coupled to an ASD Fieldspec 3 spectroradiometer (Analytical Spectral Devices Inc., Boulder, CO, USA). Leaves were obtained from two separate branches from the upper third of the tree crown on the south and north sides. The integrating sphere protocol is described by Zarco-Tejada *et al.* (2005), and further information regarding this sampling method is detailed in Melendo-Vega *et al.* (2018). Measurements of the tree canopy LAI were derived using an LAI-2200 plant canopy analyser (LI-COR, Lincoln, Nebraska, USA). Readings were taken above and below

isolated trees under direct illumination conditions with the sensor facing +/- 90º to the solar azimuth angle. The FV2200 processing tool (LI-COR, Lincoln, Nebraska, USA), which provides a mechanism (Kobayashi *et al.*, 2013) that allows correction of measurements for radiation reflected and transmitted by the foliage, was used to apply scattering corrections and to calculate LAI using crown-shape measurements derived from field images.

3.2.2. Airborne hyperspectral and LiDAR data

Airborne data collection (Fig. 3.2) was conducted on 24 June 2018 using the high-resolution triple-coupled hyperspectral solution HyPlant v3, developed by the Jülich Research Centre (Kreis Düren, Germany) in cooperation with SPECIM Spectral Imaging Ltd. (Oulu, Finland) (Siegmann *et al.*, 2019) and a long-range laser scanner onboard a Cessna aircraft. The HyPlant system consists of two hyperspectral modules as a combination of three pushbroom imaging line scanners. The DUAL imager (available commercially as AisaFENIX) comprises two integrated sensors in a single housing sharing the same optics, which provides continuous spectral information covering the visible/near-infrared (VNIR) and short-wave infrared (SWIR) regions of the spectrum (380 – 2500 nm), and yielding 3.5 and 12 nm full-width at half-maximum (FWHM) spectral resolution, respectively. The FLUO module (commercially known as AisaIBIS) is an imager that acquires data between 670 and 780 nm at higher spectral resolution (Celesti *et al.*, 2019; Siegmann *et al.*, 2019). The hyperspectral sensors were radiometrically calibrated with an integrating sphere on SPECIM's facilities by calculating coefficients derived from a calibrated light source and, prior to applying these coefficients, the dark frame correction was conducted. We calculated the top-of-canopy (TOC) spectral reflectance – Cluster II output as described in Siegmann *et al.*, (2019) – from the DUAL imager in the VNIR and SWIR regions with ATCOR4 (ReSe Applications Schläpfer, Wil, Switzerland) using available sunphotometer measurements of Aerosol Optical Depth (AOD) as input parameters. We used at-sensor-radiance from the FLUO imager (Cluster III

output), extended by the application of the point-spread function deconvolution (Siegmann *et al.*, 2019). DUAL and FLUO sensors were boresight corrected and orthorectified with CaliGeoPRO (SPECIM Spectral Imaging Ltd., Oulu, Finland) using inputs from an inertial navigation system Oxford 3052 GPS/INS (Oxford Technical Solutions Ltd., Oxford, UK) installed onboard and synchronised with HyPlant.

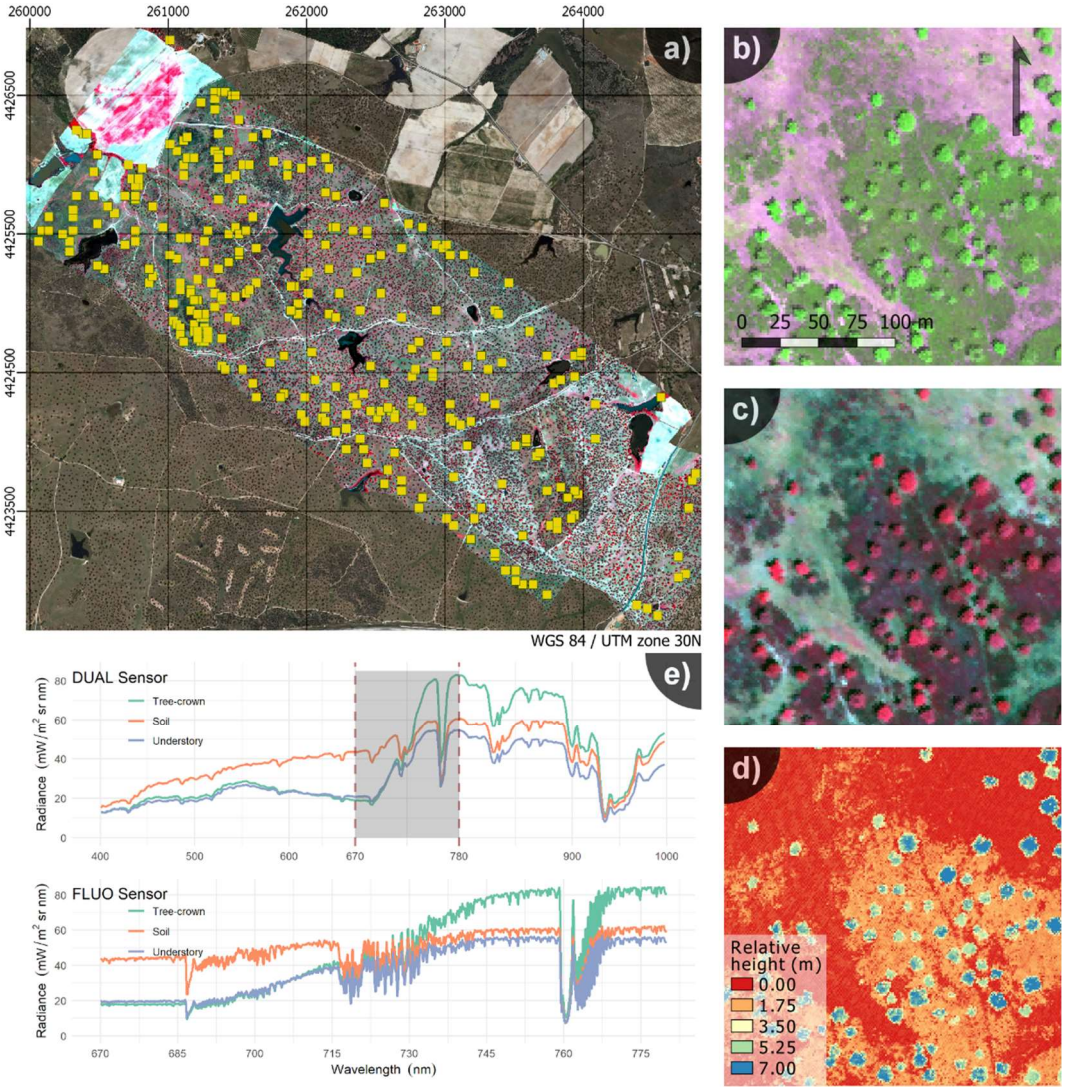

Figure 3.2 Airborne high-resolution hyperspectral flight with the HyPlant sensors (colour-infrared, {860, 650, 550 nm}) over the study area (a). Yellow squares indicate the location of the 300, 25 × 25 m, scene grid selection. The different components that comprise a scene can be visually discriminated by the images acquired from b) the FLUO (false colour, {700, 754, 674 nm}) and c) DUAL (colour-infrared) sensors of the HyPlant tandem and d) from the digital surface model of the LiDAR sensor. Spectral radiance extracted from tree crowns, understory (shrubs and grasses) and soil components of Hyplant DUAL+FLUO images is shown in (e).

LiDAR data were acquired using a Riegl LMS-Q780 system (RIEGL Laser Measurement Systems GmbH, Horn, Austria). A normalised digital surface model (nDSM), also known as canopy height model and generated from the

LiDAR point cloud, was used to measure canopy features: height, diameter and fractional cover (FC). The nDSM product also allowed image segmentation to be performed, to separate tree crowns from the understory.

The hyperspectral images had a ground resolution of 1.5 metres per pixel and allowed individual tree crowns to be distinguished from the background consisting of soil and understory vegetation. We used the images to calculate the spectral information of each scene component (Fig. 3.3), to calculate the NDVI (Rouse *et al.*, 1974) and to quantify the fluorescence signal. For this, we used the O_2 A-band in-filling method through the Fraunhofer Line Depth (FLD) principle (Plascyk, 1975), based on a total of three spectral bands (3FLD) (Maier *et al.*, 2003);

$$3\text{FLD} = \frac{E_{out} \cdot L_{in} - E_{in} \cdot L_{out}}{E_{out} - E_{in}} \qquad (2)$$

where radiance L corresponds to L_{in} (at 761 nm), L_{out} (mean value of L_{747} and L_{780} spectral bands), and irradiance E to E_{in} (at 761 nm), and E_{out} (mean value of E_{747} and E_{780} spectral bands). The decision of using 3FLD is based on the successful performance of this index in previous studies (Cendrero-Mateo *et al.*, 2016; Damm *et al.*, 2015; Liu *et al.*, 2015; Liu and Liu, 2014). 3FLD was calculated by using the at-sensor-radiance from the FLUO imager previously described, which does not take into account the atmospheric absorption and scattering effects. For this study, we assumed relatively low impact of these effects considering that we are assessing the relative contribution of SIF emitted by the understory to the full canopy with data collected from a single flight and acquired within 27 minutes in clear sky conditions. In addition, a comparison was made between FloX measurements and the hyperspectral images. Using all the measured data (transects and tree-crown measurements) the relationship was reasonably strong ($R^2 = 0.67$, RMSE = 0.12 mW m^{-2} sr^{-1} nm^{-1}), improving when the assessment was carried out using the two FloX instruments permanently installed over two tree crowns (RMSE = 0.04 mW m^{-2} sr^{-1} nm^{-1}).

The objective of using NDVI in this study is to show the behaviour of a standard and widely used vegetation index related to fractional cover, comparing the effects observed in both NDVI and SIF. The high-spatial resolution of the airborne hyperspectral images allowed the extraction of different scene components used as ground truth for the model inversion following the methodology proposed by Zarco-Tejada *et al.* (2019). A Mahalanobis Distance classification (Richards and Jia, 1999) using ENVI/IDL (Exelis Visual Information Solutions, Boulder, Colorado) was also derived from the hyperspectral DUAL-sensor imagery to classify vegetation cover, soil, roads and water ponds throughout the study area. In this way, we constructed the scene grid and filtered scenes that contained roads, water or buildings. The scene grid enabled the spectral reflectance of each component to be calculated, which was then used to evaluate the behaviour of the model with different types of soil, understory variability and FC (Fig. 3.2).

We used the tree-crown segmentation calculated from the nDSM LiDAR product to establish an external buffer of two metres, which was excluded from the analysis to avoid tree shadows, mixtures of tree branches and understory at the crown edges, and potential effects of misalignment between sensors (Fig. 3.3).

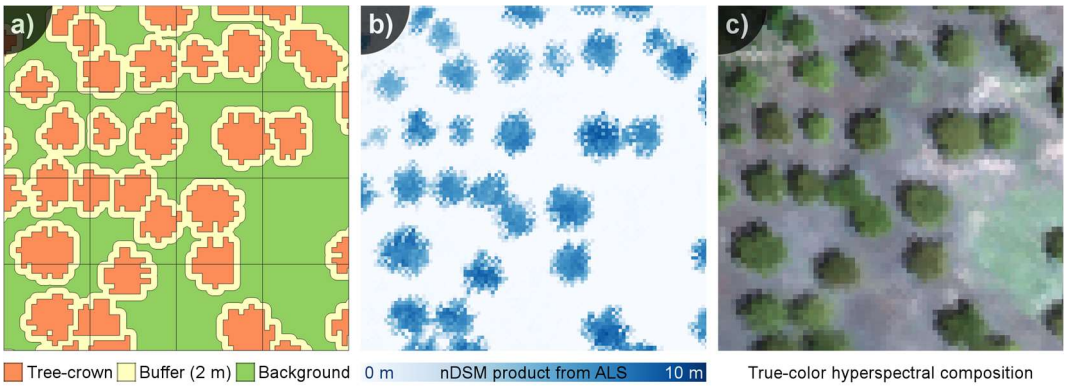

Figure 3.3 Example of a) tree-crown delineation over the b) normalised digital surface model (nDSM) and the c) True colour DUAL orthoimage.

Taking into account the difference in NDVI and 3FLD values obtained from tree-crown and aggregated pixels (Fig. 3.4), we performed an empirical analysis over a selection of 300 scenes (Fig. 3.2a) that covered all the natural range found within the study area (NDVI: 0.25 – 1.00, 3FLD: 0.10 – 0.95 mW m^{-2} sr^{-1} nm^{-1}).

Figure 3.4 Understory variability in different scenarios (colour-infrared composition; 25 × 25 m pixels along with the collected data) and how this variation affects the mean value in the NDVI (unitless) and 3FLD (mW m^{-2} sr^{-1} nm^{-1}) indices.

To assess the contribution of SIF emitted by the understory, we compared the values obtained from tree crowns and aggregated pixels at different spatial scales (Fig. 3.5a). We selected the spatial resolutions of 5, 15, 25, 50 and 100 m (Fig. 3.5b), which were either smaller than the tree crowns or much larger and even grouped several trees within the same sampling. Figures 3.5c and 3.5d show that NDVI and 3FLD values of the scene decrease as pixel aggregation increases. The spatial resolution selected is highlighted in different colours covering different aggregation levels covering the entire range. Those resolutions were used to further analyse the contribution of the SIF emitted by the understory and tree crowns using empirical data and RTM as described below.

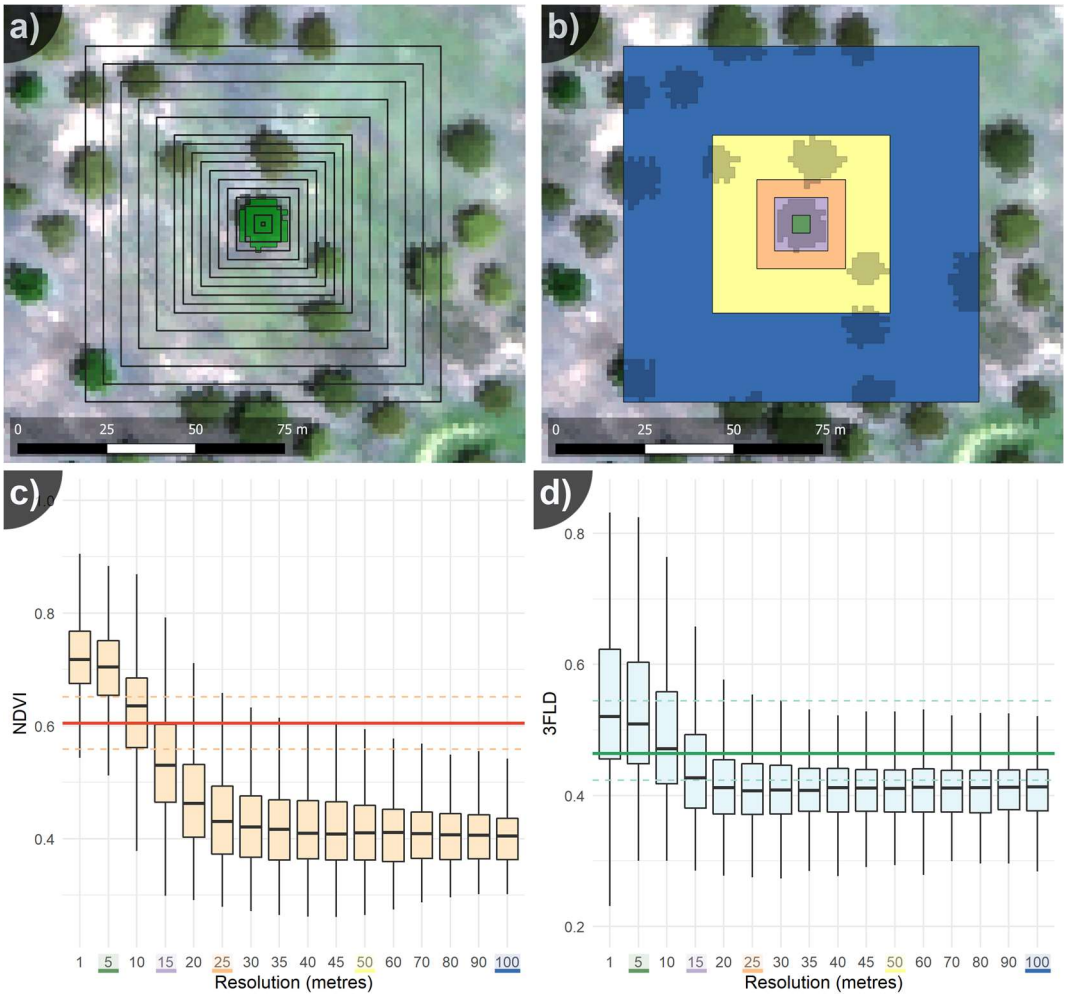

Figure 3.5 Spatial scales from 1 to 100 m (a) and its selection (b) at 5 m (green), 15 m (purple), 25 m (orange), 50 m (yellow) and 100 m (blue). Aggregated values of c) NDVI and d) 3FLD (mW m^{-2} sr^{-1} nm^{-1}) at different spatial scales from a); horizontal lines show the mean tree-crown value and the Q1-Q3 interquartile range.

3.2.3. Modified FluorFLIGHT Model to account for the understory

In this study, we extended the 3D RTM FLIGHT (North, 1996) to account for the understory layer, including the SIF contribution of the crowns from the FluorFLIGHT modification (Hernández-Clemente *et al.*, 2017). The main reason for using this model is that it has been previously validated in several applications for the quantification of biophysical parameters (Bye *et*

al., 2017; Guillen-Climent *et al.*, 2012) and plant health condition (Hernández-Clemente *et al.*, 2017; Hornero *et al.*, 2020; Zarco-Tejada *et al.*, 2018a). Furthermore, the computational speed of FLIGHT is relatively fast if compared to other more complex 3D models (DART, Raytran or Librat) because sunlit and shaded canopy fractions are based on simple geometrical-optical properties as reviewed in Malenovský *et al.* (2019). The model is available for download on https://flight-rtm.github.io.

The modification, named FLIGHT8, is based on the existing theory of RTM and couples an additional layer into the 3D ray-tracing model FLIGHT to account for the understory, including changes related to SIF and the interaction between the existing and new components (Fig. 3.6). We considered the contribution of SIF within the understory, as well as the multiple scattering events between components. Similar to FluorFLIGHT, this approach is also coupled with the leaf fluorescence model FLUSPECT (Vilfan *et al.*, 2016), which is a physical model based on Kubelka-Munk theory that includes the fluorescence quantum efficiency parameterisation according to its core-original model PROSPECT (Feret *et al.*, 2008; Jacquemoud and Baret, 1990).

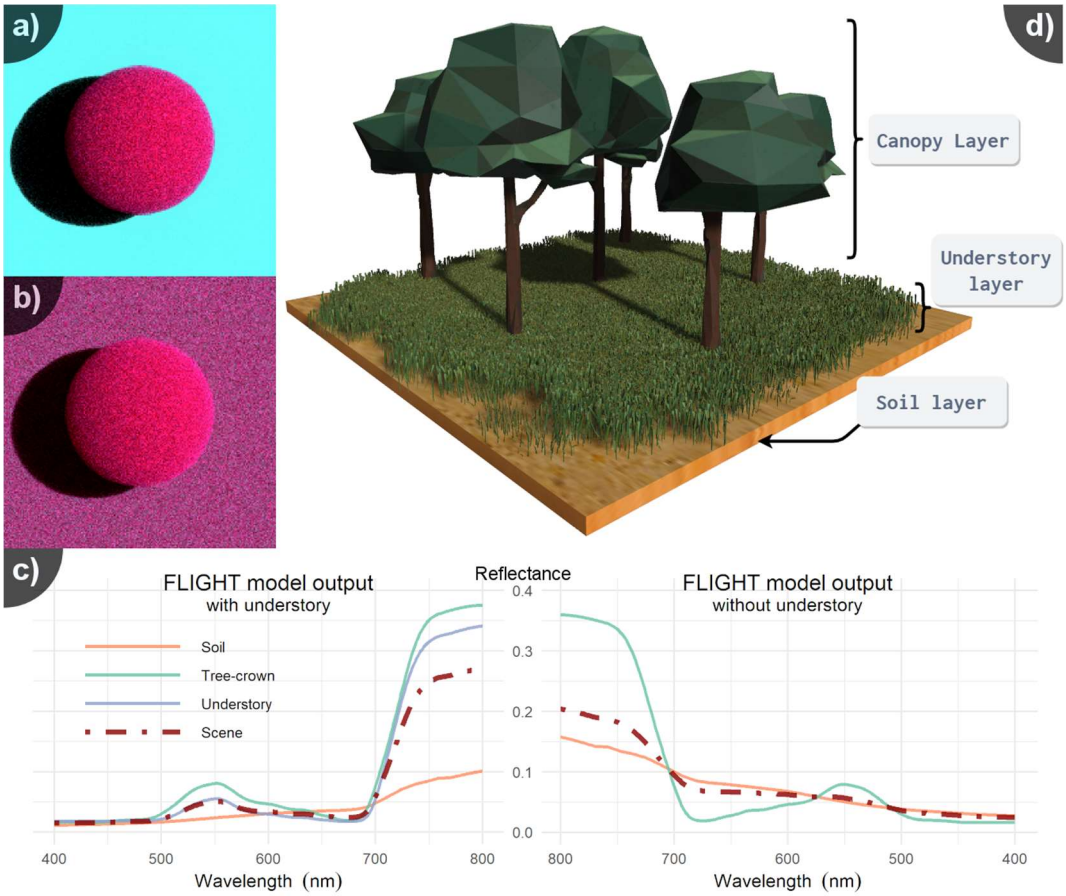

Figure 3.6 Example tree-canopy simulations a) without and b) with understory, c) including their spectra; d) graphical abstract representation of FLIGHT8.

The Monte Carlo ray-tracing model FLIGHT was designed to rapidly simulate light interaction with 3D vegetation canopies at high-spectral resolution, to produce reflectance spectra and LiDAR returns for both forward simulation and use in inversion (North, 1996; North *et al.*, 2010), and recently extended to model solar-induced fluorescence (Hernández-Clemente *et al.*, 2017). Foliage is represented by structural properties of leaf area, leaf angle distribution, crown dimensions and fractional cover, and the optical properties of leaves, branch, shoot and ground components. The model explicitly represents multiple scattering and absorption of light within the canopy and with the ground surface and used as a benchmark by the Radiative Transfer Model Intercomparison (RAMI) (Widlowski *et al.*, 2007). Scattering within

crown and understory components is evaluated by the Monte Carlo method of radiative transfer modelling approximation, where a photon can be stochastically either absorbed or scattered into a new direction. Outside these components, the photon trajectory simulation proceeds by a deterministic ray-tracing approach.

The new model includes an additional parameterisation that defines the understory layer. The understory extends from the soil layer (Fig. 3.6d) to a user-defined height. More input values were added to also define the understory leaf size and its distribution (leaf angle distribution), as well as the mean one-sided total foliage area index (LAI). At leaf level, both the existing model and the understory addition use the same equations (3) to (6) described below to calculate radiance, with appropriate values for optical and structural properties, and here detailed for understory.

Within the homogeneous understory layer, the illumination of a leaf is calculated as the sum of direct and diffuse incoming light. For a leaf L_{US}, viewed from direction vector Ω and illuminated from vector Ω_0, the contribution of the radiation leaving the surface to the detector without taking into account the fluorescence is defined as follows:

$$I_{L_{US}}(\lambda) = I_0(\lambda)\gamma_{L_{US}}(\lambda, \Omega_0 \rightarrow \Omega)P_0 + \frac{1}{m}\sum_1^m I_m(\lambda, \Omega_m) \;\; \gamma_{F_{US}}(\lambda, \Omega_m \rightarrow \Omega) \quad (3)$$

where I_0 corresponds to the illumination radiance of the direct solar beam at the wavelength λ, I_m represents the sample of the incoming diffuse field from the Ω_m direction, and γ_{LUS} denotes the bidirectional reflectance/transmittance factor for each leaf from the understory. If there is a direct path to the light source, P_0 has a value 1, and 0 if not. The incoming diffuse light field is sampled using *m* directions over a sphere. Each sample traces a ray from the leaf to the next interaction in that direction, or sky, and which may leave the understory canopy and so be a contribution from non-understory components; radiance from this is calculated recursively using (3). The non-fluorescent scattering phase function within the understory component

at wavelength λ and leaf normal vector Ω_L, has been approximated using a bi-Lambertian reflectance model:

$$\gamma_{L_{US}}(\lambda, \Omega_L, \Omega' \rightarrow \Omega) = \begin{cases} \pi^{-1}\rho_n(\lambda)|\Omega \cdot \Omega_L|, & (\Omega \cdot \Omega_L)(\Omega' \cdot \Omega_L) < 0 \\ \pi^{-1}\tau_n(\lambda)|\Omega \cdot \Omega_L|, & (\Omega \cdot \Omega_L)(\Omega' \cdot \Omega_L) > 0 \end{cases} \quad (4)$$

Following similar equations, the fluorescence contribution for an individual leaf within this layer ($F_{L\text{-}US}$) is calculated using full fluorescent scattering matrices, through sampling direct and diffuse incident illumination within the excitation range from 400 to 750 nm:

$$F_{L_{US}}(\lambda) = \sum_{k=400}^{750}(I_0(k)\gamma_{F_{US}}(k, \lambda, \Omega_0 \rightarrow \Omega)P_0 + \frac{1}{m}\sum_1^m I_m(k, \Omega_m)\ \gamma_{F_{US}}(k, \lambda, \Omega_m \rightarrow \Omega)) \quad (5)$$

where γ_{FUS}:

$$\gamma_{F_{US}}(k, \lambda, \Omega_L, \Omega' \rightarrow \Omega) = \begin{cases} \pi^{-1}Mb[k, \lambda]|\Omega \cdot \Omega_L|, & (\Omega \cdot \Omega_L)(\Omega' \cdot \Omega_L) < 0 \\ \pi^{-1}Mf[k, \lambda]|\Omega \cdot \Omega_L|, & (\Omega \cdot \Omega_L)(\Omega' \cdot \Omega_L) > 0 \end{cases} \quad (6)$$

where *Mb* and *Mf* represent the backward- and forward-scattering fluorescence matrices for both photosystems PS-I and PS-II, respectively. Similar to FluorFLIGHT at tree-crown level, total measured radiance in the understory component is calculated as the sum of the reflected light (I_{LUS}) and fluorescent emission contribution (F_{LUS}).

The other components within the scene (Fig. 3.6d), the fluorescence contribution within a tree crown, and the consideration of the incident diffuse field remain as described in North (1996), North *et al.* (2010) and Hernández-Clemente *et al.* (2017). The Monte Carlo formulation allows the leaf-level fluorescence contribution to be readily scaled by an estimate of local fluorescence quantum efficiency if available. While single constant values are used separately for understory and canopy here, other recent studies have explored separation of values for sunlit and shaded leaves, or parameterisation by leaf-level PAR (Gastellu-Etchegorry *et al.*, 2017; Zeng *et al.*, 2020; Zhao *et al.*, 2016).

To evaluate the included features in FLIGHT8, we compared the new understory layer as a single 1D simulation with homogeneous cases from the RAMI-3 experiments (Widlowski *et al.*, 2007), which is the most recent and updated RAMI phase built for this purpose. No crowns were considered in this comparison because there is no existing model intercomparison that accounts for a two-layer homogeneous (HOM) and heterogeneous (HET) approach; for fluorescence there is no agreed intercomparison to date. A more recent experiment, RAMI-IV, featured a completely new set of experiments for abstract canopies (Widlowski *et al.*, 2013), but this exercise neither included any case with the HOM-HET combination nor purely homogeneous scenes.

One of the difficulties in evaluating an RT model by comparison with other models is the absence of an absolute reference standard; therefore, to compare the output of the model with a reference value, an alternative truth should be identified. This truth was generated as the mean of a series of models that were identified during the third phase of the RAMI-3 exercise. The radiative transfer models DART (Gastellu-Etchegorry *et al.*, 1996), Drat (Lewis, 1999), FLIGHT (North, 1996), Rayspread (Widlowski *et al.*, 2006), Raytran (Govaerts and Verstraete, 1998) and Sprint (Thompson and Goel, 1998) participated in the generation of the reference data (RAMIREF).

To cover the entire range of the different inputs (Table B1, Appendix B.), we summarised the intercomparison in 12 cases for the Bi-directional Reflectance Factor (BRF) in the principal planes and orthogonal planes by varying the solar viewing angles. Root Mean Squared Error (RMSE) and Mean Absolute Error (MAE) were then calculated between the simulated signal and the RAMIREF.

3.2.4. Model simulation approaches

Firstly, we evaluated the SIF of the understory on a theoretical set of simulations with a single tree by varying its fluorescence quantum efficiency (F_i

from 0 to 0.05) and setting the LAI to the maximum nominal value (LAI = 3). Under the tree canopy, we defined an understory layer and varied its F_i (from 0 to 0.05) and LAI (from 0 to 3). These analyses aimed to understand the contribution of the SIF emitted by the understory layer with a minimum impact from structural tree canopy variables and shadowing.

A more complex scenario was then designed to evaluate the impact on the SIF calculated by aggregating the tree canopy and the understory components. For this purpose, high-resolution airborne images were used to set up the different scenes, and field measurements were taken to establish ranges of biophysical parameters and biochemical variables (Table 3.2). The parameters required by the models that could not be measured in the field (leaf mesophyll structure, leaf angle distribution, senescence material and fluorescence quantum efficiency) were established through previous studies using the values evaluated by Hernández-Clemente *et al.*, (2017) for oak trees and by Melendo-Vega *et al.* (2018) for the understory.

Table 3.2 Values used in the model simulation analysis.

Variable	Units	Acronym	Range
Chlorophyll a+b content	µg cm^{-2}	Cab	0 – 64
Carotenoid content	µg cm^{-2}	Cca	0 – 30
Water content	cm	Cw	0 – 0.03
Dry matter content	g cm^{-2}	Cdm	0.003 – 0.018
Senescence material	Fraction	Cs	0 – 0.3
Mesophyll structure	-	N	1 – 3
Fluorescence quantum efficiency	-	F_i	0 – 0.2
Leaf Area Index	m^2 m^{-2}	LAI	0 – 3
Leaf Size	m	LFS	0.01 – 0.05
Leaf angle distribution	-	LAD	Spherical
Soil reflectance	%	Soil	4 samples
Solar Zenith	deg.	SZA	25.84
Solar Azimuth	deg.	SAA	122.89

The inversion scheme was a multi-step LUT-based approach using NDVI, 3FLD and 650 – 800 nm as described in Hernández-Clemente *et al.* (2017).

In the first stage of the analysis, we built a lookup-table (LUT) of +400k simulations by coupling FLUSPECT-B with FLIGHT8 in 1D mode. The LUT is used to estimate leaf parameters and LAI from the tree canopy and understory independently. The inversion was carried out in different steps by minimising the merit function consecutively for LAI and leaf biochemical parameters. In the next stage, the parameterisation retrieved for each of the scenes and components was used in a second set of simulations by coupling FLUSPECT-B with FLIGHT8 in 3D mode. The topography in the simulations was simplified as flat terrain. The forward simulations were used to calculate the aggregated value of NDVI and 3FLD for the 300 scenes of 25 m selected as described in section 2.2. This last step was applied using FLIGHT8 in two different modes, accounting for the specific contribution of SIF emitted by the understory layer (full mode) and disabling the SIF emitted by the understory (single mode). Model simulations in single-mode use only one layer for the background (assumed Lambertian) and, for this analysis, we used the mean spectral reflectance extracted from the image which includes the average proportion of soil and understory found in the study area. Finally, the model-simulated aggregated pixel, from both the full- and single-mode approaches, was compared to that extracted from the hyperspectral image. The modelling approach performed is depicted in Fig. 3.7. The comparison between single-mode and full-mode approach was intended to understand the theoretical contribution of the understory integrated into FLIGHT8.

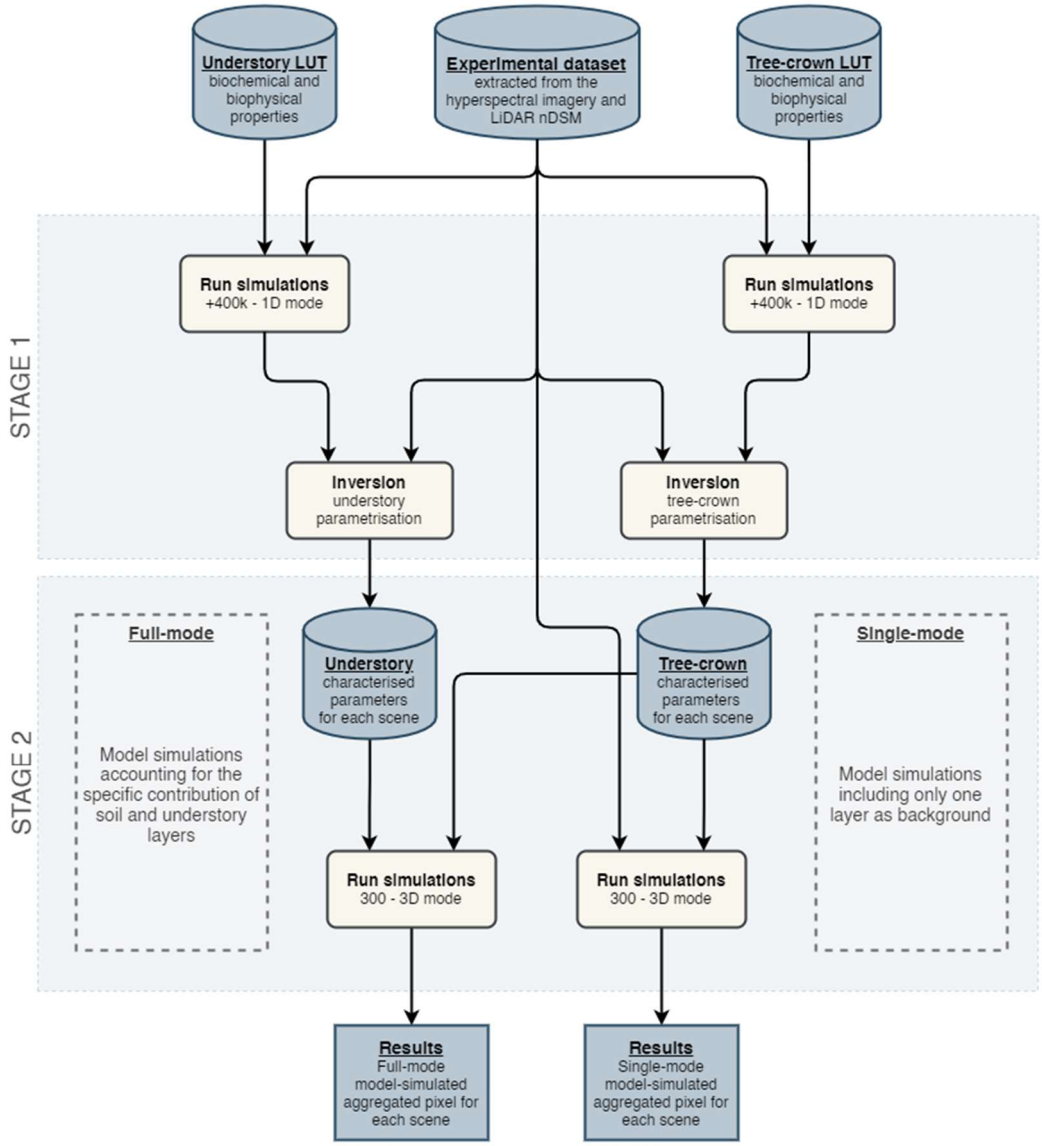

Figure 3.7 Model simulation approach diagram.

3.3. Results

Results from empirical approaches are presented to show the effect of the understory on NDVI and 3FLD derived from different pixel aggregation scales. Based on the need to correct these effects, we present results showing the performance of FLIGHT8 to account for the understory variations that affect the reflectance calculated from aggregated pixels. FLIGHT8 was additionally compared with other models and widely accepted reference data.

3.3.1. Effects of the understory on airborne data calculated from aggregated pixels

The comparison between the aggregated pixel and the tree-crown segmented value extracted from the airborne imagery showed the impact of the background at different scales for NDVI and 3FLD indices (Fig. 3.8a and 3.8b, respectively). In the case that the aggregated pixel includes more than one tree (Fig. 3.5), these are taken into account when computing the average value of the tree-crown and understory components. At a resolution of 5 m, where aggregated areas were centred on crowns (green points in Fig. 3.8a, b), the pixel size was smaller than the mean crown size (μØ = 11.98 m), and the impact of the background was relatively low for both NDVI and 3FLD, with a high correlation between aggregated and pure crown values ($R^2 > 0.99$; NRMSE < 0.01). The goodness of fit between tree-crown and aggregated pixels decreased with a pixel size slightly higher than the crown size (15 m), and the errors doubled with a crown size of 25 m (orange points) for NDVI ($R^2 = 0.47$; NRMSE = 0.33) and 3FLD ($R^2 = 0.58$; NRMSE = 0.2). To elucidate the contribution of each component at this scale, we plotted the relationship between the canopy and the understory FC (Fig. B2, Appendix B.). The dispersion of points increased and diverged from a linear fitting as the soil FC increased. The contribution of each component at the same resolution (25 m, Fig. 3.8c and 3.8d) showed that the slope of the linear relationship between the NDVI from aggregated pixels and understory was closer to the identity line than that of the tree crowns, confirming that the contribution of the understory is significant.

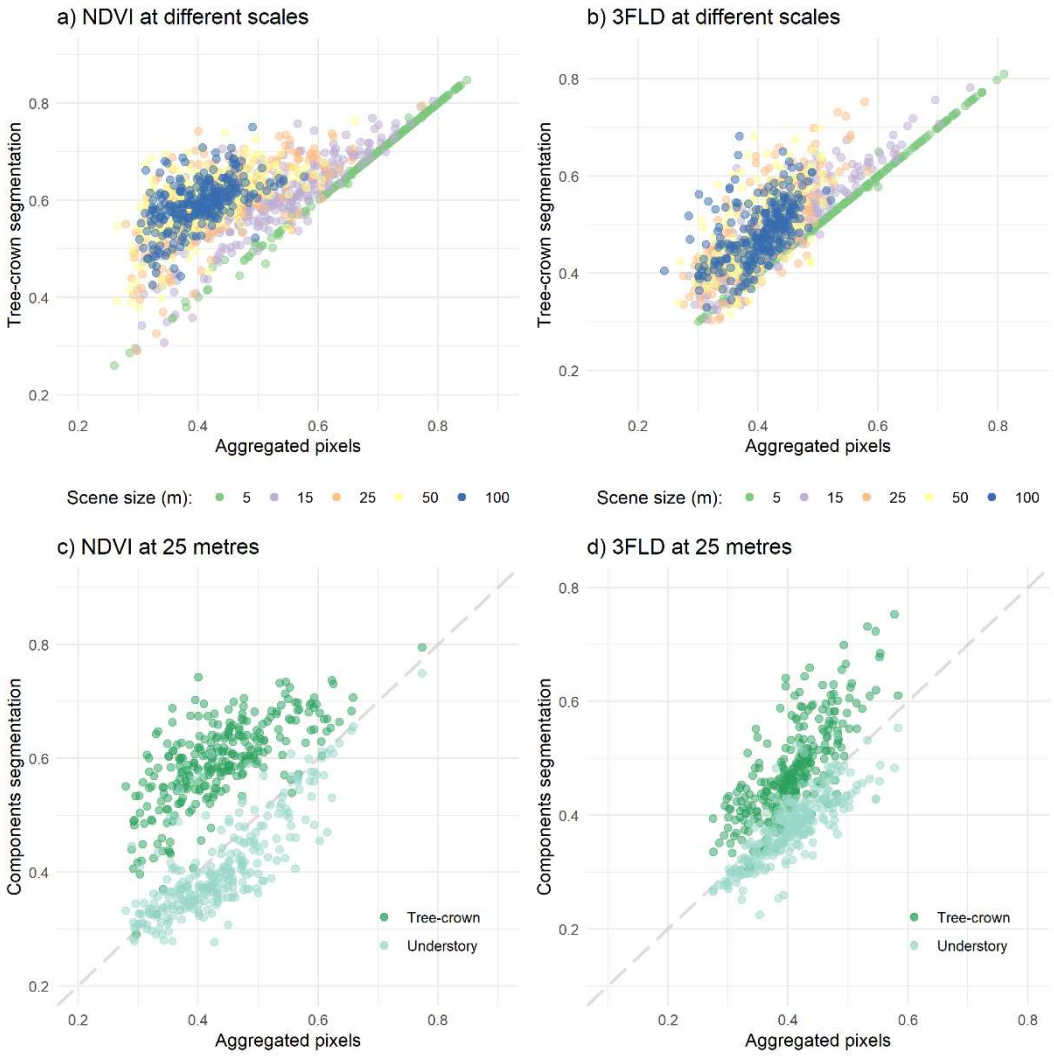

Figure 3.8 Relationship between airborne image data obtained from pure tree crowns and aggregated pixels from a 5 m window to a 100 m window for a) NDVI and b) 3FLD (mW m^{-2} sr^{-1} nm^{-1}). Spatial scales start at 5 m (green points) and increase to 15, 25, 50 and 100 m (purple, orange, yellow and blue points, respectively). Relationship between c) NDVI and d) 3FLD values aggregated by tree-crown and understory components, and the total aggregated value at 25 m.

3.3.2. The FLIGHT8 model approach to account for background effects

As a previous step to the modelling approach, the performance of FLIGHT8 was analysed using controlled conditions. A comparison against other RTM

models is included in Appendix B. Fig. B3 shows that the simulations obtained (dark-green line) through the range of input variables agreed in RAMI showed a similar performance to that of the models used to generate the reference data RAMIREF (dashed light-green line). The shaded yellow area displays the absolute coverage range of these models, and in all cases, the simulations with FLIGHT8 were contained within this zone. More comparison results are presented in Appendix B. (Fig. B4), including the results from the RAMI On-line Model Checker (ROMC). In all cases, the observed degree of relationship between the reference value and the simulations from the modified model was very high, showing a coefficient of determination (R^2) that exceeded 0.98, with a mean value of 0.99. The differences between these data sets were also minimal, and the greatest error was 0.007 for both RMSE and MAE metrics. The first set of results showed the sensitivity of aggregated pixel 3FLD to variation in the understory and tree-crown F_i and the understory LAI (Fig. 3.9). The total scene SIF increases with LAI and the F_i of both the understory and crowns (Fig. 3.9a). Understory LAI is shown to have the greatest impact on aggregate pixel SIF for the ranges shown. Within each subgroup of LAI (0.5 size step), there was a gradual increase in the variation in the aggregated pixel, which followed a similar pattern, except when the understory LAI was zero, where the scene SIF only varied depending on the tree parametrisation. For values of LAI in the understory above zero, a similar increase in SIF of the scene was observed with increasing values of understory and tree-crown F_i. Furthermore, there was a linear relationship between the SIF extracted from sunlit (Fig. 3.9b left) and full-crown pixels (Fig. 3.9b right) with respect to the aggregated pixels as a function of the variation in F_i (0 – 0.05) of the understory and the tree crowns. The SIF signal quantified from sunlit and full-crown pixels was higher than that from 25 m aggregated pixels. The differences were greater for sunlit crown pixels, where the impact of the background was lower. For lower values of crown F_i, the relative contribution of the background for sunlit and full tree crowns increased, and the differences between SIF quantified from crown and aggregated pixels decreased. The F_i of the understory also affected the relationship, with fewer differences observed between SIF

quantified from tree crowns and aggregated pixels for the understory with a higher F_i. Fig. 3.9c and d show that if we try to calculate the SIF from the crown component based on the relationship between full-tree crowns and aggregated pixels, the increasing of the understory LAI reduces the correlation between them. The highest increase in NRMSE is observed with understory LAI values between 0-1. These results show the contribution of the SIF emitted by the understory not only in the whole scene, but also at the tree-crown level, and illustrate the difficulties in interpreting SIF from coarse resolution images.

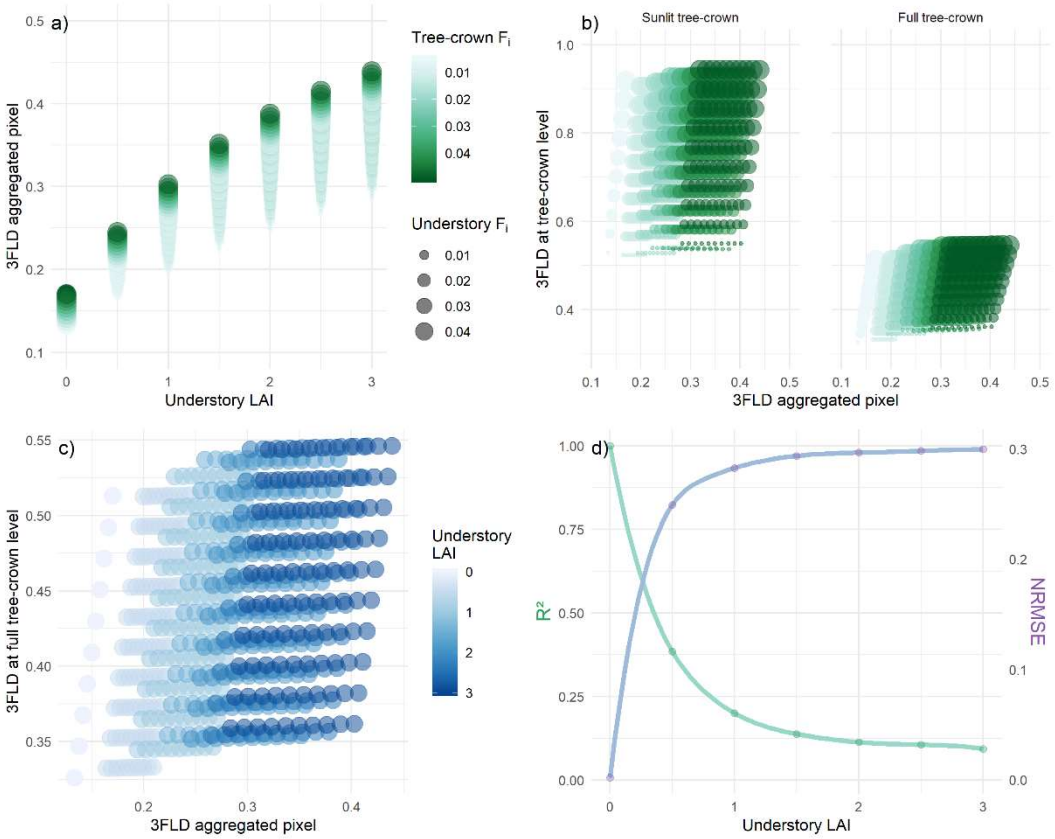

Figure 3.9 Effects of the variation in fluorescence quantum efficiency (F_i, 0 – 0.05) of the forest understory and the tree crown on the 3FLD (mW m^{-2} sr^{-1} nm^{-1}) quantified from 25 m aggregated pixels against the a) understory LAI and b) 3FLD from tree-crowns, where either only the sunlit component (left side) or the entire crown (right side) were aggregated. c) Effects of the variation in LAI (0 – 3) of the forest understory on the relationship between 3FLD calculated from tree-crowns and 25 m aggregated pixels and d) the

associated R^2 and NRMSE values for the linear model established for each subgroup of understory LAI.

Based on the proposed modelling approach (Fig. 3.7), FLIGHT8 was then used to calculate NDVI and 3FLD from aggregated pixels that either did or did not account for the specific contribution of the soil and the understory layer (full or single mode, respectively; Fig. 3.10). The model simulations and the hyperspectral data were significantly related for NDVI (R^2 = 0.95, RMSE = 0.04, Fig. 3.10a) and 3FLD (R^2 = 0.83, RMSE = 0.03 mW m^{-2} sr^{-1} nm^{-1}, Fig. 3.10b) when the model accounted for the contribution of the understory. Similar results were obtained for NDVI using the single-mode model approach, where the specific understory contribution was not considered (R^2 = 0.96, RMSE = 0.04, Fig. 3.10c). However, based on the same assumption, 3FLD was underestimated by the model and the retrieval accuracy was significantly affected (R^2 = 0.4, RMSE = 0.28 mW m^{-2} sr^{-1} nm^{-1}, Fig. 3.10d). These results show the need to consider the contribution of the understory layer in assessing SIF from the aggregated pixels and confirm the ability to use RTM for modelling these effects.

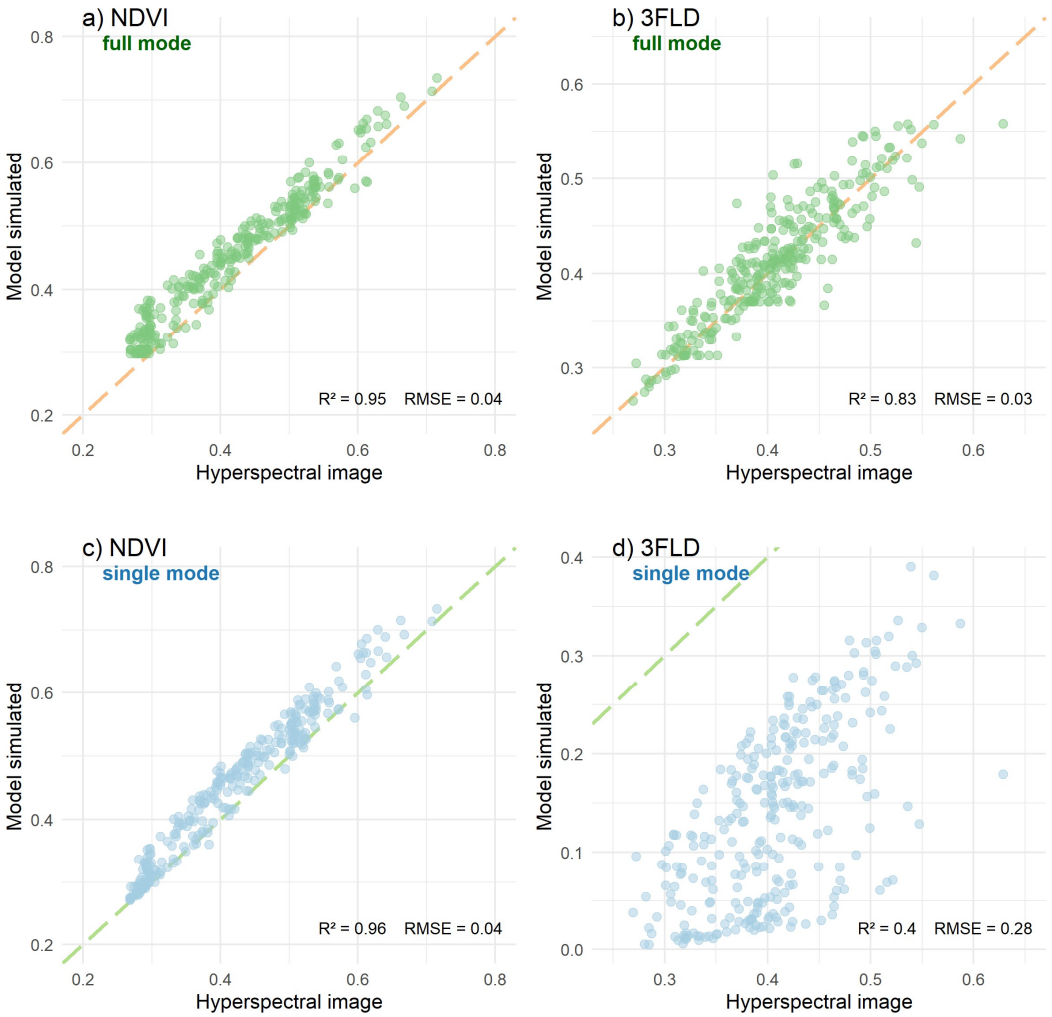

Figure 3.10 Relationship between hyperspectral data from 25 m aggregated pixels and model-simulated NDVI and 3FLD (mW m^{-2} sr^{-1} nm^{-1}) indices accounting for the contribution of SIF on the understory (full mode, *a* and *b*, green points with orange dashed line as 1:1 relationship). The same relationships obtained from model simulations without accounting for the contribution of SIF on the understory and using the empirical reflectance of the background as soil layer (single mode, *c* and *d*, light-blue points with a green dashed line as the identity line).

3.4. Discussion

The availability of SIF observations from space raises the need to develop and validate new approaches for modelling SIF scattering and re-absorption at the canopy level. The quantification of the fluorescence contribution to top-of-canopy radiance is challenging due to the reduced availability of studies and models with which to interpret the scattering processes within the canopy (Qiu *et al.*, 2019; Romero *et al.*, 2018; Yang and van der Tol, 2018; Zeng *et al.*, 2019). Seeking to fill this gap, the results of this study show the contribution of the SIF emitted by the understory and tree crown components of the total forest canopy. A critical issue found was the selection of a model from among the available ones that can represent the main components of the forest canopy, but that avoids laborious parameterisation that hinders the retrieval of the biophysical properties of the vegetation from images (Hernandez-Clemente *et al.*, 2014). Early attempts at using a 3D-RTM to simulate SIF from heterogeneous canopies (Hernández-Clemente *et al.*, 2017) reported the impact of soil background on the estimation of SIF at the canopy level. Our study introduces a new factor, considering the combined effect of soil and understory vegetation that contributes to the spectral reflectance of the background of an oak grassland at the end of the spring. We used data collected with HyPlant to demonstrate empirically that the understory affects the aggregated pixel values. The higher the aggregation, the more significant were the differences between the pure tree-crown value and the aggregated pixel, and these differences became less relevant at values close to or below the mean crown size. The empirical degradation of the NDVI and SIF by increasing the pixel size (Fig. 3.5) reinforces the results shown in Figure 3.8. The aggregated pixels larger than the mean crown diameter deviate significantly from the crown values. Therefore, it follows that to accurately interpret signals arising from spatially heterogeneous canopies using a larger pixel size, further development is required. The 3FLD and NDVI quantification were similarly affected by the difference in scale size. Hence, this study demonstrates that the spectral contribution of the understory in heterogeneous canopies might introduce large inaccuracies into

measurements calculated from satellite imagery with medium and low spatial resolutions when the quantification of SIF is needed from separated components (tree crowns and understory). This aggregation increases the uncertainties in modelling SIF and other vegetation indices on a global scale when the spatial distribution and composition of the understory varies over the seasons. In a relatively constant dominant layer (e.g. evergreen canopies), phenological changes of the understory through the season translate into changes in the canopy structure that alter the relationship between GPP and SIF (due to the SIF scattered by the canopy and the re-absorption pattern) (Ahl *et al.*, 2006; Xiaoliang Lu *et al.*, 2018). Even if seasonality remains unchanged, several ecosystems are characterised by a heterogeneous distribution of understory vegetation, which affects the spectral reflectance observed at coarse satellite resolutions. Although this study is carried out with constant values of solar and viewing angles, future work could consider the variation of these parameters. This is possible because FLIGHT8 allows to simulate BRF using different illumination and viewing geometries as it is shown in Fig. B3. Upcoming studies focused on the analysis of the impact of the illumination condition on the quantification of SIF will be very interesting for assessing temporal trends of SIF from different sensors. Another important parameter to consider in that case will be the adjustment of F_i for sunlit and shaded canopies which may vary depending on the short and long term light adaptation of the leaves.

The quantification of SIF emitted by the tree crowns and the understory separately may not always be necessary, in particular for modelling global GPP (Joiner *et al.*, 2014). However, for other studies such as the temporal evolution of photosynthesis related with decay, stress or disease, the physiological state of each component independently should be accurately understood (Stoy *et al.*, 2019). This approach could also be useful for partitioning fluxes of canopy components, which is very challenging from eddy covariance techniques. It is therefore critical that we are able to separate components to take into account the evolution that each of them has over time. The relevance of assessing the contribution of SIF of the understory is consistent

with the model simulation reconstruction from terrestrial laser scanning shown by Liu *et al.* (2019). Future studies should consider the impact of spatial and temporal variations driving global plant dynamics. For these cases, it would be interesting to analyse the sensitivity of these factors on different SIF proxies such as iFLD (Alonso *et al.*, 2008), pFLD (Liu and Liu, 2015), SFM (Mazzoni *et al.*, 2012; Meroni *et al.*, 2010) or NIRv (Badgley *et al.*, 2017; Dechant *et al.*, 2020). The latter, which without explicitly including the telluric oxygen absorption bands, is strongly related to sun-induced chlorophyll fluorescence (Fig. B5) and to global and site-level estimates of GPP (Badgley *et al.*, 2017). Similarly, Wu *et al.* (2020) demonstrate the great potential of NIRv for estimating daily or sub-day GPP from remote sensing data from high-resolution satellites. In physical terms, NIRv represents the proportion of the pixel reflectance attributable to the vegetation in the pixel, so it seems reasonable that the following advances were aimed at using hybrid models that allow us to separate the scene components and use indicators such as NIRv that, by isolating the signal from the vegetation, could reduce the effect of mixed pixels.

The empirical results of the contribution of SIF emitted by the understory and tree crowns on the quantification of SIF from Hyplant images were in agreement with model simulations. The simulation analysis was performed with a new RTM that includes the option to analyse the contribution of the SIF emitted by the understory and the tree crowns. Although in this work it has not been possible to validate SIF through the RAMI experimental exercises because they are not yet available, RAMI-3 has allowed us to validate the model's ability to represent a new layer. Using a straightforward set of simulations, we show that the higher the LAI of the understory, the smaller the effect of the soil, and therefore, the SIF of the canopy is more similar to the SIF of the scene (Fig. 3.9), reducing the impact of pixel size variation and scene heterogeneity. However separation of crown and understory is also complicated, and beyond approximately an understory LAI of 0.5 the understory SIF contribution dominates the aggregated pixel. These results are consistent with the significant contribution of the SIF understory

to the TOC SIF reported by Liu *et al.* (2019) using an ASD hand-held spectrometer in an open-canopy boreal forest. Based on the need to understand the contribution of the understory at the landscape level, this study shows the accuracy of full tree-crowns SIF calculated from 25m aggregated pixels with the highest increase in NRMSE observed with understory LAI from 0 to 1. These results strengthen the interpretation of the aggregated pixel covered by previous studies in which only the soil effect was taken into account (Hernández-Clemente *et al.*, 2017; Zarco-Tejada *et al.*, 2018a). The evaluation of a larger set of simulations against the airborne imagery (Fig. 3.10) revealed the capabilities of FLIGHT8 to model different ecosystem components. The comparison between airborne and model-simulated retrievals showed different effects on NDVI and 3FLD under the two proposed approaches: model simulations that included only one layer as background (single-mode) or those that accounted for the specific contribution of soil and understory layers (full-mode). The relationship between model-simulated and airborne NDVI was similar (R^2 = 0.95, RMSE = 0.04) in both cases (Fig. 3.10 a, c). This result was predictable as the presence of soil and vegetation cover is included in both approaches. In full-mode simulations, we account for the contribution of two different layers, understory and soil (Fig. 3.10 a). In single-mode simulations, the layer of the soil is the spectral response of the background extracted from an image with a pixel size of 1.5 m in which both components (soil and vegetation) are mixed (Fig. 3.10 c). The main difference was observed in the quantification of SIF, as model simulations in single mode do not take into account the fluorescence emission of the understory. In this case, the relationship between airborne and model-simulated 3FLD significantly improved using FLIGHT8 in full mode (R^2 = 0.83, RMSE = 0.03 mW $m^{-2}sr^{-1}nm^{-1}$) in comparison with simulations performed in single mode (R^2 = 0.4, RMSE = 0.28 mW $m^{-2}sr^{-1}\,nm^{-1}$) (Fig. 3.10. b, d), because the canopy model does not include the understory contribution of the fluorescence emission in single mode. The results demonstrated that understory SIF could substantially contribute to the total canopy SIF quantified from aggregated pixels in open-canopy forests. Moreover, FLIGHT8 can be used to resolve the problem of interpreting information on

a large scale when the effect of the understory plays a fundamental role, such as in tree-grass ecosystems or open forests.

The heterogeneous spatial distribution of trees and understory layers in the landscape is one of the main factors that inherently introduces uncertainty into the retrieval of biophysical parameters of vegetation through models (Eriksson *et al.*, 2006; Yu *et al.*, 2018). The estimation of these parameters simultaneously contains many implications for the recovery of GPP (Li *et al.*, 2018) and even the interpretation of GPP using SIF as a proxy varies greatly depending on the type of cover (Tagliabue *et al.*, 2019). This study highlights the need for a solution that allows the contribution of the understory in aggregated pixels and its impact on the fluorescence estimation of the total canopy to be modelled. Future studies should also take into account the vertical variability of the maximum rate of carboxylation (Vcmax), which has been proven to be a key parameter for estimation CO_2 assimilation in crops (Camino *et al.*, 2019) and the xanthophyll cycle included in the extended version of Fluspect (Vilfan *et al.*, 2018).

The results of this study contribute to understanding how the quantification of SIF from aggregated pixels can be improved for mixed tree, grass and woodland ecosystems, which cover a large part of the globe (up to 33% according to Hanan and Hill (2012)). The understory of Mediterranean oak woodlands is mainly covered by grasslands, where light availability and nutrient-induced changes alter plant functional traits and canopy structure and control the relationship between GPP and SIF (Migliavacca *et al.*, 2017). However, in other types of ecosystems with higher density, the contribution of the understory may be different. Hence, future efforts should focus on assessing the contribution of the SIF emitted by the understory in the quantification of total canopy SIF in other types of ecosystems and forest complexities. These studies will be decisive for the ability to measure and interpret SIF at the global scale.

3.5. Conclusions

The results presented here demonstrate that the fluorescence signal calculated from medium spatial resolution is significantly affected by variations in the understory. The contribution of understory SIF increased rapidly with understory LAI values, dominating the total scene SIF for LAI greater than 0.5. Beyond this range, the correlation strength of crown SIF with aggregated pixel SIF reduces, requiring modelling of the system if separation of crown and understory SIF is necessary, for example in assessing forest health or seasonality. Thus, the use of medium- to low-resolution images for assessing the physiological condition of forest and agricultural canopies requires taking into account the contribution of the SIF emitted by the understory when working with heterogeneous ecosystems.

This study demonstrates the need to include the contribution of SIF emitted by the understory in the interpretation of SIF emitted by forest canopies with RTM approaches. The use of FLIGHT8, which integrates the effect of fluorescence (FluorFLIGHT), has allowed a new model to be developed that takes into account the effect of the understory to model SIF signals and discriminate this information in each of its components. The model has been tested by intercomparison with other models and validated empirically using high spatial and spectral resolution imagery. Due to its spatial variability throughout, our study area enabled comprehensive evaluation. Multitemporal analysis of the impact of phenological changes of the understory over the vegetation canopy is beyond the scope of this study but will be the central topic of a follow-up contribution.

The results suggest that this model could be used to improve the interpretation of SIF at the tree canopy level when we need to separate between different aggregated components and account for the background effects. The ability to quantify SIF from coarse resolution images is a further advantage for quantification of the model at a global scale. Future studies should be focused on the potential use of 3D-RTM to provide information

at a high-spectral resolution and frequency from current and future satellite missions as OCO-2, TROPOMI or FLEX-Sentinel.

Chapter 4

Modelling hyperspectral- and thermal-based plant traits for the early detection of *Phytophthora*-induced symptoms in oak decline

Abstract

Oak decline is a complex phenomenon influenced by abiotic and biotic factors that increasingly threatens oak species worldwide, necessitating the development of scalable early detection methods for effective management. Spectral-based physiological plant traits (PTs) can be sensitive to disease-induced stress, as they depend on photosynthetic processes and vegetation structure. However, the specificity of PT responses to disease-induced decline remains largely unknown. This study examines the relationship between spectral-based PTs and oak decline incidence and severity. We evaluate the use of high-resolution hyperspectral and thermal imagery together with a 3-D radiative transfer model (RTM) to assess a supervised classification model of *Phytophthora*-infected oak trees. Field surveys comprising more than 1100 trees with varying disease incidence and severity were used to train and validate the model and predictions. Declining trees showed decreases of model-based PTs such as water, chlorophyll, carotenoid, and anthocyanin contents, as well as fluorescence and leaf area index, and increases in crown temperature and dry matter content, compared to healthy trees. Our classification model built using different PT indicators showed up to

82% accuracy for decline detection and successfully identified 34% of declining trees that were not detected by visual inspection and confirmed in a re-evaluation 2 years later. Among all variables analysed, canopy temperature was identified as the most important variable in the model, followed by chlorophyll fluorescence. This methodological approach identified spectral plant traits suitable for early detection and mapping of oak forest disease outbreaks up to 2 years in advance of identification via field surveys. Early detection can guide management activities such as tree culling and clearance to prevent the spread of dieback processes. Our study demonstrates the utility of 3-D RTM models to untangle the PT alterations produced by oak decline due to its heterogeneity. In particular, we show the combined use of RTM and machine learning classifiers to be an effective method for early detection of oak decline potentially applicable to many other forest diseases worldwide.

4.1. Introduction

Plant functional traits, such as biochemical composition, chlorophyll fluorescence, water and dry matter content, crown temperature, and vegetation structure, are closely linked to plant health conditions and the responses to environmental and biotic stressors (Ahrens *et al.*, 2020). Changes in plant traits (PTs) may alert managers to biotic and abiotic stressors and thus enable timely management interventions (Cunniffe *et al.*, 2016). Hyperspectral signatures of plants provide an efficient alternative to standard field surveys by enabling monitoring of vegetation status (including biochemical and functional assessments) over large areas at a reduced cost (Homolová *et al.*, 2013; Rocha *et al.*, 2019). Recent studies provide evidence that the quantification of PT from hyperspectral and thermal images can successfully detect pre-visual symptoms of harmful crop pathogens, such as *Xylella fastidiosa* (*Xf*) infection in olive trees (Zarco-Tejada *et al.*, 2018a).

Retrieving PTs from spectra obtained in non-agricultural contexts, such as forest canopies, is challenging because of their high variability. Natural forests, for example, are highly heterogenous in species composition and canopy structure, resulting in spectral mixture effects produced by forest canopy structure, shadows, and understory. Furthermore, they may have high levels of intraspecific variability, driven by microsite and ecophysiological conditions (Fernández i Marti *et al.*, 2018; Navarro-Cerrillo *et al.*, 2018). The spectral mixing produced in heterogeneous forest canopies reduces the accuracy of PTs retrieved from images, especially those derived from narrow regions of the spectrum such as the chlorophyll fluorescence emission region (Hernández-Clemente *et al.*, 2017).

Forest decline is a pervasive decrease of forest health resulting from a complex interaction of a potentially large number of biotic and abiotic factors (Hutchings *et al.*, 2000), including stresses such as water deficit, air pollution, and invasive pests (Manion and Lachance, 1992; Trumbore *et al.*, 2015). In the case of oak decline on the Iberian Peninsula, water stress and root rot caused by *Phytophthora cinnamomi* and related oomycetes are thought to be the main drivers of tree death (Ruiz-Gómez *et al.*, 2019). This pathogen is one of the most pervasive invasive alien species in forest ecosystems of the northern hemisphere (Burgess *et al.*, 2017). Infected trees exhibit regressive decline immediately after showing visual symptoms such as defoliation, crown or canopy discolouration, and brown foliage remaining attached to the canopy. After these symptoms are detected, there is no opportunity for forest management to prevent tree death. For this reason, it is critical to develop methods for early detection of oak decline that maximises the effectiveness of silvicultural treatments such as calcium soil fertilisers, biofumigant crops, or fosetyl-aluminium treatments (Romero *et al.*, 2019).

Several spectral-based strategies have been developed to quantify critical PTs in natural forest canopies, as recently reviewed by Hernández-Clemente *et al.* (2019). Methodologies range from those based on simple empirical relationships between field observations and specific spectral bands or

vegetation indices (VIs) to more complex approaches involving 3-D radiative transfer models (RTMs) or machine learning (ML) techniques. While empirical relationships can be readily developed for a wide range of traits of interest, 3-D RTM requires significant computational effort. A main disadvantage of the simple empirical approach is its limited generalisability to different spatial and temporal contexts. By contrast, RTMs are robust to variations in geometry, illumination, and scene components (i.e., canopy, understory, soil), helping incorporate context dependency and enabling generalisation to different environments. These properties are important for deriving PTs from forest canopies, where 3-D RTMs such as FLIGHT (North, 1996) or DART (Gastellu-Etchegorry *et al.*, 1996) represent the spatial heterogeneity of forest canopies fairly effectively (Hernández-Clemente *et al.*, 2017, 2012; Kötz *et al.*, 2004; Liu *et al.*, 2020; Roberts *et al.*, 2020). A recent study using FLIGHT8 has shown the need to account for effects of shrub and/or grass understories in addition to tree canopies in quantifying variables such as chlorophyll fluorescence (Hornero *et al.*, 2021).

Another method is the combined use of PTs retrieved with RTMs and VIs (Zarco-Tejada *et al.*, 2018a). Numerous VIs have been formulated and tested for quantifying biomass loss related to advanced stages of plant diseases (Castrignano *et al.*, 2020). Some formulations, such as the soil-adjusted vegetation index (SAVI) or the modified chlorophyll absorption ratio index (MCARI), have been shown to minimise the background and atmospheric effects and perform better for forest canopies than traditional formulations such as NDVI (Hornero *et al.*, 2020). Zarco-Tejada *et al.* (2001) demonstrated that a red edge spectral index, R_{750}/R_{710}, reduced forest shadow effects better than other standard chlorophyll indicators used to estimate chlorophyll *a* and *b* content.

The diagnosis of plant diseases requires quantifying not only forest biomass but also the physiological condition of that biomass (Cunniffe *et al.*, 2016). Functional PTs such as photosynthetic rate, water stress, leaf anthocyanin, chlorophyll *a* and *b*, and carotenoid content may be used for early detection

of diseases (Hernández-Clemente *et al.*, 2019). Also, a group of carotenoids, the xanthophyll cycle carotenoids, plays a photoprotective role, preventing damage from excess light to photosynthetic systems, and are potentially detected through the photochemical reflectance index (PRI), thus serving as a proxy for forest health (Hernández-Clemente *et al.*, 2011; Sims and Gamon, 2002). Other useful indicators of plant health include sun-induced chlorophyll fluorescence (SIF) emission and canopy temperature, which are often used as powerful non-invasive markers to track the status, resilience, and recovery of vegetation (Gonzalez-Dugo *et al.*, 2014; Mohammed *et al.*, 2019; Zarco-Tejada *et al.*, 2012).

However, the relative importance of different PT indicators for detecting disease remains largely unknown for many forest species and ecosystems. Understanding the sensitivity of different spectral-based physiological indicators for detecting forest decline in these heterogeneous environments will help guide management and future monitoring campaigns. In this study, we i) expanded our understanding of the contributions of different PTs in detecting symptomatic and asymptomatic trees affected by biotic and abiotic stressors in a holm oak forest and ii) used this information to construct a PT-based analytical approach for the early detection and severity assessment of forest decline.

4.2. Materials and methods

4.2.1. Study site and field data collection

The study was conducted in an open Mediterranean-like oak savannah or *dehesa* located in Andalusia, southern Spain (37°36′45″ N, 7°21′8″ W, 148 ha, Fig. 4.1). The dominant species in the forest was holm oak, *Quercus ilex* subsp. *ballota* (Desf.) Samp. Tree density ranged from 30 to 40 trees ha^{-1}. There was an understory of annual plants and typical Mediterranean

sclerophyllous and sub-sclerophyllous shrub species, i.e., *Cistus* spp., *Pistacia* spp., *Phillyrea* spp., and *Rosmarinus officinalis*. The climate at the study site is dry thermo-Mediterranean, with mild winters and hot summers, including approximately 120–150 biologically dry days, a mean annual rainfall of 570 mm, and an average annual temperature of 16.8°C, according to the Agroclimatic Information Network of Andalusia (Meteorological Station of Puebla de Guzmán, 37º33′07″ N, 07º14′54″ W). The bedrock is calcareous, and the terrain is characterised by smooth hills (slope <15%). Soils are Eutric Cambisols, Chromic Luvisols, and Lithosols with Dystric Cambisols and Rankers (REDIAM, Junta de Andalucía, 2021). The study area is also affected by the combined effect of water deficiency and erosion, soil compaction, and nutrient losses (Moralejo *et al.*, 2009).

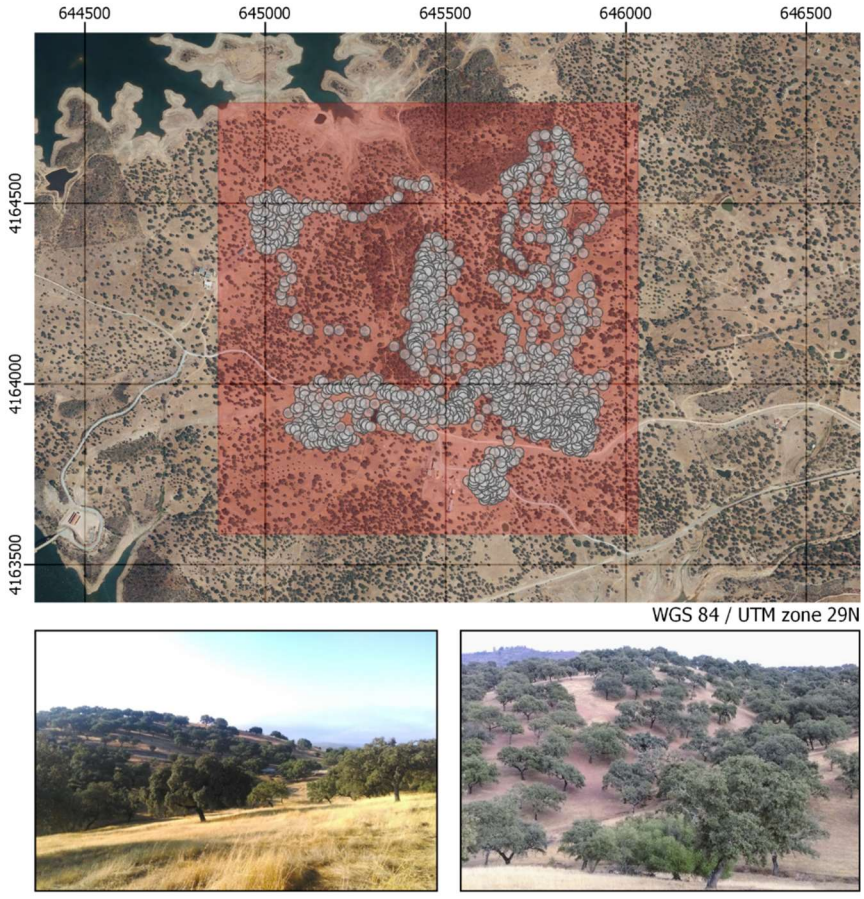

Figure 4.1 Location of the study site selected for PT retrieval through high-resolution imaging (top). The square shaded in red represents the area of the field survey, and the grey dots indicate individual evaluation. Photographs illustrating the heterogeneity of the landscape within the study area are shown below.

Two field surveys were conducted in the study site in summer 2017 and summer 2019. During the surveys, disease severity (DS) and disease incidence (DI) were assessed for 1146 individual holm oak trees. Seem (1984) defined DS as the quantity of disease affecting entities within a sampling unit; DI is a quantal measure, defined as the proportion or percentage of diseased entities within a sampling unit. DS thus accounts for disease severity, while DI considers only whether a tree is affected or not. DI is therefore quicker and easier to measure and is generally more accurate and reproducible than other quantitative measures, making it the commonly preferred measurement method for the detection and modelling of disease spreading patterns (Horsfall and Cowling, 1978).

Based on visual inspection, we assigned individual trees to one of the four DS categories available (Fig. 4.2) depending on the proportion of the crown affected by defoliation (Eichhorn *et al.*, 2017) and other typical *Phytophthora* symptoms, including dead branches in the crown, stem cankers, and adventitious epicormic sprouts (Jung *et al.*, 2000). DS ranged from 0, indicating the absence of visual symptoms, to 3, in which most of the branches in the crown were dead, following the classification of the Andalusian Forest Damage Monitoring Network (Consejería de Medio Ambiente y Ordenación del Territorio, 2018) (Table 4.1; Fig. 4.2). According to this classification, defoliation refers to both reduced leaf retention and premature loss compared to regular tree growth cycles. The part of the crown that is evaluated includes all live branches and thin branches that are dead but still bear leaves. However, it excludes thick branches that have been dead for years and have already lost their natural buds, epicormic shoots below the crown, and gaps in the crown where branches have never existed. DI was either 0 or 1, indicating non-symptomatic trees and symptomatic trees, respectively, where non-symptomatic trees corresponded to a DS of 0 and symptomatic trees to any other severity (DS $\geq$ 1).

The presence of *Phytophthora cinnamomi* on holm oak roots was confirmed through molecular analyses in the study area. Soil samples were collected on

three different trees located in the centre of the study area. The analysis and the results are detailed in Ruiz-Gómez *et al.* (2019).

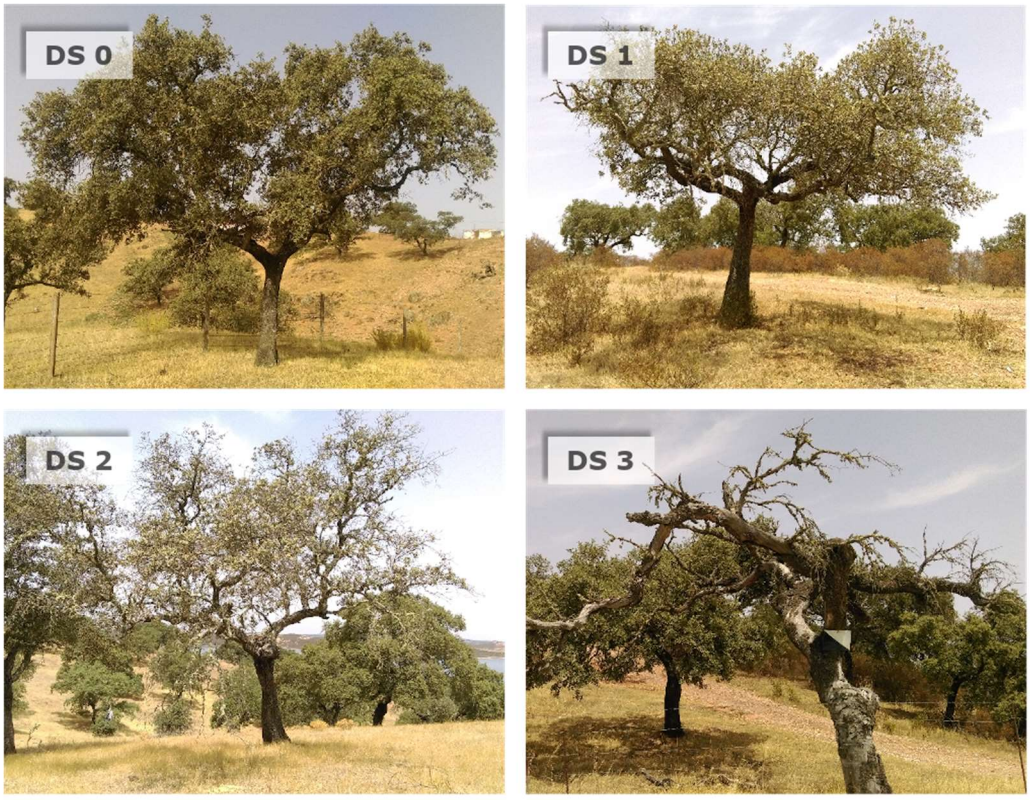

Figure 4.2 Examples of the four forest disease severity (DS) levels assigned to holm oak trees ($N = 1146$) during a field survey in 2017, which was repeated in 2019. The classes range from apparently healthy trees (DS = 0) to trees whose canopies show a prevalence of dead branches (DS = 3).

Table 4.1 Forest health condition assessment: crown-level severity and incidence levels.

DS Level	Severity	Description	Defoliation	Incidence
0	Healthy	Symptomless or low symptom incidence	0–15%	No incidence
1	Low to moderate severity	Low to moderate defoliation and no or few additional symptoms affecting a limited part of the canopy	15–50%	Incidence
2	Medium to high severity	Medium to high defoliation of the crown and several additional symptoms	50–85%	Incidence
3	High to extreme severity	High defoliation uniformly distributed all over the crown, totally defoliated trees, and additional symptoms	85–100%	Incidence

Leaf pigment quantification

Biochemical measurements were taken on leaves from 15 selected trees in the study area in the summers of 2013, 2015, and 2017, in which the chlorophyll (C_{ab}), carotenoid (C_{ar}), and anthocyanin (A_{nth}) contents were measured (Table 4.2). Leaf pigment content was measured by destructive methods on 12 samples per tree (three biological replicates per orientation, i.e., North, East, South, and West). Samples were collected from the sunlit branches at the top of the crown during a 1-hour window around solar noon. Leaves were immediately frozen in liquid nitrogen in the field and kept below –20°C until the analysis of pigment concentration was performed in the laboratory. Photosynthetic pigment extracts (chlorophylls and carotenoids) were obtained from a mixture of 2-cm^2 ground leaf material per sample (four discs of 0.5 cm^2); the leaves were milled in a mortar bed on ice with liquid nitrogen and diluted in acetone to 5 mL (in the presence of sodium ascorbate). Extracts were then filtered through a 0.45-µm PTFE hydrophobic filter to separate pigment extracts from remaining fractions. Extractions and measurements were performed under reduced light conditions to avoid degradation of the pigments, with five technical replications conducted per biological sample. Photosynthetic pigment quantification was done through

absorbance measurement after separation by high-precision liquid chromatography (HPLC) following the methodology detailed by Hernández-Clemente *et al.* (2012).

Anthocyanins were extracted by suspending two 0.5-cm^2 leaf discs in acidic solution (methanol 1% HCl) following Murray and Hackett (1991). The absorbance of anthocyanins (AAs) in the samples was calculated by subtracting 24% of the maximum absorbance of chlorophylls (653 nm) from the maximum absorbance of the anthocyanins (532 nm) (1)

$$\mathrm{AA} = A_{532} - 0.24A_{653} \qquad (1)$$

Concentrations were estimated using a molar extinction coefficient of 30 mL mol^{-1} cm^{-1} (Steele *et al.*, 2009). Five technical replicates were performed for each biological sample, and results are shown in units of µg cyanidin-3-glucoside equivalents per cm^2 (Lee *et al.*, 2008).

Plant functional traits

Steady-state leaf fluorescence (F_s) was measured for 15 trees using 12 leaves per tree (three per orientation) with a FluorPen FP100 (Photon Systems Instruments, Drásov, Czech Republic). These measurements were used as a proxy of the airborne SIF retrievals and a field-level assessment of plant functional stress for each severity level.

In July 2013, the leaf area index (LAI) was measured using an LAI-2000 Plant Canopy Analyzer (LI-COR, Inc., Lincoln, NE, USA) for the same 15 trees as above. At each tree, the device was placed with the optical sensor in eight different orientations under the canopy, 1 m above the ground, and using a 90° view-restricting cap. Measurements for LAI estimation included a reference reading above the canopy and several readings below the canopy. All measurements were made at dawn. The coordinates for all trees (both sampled and visually scored) were recorded using a GPS (Garmin GPSMAP 64s) device with a spatial accuracy below 3 m.

Table 4.2 Summary of field measurements and surveys

Year	Tree-health field survey	C_{ab}	C_{ar}	A_{nth}	F_s	LAI
2013		✓	✓	✓	✓	✓
2015		✓	✓		✓	
2017	✓	✓	✓		✓	
2019	✓					

C_{ab}: chlorophyll a + b content; C_{ar}: carotenoids; A_{nth}: anthocyanins; F_s: steady-state leaf fluorescence; LAI: leaf area index.

4.2.2. Airborne hyperspectral and thermal imagery

High-resolution image data collection

We collected high-resolution images on 19 July 2017 using a visible near-infrared (VIS-NIR) hyperspectral imager (Hyperspec model, Headwall Photonics Inc., Fitchburg, MA, USA), a hyperspectral sensor covering NIR and short-wave infrared (SWIR) regions (Hyperspec NIR-100, Headwall Photonics), and a thermal camera (FLIR SC655, FLIR Systems, Wilsonville, OR, USA) installed in tandem onboard a Cessna aircraft operated by the Laboratory for Research Methods in Quantitative Remote Sensing (QuantaLab), Spanish National Research Council (CSIC). The imagery was acquired at 350 m above ground level with the aircraft flying on the solar plane, with a track width of 185 m, resulting in 720 ha of ground surface covered (Fig. 4.3). The VIS-NIR camera operated with 260 spectral bands (400–885 nm) and a radiometric resolution of 12 bits at a 1.865-nm centre wavelength (CWL) interval, yielding 6.4-nm full-width at half-maximum (FWHM) spectral resolution with a 25-µm slit. The acquisition frame rate on board the aircraft was 50 frames per second with an integration time of 18 ms. The focal length was 8 mm, producing an angular field of view (FOV) of 49.82°. The images derived from this sensor resulted in a ground resolution of 60 cm, allowing us to distinguish individual oak tree crowns from the

background. Further details regarding the platform and sensor configuration can be found in Zarco-Tejada *et al.* (2013). The NIR-SWIR sensor was operated with 165 spectral bands (950–1750 nm), yielding 6.05 nm FWHM (25-µm slit size) and 16-bit radiometric resolution. The sensor was configured with an acquisition rate of 25 fps with an integration time of 40 ms. The 12.5-mm-focal-length lens resulted in an angular FOV of 38.6°, with a 90 cm/px spatial resolution. The FWHM and the centre wavelength for each spectral band were derived after spectral calibration using a monochromator (Cornerstone 260 1/4 m, model 74100, Newport Oriel Instrument, CA, USA) and an XE-1 Xenon calibration light source (Ocean Optics, USA).

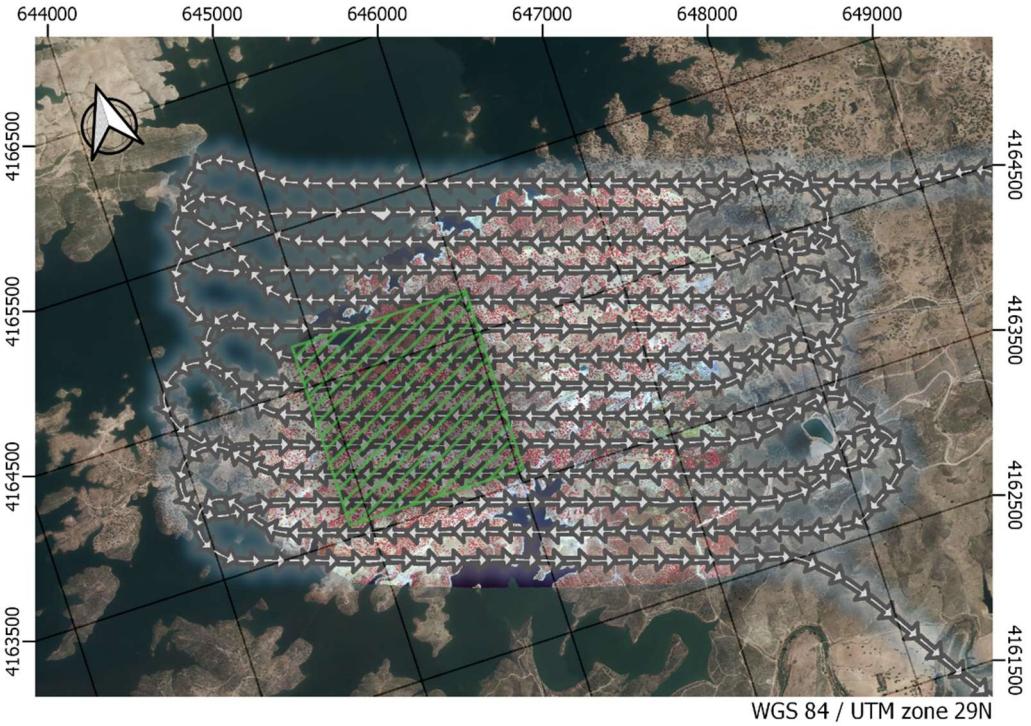

Figure 4.3 Flight path for image acquisition. White arrows and line indicate the flight path and the hashed green square is framed over the study area. The background shows the VIS-NIR hyperspectral mosaic, overlaid on an orthophoto from the Spanish National Geographic Institute (IGN, OrtoP-NOA 2017 CC-BY 4.0)

The thermal sensor (FLIR SC655, FLIR Systems, Inc., USA) had a resolution of 640 × 480 pixels and was connected to an acquisition board via the Gigabit Ethernet protocol. It was equipped with a 24.5-mm F-number 1.0 lens providing an angular FOV of 45 × 33.7°. The detector is a focal plane array uncooled microbolometer and has a spectral range from 7.5 to 14 µm. This camera is equipped with a thermoelectric cooling (TE) stabilisation system, which enables a thermal sensitivity below 50 mK. The characteristics of the sensors on board, as well as their specific setup in this study, are detailed in Table 4.3.

Table 4.3 Technical characteristics of the airborne imaging sensors and operational settings

	Hyperspectral		Thermal
	VNIR	**NIR-100**	**SC655**
Wavelength range (µm)	0.4–0.885	0.95–1.75	7.5–14
Spectral bands	260	165	1
Spatial bands	1004	320	640 × 480
Focal plane array detector	Silicon CCD	InGaAs	VOx
TE cooling	No	Yes	Yes
Detector pixel pitch (µm)	7.4	12	17
FWHM (nm)	6.4	6.05	–
Slit size (µm)	25	25	–
Radiometric resolution (bits)	12	16	16
Integration time (ms)	18	40	8
Frame period (ms)	55.55	18	1000
Aperture	F/1.4	F/2.0	F/1.0
Focal length (mm)	8	12.5	24.5
Spatial resolution (cm/px)	60	90	60
FOV (deg)	49.82	38.6	45 × 33.7
Communication protocol	CameraLink	USB	GigE

Image post-processing

Both hyperspectral sensors were radiometrically calibrated by means of an integrating sphere (Uniform Source System, model CSTM-USS-2000C, Labsphere Inc., North Sutton, NH, USA) using coefficients derived from the calibrated light source at four constant levels of illumination. Atmospheric correction for the VIS-NIR sensor was performed using the total incoming radiance measured with a field spectroradiometer (ASD HandHeld Pro, Malvern Panalytical Ltd, Malvern, England). Atmospheric correction was simulated with the SMARTS model (Gueymard, 1995, 2001) for the NIR-100 sensor, which allowed the conversion of the radiance images to reflectance for the full range of both sensors. Optical thickness measurements from a Microtops II sunphotometer (Solar Light Co., Philadelphia, PA, USA) and meteorological measurements from a weather station (model WXT510, Vaisala Corporation, Vantaa, Finland) were used as input parameters for

the model. Additionally, the effects of illumination and viewing angle were also adjusted using cross-track correction (San and Süzen, 2011) in both hyperspectral processing chains (Fig. 4.4).

Thermal calibration was conducted in the laboratory using a black body calibration source (LANDCAL model P80P, Land Instruments International Ltd, Dronfield, England) and by indirect calibration using ground temperature measurements with a handheld infrared thermometer (LaserSight from Optris GmbH, Berlin, Germany) as described by Calderón *et al.* (2015) (Fig. 4.4). Standardised canopy temperature (T_c-T_a) was calculated by subtracting weather station air temperature (T_a, constant value) from canopy temperature derived from calibrated thermal imagery (T_c).

Orthorectification of hyperspectral images was performed using PARGE (ReSe Applications LLC, Wil, Switzerland) image rectification software for airborne optical scanner systems. Data from inertial measurement units installed on each sensor (IG-500N, SBG Systems S.A.S., Carrières-sur-Seine, France) were synchronised with each camera's imager and used as inputs for the software. Orthomosaicing thermal imagery was performed using Pix4D (version 3.1.23, Lausanne, Switzerland) photogrammetry software. Data preprocessing and image correction were as described in detail by Hernández-Clemente *et al.* (2012) and Zarco-Tejada *et al.* (2013).

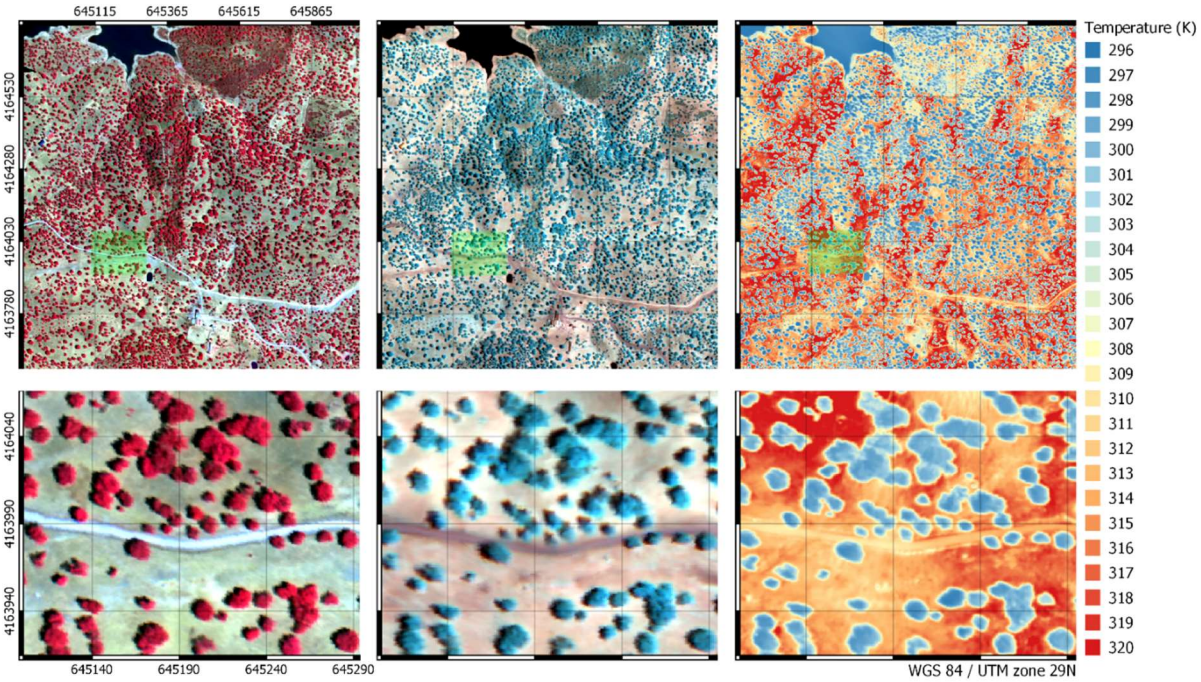

Figure 4.4 From left to right, the images from the VIS-NIR, NIR-SWIR, and thermal sensors are shown over the study area. Bottom row contains zoomed-in views of scenes above (green rectangle).

Spectral-based indicators

The high-resolution imagery acquired from each airborne sensor allowed us to identify and delineate tree crowns independently, seeking to minimise the effect of background and shadowing. This image processing was achieved using object-based segmentation methods through Niblack's threshold (Niblack, 1986) and Sauvola's binarisation techniques (Sauvola and Pietikäinen, 2000). Finally, we applied a binary watershed analysis using the Euclidean distance map for individual objects to automate the separation of the trees with overlapping crowns (Fig. 4.5).

Mean reflectance values for each tree were used to calculate 96 spectral-based indicators, including: i) VIs related to tree crown structure, chlorophyll, carotenoid, anthocyanin and water contents, and the epoxidation state of the xanthophyll cycle (detailed in Appendix C.); ii) chlorophyll fluorescence emission through the Fraunhofer line depth (FLD) method as described by Maier *et al.* (2003) using three bands for the in ($L_{763\,nm}$) and out

($L_{750\ nm}$; $L_{780\ nm}$) bands (3FLD); and iii) thermal dissipation using T_c-T_a, as previously described.

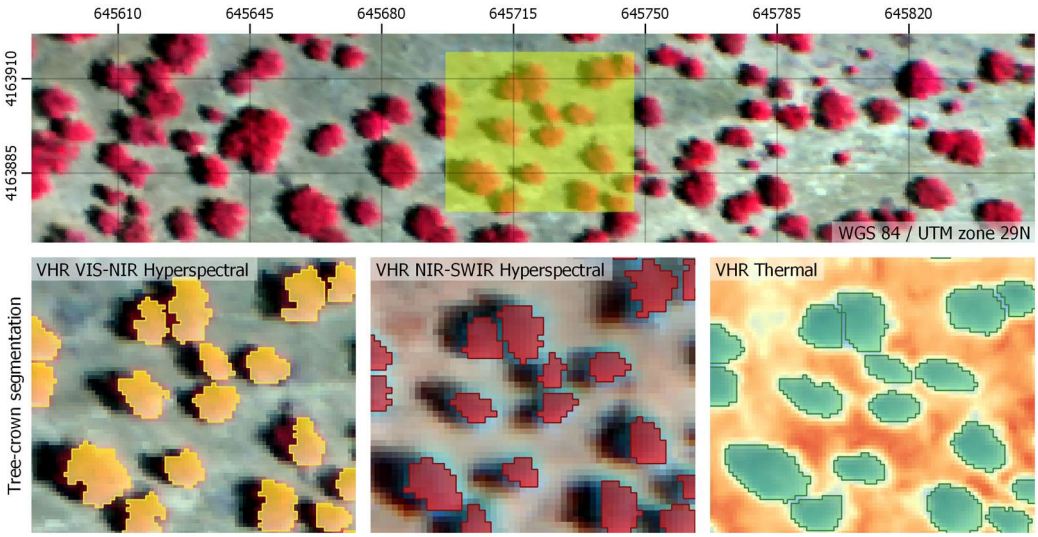

Figure 4.5 Overview of the entire crowns in the study area. Zoomed-in views (of the area in the yellow box) in the bottom row show the tree-crown segmentation for each sensor.

4.2.3. Model simulation analysis and plant trait retrieval

Canopy structural traits and biochemical composition were quantified by inverting the 3-D RTM FLIGHT8 model, using the pixels extracted from the tree crowns. The model simulations were conducted using the atmospheric and ground data set collected during the image acquisition. Input variables for the model (Table 4.4) were established according to the field measurements, estimates from existing literature, and nominal parameters to ensure that the generated look-up table (LUT) covered the range of spectral variability in the tree crowns. The ill-posed problem generated when a wide range of PTs can be obtained from the same spectrum was alleviated using restricting ranges of input parameters based on field data measurements (Combal *et al.*, 2003).

Table 4.4 Inputs for the model simulation analysis.

Variable	Units	Acronym	Phase 1	Phase 2
Chlorophyll $a + b$ content	µg cm^{-2}	C_{ab}	10–60	21–33
Carotenoid content	µg cm^{-2}	C_{ar}	1–20	1–7
Water content	Cm	C_w	0.013	0–0.03
Dry matter content	g cm^{-2}	C_{dm}	0.024	0.003–0.018
Anthocyanin content	g cm^{-2}	A_{nth}	*NA**	0–6
Senescence material	Fraction	C_s	0	0
Mesophyll structure	–	N	2.1	2.1
Fluorescence quantum efficiency	–	F_i	0–0.2	*NA**
Leaf area index	m^2 m^{-2}	LAI	0–4	0.1–2.5
Leaf size	m	LFS	0.05	0.05
Leaf angle distribution	–	LAD	Spherical	Spherical
Fractional cover	%	FC	70	70
Soil reflectance	%	Soil	1 sample	1 sample
Understory reflectance	%	US	4 samples	4 samples
Crowns shape	–	CSh	Ellipsoid	Ellipsoid
Solar Zenith	deg.	SZA	25.84	25.84
Solar Azimuth	deg.	SAA	108.98	108.98

**NA*: F_i and A_{nth} are not modelled in PROSPECT-D and in Fluspect-B, respectively.

In the first phase of analysis (Fig. 4.6 top), we determined LAI, C_{ab}, C_{ar}, and the sun-induced fluorescence quantum efficiency (F_i). We built a LUT of +800k simulations coupling the FLUSPECT-B (Vilfan *et al.*, 2016) leaf reflectance model with the FLIGHT8 (Hornero *et al.*, 2021) canopy model. FLUSPECT-B considers the pigment concentrations in the leaf and its photosynthetic efficiency, and FLIGHT8 takes into account the structural properties of the canopy and the effect of the soil and the understory. The senescence material, water (C_w), and dry matter (C_{dm}) contents, and the structural parameter N were set to nominal values using a value previously determined on this particular species in the same study area following Hernández-Clemente *et al.* (2017) (Table 4.4 – Phase 1). For comparisons with airborne hyperspectral images, we used convoluted model simulations assuming Gaussian band spectral response functions for their corresponding FWHM, centred on the band locations of each imager. The LUT-based

inversion followed a multi-step approach in which the LAI values were determined first, followed by C_{ab}, C_{ar}, and finally, F_i, using the MSR, $PSSR_b$, CRI_{700m}, and 3FLD spectral-based indicators as proxies for each PT, respectively.

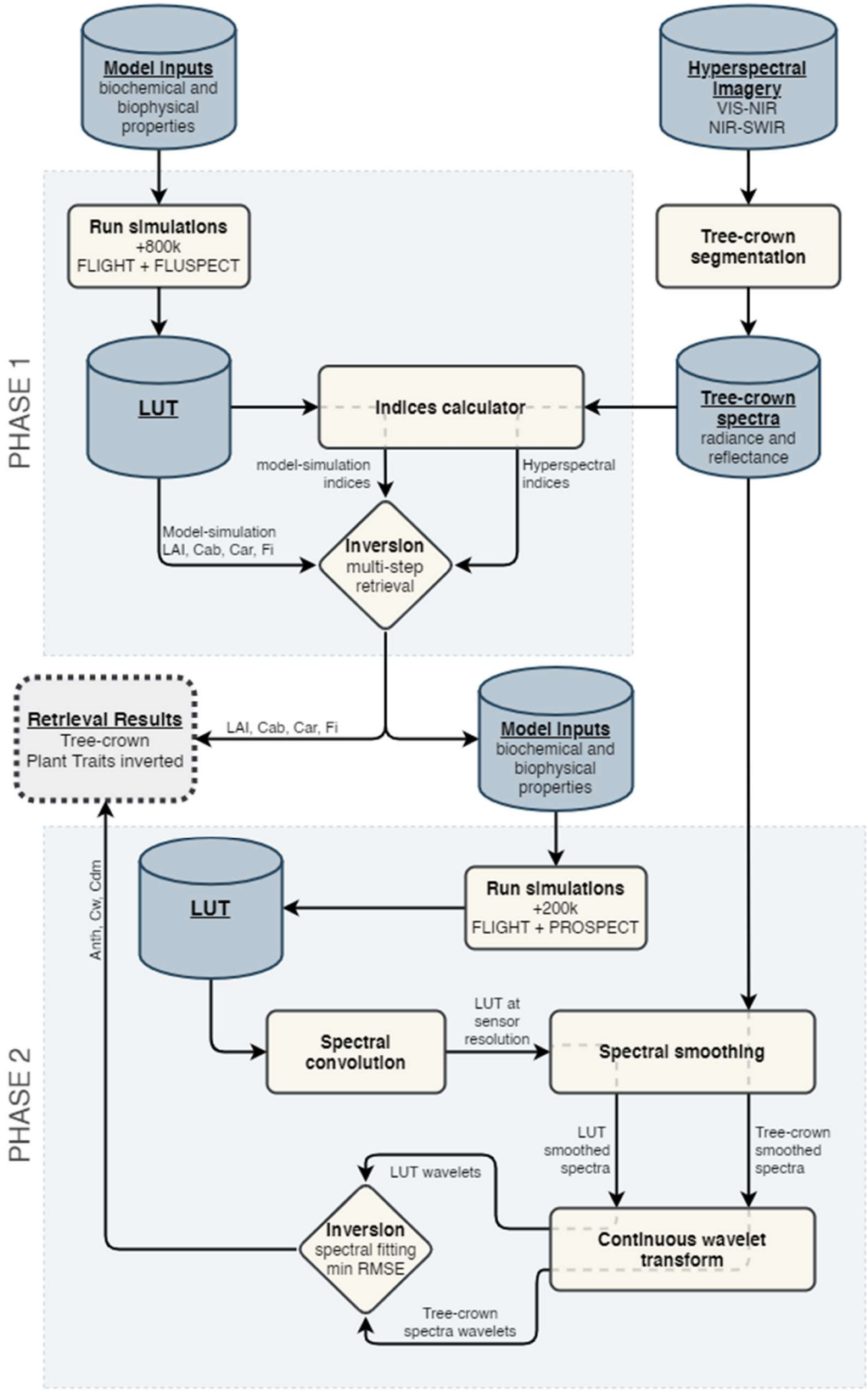

Figure 4.6 Model simulation approach diagram.

In the second phase, parameterisations retrieved from each tree were used to build a LUT of +200k simulations by coupling the PROSPECT-D (Feret *et al.*, 2017) leaf reflectance model with the FLIGHT8 canopy model. The leaf reflectance model was used to specifically quantify A_{nth}, as well as C_w and C_{dm} (Fig. 4.6 bottom). For the simulations and images, a smoothing algorithm based on local polynomial regression fitting (Cleveland *et al.*, 1992) was applied to eliminate the noise affecting the model inversion. Through the use of wavelets (Strang and Nguyen, 1996), we decomposed the hyperspectral signatures into frequency components at different spectral scales, allowing us to identify the LUT spectra that showed a closer correspondence to the image spectra. The continuous wave transformation was performed over three spectral ranges, a) 470–710 nm, b) 670–850 nm, and c) 1000–1300 nm and 1500–1700 nm, for the retrieval of A_{nth}, C_{dm}, and C_w, respectively. At this stage, Kattenborn *et al.* (2017) and, more recently, Suarez *et al.* (2021) used a similar method to obtain the PTs from hyperspectral images; however, the methods used in this study differ in that a) an extended spectral range was used based on double-coupled hyperspectral imagers, and b) only the first four transformation scales were used to characterise more specific spectral regions of interest, instead of the whole range of the signal.

4.2.4. Plant trait selection and classification model approach

Once the PTs were obtained for each tree, feature selection was performed using a random forest (RF) classifier (Breiman, 2001; Liaw and Wiener, 2002) combined with an adaptation of an algorithm developed by Kursa and Rudnicki (2010), henceforth referred to as the Boruta algorithm. In the Boruta algorithm, shadow variables (permuted copies) are created by shuffling the original ones. The RF classifier is then applied to the initial data set, which is composed of the original variables and their shadow counterparts at the same time. The Boruta algorithm evaluates iteratively the importance of each original variable against the shadow variables to determine which

variables are essential and at what magnitude. Variables are marked "Unconfirmed" when they are significantly lower than the shadows and are permanently discarded, while variables that are significantly higher than the shadows are marked "Confirmed". The process is repeated by re-generating the shadow variables and continues until only confirmed variables are left or until the maximum number of iterations defined at this stage is reached (set at 100 iterations). If the second scenario occurs, some variables may remain undecided, and they are considered "Tentative." The confidence level defined in the Boruta algorithm was established at 99% with a multiple comparisons adjustment using the Bonferroni method (Haynes, 2013) to control false positives. Once this process was completed, the importance of each PT in the severity and incidence classification process was obtained.

As an initial step, we performed the Boruta analysis using the field-based PT measurements, combining 2013, 2015, and 2017 evaluations, using only the three variables that were measured in all three years (F_s, C_{ab}, and C_{ar}) on 45 observations (15 evaluations and physiological measurements per year) and comparing them to the levels of severity and incidence. The purpose of this analysis was to understand the sensitivity of field-based PT to forest decline.

The feature selection process started using all the model-based PTs retrieved for each tree, including 8 variables and 1146 observations. Then, the Boruta analysis was repeated for all the spectral-based indicators ($N = 96$). The objective was to improve the reliability of the model using complementary information added by VIs to the initial model-based PT feature selection. Due to the high fluctuations in the importance calculation when a large number of variables are used, the process in Boruta starts with three rounds, in which only the selected shadow variables are compared, while in the remaining rounds — up to 100 iterations — the original variables are compared with all the shadow variables. Figure 4.7a presents an overview of the entire process for the selection of variables conducted in this study.

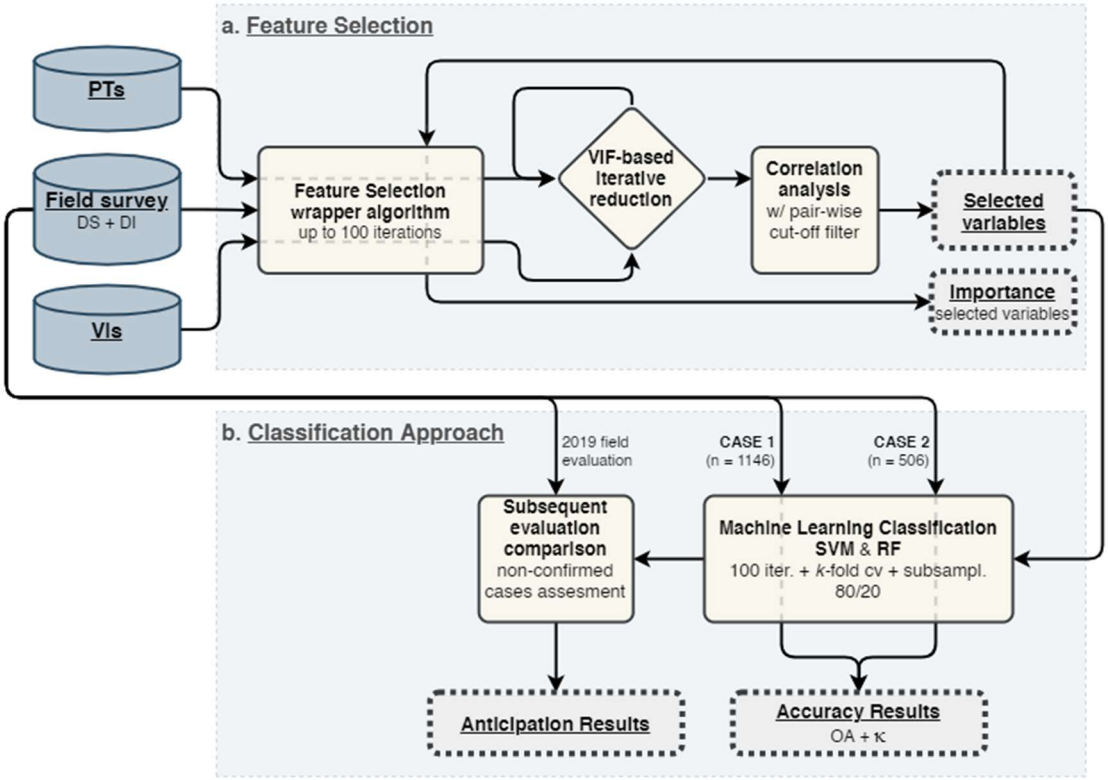

Figure 4.7 Overview of the methodology used for a) the feature selection using the Boruta algorithm, including the iterative reduction of variables and the correlation analysis; and b) the classification approach based on 2017 with the different cases assessed and a final comparison with a subsequent evaluation in 2019.

To strengthen the selection of features used in the classification model, the PTs were set in the established order according to their importance, and the VIs were added based on their previously calculated importance as well. At each stage of accumulation, the variance inflation factor (VIF) — an indicator that measures the extent to which the variance of an estimated regression coefficient increases due to collinearity (James *et al.*, 2013) — was calculated to avoid multicollinearity among the predictor variables. The variable was included only if the VIFs for all variables were below the threshold of 10. The final set of selected variables (PTs + VI) was used in the next screening stage.

Finally, Pearson's correlation analysis and *p*-values were used to determine the degree of relationship between the previously selected variables. Through the calculated correlation matrix, the variables to be excluded were chosen to reduce the pair-wise correlations establishing a cutoff filter of 0.85 (Dormann *et al.*, 2013). The Boruta algorithm was applied to the remaining variables to determine the importance of each selected variable. A principal component analysis (PCA) was also conducted to determine to what extent the components capture the majority of the variance and to identify the variables that provide the most information and whether the less relevant ones could be discarded to reduce the dimensionality of the data set. The filtered variables were retained for the development of the classification model, as shown in Figure 4.7.

Two ML algorithms were used to classify disease incidence and severity levels: a supervised non-linear support vector machine (SVM) with a Gaussian kernel radial base function (Scholkopf *et al.*, 1997) and the RF algorithm (Breiman, 2001), which were reported as the predominant classifiers on airborne imaging (Gigović *et al.*, 2019; Gualtieri *et al.*, 1999; Liu *et al.*, 2017; Pal, 2005).

We evaluated models for two different cases (Fig. 4.7b), assessing incidence and severity classification from i) CASE 1, all trees assessed in 2017 ($N = 1146$), and ii) CASE 2, only confirmed trees, which were either still affected or unaffected again in 2019 ($N = 506$). To validate the selected models, we performed 100 iterations in which the data set was randomly divided into two samples, the training and the test samples by 80% and 20%, respectively, including *k*-fold cross-validation, in which the original sample was randomly partitioned into 10 equal-sized subsamples and repeated five times. Training data were subsampled for each iteration to avoid disproportionate frequencies of classes, which could negatively impact the model fit. Finally, we assessed the classification accuracy by calculating the overall accuracy (OA) and the Cohen's kappa coefficient (κ), which is based on comparing the

observed agreement in a data set compared to what could occur by mere randomness (Richards and Jia, 1999).

After assessing the models' accuracy, we evaluated the anticipation capability using the visual evaluation 2 years later. In particular, we analysed whether the model was able to predict the unconfirmed cases — trees that were assessed at a given incidence level and in the subsequent assessment, 2 years later, were assessed at the opposing level — and refined towards those that improve or worsen, i.e., those that change from having incidence to not having it and the opposite, respectively. This last analysis helped us understand the applicability of the model to predict a subsequent evaluation of forest decline using the data from previous images and evaluations.

4.3. Results

In this section, we present the results of the evaluation of the field and PT indicators to predict oak decline. Then, the remote sensing spatial model's predictions are described, focusing on the importance of each PT in the screening of the physiological alterations caused by oak decline.

4.3.1. Plant trait indicator assessment based on forest health field measurements

The bi-annual empirical data collected from 2013 to 2017 show the capability of the field-based PTs — C_{ab}, C_{ar}, and F_s — to discriminate different levels of severity. Trees with low disease severity levels consistently had high values for F_s, C_{ab}, and C_{ar} content (Fig. 4.8). F_s was identified as having importance values two times higher than C_{ab} and C_{ar} in both severity and incidence levels (Fig. 4.8 right side).

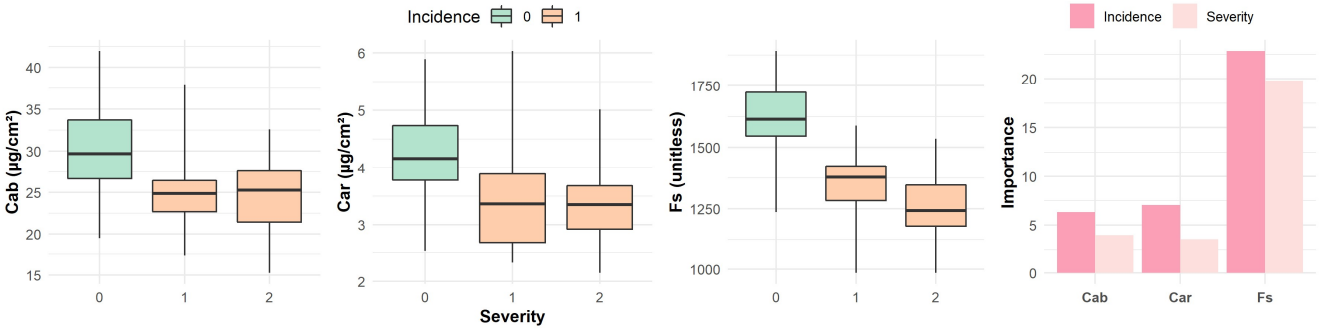

Figure 4.8 Relationship between the level of severity and field-based plant traits – chlorophyll content (C_{ab}), carotenoid content (C_{ar}), and steady-state leaf fluorescence (F_s) – in $N = 45$ trees measured in 2013, 2015, and 2017. Importance scores for field-based plant traits in detecting oak decline computed via the Boruta algorithm are shown at right.

4.3.2. Spectral- and model-based plant trait predictors of oak decline

As with empirical measurements, model-based values of F_i and pigment content (C_{ab} and C_{ar}) were inversely related to severity level (Fig. 4.9). The model-based PTs corresponded well with field data, having relatively low normalised error ($NRMSE_{LAI} = 0.13$, $NRMSE_{Cab} = 0.16$, $NRMSE_{Car} = 0.2$, and $NRMSE_{Anth} = 0.12$) and values within the expected range (data not shown). In Fig. 4.9, we also included the model-based retrievals of three other PTs (C_w, C_{dm}, and A_{nth}) and T_c-T_a derived from thermal data. Severity level was positively associated with T_c-T_a and C_{dm} but negatively associated with LAI, A_{nth}, and C_w. These results are also consistent with the classification of incidence and severity obtained from field-based PT measurements, described in the previous section, where F_s was one of the most relevant variables to detect oak decline.

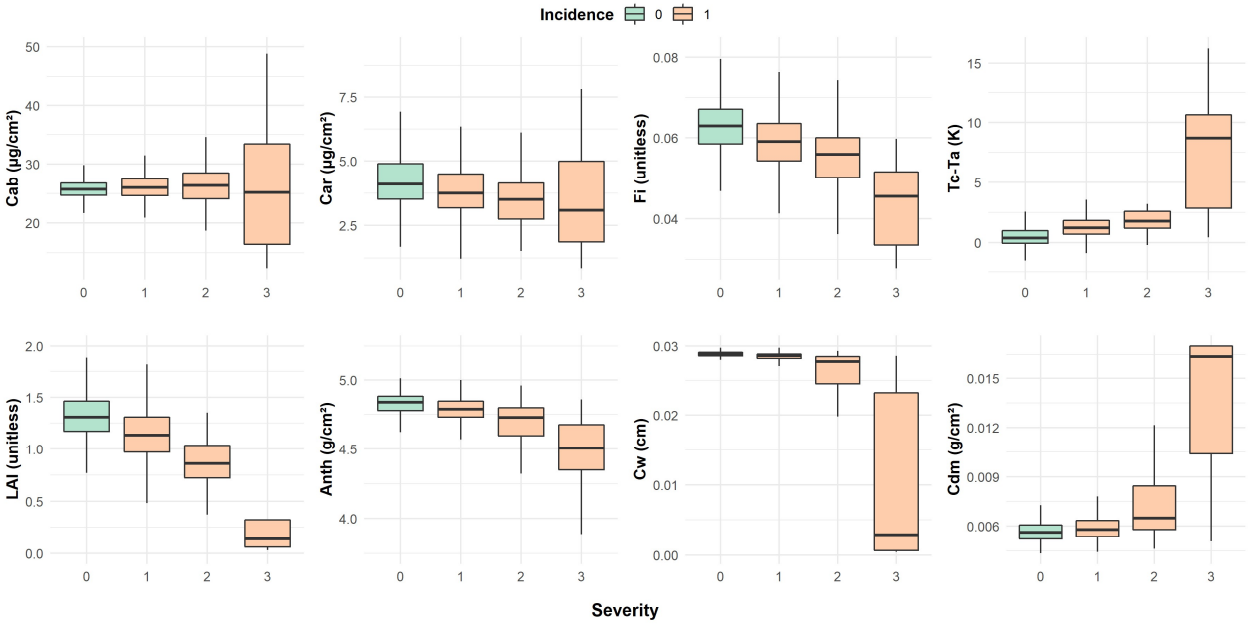

Figure 4.9 Relationship between severity and plant traits retrieved from hyperspectral and thermal images in 2017.

Variable importance scores for model-based PTs and T_c-T_a are presented in Fig. 4.10. T_c-T_a and F_i had the highest importance scores in models discriminating the first and second severity levels, while LAI and C_{dm} were determined to be the most important for differentiating the remaining severity levels (Fig. 4.11a).

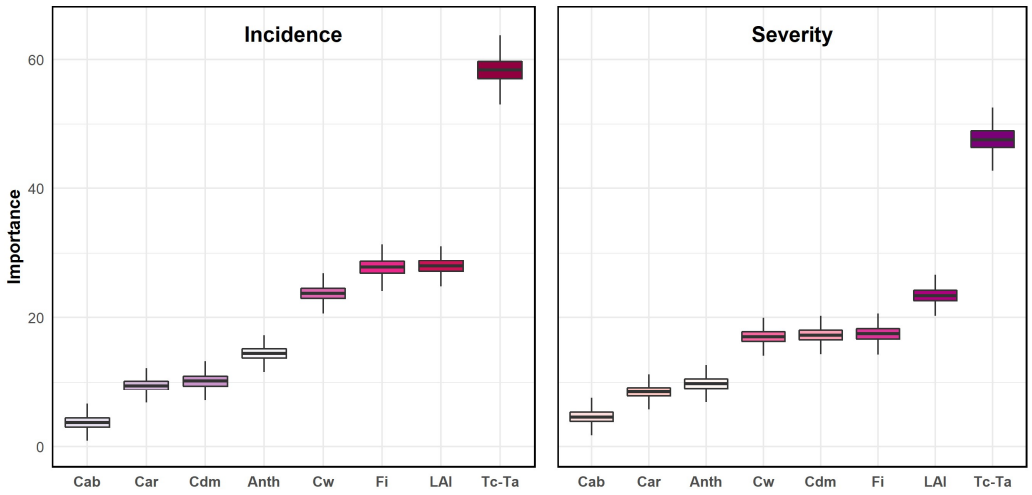

Figure 4.10 Overall importance scores for each plant trait when classifying both incidence and severity disease levels using the Boruta algorithm.

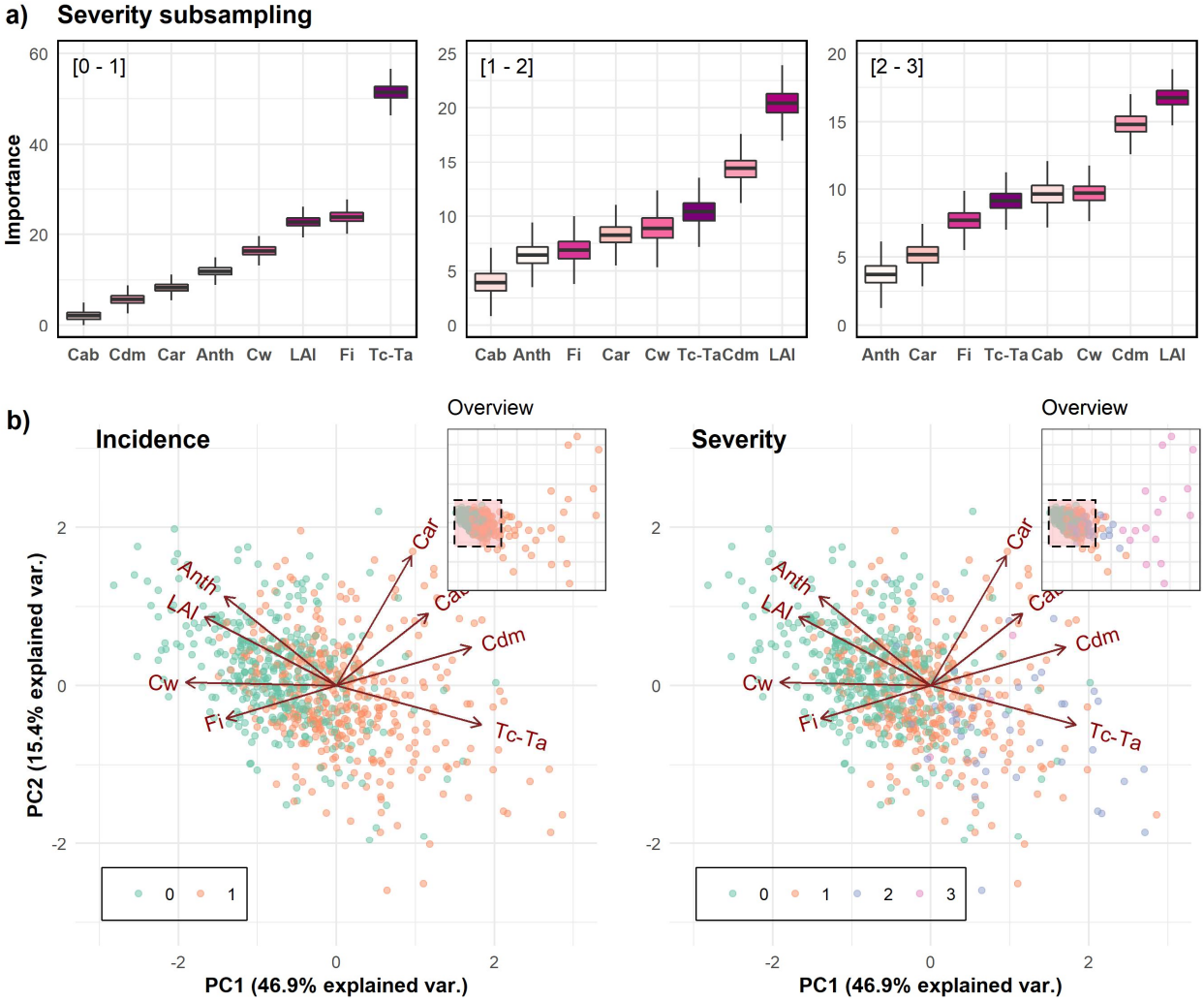

Figure 4.11 Severity subsampling importance scores for each plant trait (PT) (a) and spectral-based principal component (PC) predictors' analysis (b) for both incidence (0–1) and severity (0–3) levels using the model-based PTs (C_{ab}, C_{ar}, A_{nth}, C_w, C_{dm}, LAI, and F_i) and the thermal-image-based PT (T_c-T_a). The bidimensional plots display each variable's loading, with vectors and the tree samples as points coloured by severity and incidence levels. The vectors' length approximates the variance represented by each variable, whereas the angles between them represent their correlations.

The principal components PC1 and PC2 explain 59.2% of the total variability, with 42.5% for PC1 and 16.7% for PC2 (Fig. 4.11b). The PTs T_c-T_a and LAI were strongly negatively correlated in PC1 and PC2 space, having nearly the same magnitude and angle but different directions. These results may indicate that the more abundant the vegetation, the greater the

transpiration capacity and the lower the temperature difference. On an orthogonal ray, we find C_{ar}, which is scarcely related to them, and its importance indicates its limited contribution to the model. The projection of F_i in the first two components was opposite that of C_{ar}, and this variable contributed substantially to model performance. This variable was more important than LAI for the development of an incidence classification model as well as distinguishing the first two severity levels.

4.3.3. Remote sensing spatial model predictions of oak decline

To find the best variables for predicting oak decline, the model-based PTs were combined with 95 VIs, of which only four passed the iterative VIF screening and pair-wise correlation threshold: LIC_3, CI_2, GnyLi, and MND (Fig. 4.12a). The variables with the lowest correlation coefficient (<0.05) were C_{ar} with LAI, A_{nth}, and MND, a result that is consistent with the PCA showing C_{ar} as largely independent from other variables.

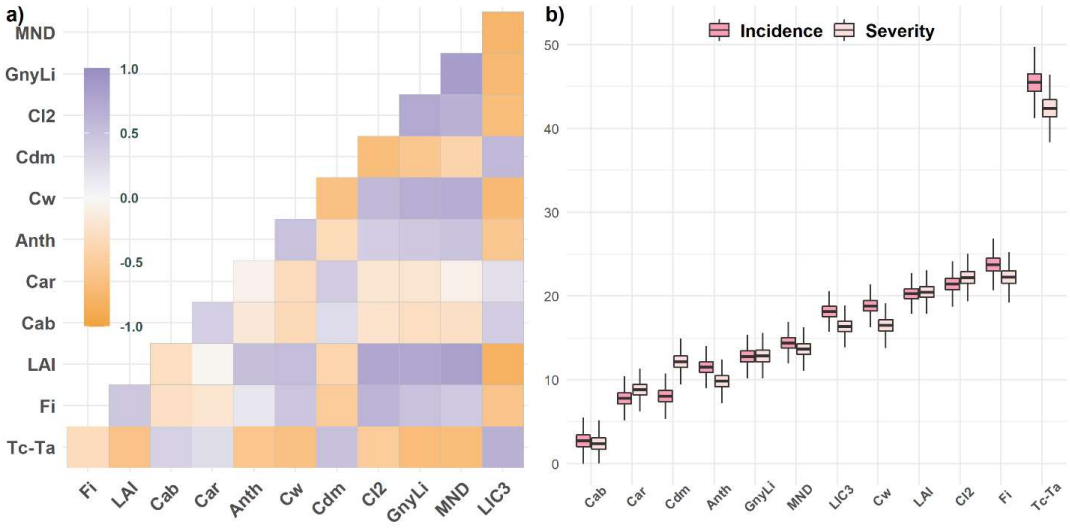

Figure 4.12 Plant traits (PTs) and vegetation indices (VIs) correlations (a) and variable importance scores for spectral-based PT and VIs with severity and incidence (b) to detect oak decline.

The variable selection process yielded 12 final indicators with a VIF below the established threshold. Two indicators were associated with photosynthesis regulation: F_i and T_c-T_a. Four indicators were related to pigment content: C_{ab}, C_{ar}, A_{nth}, and CI_2. One indicator was related to fractional cover, namely, LAI. Five indicators were related to water content: C_w, C_{dm}, GnyLi, MND, and LIC_3. Among all the indicators, the variables contributing the most to detecting different levels of incidence and severity were T_c-T_a and F_i. These PTs were included as predictors for the final classification model of oak decline; their importance scores are presented in Figure 4.12b. Variables with the highest importance included T_c-T_a, F_i, and CI_2.

Model accuracy was estimated on the basis of the total number of trees evaluated and confirmed cases reported in the subsequent survey (Fig. 4.13). Models classifying severity had an overall accuracy of 0.71 ($\kappa = 0.51$) in the best case (sampling of confirmed cases with RF algorithm). Models classifying incidence were more accurate (OA = 0.82; $\kappa = 0.62$) for this same scenario. The SVM algorithm was slightly more accurate when we used the complete data set (all trees; $N = 1146$), while RF performed better with the reduced-input data set (confirmed cases; $N = 506$). For models predicting incidence, the OAs were greater than 0.75 (thus considered 'high'), and the Cohen's kappa scores were fair to excellent, according to Cicchetti and Sparrow (1981).

The findings obtained when evaluating the anticipation capabilities (Table 4.5) indicate a better behaviour of the RF algorithm when building the model with both confirmed cases — in which the best result is found — and all cases. When we analyse the prediction rate while segregating between trees that worsen (incidence: $0 \rightarrow 1$) and those that improve ($1 \rightarrow 0$), for the former, the RF algorithm behaves better, and for the latter, SVM.

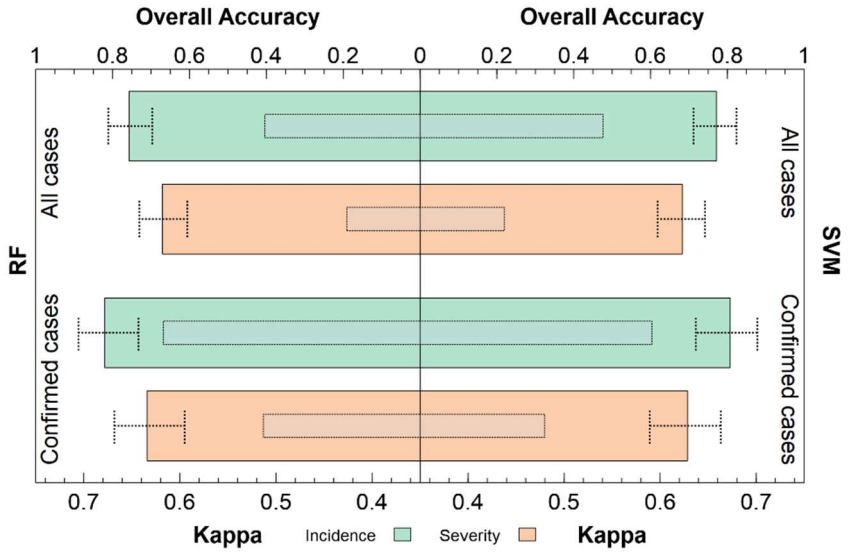

Figure 4.13 Overall accuracy (OA) and Cohen's kappa scores for classification models. Results were obtained from 100 iterations of random data subsets for training and validation (80/20). Average OA and kappa values are shown as horizontal bars, the former in colour and the latter as narrower grey bars with dotted edges. The error bars indicate the minimum and maximum OA values across iterations.

Table 4.5 Prediction rate for non-confirmed cases (NC) using models built with all cases or only confirmed ones. The best results for each case are highlighted in light green and in darker green overall.

Method	Sample	NC $_{0\leftrightarrow1}$ (%)	NC $_{0\rightarrow1}$ (%)	NC $_{0\leftarrow1}$ (%)
SVM	All cases	29.9	27.4	34.0
SVM	Confirmed cases	33.8	34.8	32.1
RF	All cases	32.1	31.9	32.0
RF	Confirmed cases	35.5	40.2	27.4

All cases: $N = 1146$; confirmed cases: $N = 506$.

Example predictions from a final incidence classification model using the SVM algorithm are presented in Fig. 4.14. Through this map and the field evaluations, the differences found can be appreciated, as well as their spatial variability.

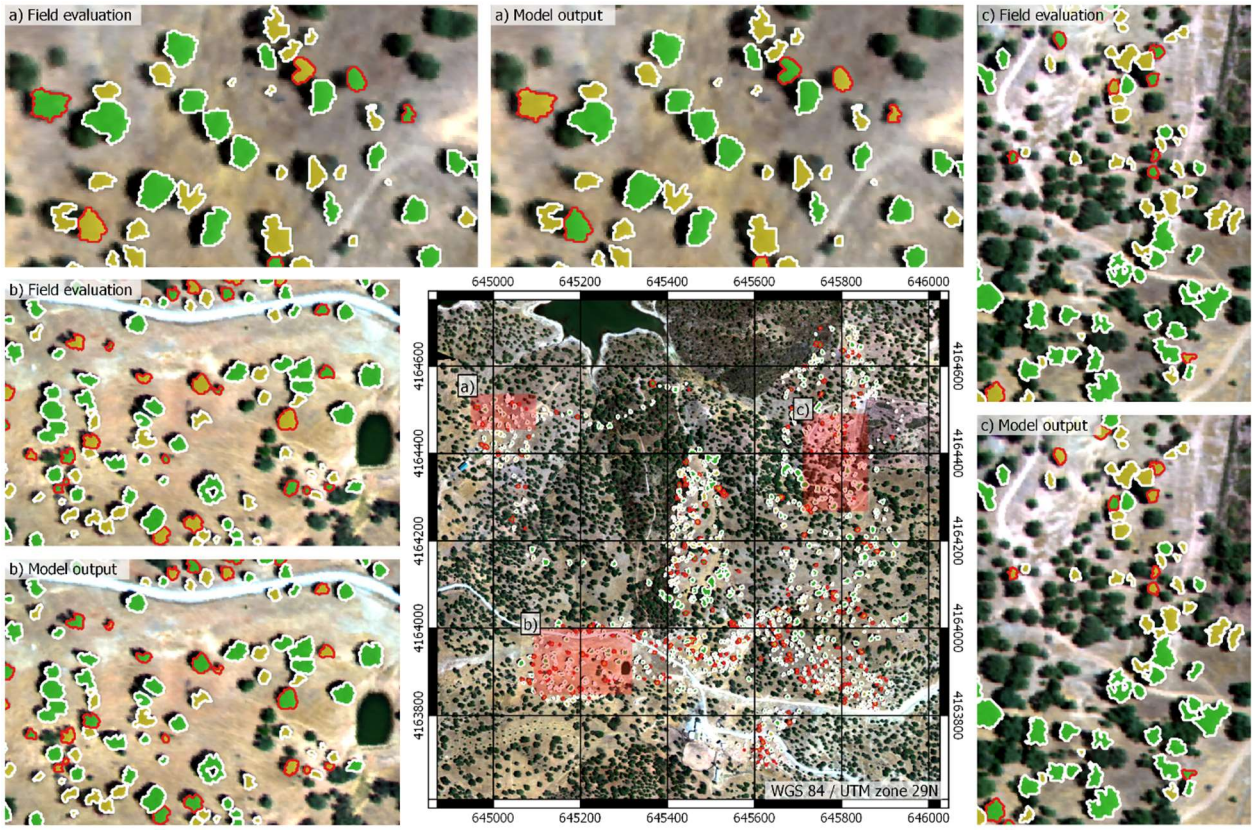

Figure 4.14 Field evaluation and spatial prediction map from the model output. Yellow and green filling indicates incidence or not, respectively. Tree crowns with a red outline are those that differ between the field evaluation and the model output.

4.4. Discussion

The first objective of this study was to identify the PTs that are most useful for detecting the incidence and severity of decline symptoms in holm oak. While Zarco-Tejada *et al.*, (2018a) successfully used spectral-based PTs to improve the detection of *X. fastidiosa* symptoms in olive trees, quantifying PTs in heterogeneous forest canopies is significantly more difficult because

of the impacts of shadows, soil background, and understory, which dilute the spectral signature of pure crowns (Hernández-Clemente *et al.*, 2019; Liu *et al.*, 2020; Markiet *et al.*, 2016; Pisek *et al.*, 2015). For this reason, advanced 3-D simulation models designed specifically for heterogeneous forest canopies were a major methodological component of this study. The critical step resided in the successful retrieval of model-based PTs that allowed us to understand the contribution to each PT and complete the ML modelling approach with additional information derived from other spectral-based, uncorrelated variables. By applying a combination of 3-D model simulation and statistical analysis using ML approaches, we found that oak forest decline can potentially be detected at an earlier stage and that severity levels can be accurately assessed at broad scales.

Field data confirmed the association between *Q. ilex* status and several key PTs. Trees with lower disease incidence had higher values of C_{ab}, C_{ar}, and F_s. As symptom severity increases, the concentration of these pigments and the chlorophyll fluorescence decrease. The decrease rate we observed in chlorophyll fluorescence and pigment content associated with disease incidence are consistent with declines associated with drought and root rot stress found in other experiments under controlled conditions (Früchtenicht *et al.*, 2018; Koller *et al.*, 2013; Ruiz Gómez *et al.*, 2018) and field surveys (Baquedano and Castillo, 2007; Camarero *et al.*, 2012).

It is notable that we found F_s to be more important than the other two PTs in identifying disease incidence from field data. Among model-based PTs retrieved from hyperspectral images, F_i similarly had a higher importance score than any other pigment content indicator for discriminating severity. This pattern is consistent with the variable importance ranking of variables in Zarco-Tejada *et al.* (2018a) for detecting *Xf*-induced symptoms in olive trees.

Including spectral-based PT indicators in our analysis provided insight into the functional responses of oak trees to different disease levels. T_c-T_a was the most important indicator, regardless of whether we discriminate by

incidence or severity. Thermal imaging has improved the detection of several crop diseases in other studies, including *Verticillium* wilt in olive orchards (Calderón *et al.*, 2015), water stress in peach orchards (Gonzalez-Dugo *et al.*, 2020), and red leaf blotch in almond orchards (López-López *et al.*, 2016). In this study, other important PTs included LAI and F_i, followed by C_{dm}, C_w, and A_{nth}, and to a lesser extent C_{ab} and C_{ar}.

Focusing on the discrimination capacity of each PT between the different stages of severity, T_c-T_a was generally an important predictive variable for determining disease incidence, but LAI and C_{dm} were more relevant for discriminating mild and advanced severity classes. Principal component analysis showed that T_c-T_a and LAI contributed strongly to the same component but in opposite directions. Severity subsampling supports that while canopy temperature is particularly important for early incidence detection, LAI may provide more information about severity levels when a tree is infected.

Another important aspect of this study is the consideration of VIs alongside other model-based PTs for classification. CI_2, GnyLi, MND, and LIC_3 were variables that passed through selection criteria, providing additional information and avoiding collinearity with other variables. In the final model, F_s was selected as highly important, since part of the weight of LAI was distributed among other indicators such as CI_2 or LIC_3. The importance of indicators from the SWIR region (MND and GnyLi) also exceeded that of C_{ab}, C_{ar}, C_{dm}, and A_{nth}.

This study showed that remotely derived PTs can support the early detection of holm oak decline. These results help bridge a gap in the understanding of how forest decline affects PTs via complex interactions between biotic and abiotic factors. These interactions are difficult to disassociate, unlike in agricultural studies in which factors such as nutrient deficiency or water availability can be controlled.

Predictive model accuracy was high, with an OA > 0.8 and $\kappa > 0.6$, indicating that the PTs we identified may be helpful for understanding

physiological responses to disease and other stressors. The model accuracy achieved in this study is comparable to that of prediction models developed for olive trees by Zarco-Tejada *et al.* (2018a). Taking advantage of a subsequent field evaluation performed 2 years later, the model's anticipation ability was evaluated, which brought us significantly improved results since it managed to anticipate up to 40% in the best scenario.

Forest canopy heterogeneity poses a challenge for spectral data modelling, due to discontinuous architectures and interference from shadows, understory, and soil composition. The utility of satellite-based spectral indicators for detecting diseases has been examined by Hornero *et al.* (2020) in olive trees and Hernández-Clemente *et al.* (2017) in holm oak. A common finding in these studies was that the soil and the understory both influence the spectral signature and the fluorescence signal of aggregated pixels. In this work, we used the FLIGHT8 model, a recently improved version of the FLIGHT model, which minimises background effects by considering the spectral contribution of the understory. The success of the methods presented here may be partially due to the high spatial resolution of hyperspectral images collected and to the open nature of the woodland landscape. However, the FLIGHT8 model also accounts for increasing levels of pixel aggregation (e.g., using medium- to low-resolution satellite imagery) in heterogeneous canopies (Hornero *et al.*, 2021). Future work should investigate the assessment and validation of the methods presented here performed with satellite imagery and/or different types of forest canopies.

Monitoring and anticipating forest decline are clearly advantageous for effective management and mitigation. Large-scale monitoring may be further improved by including multitemporal data to track disease evolution. However, such data will increase the complexity of analyses, particularly due to variation in understory and soil reflectance from image to image, their impact on aggregated pixels, and the need to account for those variations with RTM. The methodology presented here may be particularly relevant for the Sentinel-2 mission, which provides multitemporal data in the visible,

infrared, and short infrared regions, and the FLEX mission, which will provide fluorescence data after 2022.

4.5. Conclusions

This study proposes a methodology that integrates field data, airborne imagery, physical RTM, and empirical modelling to retrieve PTs and assess their association with forest decline and provides a tool to detect early-onset symptoms of decline in holm oak. Hyperspectral image data, including VNIR and SWIR spectral regions, combined with thermal imaging and RTM can be used to monitor the spread of forest decline over large areas. Thermal-based canopy temperature (T_c-T_a) was the most important PT in the model to discriminate between different levels of severity and incidence, followed by the fluorescence (F_i) and LAI, whereas LAI and C_{dm} were the most relevant indicators for discriminating advanced stages of severity. Additional spectral indicators such as CI_2 or LIC_3 complemented LAI, and VIs in the SWIR region (GnyLi and MND) were more important than PTs such as C_{ab}, C_{ar}, or A_{nth}. Overall, our results demonstrate that an integrated approach combining spectral- and model-based PT retrievals using 3-D RTM and classification methods is needed for the large-scale monitoring of forest decline. This approach enabled the successful prediction of holm oak decline at an early stage; it is essential to monitor harmful forest diseases, and this task can be augmented through the retrieval of accurate forest health traits from advanced airborne imagery and satellite data observations.

Chapter 5

Conclusions

5.1. Overview

In the preceding chapters, a specific and detailed discussion of the findings associated with each study has been carried out. This chapter aims to summarise the main findings, discuss them in a general context, show applications and practical implications, and suggest new directions for further research. Throughout this thesis, new methods have been developed based on the quantitative estimation of vegetation dynamics using satellite images (chapter 2), high-resolution airborne imagery (chapter 3 and 4), and radiative transfer modelling (RTM) (chapter 2, 3 and 4). Remote sensing data have been combined with field measurements and RTM to determine plants' physiological status (chapters 2 and 4) in two different heterogeneous canopies: olives groves and holm oak trees. Different strategies have been applied through imaging, as well as empirical and physical modelling, to detect the incidence of i) a bacterium, *Xylella fastidiosa* (*Xf*), in olive groves (chapter 2), and ii) an oomycete, *Phytophthora cinnamomi* (*Pc*), in holm oak forests (chapter 4), where the understory plays a key role with more nutrients available in the soil. Also, in another holm oak area, the validation of the new features incorporated in an RTM model (chapter 3) has been developed, as well as their evaluation and robustness. At the image level, it is challenging to assess the incidence of the different factors, so the proposed methodologies have been used to not only retrieve the biophysical parameters of the

vegetation (chapter 2 and 3) but also to improve the understanding of each plant trait (PT) (chapter 4).

This chapter discusses the implications of the previous chapters' results for the development of methods to estimate vegetation health, the influence of understory, and the role of fluorescence along with other PTs. Figure 5.1 summarises the key findings achieved for each of the objectives outlined and suggests where future work in this direction should be focused.

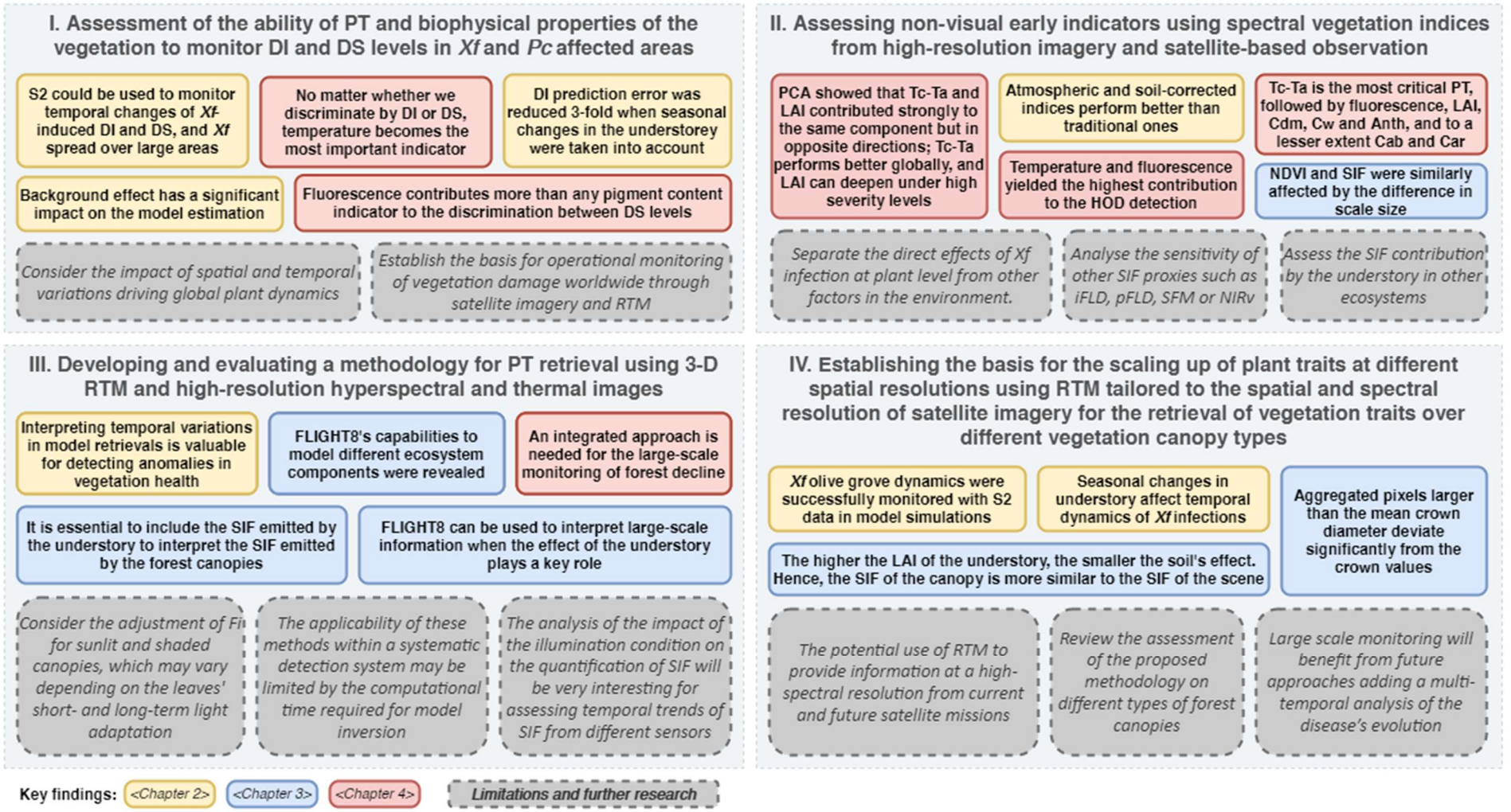

Figure 5.1 Key findings, limitations, and recommendations for future studies are shown under each objective. Key findings are coloured according to the chapter from which they were extracted; limitations and possible future works are in grey boxes and italics.

5.2. Synthesis and general conclusions

Monitoring vegetation dynamics on a large scale using remote sensing is key to detecting the early signs of vegetation decline and addressing plant health's biotic and abiotic drivers. This thesis integrates different approaches combining field data, satellite and airborne images and physical and empirical models that allow the analysis of functional PTs used as indicators of vegetation health. In particular, the methods have been tested for detecting and monitoring symptoms induced by *Xf* in olive trees and the forest decline in holm oaks associated with *Pc* and drought stress. A key aspect of the successful monitoring of vegetation health using RTM has been to consider the spectral contribution and the effects associated with understory in heterogeneous canopies, which has been ignored so far. This has resulted in the achievement of a tool to detect early symptoms considering the contribution of the different components of the environment, thanks to the use of advanced RTM and the proposed methodology.

First, a dataset collected in the first declared *Xf*-infected area in Europe, in southern Italy, integrating Sentinel-2 satellite imagery and high-resolution hyperspectral imagery, field observations, and radiative transfer modelling has been used to demonstrate that Sentinel-2 data allow the detection of changes associated with temporal variations of *Xf*-induced symptoms. Different vegetation indices (VIs) were used to assess the temporal rate of change of disease incidence (DI) and severity (DS), showing that the monitoring of *Xf*-infected orchards required the use of autocorrected VIs and adjusted to the influence of the soil. The latter suggested the possible impact of background, given the heterogeneity of the crop, and how the disease spread left more nutrients available in the ground, and, consequently, for understory growth. On the one hand, the literature lacked studies focusing on the sensitivity of VIs to variations in both vegetation health and temporal change, including the contribution of understory changes that significantly

affect reflectance acquired by satellite imagery. On the other hand, the understory's confounding effects had a considerable impact on the VIs obtained from Sentinel-2 over *Xf*-infected olive orchards due to the discontinuous canopy that characterises this crop. Therefore, the next part of the work was focused on improving the RTM used hitherto by including an additional component, the understory, and studying its impact one step further, while also focusing on the effect of sun-induced fluorescence (SIF) on the aggregated pixel, which had not been studied to date and remains of particular interest for understanding the physiological state of the vegetation.

Out of all the indicators evaluated with the satellite imagery, those that minimised atmospheric and background effects, such as ARVI, OSAVI and ATSAVI, performed better than traditional indices such as NDVI, MSR, or RDVI. It was shown that the use of 3-D RTM and field observations could correctly explain the temporal variations experienced in both the tree canopy and the background, which is critical for accurately predicting the increase in DI and DS. The background effect had a significant impact on the estimation of the model compared to the field measurements, yielding an improvement in the retrieval of DI increase of 33.5% when background effects were considered and an additional improvement of 9.5% when its heterogeneity was also taken into account. For monitoring *Xf* damage over large areas, the results suggest that Sentinel-2 time series together with RTM, which considers environmental variations, can provide useful spatio-temporal indicators, both to improve the understanding and to take the necessary phytosanitary interventions to stop the spread of *Xf*.

Simultaneous studies in which the author participated demonstrated that fluorescence was a key factor for disease detection (Poblete *et al.*, 2020; Zarco-Tejada *et al.*, 2018a); therefore, the next steps were designed to address both biophysical parameters and fluorescence emission, creating a new RTM model that dealt with the aspects found so far. Prior to its use in another heterogeneous canopy on a different scenario, a validation study was performed, together with the effect of the understory and the aggregated

signal. Modelling of the understory within the 3-D RTM approach led to the interpretation of results showing that the fluorescence signal calculated from medium-to-low resolutions is significantly affected by variations in the understory. Leveraging the development effort on an existing model, which already integrated the effect of fluorescence on tree leaves, has allowed the development of a new model that takes into account the impact of understory to discriminate between each of its components — addressing one of the first questions that arose after the first analysis — and also to model the fluorescence signal, which will be shown below to be one of the most important indicators when modelling forest decline.

The model developed was tested in an intercomparison with other models and empirically validated using high spectral and spatial resolution imagery in the framework of a campaign — over a tree-grass ecosystem within the FLEX preparatory missions at the Majadas de Tiétar research station in western Spain — specially dedicated to the study of fluorescence, which at the same time allowed us to have field measurements to support this applied study. The selected study area, given its spatial variability and heterogeneity, allowed us to carry out an exhaustive evaluation that assessed not only the influence of the understory component in particular but also its characterisation in the global impact over the scene. It was concluded that, in order to assess the physiological condition of heterogeneous agricultural and forest canopies using medium- and low-resolution images, the contribution of the SIF emitted by the understory had to be taken into account using RTM-based approaches.

Additionally, the proposed model could be used to improve the interpretation of SIF at the tree canopy level when it is necessary to separate between different aggregated components and to consider background effects. The ability to quantify SIF not only at the leaf or canopy level but also at lower spatial resolution is needed for the interpretation of SIF at a global scale.

In the framework of a more extensive field campaign, using high-resolution thermal and hyperspectral imagery, spanning VNIR and SWIR spectral

regions, all of the aforementioned findings were gathered and further deepened the understanding of the physiological state of the vegetation in the context of agroforestry decline. This study — conducted in a *Pc*-infected *dehesa* located in Andalusia, southern Spain — revealed the need for an integrated approach combining RTM-based PTs retrievals, complemented with VIs and subsequently building a machine learning (ML) classification model for monitoring forest condition. The importance of fluorescence for vegetation health monitoring was also confirmed in this third study.

Among all of the PTs that were determined and analysed, the temperature-based Tc-Ta indicator, followed by the fluorescence and the LAI, were the most relevant ones in the model development that distinguishes between different levels of DI and DS (OA = 0.82/0.71; κ = 0.62/0.51, respectively). LAI and dry matter content (Cdm) play a more relevant role in discriminating between advanced levels of severity. Complementarily, indicators such as CI2 or LIC3 cause a drop in the importance of LAI given their contribution to the model, and indicators in the SWIR region (e.g. Gny or MND) become more significant than Cab, Car, or Anth. Thanks to the proposed strategy, it has been possible to successfully predict holm oak forest decline at an early stage, which is key to monitoring damaging forest diseases and their management.

Overall, due to all of the analyses conducted throughout this thesis and the combined methodologies proposed, an overarching conclusion can be drawn regarding the importance of integrated approaches that combine the retrieval of indicators from RTM to provide a better understanding of the physical and physiological processes that are taking place in the vegetation. This allows us to not only have more accurate information from larger scales but also to be able to model it, anticipate it, and take preventive action in the field, or at least in the early stages of vegetation decline.

5.3. Practical implications

5.3.1. Monitoring the spread of *Xylella Fastidiosa* from space

The first research question was to assess whether satellite data could be used to monitor temporal changes in DI and DS induced by *Xf* and whether it was likely to provide information on the widespread *Xf* epidemiology over large areas. Zarco-Tejada *et al.* (2018a) showed how non-visual symptoms of this infection could be detected from very high-resolution hyperspectral imagery and RTM, and more recently, Poblete *et al.* (2020) evaluated spectral bands and indices and the contribution of SIF and the thermal region for *Xf* detection, advancing operational detection using airborne platforms. However, as *Xf* has spread rapidly in recent years, monitoring more visible damage over large areas could help measure, forecast and potentially mitigate the impact of *Xf* on the landscape (White *et al.*, 2017), and hence on the socio-economic sectors that depend on it (Luvisi *et al.*, 2017).

The rapid propagation of *Xf* in the field was reported in the observations carried out. In fact, there was a considerable increase in DI and DS in the period analysed. As indicated by Nutter *et al.* (2006), an accurate assessment of the disease requires a quantitative estimation of the disease's temporal evolution. Thus, the availability of high temporal resolution multispectral data from Sentinel-2 offers the opportunity to evaluate indicators for monitoring *Xf* infections in olive orchards over time. The results obtained show the feasibility of modelling changes in DI from satellite image data using different VIs and RTM. However, multitemporal data must also consider the variation of other components, such as understory and soil, and their impact on the aggregated pixels, being a challenge to disentangle spectral reflectance changes produced by alterations in vegetation condition from those produced by atmospheric and background factors. After an initial analysis, the best performing VIs were OSAVI and ARVI, which were shown

in previous studies (Kaufman and Tanre, 1992; Rondeaux *et al.*, 1996) to be reasonably robust to the background and atmospheric effects. Both empirical and model results agreed on the accuracy of OSAVI as the best performing index for tracking ΔDI; however, the overall robustness shown is discordant with some other studies in which traditional indices performed better. Frampton *et al.* (2013) found that both LAI and chlorophyll could be extracted from NDVI sentinel-2 images for crops. The most evident difference between these studies is in the homogeneity of crops versus the heterogeneous canopies of olive orchards, explaining this apparent contradiction.

5.3.2. The impact of the understory on monitoring vegetation dynamics

The background's contribution was found to affect not only the spectral reflectance of the canopy using satellite data but also through high-resolution hyperspectral imagery. The impact of the background on the spectral response of the tree canopy could be related to the natural canopy structure of olive trees (Gómez Calero *et al.*, 2011) and their high level of defoliation in more severe stages. Analogously, in the present work, an increase in *Xf* infections was associated with a decrease in the tree fractional cover (FC) and an increase in the background FC, further increasing the understory contribution to the aggregated signal at the orchard level. This inverse effect of an increase in background greenness with a decrease in the functionality of *Xf*-infected trees could be explained ecologically on the basis that diseased trees leave more nutrients and water available for the understory (Peltzer and Köchy, 2001). This pattern further emphasises the relevance of incorporating RTM if we seek to model the background effect with considerable accuracy (Meggio *et al.*, 2008).

The findings achieved have very relevant implications for the use of VIs to assess the temporal evolution of diseases and pathologies due to non-homogeneous background effects in *Xf*-affected orchards. The modelling approach

showed the need to use a 3-D RTM approach that considers these effects, which is essential to monitor the future spread of *Xf* infections and to understand their epidemiological evidence (Fuente *et al.*, 2018).

So far, the challenge of mapping disease infections has mainly been developed through the use of environmental data and probabilistic models (Hay *et al.*, 2006) and is rarely implemented in quantitative terms. The prospect of mapping the evolution of disease incidence using RTM and satellite imagery is a new approach with high potential to assess vegetation health dynamics.

The heterogeneous spatial distribution of trees and understory layers in the landscape is one of the main factors that inherently introduces uncertainty in retrieving biophysical vegetation parameters through modelling (Yu *et al.*, 2018). The estimation of these parameters simultaneously contains many implications for GPP retrieval (Li *et al.*, 2018); even the interpretation of GPP using SIF as a proxy varies greatly depending on the canopy type (Tagliabue *et al.*, 2019). Chapter 3 highlights the need for a solution that allows for modelling the understory's contribution in aggregated pixels and its impact on the total canopy fluorescence estimation. Mixed tree-grass ecosystems cover up to 33% of the global surface (Hanan and Hill, 2012), so the contribution of this work to understanding how to improve signal quantification from aggregated pixels is key.

5.3.3. The aggregated signal and its impact on sun-induced fluorescence

The increasing availability of SIF observations from space raises the need to develop and validate new approaches for modelling SIF dispersion and reabsorption at the canopy level. Upcoming missions with satellite data are expected to bring another step forward in estimating the physiological state of plants, as operating with global sensors has the clear advantage of covering more area; however, quantifying the fluorescence contribution above the

canopy is difficult due to the limited availability of studies and models with which to interpret dispersion processes within the canopy (Qiu *et al.*, 2019; Romero *et al.*, 2018; Yang and van der Tol, 2018; Zeng *et al.*, 2019). Seeking to fill this gap, the results in Chapter 3 show how to aggregate the SIF contribution emitted by scene components within an agroforestry canopy. Data collected with the high spatial and spectral resolution HyPlant sensor was first used to demonstrate empirically that understory does affect the aggregated pixel values.

Not surprisingly, the higher the aggregation, the more significant were the differences between the pure tree crown values and the aggregated pixel, and these differences became less relevant at values close to or below the mean crown size. This aggregation increases uncertainties in the modelling of SIF and other global-scale vegetation indices when the spatial distribution and composition of understory vary across seasons. As reported by Joiner *et al.* (2014), the quantification of SIF emitted by tree crowns and understory separately may not always be necessary, in particular for modelling global GPP. However, for other studies, such as the temporal evolution of photosynthesis related to vegetation decline, stress, or diseases, each component's physiological state must be accurately understood independently (Stoy *et al.*, 2019).

5.3.4. The need for modelling heterogeneous canopies

At this point, the next question that arose was whether a model could represent the components within a heterogeneous canopy, and at the same time, model SIF scattering and reabsorption. Zhao *et al.*, (2016) and Hernández-Clemente *et al.*, (2017) made the first steps to using 3-D RTM to simulate SIF from heterogeneous canopies and reported the impact of background on the estimation of SIF at the canopy level; however, no studies had taken into account the combined effect of soil and understory to date. Therefore, the ability to assume the understory as an additional layer was developed,

enriching the modelling processes in heterogeneous canopies. With this new RTM, FLIGHT8[1], a simulation analysis was performed to analyse the contribution of SIF emitted by understory and tree canopy. The importance of evaluating this contribution is consistent with Liu *et al.*'s findings (2019) using model simulation reconstruction from terrestrial laser using an ASD hand-held spectrometer in an open-canopy boreal forest.

By evaluating a large set of simulations over the airborne imagery, the capabilities to model different ecosystem components were revealed, results that at the same time reinforce the interpretation of the aggregated pixel covered by previous studies in which only the soil effect was taken into account (Hernández-Clemente *et al.*, 2017; Zarco-Tejada *et al.*, 2018a) without considering additional components from the background. FLIGHT8 can be used to solve the problem of interpreting large-scale information when the understory effect plays a key role, such as tree-grass or open forest ecosystems, as shown in Chapter 4. Moreover, in relatively constant dominant layers, such as evergreen forest canopies, phenological changes in understory over the same season translate into canopy structure changes that alter the relationship between GPP and SIF (Ahl *et al.*, 2006; Xiaoliang Lu *et al.*, 2018).

5.3.5. Understanding the role of PTs in assessing vegetation decline

One of the final objectives was to understand the contribution of different PTs to detect severity levels of affected trees caused mainly by *Pc* and drought stress. Zarco-Tejada *et al.* (2018a) demonstrated that quantification of PTs from spectral imaging data could substantially improve the detection of *Xf*-infection symptoms in olive trees. However, some other studies

[1] Forest Light model v.8 — *https://flight-rtm.github.io*

(Hernández-Clemente *et al.*, 2019; Liu *et al.*, 2019; Markiet *et al.*, 2016) show the limitations of quantifying PTs in heterogeneous forest canopies and challenges related to the impact of shadows, background, and understory that hamper the extraction of the spectral signature of pure crowns. Focusing the last case study on using advanced 3-D simulation models using hyperspectral and thermal airborne imagery allowed us to characterise the heterogeneous composition of forest canopies, which was crucial to the methodological approach of this work. A critical step in chapter 4 was the successful retrieval of PTs that enabled us to understand their contribution and carry out a supervised classification in order to identify the severity level of each tree independently. Based on a combination of 3-D RTM and statistical analysis, it was found that the decline of oak forests can potentially be detected and severity levels assessed.

Among all the PTs analysed, the decrease in chlorophyll fluorescence and pigment content found in this study are in line with the decreasing rates reported in experiments induced by drought stress and root rot under controlled (Früchtenicht *et al.*, 2018; Koller *et al.*, 2013; Ruiz Gómez *et al.*, 2018) and field conditions (Baquedano and Castillo, 2007; Camarero *et al.*, 2012). Empirical data showed that the discriminatory ability of PTs to determine different severity levels is affected by biotic and abiotic factors. Trees with lower incidence have a higher chlorophyll and carotenoid content, and fluorescence emission. The more severe the tree, the lower the concentration of these pigments and fluorescence, results that were also confirmed by model-based PTs retrieved from hyperspectral images, in which fluorescence again takes a more important role in discriminating between severity levels than any other indicator of pigment content.

Disregarding whether discriminating by incidence or severity, the results showed that canopy temperature becomes the most important indicator, which is in line with previous work where thermal data were used for the detection of diseases in olive (Calderón *et al.*, 2015) and almond trees (López-López *et al.*, 2016) or water stress (Gonzalez-Dugo *et al.*, 2020). This

observation was complemented by studying the importance of each indicator in the most advanced stages of the disease, where LAI and Cdm were the most relevant variables in the model, with temperature and fluorescence taking a secondary role.

5.3.6. Providing a comprehensive approach for monitoring heterogeneous canopies

Another critical issue requiring attention is the potential impact of forest canopy heterogeneity characterised by discontinuous architectures, shadows and soil composition, which makes the extraction of pure crown spectral data more challenging. The suitability of spectral-based indicators for disease detection on a larger scale using satellite data was questioned in Chapter 2, which formed the third chapter's basis and this focused on demonstrating the significant impact of soil and understory on the fluorescence signal recovered from higher to lower spatial resolution images. This proved the need to consider those effects for a proper interpretation, thus developing the new FLIGHT8 model, which ensures the minimisation of errors due to the background effect by adding the spectral contribution of the understory.

For all of the above, having a tool to monitor and anticipate vegetation decline in agricultural and silvicultural areas gives a clear timing advantage by allowing the necessary management measures to reverse the process. Large-scale monitoring will benefit from future approaches that add multitemporal analysis of disease evolution. However, the use of multitemporal image data will be conditioned by background variation and its impact on the aggregated pixels.

5.4. Recommendations for further research

The combined use of RTM, PTs, and VIs in remote sensing enables mapping the physiological state of vegetation and the biophysical changes that occur

due to biotic and abiotic agents. Given the high temporal resolution that satellites such as Sentinel-2 offer, or even in combination with Landsat or together with the upcoming FLEX mission, this global mapping would allow us to evaluate diseases or the monitoring of forest decline over large areas, bringing new opportunities for treatments at early stages that can be carried out to prevent its spread. Future studies should consider the impact of spatial and temporal variations that drive global plant dynamics, establishing practices that can benefit the environment's protection and encourage sustainable multi-use management.

The understory of Mediterranean oak forests is mainly covered by grassland, where changes induced by nutrients and light availability alter plant functional traits and canopy structure. However, in other ecosystems with higher density, the contribution of the understory may be different. Therefore, future efforts on disease detection should be focused on assessing the contribution of SIF emitted by the understory to the quantification of total canopy SIF in other ecosystem types and forest complexities. At the same time, these studies will be essential for analysing the ability to measure and interpret SIF on a global scale.

Future studies should consider methods to i) unravel the direct plant-level effects of either *Xf* infection in olive trees or *Pc* in holm oaks from those that manifest themselves in other components of the landscape due to changes in vegetation composition or management, and ii) to move even one step forward and determine if the plant is only affected by the incidence caused by that factor and what role other factors play and to what extent.

Disentangling these effects and being able to separate the components of the environment to take into account the evolution of each of them over time is key, and the applications are multiple, from helping to understand how different species sharing an environment behave, to characterising different background compositions, or even partitioning canopy component fluxes.

From a physical modelling perspective, it would be interesting to analyse the sensitivity of the impact of spatial and temporal variations with different SIF proxies, including other telluric oxygen absorption bands and formulations, such as iFLD (Alonso *et al.*, 2008); pFLD (Liu and Liu, 2015); SFM (Mazzoni *et al.*, 2012; Meroni *et al.*, 2010); or NIRv (Badgley *et al.*, 2017). Future studies could also take into account the vertical variability of the maximum carboxylation rate, which is a crucial parameter for estimating CO2 assimilation in crops (Camino *et al.*, 2019) or consider the cycle of xanthophylls included in the extended version of Fluspect (Vilfan *et al.*, 2018). Given the importance of temperature in estimating the level of stress in vegetation (Gonzalez-Dugo *et al.*, 2020) and the impact it has on the early detection of diseases (Calderón *et al.*, 2015; López-López *et al.*, 2016), it would be helpful to deepen more in developing models and tools that grant us a better understanding of the behaviour of temperature variation in the plant canopy and its impact on other components.

5.5. Concluding Remarks

The findings and achievements made throughout this work should be considered as valuable tools to improve the understanding of the impact of the aggregated signal on the vegetation cover and its composition. In particular, detecting processes related to vegetation health and the influence of biotic and abiotic factors contributes to establishing different management actions in terms of precision agriculture and forestry. A key point from the proposed methodology is that, despite using spectral information from various sensors and resolutions, the results showed high consistency with field measurements when using the proposed indicators and PTs. It is expected that thanks to the use of the methods presented, future developments, and the high performance of available remote sensors, the ability to remotely detect and assess vegetation health using air- and space-borne sensors will contribute to a better understanding and evaluation of our environment, which has a strong

impact not only on socio-economic factors but also on the preservation of our ecosystem as a whole.

Appendix A.

Supplementary Material: chapter 2

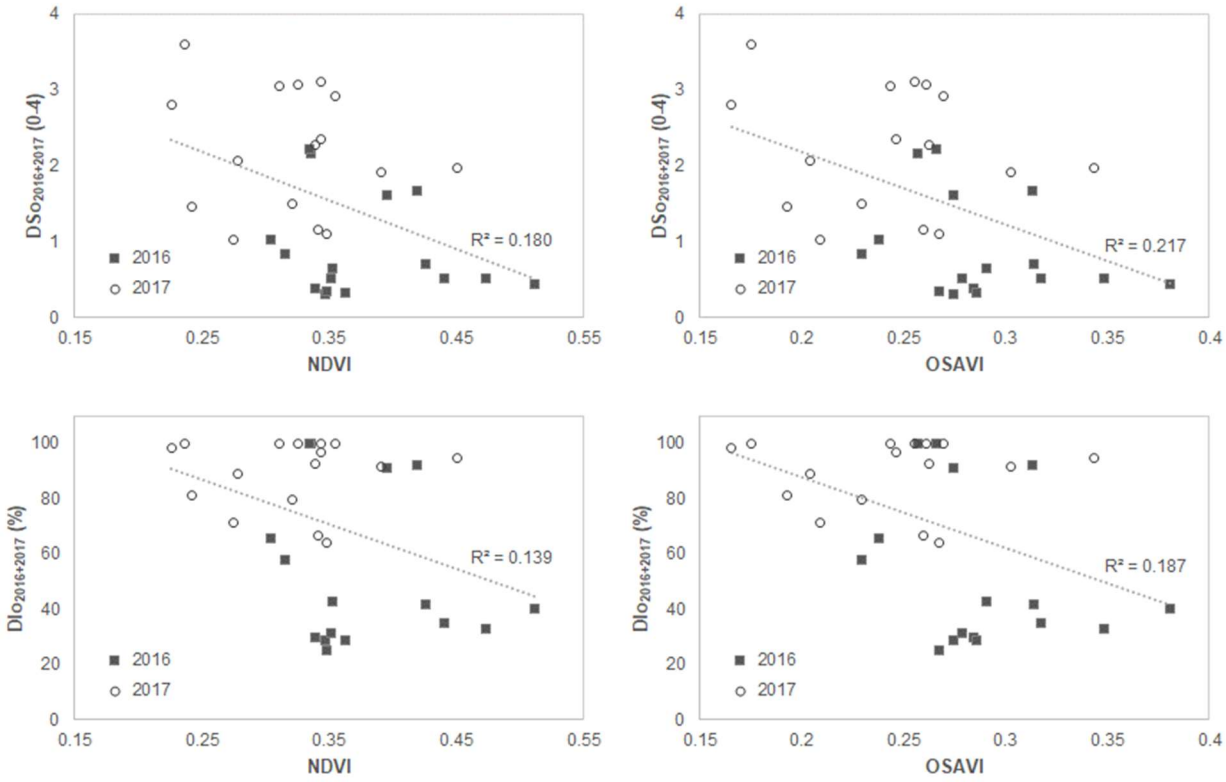

Figure A.1 Relationship between severity (DSo) and incidence (DIo) and vegetation indices (VIs) calculated from Sentinel-2A imagery in 2016 and 2017.

Appendix B.

Supplementary Material: chapter 3

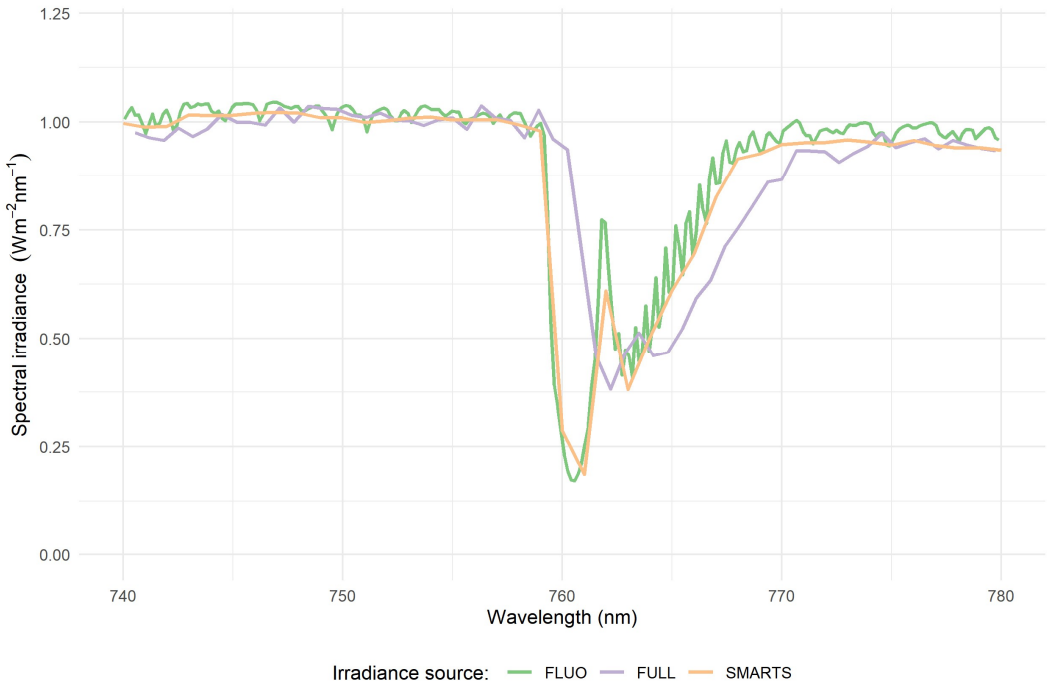

Figure B.1 Comparison between different sources of solar irradiance information.

Table B.1 Input range for FLIGHT8 according to the model intercomparison.

Simulation* \ Parameters	Solar Zenith Angle (deg)	Scattered Radius (m)	Leaf Area Index (m^2 m^{-2})	Canopy Height (m)	Leaf Angle Distribution	Leaf ρ/τ (%)	Soil ρ (%)
HOM01,TUR,ERE,NR1,00	0	0	1	1	Erectophile	0.5/0.5	1.0
HOM03,DIS,ERE,RED,50	50	0.05	3	2	Erectophile	0.0546/ 0.0149	0.127
HOM05,TUR,ERE,NR1,60	60	0	5	1	Erectophile	0.5/0.5	1.0
HOM12,DIS,ERE,NR1,30	30	0.05	2	1	Erectophile	0.5/0.5	1.0
HOM13,DIS,PLA,RED,20	20	0.1	3	2	Planophile	0.0546/ 0.0149	0.127
HOM03,TUR,UNI,NIR,20	20	0	3	1	Uniform	0.4957/ 0.4409	0.159

* HOM (Homogeneous)
TUR (Turbid), DIS (Discrete)
ERE (Erectophile), PLA (Planophile), UNI (Uniform)
NR1 (Purist corner), RED (Red, solar domain), NIR (Near-infrared, solar domain)

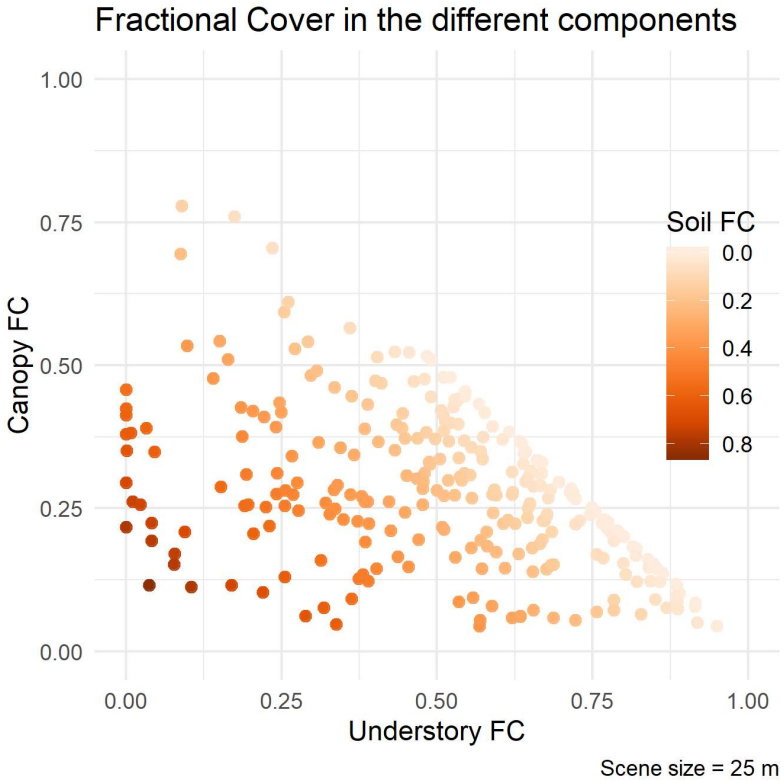

Figure B.2 Example of the contribution of scene components for a 25 m window based on the relationship between canopy and understory fractional cover (FC) and soil FC shown as different intensity orange points.

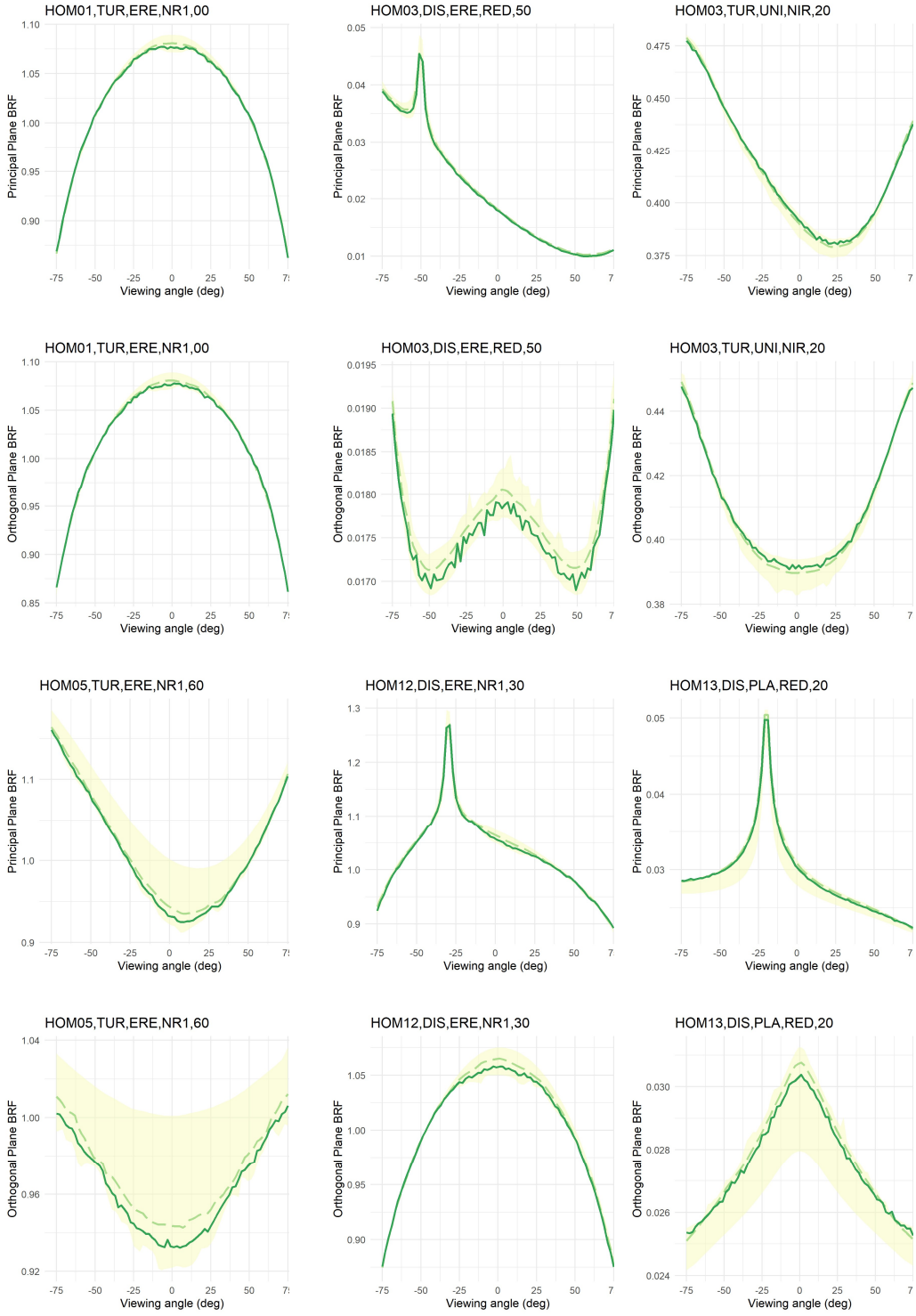

Figure B.3 Comparison of FLIGHT8 with other RTMs using the set of scenarios proposed by the RAMI intercomparison exercise. The results of

RAMIREF are shown by the dashed light-green line and those from other models within the shaded area

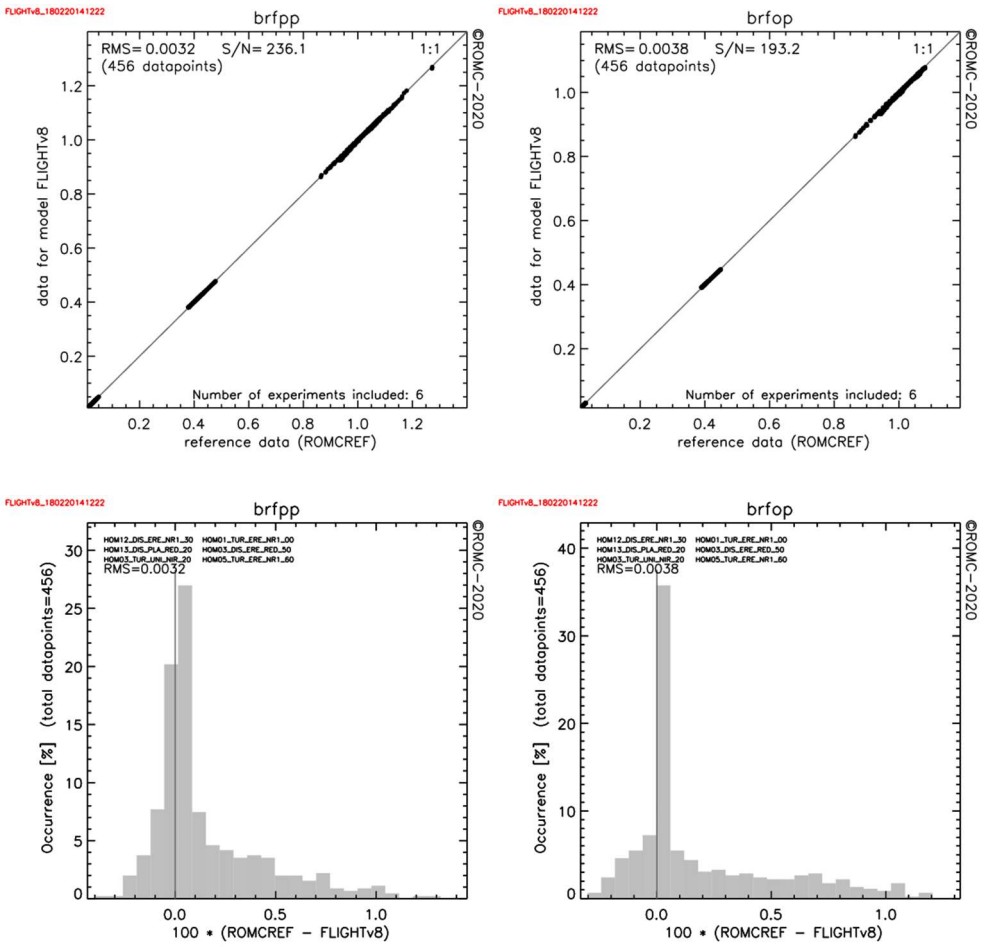

Figure B.4 Global bi-directional reflectance factor 1-to-1 comparison (top) and histogram differences (bottom) for principal (left) and orthogonal planes (right) within the ROMC-generated results.

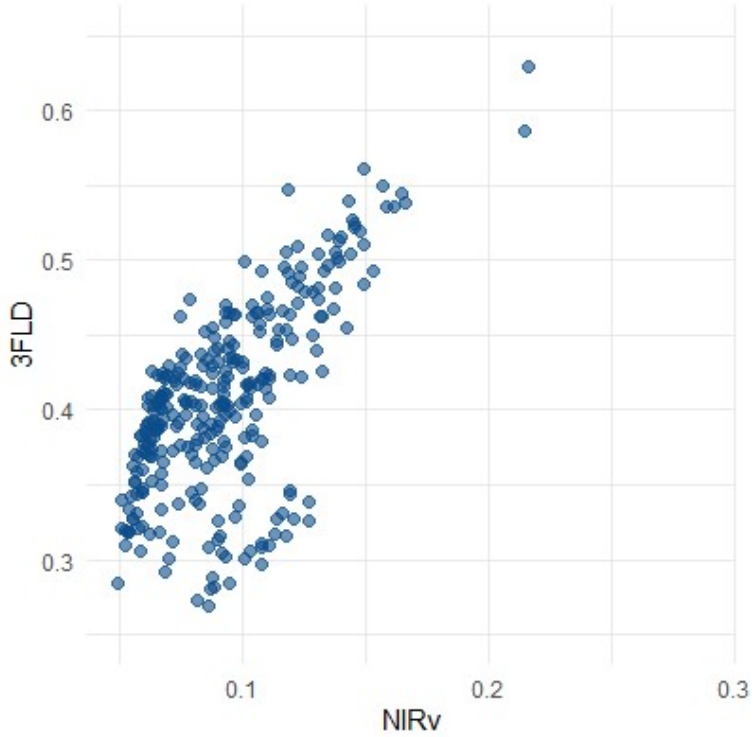

Figure B.5 Relationship between NIRv and 3FLD from hyperspectral data from 25 × 25 m aggregated pixels in the 300 scenes used in this study.

Appendix C.

Supplementary Material: chapter 4

Table C.1 Vegetation indices derived from airborne imagery included in this study and their formulations.

Vegetation index	Equation	Reference
Structural		
Normalized Difference Vegetation Index	$NDVI = (R_{800} - R_{670})/(R_{800} + R_{670})$	(Rouse *et al.*, 1974)
Near-Infrared Reflectance of Vegetation	$NIR_V = R_{800}(R_{800} - R_{670})/(R_{800} + R_{670})$	(Badgley *et al.*, 2017)
Renormalized Difference Vegetation Index	$RDVI = (R_{800} - R_{670})/\sqrt{(R_{800} + R_{670})}$	(Roujean and Breon, 1995)
Simple Ratio	$SR = R_{800}/R_{670}$	(Jordan, 1969)
Modified Simple Ratio	$MSR = (R_{800}/R_{670} - 1)/($ ⟦(R_{800}/R_670)⟧ ^0.5 $+ 1)$	(Chen, 1996)
Optimized Soil-Adjusted Vegetation Index	$OSAVI = (1 + 0.16)\ \frac{R_{800} - R_{670}}{R_{800} + R_{670} + 0.16}$	(Rondeaux *et al.*, 1996)

Modified Soil-Adjusted Vegetation Index	$\mathrm{MSAVI} = (1+\mathrm{L})\dfrac{\mathrm{R}_{800}-\mathrm{R}_{670}}{\mathrm{R}_{800}+\mathrm{R}_{670}+\mathrm{L}}$	(Qi *et al.*, 1994)
Modified Triangular Vegetation Index 1	$\mathrm{MTVI}_1 = 1.2(1.2(\mathrm{R}_{800}-\mathrm{R}_{550}) - 2.5(\mathrm{R}_{670} - \mathrm{R}_{550}))$	(Haboudane *et al.*, 2004)
Modified Triangular Vegetation Index 1	$\mathrm{MTVI}_2 = 1.5\dfrac{1.2(\mathrm{R}_{800}-\mathrm{R}_{550}) - 2.5(\mathrm{R}_{670}-\mathrm{R}_{550})}{\sqrt{(2\mathrm{R}_{800}+1)^2 - (6\mathrm{R}_{800} - 5\sqrt{\mathrm{R}_{670}}) - 0.5}}$	(Haboudane *et al.*, 2004)
Modified Chlorophyll Absorption Ratio Index	$\mathrm{MCARI} = ((\mathrm{R}_{700}-\mathrm{R}_{670}) - 0.2(\mathrm{R}_{700}-\mathrm{R}_{550}))\left(\dfrac{\mathrm{R}_{700}}{\mathrm{R}_{670}}\right)$	(Haboudane *et al.*, 2002)
Modified Chlorophyll Absorption Ratio Index 1	$\mathrm{MCARI}_1 = 1.2(2.5(\mathrm{R}_{800}-\mathrm{R}_{670}) - 1.3(\mathrm{R}_{800} - \mathrm{R}_{550}))$	(Haboudane *et al.*, 2004)
Modified Chlorophyll Absorption Ratio Index 2	$\mathrm{MCARI}_2 = 1.5\dfrac{2.5(\mathrm{R}_{800}-\mathrm{R}_{550}) - 1.3(\mathrm{R}_{670}-\mathrm{R}_{550})}{\sqrt{(2\mathrm{R}_{800}+1)^2 - (6\mathrm{R}_{800} - 5\sqrt{\mathrm{R}_{670}}) - 0.5}}$	(Haboudane *et al.*, 2004)
Enhanced Vegetation Index	$\mathrm{EVI} = 2.5(\mathrm{R}_{800}-\mathrm{R}_{670})/(\mathrm{R}_{800}+6\mathrm{R}_{670}-7.5\mathrm{R}_{400}+1)$	(Huete *et al.*, 2002)
Lichtenthaler 1	$\mathrm{LIC}_1 = (\mathrm{R}_{800}-\mathrm{R}_{680})/(\mathrm{R}_{800}+\mathrm{R}_{680})$	(Lichtenthaler, 1996)
Pigments		
Vogelmann 1	$\mathrm{VOG}_1 = \mathrm{R}_{740}/\mathrm{R}_{720}$	(Vogelmann, 1993)
Vogelmann 2	$\mathrm{VOG}_2 = (\mathrm{R}_{734}-\mathrm{R}_{747})/(\mathrm{R}_{715}+\mathrm{R}_{726})$	(Vogelmann, 1993)
Vogelmann 3	$\mathrm{VOG}_3 = (\mathrm{R}_{734}-\mathrm{R}_{747})/(\mathrm{R}_{715}+\mathrm{R}_{720})$	(Vogelmann, 1993)
Gitelson and Merzlyak 1	$\mathrm{GM}_1 = \mathrm{R}_{750}/\mathrm{R}_{550}$	(Gitelson and Merzlyak, 1996)
Gitelson and Merzlyak 2	$\mathrm{GM}_2 = \mathrm{R}_{750}/\mathrm{R}_{700}$	(Gitelson and Merzlyak, 1996)

Transformed Chlorophyll Absorption Ratio	$\mathrm{TCARI} = 3\left((\mathrm{R}_{700} - \mathrm{R}_{670}) - 0.2\,(\mathrm{R}_{700} - \mathrm{R}_{550})\frac{\mathrm{R}_{700}}{\mathrm{R}_{670}}\right)$	(Haboudane *et al.*, 2002)
TCARI/OSAVI	$\mathrm{TCARI/OSAVI} = \frac{\mathrm{TCARI}}{\mathrm{OSAVI}}$	(Haboudane *et al.*, 2002)
Chlorophyll Index	$\mathrm{CI} = \frac{\mathrm{R}_{750}}{\mathrm{R}_{710}}$	(Zarco-Tejada *et al.*, 2001)
Triangular Vegetation Index	$\mathrm{TVI} = 0.5(120(\mathrm{R}_{750} - \mathrm{R}_{550}) - 200(\mathrm{R}_{670} - \mathrm{R}_{550}))$	(Broge and Leblanc, 2001)
Simple Ratio Pigment Index	$\mathrm{SRPI} = \mathrm{R}_{430}/\mathrm{R}_{680}$	(Penuelas *et al.*, 1995)
Normalized Phaeophytinization Index	$\mathrm{NPQI} = (\mathrm{R}_{415} - \mathrm{R}_{435})/(\mathrm{R}_{415} + \mathrm{R}_{435})$	(Barnes *et al.*, 1992)
Normalized Pigment Chlorophyll Index	$\mathrm{NPCI} = (\mathrm{R}_{680} - \mathrm{R}_{430})/(\mathrm{R}_{680} + \mathrm{R}_{430})$	(Penuelas *et al.*, 1995)
Simple Ratio 695/420 Carter	$\mathrm{CTR} = \mathrm{R}_{695}/\mathrm{R}_{420}$	(Carter, 1994)
Simple Ratio Carotenoids	$\mathrm{CAR} = \mathrm{R}_{515}/\mathrm{R}_{570}$	(Hernández-Clemente *et al.*, 2012)
Datt Cab Cx+c Index	$\mathrm{DCabxc} = \mathrm{R}_{672}/\ (3\ \mathrm{R}_{550}\mathrm{R}_{708})$	(Datt, 1998)
Datt NIR Cab Cx+c Index	$\mathrm{DNCabxc} = \mathrm{R}_{860}\ /\ (\mathrm{R}_{550}\mathrm{R}_{708})$	(Datt, 1998)
Structure Insensitive Pigment Index	$\mathrm{SIPI} = (\mathrm{R}_{800} - \mathrm{R}_{445})/(\mathrm{R}_{800} + \mathrm{R}_{680})$	(Penuelas *et al.*, 1995)
Chlorophyll Reciprocal Reflectance Index 550	$\mathrm{CRI}_{550} = 1/\mathrm{R}_{510} - 1/\mathrm{R}_{550}$	(Gitelson *et al.*, 2006, 2003)
Chlorophyll Reciprocal Reflectance Index 700	$\mathrm{CRI}_{700} = 1/\mathrm{R}_{510} - 1/\mathrm{R}_{700}$	(Gitelson *et al.*, 2006, 2003)
Modified Chlorophyll Reciprocal Reflectance Index 550	$\mathrm{CRI}_{550\mathrm{m}} = 1/\mathrm{R}_{515} - 1/\mathrm{R}_{550}$	(Gitelson *et al.*, 2006, 2003)
Modified Chlorophyll Reciprocal Reflectance Index 700	$\mathrm{CRI}_{700\mathrm{m}} = 1/\mathrm{R}_{515} - 1/\mathrm{R}_{700}$	(Gitelson *et al.*, 2006, 2003)
Near-Infrared Chlorophyll Reciprocal Reflectance Index 550	$RCRI_{550} = 1/R_{510} - (1/R_{550})\ R_{770}$	(Gitelson *et al.*, 2006, 2003)

Near-Infrared Chlorophyll Reciprocal Reflectance Index 700	$RCRI_{700} = 1/R_{510} - (1/R_{700}) \;\; R_{770}$	(Gitelson *et al.*, 2006, 2003)
Plant Senescence Reflectance Index	$PSRI = (R_{680} - R_{500})/R_{750}$	(Merzlyak *et al.*, 1999)
Lichtenthaler 3	$LIC_3 = R_{440}/R_{740}$	(Lichtenthaler, 1996)
PRIs		
Photochemical Reflectance Index	$PRI = (R_{570} - R_{530})/(R_{570} + R_{530})$	(Gamon *et al.*, 1992)
Photochemical Reflectance Index 515	$PRI_{515} = (R_{515} - R_{530})/(R_{515} + R_{530})$	(Hernández-Clemente *et al.*, 2011)
Modified Photochemical Reflectance Index 1	$PRIM_1 = (R_{512} - R_{531})/(R_{512} + R_{531})$	(Gamon *et al.*, 1992)
Modified Photochemical Reflectance Index 2	$PRIM_2 = (R_{600} - R_{531})/(R_{600} + R_{531})$	(Gamon *et al.*, 1992)
Modified Photochemical Reflectance Index 3	$PRIM_3 = (R_{670} - R_{531})/(R_{670} + R_{531})$	(Gamon *et al.*, 1992)
Modified Photochemical Reflectance Index 4	$PRIM_4 = (R_{570} - R_{531} - R_{670})/(R_{570} + R_{531} + R_{670})$	(Gamon *et al.*, 1992)
Normalized PRI	$PRIn = PRI/(RDVI \;\; R_{700}/R_{670})$	(Zarco-Tejada *et al.*, 2013a)
PRI×CI	$PRI \times CI = PRI(R_{760}/R_{700} - 1)$	(Garrity *et al.*, 2011)
BGR		
Blueness Index	$B = R_{450}/R_{490}$	-
Greenness Index	$G = R_{550}/R_{670}$	(Zarco-Tejada *et al.*, 2001)
Redness index	$R = R_{700}/R_{670}$	(Gitelson *et al.*, 2000)
Blue/Green Index 1	$BGI_1 = R_{400}/R_{550}$	(Zarco-Tejada *et al.*, 2012; Zarco-Tejada *et al.*, 2005)
Blue/Green Index 2	$BGI_1 = R_{450}/R_{550}$	(Zarco-Tejada *et al.*, 2012; Zarco-Tejada *et al.*, 2005)
Blue Fraction 1	$BF_1 = R_{400}/R_{410}$	-

Blue Fraction 2	$BF_2 = R_{400}/R_{420}$	-
Blue Fraction 3	$BF_3 = R_{400}/R_{430}$	-
Blue Fraction 4	$BF_4 = R_{400}/R_{440}$	-
Blue Fraction 5	$BF_5 = R_{400}/R_{450}$	-
Blue/Red Index 1	$BRI_1 = R_{490}/R_{690}$	(Zarco-Tejada *et al.*, 2012)
Blue/Red Index 2	$BRI_2 = R_{450}/R_{690}$	(Zarco-Tejada *et al.*, 2012)
Relative Greenness Index	$RGI = R_{690}/R_{550}$	(Ceccato *et al.*, 2001)
Ratio Analysis of Reflectance Spectra	$RARS = \ R_{746}/R_{513}$	(Chappelle *et al.*, 1992)
Lichtenthaler 2	$LIC_2 = R_{440}/R_{690}$	(Lichtenthaler, 1996)
Healthy Index	$HI = (R_{534} - R_{698})/(R_{534} + R_{698}) - \ R_{704}/2$	(Mahlein *et al.*, 2013)
Curvature Optical Index	$CUR = (R_{675} \ R_{690})/(R_{683})^2$	(Zarco-Tejada *et al.*, 2000)
NIR-VIS		
Pigment Specific Simple Ratio A	$PSSR_a = R_{800}/R_{680}$	(Blackburn, 1998)
Pigment Specific Simple Ratio B	$PSSR_b = R_{800}/R_{635}$	(Blackburn, 1998)
Pigment Specific Simple Ratio C	$PSSR_c = R_{800}/R_{470}$	(Blackburn, 1998)
Pigment Specific Normalised Difference C	$PSND_c = (R_{800} - R_{470})/(R_{800} + R_{470})$	(Blackburn, 1998)
Anthocyanins		
Visible Atmospherically Resistant Index	$VARI = (R_{555} - R_{650})/(R_{555} + R_{650} - R_{475})$	(Gitelson *et al.*, 2001)
Visible Atmospherically Resistant Index 2	$VARI_2 = (R_{560} - R_{668})/(R_{560} + R_{668} - R_{475})$	(Gitelson *et al.*, 2001)
Anthocyanin Reflectance Index 1	$ARI_1 = 1/R_{550} - 1/R_{700}$	(Gitelson *et al.*, 2001)
Anthocyanin Reflectance Index 2	$ARI_2 = 1/R_{550} - 1/R_{700}$	(Gitelson *et al.*, 2002)
Modified Anthocyanin Reflectance Index	$mARI = R_{760:800}(1/R_{540:560} - 1/R_{690:710})$	(Gitelson *et al.*, 2006)
Modified Anthocyanin Reflectance Index 1	$ARI_1m = R_{760:800}(1/R_{550} - 1/R_{700})$	-
Modified Anthocyanin Reflectance Index 2	$ARI_1m_2 = R_{800}(1/R_{550} - 1/R_{700})$	-

Nitrogen		
Double-peak Canopy Nitrogen Index	$DCNI = (R_{720} - R_{700})/(R_{700} - R_{670})/(R_{720} - R_{670} + 0.03)$	(Chen *et al.*, 2010)
SWIR		
Gnyp and Li Index	$GnyLi = \frac{(R_{900}\ R_{1050}) - (R_{955}\ R_{1220})}{(R_{900}\ R_{1050}) + (R_{955}\ R_{1220})}$	(Gnyp *et al.*, 2014)
CI_1	$CI_1 = (R_{736} - R_{735})\ R_{990}\ /\ R_{720}$	(Bao *et al.*, 2013)
CI_2	$CI_2 = (R_{736} - R_{735})\ R_{900}\ /\ R_{720}$	(Bao *et al.*, 2013)
Modified Chlorophyll Absorption Ratio Index 1510	$MCARI_{1510} = ((R_{700} - R_{1510}) - 0.2(R_{700} - R_{550}))\left(\frac{R_{700}}{R_{1510}}\right)$	(Herrmann *et al.*, 2010)
Transformed Chlorophyll Absorption Ratio 1510	$TCARI_{1510} = 3\left((R_{700} - R_{1510}) - 0.2\ (R_{700} - R_{550})\frac{R_{700}}{R_{1510}}\right)$	(Herrmann *et al.*, 2010)
Optimized Soil-Adjusted Vegetation Index 1510	$OSAVI_{1510} = (1 + 0.16)\ \frac{R_{800} - R_{1510}}{R_{800} + R_{1510} + 0.16}$	(Herrmann *et al.*, 2010)
TCARI/OSAVI 1510	$T/O_{1510} = TCARI_{1510}\ OSAVI_{1510}$	(Herrmann *et al.*, 2010)
Normalized Ratio Index 1510	$NRI_{1510} = (R_{1510} - R_{660})/(R_{1510} + R_{660})$	(Herrmann *et al.*, 2010)
Ratio Spectral Index 990 720	$RSI_{990,720} = R_{990})/R_{720}$	(Yao *et al.*, 2010)
Normalized Ratio Index 1770	$NRI_{1770} = (R_{1770} - R_{693})/(R_{1770} + R_{693})$	(Ferwerda *et al.*, 2005)
Normalized Difference Nitrogen Index	$NDNI = \frac{log_{10}(1/R_{1510}) - log_{10}(1/R_{1680})}{log_{10}(1/R_{1510}) + log_{10}(1/R_{1680})}$	(Serrano *et al.*, 2002)
Sulphur index 1080	$S_{1080} = (R_{1080} - R_{660})/(R_{1080} + R_{660})$	(Mahajan *et al.*, 2014)
Sulphur index 1260	$S_{1260} = (R_{1260} - R_{660})/(R_{1260} + R_{660})$	(Mahajan *et al.*, 2014)
Normalized 1645 1715	$N_{1645,1715} = (R_{1645} - R_{1715})/(R_{1645} + R_{1715})$	(Pimstein *et al.*, 2011)
Normalized 870 1450	$N_{870,1450} = (R_{870} - R_{1450})/(R_{870} + R_{1450})$	(Pimstein *et al.*, 2011)

Normalized 850 1510	$N_{850,1510} = (R_{850} - R_{1510})/(R_{850} + R_{1510})$	(Camino *et al.*, 2018)
Middle-infrared Normalized Difference	$MND = (R_{1080} - R_{1675})/(R_{1080} + R_{1675})$	(Malthus *et al.*, 1993)
Normalized Difference Water Index	$NDWI = (R_{860} - R_{1240})/(R_{860} + R_{1240})$	(Gao, 1996)
Fluorescence		
3FLD	$3FLD = \frac{E_{out} \cdot L_{in} - E_{in} \cdot L_{out}}{E_{out} - E_{in}}$	(Maier *et al.*, 2003; Plascyk, 1975)

Appendix D.

Further scientific contributions

During the course of this thesis, the author has made further related scientific contributions. For a comprehensive reference, they are listed below:

Publications in ISI-listed journals

2018. Zarco-Tejada, P.J., Camino, C., Beck, P.S.A., Calderon, R., **Hornero, A.**, Hernández-Clemente, R., Kattenborn, T., Montes-Borrego, M., Susca, L., Morelli, M., Gonzalez-Dugo, V., North, P.R.J., Landa, B.B., Boscia, D., Saponari, M., Navas-Cortes, J.A., *Pre-visual symptoms of Xylella fastidiosa infection revealed in spectral plant-trait alterations*, **Nature Plants**, DOI: 10.1038/s41477-018-0189-7

2019. Caruso, G., Zarco-Tejada, P.J., Gonzalez-Dugo, V., Moriondo, M., Tozzini, L., Palai, G., Rallo, G., **Hornero, A.**, Primicerio, J., Gucci, R., *High-resolution imagery acquired from an unmanned platform to estimate biophysical and geometrical parameters of olive trees under different irrigation regimes*, **PLoS ONE**, DOI: 10.1371/journal.pone.0210804

2019. Zarco-Tejada, P.J., **Hornero, A.**, Beck, P.S.A., Kattenborn, T., Kempeneers, P., Hernández-Clemente, R. *Chlorophyll content estimation in an open-canopy conifer forest with Sentinel-2 and hyperspectral imagery in the context of forest decline*, **Remote Sensing of Environment**, DOI: 10.1016/j.rse.2019.01.031

2019. Hernández-Clemente R., **Hornero A.**, Mottus M., Penuelas J., Gonzalez-Dugo V., Jimenez-Muñoz J.C., Suárez-Barranco L., Alonso L., Zarco-Tejada P.J. *Early diagnosis of vegetation health from high-resolution*

hyperspectral and thermal imagery. Lessons learned from empirical relationships and radiative transfer modelling, **Current Forestry Reports**, DOI: 10.1007/s40725-019-00096-1

2020. Poblete, T., Camino, C., Beck, P.S.A., **Hornero, A.**, Kattenborn, T., Saponari, M., Boscia, D., Navas-Cortes, J.A., *Detection of Xylella fastidiosa infection symptoms with airborne multispectral and thermal imagery: assessing bandset reduction performance from hyperspectral analysis*, **ISPRS Journal of Photogrammetry and Remote Sensing**, DOI: 10.1016/j.isprsjprs.2020.02.010

2020. Prada, M., Cabo, C., Hernández-Clemente, R., **Hornero, A.**, Majada, J., Martínez-Alonso, C., *Assessing Canopy Responses to Thinnings for Sweet Chestnut Coppice with Time-Series Vegetation Indices Derived from Landsat-8 and Sentinel-2 Imagery*, **Remote Sensing**, DOI: 10.3390/rs12183068

2020. Monterroso-Checa, A., Redondo-Villa, A., Gasparini, M., **Hornero, A.**, Iraci, B., Martín-Talaverano, R., Moreno-Escribano, J.C., Muñoz-Cádiz, J., Murillo-Fragero, J.I., Obregón-Romero, R., Vargas, N., Young, S.J., Yuste, R., Zarco-Tejada, P., *A Heritage Science Workflow to Preserve and Narrate a Rural Archeological Landscape Using Virtual Reality: The Cerro del Castillo of Belmez and Its Surrounding Environment*. **Applied Sciences**, DOI: 10.3390/app10238659

2021. Suarez, L., González-Dugo, V., Camino, C., **Hornero, A.**, Zarco-Tejada, P.J., Physical model inversion of the green spectral region to track assimilation rate in almond trees with an airborne nano-hyperspectral imager, **Remote Sensing of Environment** , DOI: 10.1016/j.rse.2020.112147

2021. Suarez, L., Zhang, P., Sun, J., Wang, Y., Poblete, T., **Hornero, A.**, Zarco-Tejada, P.J., *Assessing wine grape quality parameters using plant traits derived from physical model inversion of hyperspectral imagery*, **Agricultural and Forest Meteorology**, DOI: 10.1016/j.agrformet.2021.108445

2021. Zarco-Tejada, P.J., Poblete, T., Camino, C., Gonzalez-Dugo, V., Calderon, R., **Hornero, A.**, Hernández-Clemente, R., Román-Écija, M., Velasco-Amo, M.P., Landa, B.B., Beck, P.S.A., Saponari, M., Boscia, D.,

Navas-Cortes, J.A., Spectral fingerprints of plant pathogen infection diverge from abiotic signals, *Under Review*.

2021. Poblete, T., Navas-Cortes, J.A., Camino, C., Calderon, R., **Hornero, A.**, Gonzalez-Dugo, V., Landa, B.B., Zarco-Tejada, P.J. *Discriminating Xylella fastidiosa from Verticillium dahliae infections in olive trees using thermal- and hyperspectral-based plant traits*, *Under Review*.

Communications at conferences

2018. **Hornero, A.**, Hernández-Clemente, R., Beck, P.S.A., Navas-Cortés, J.A., Zarco-Tejada, P.J. *Using Sentinel-2 imagery to track changes produced by Xylella fastidiosa in olive trees*. International Geoscience and Remote Sensing Symposium, IGARSS. 22nd - 27th July 2018, Valencia, Spain.

2018. Hernández-Clemente, R., North, P.R.J., **Hornero, A.**, Zarco-Tejada, P.J. Monitoring forest health with sun-induced chlorophyll fluorescence observations and 3-D radiative transfer modeling. International Geoscience and Remote Sensing Symposium, IGARSS. 22nd - 27th July 2018, Valencia, Spain.

2018. Beck, P.S.A., Zarco-Tejada, P.J., Camino, C., Calderon, R., **Hornero, A.**, Hernández-Clemente, R., Montes-Borrego, M., Susca, L., Morelli, M., Gonzalez-Dugo, V., Landa, B.B., Boscia, D., Saponari, M., Navas-Cortes, J.A. *Anticipating and understanding new Xylella fastidiosa epidemics across European landscapes; insights from remote sensing and network analysis*. International Congress of Plant Pathology (ICPP): Plant Health in A Global Economy, 29th July – 3rd August 2018, Boston, MA, USA.

2018. R. Calderon, C. Camino, P.S.A. Beck, **A. Hornero**, R. Hernández-Clemente, T. Kattenborn, M. Montes-Borrego, L. Susca, M. Morelli, V. Gonzalez-Dugo, P.R.J. North, B.B. Landa, D. Boscia, M. Saponari, P.J. Zarco-Tejada and J.A. Navas-Cortes. *Detección pre-visual de la infección por Xylella fastidiosa en olivo a partir de imágenes hiperespectrales y térmicas*. Phytoma, December 2018, Ed. 304.

2019. Beck, P.S.A., **Hornero, A.**, Martinez-Sanchez, L., Scholten, R., Hernández-Clemente, R., North, P.R.J., Boscia, D., Navas-Cortes, J.A., Zarco-Tejada, P.J. *Insights into the spread of Xylella fastidiosa in Italy, from early detection of symptoms to damage mapping through remote sensing from air and space*. ESA Living Planet Symposium 2019: From Agriculture mapping to monitoring, 13th - 17th May 2019; Milan, Italy.

2019. Zarco-Tejada, P.J., Camino, C., Beck, P.S.A., Calderon, R., **Hornero, A.**, Hernández-Clemente, R., Kattenborn, T., Montes-Borrego, M., Susca, L., Morelli, M., Gonzalez-Dugo, V., North, P.R.J., Landa, B.B., Boscia, D., Saponari, M., Navas-Cortes, J.A. *Remote sensing detection of Xylella fastidiosa using airborne hyperspectral and thermal imagery: lessons learned from the European outbreaks*. 2019 Australian Biosecurity Symposium, 12nd-13rd June 2019; Gold Coast, Queensland.

2019. Caruso, G., Palai, G., Caruso, M., Roccuzzo, G., Stagno, F., Zarco-Tejada, P.J., Gonzalez-Dugo, V., **Hornero, A.**, Gucci, R. *Using an unmanned platform and VIS-NIR cameras to determine biophysical and geometrical parameters of olive, grapevine and citrus canopies*. International Symposium on Precision Management of Orchards and Vineyards, 7th - 11th October 2019; Palermo, Italy.

2019. **Hornero, A.**, Hernández-Clemente, R., North, P.R.J., Beck, P.S.A., Boscia, D., Navas-Cortes, J.A., Zarco-Tejada, P.J. *Spatio-temporal monitoring of Xylella fastidiosa in olive trees using radiative transfer models and Sentinel-2 images*. "Detection and surveillance" session on the 2nd EU conference on *Xylella fastidiosa*. 29th - 30th October 2019, Ajaccio, Corsica.

2019. Scholten, R., Martinez Sanchez, L., **Hornero, A.**, Navas-Cortés, J.A., Zarco-Tejada, P.J., Beck, P.S.A. *Monitoring the impact of Xylella on Apulia' s olive orchards using Sentinel-2 satellite data and aerial photographs*. "Risk assessment and impact assessment" session on the 2nd EU conference on *Xylella fastidiosa*. 29th - 30th October 2019, Ajaccio, Corsica.

2021. Poblete, T., Navas-Cortes, J.A., Camino, C., Calderon, R., **Hornero, A.**, Gonzalez-Dugo, V., Landa, B.B., Zarco-Tejada, P.J. *Using hyperspectral imagery and a multi-stage machine learning algorithm to distinguish infection symptoms caused by two xylem-limited pathogens*. 3rd EU conference on *Xylella fastidiosa*. 29th - 30th April 2021, online.

2021. Zarco-Tejada, P.J., Poblete, T., Camino, C., Calderon, R., **Hornero, A.**, Hernández-Clemente, R., Kattenborn, T., Montes-Borrego, M., Román-Écija, M., Velasco-Amo, M.P., Susca, L., Morelli, M., Gonzalez-Dugo, V., Landa, B.B., Beck, P.S.A., Boscia, D., Saponari, M., Navas-Cortes, J.A. *Progress and achievements on the early detection of Xylella fastidiosa infection and symptom development with hyperspectral and thermal remote sensing imagery*. 3rd EU conference on *Xylella fastidiosa*. 29th - 30th April 2021, online.

2021. Belwalkar, A., Poblete, T., Longmire, A., **Hornero, A.**, Zarco-Tejada, P.J. *Comparing the retrieval of chlorophyll fluorescence from two airborne hyperspectral imagers with different spectral resolutions for plant phenotyping studies*. International Geoscience and Remote Sensing Symposium, IGARSS. 11th - 16th July 2021, Brussels, Belgium.

Bibliography

Ahl, D.E., Gower, S.T., Burrows, S.N., Shabanov, N.V., Myneni, R.B., Knyazikhin, Y., 2006. Monitoring spring canopy phenology of a deciduous broadleaf forest using MODIS. Remote Sensing of Environment 104, 88–95. https://doi.org/10.1016/j.rse.2006.05.003

Ahrens, C.W., Andrew, M.E., Mazanec, R.A., Ruthrof, K.X., Challis, A., Hardy, G., Byrne, M., Tissue, D.T., Rymer, P.D., 2020. Plant functional traits differ in adaptability and are predicted to be differentially affected by climate change. Ecology and Evolution 10, 232–248. https://doi.org/10.1002/ece3.5890

Allen, C.D., Breshears, D.D., McDowell, N.G., 2015. On underestimation of global vulnerability to tree mortality and forest die-off from hotter drought in the Anthropocene. Ecosphere 6, art129. https://doi.org/10.1890/ES15-00203.1

Allen, C.D., Macalady, A.K., Chenchouni, H., Bachelet, D., McDowell, N., Vennetier, M., Kitzberger, T., Rigling, A., Breshears, D.D., Hogg, E.H. (T.), Gonzalez, P., Fensham, R., Zhang, Z., Castro, J., Demidova, N., Lim, J.-H., Allard, G., Running, S.W., Semerci, A., Cobb, N., 2010. A global overview of drought and heat-induced tree mortality reveals emerging climate change risks for forests. Forest Ecology and Management 259, 25. https://doi.org/10.1016/j.foreco.2009.09.001

Almeida, R.P.P., Nunney, L., 2015. How Do Plant Diseases Caused by Xylella fastidiosa Emerge? Plant Disease 99, 1457–1467. https://doi.org/10.1094/PDIS-02-15-0159-FE

Alonso, L., Gomez-Chova, L., Vila-Frances, J., Amoros-Lopez, J., Guanter, L., Calpe, J., Moreno, J., 2008. Improved Fraunhofer Line Discrimination Method for Vegetation Fluorescence Quantification. IEEE Geoscience and Remote Sensing Letters 5, 620–624. https://doi.org/10.1109/LGRS.2008.2001180

Araya-López, R.A., Lopatin, J., Fassnacht, F.E., Hernández, H.J., 2018. Monitoring Andean high altitude wetlands in central Chile with seasonal optical data: A comparison between Worldview-2 and Sentinel-2 imagery. ISPRS Journal of Photogrammetry and Remote Sensing. https://doi.org/10.1016/j.isprsjprs.2018.04.001

Assal, T.J., Anderson, P.J., Sibold, J., 2016. Spatial and temporal trends of drought effects in a heterogeneous semi-arid forest ecosystem. Forest Ecology and Management 365, 137–151. https://doi.org/10.1016/j.foreco.2016.01.017

Atherton, J., Liu, W., Porcar-Castell, A., 2019. Nocturnal Light Emitting Diode Induced Fluorescence (LEDIF): A new technique to measure the chlorophyll a fluorescence emission spectral distribution of plant canopies in situ. Remote Sensing of Environment 231, 111137. https://doi.org/10.1016/j.rse.2019.03.030

Atzberger, C., Richter, K., 2012. Spatially constrained inversion of radiative transfer models for improved LAI mapping from future Sentinel-2 imagery. Remote Sensing of Environment, The Sentinel Missions - New Opportunities for Science 120, 208–218. https://doi.org/10.1016/j.rse.2011.10.035

Badgley, G., Field, C.B., Berry, J.A., 2017. Canopy near-infrared reflectance and terrestrial photosynthesis. Sci Adv 3, e1602244. https://doi.org/10.1126/sciadv.1602244

Bannari, A., Morin, D., Bonn, F., Huete, A.R., 1995. A review of vegetation indices. Remote Sensing Reviews 13, 95–120. https://doi.org/10.1080/02757259509532298

Bao, Y., Xu, K., Min, J., Xu, J., 2013. Estimating Wheat Shoot Nitrogen Content at Vegetative Stage from In Situ Hyperspectral Measurements. Crop Science 53, 2063–2071. https://doi.org/10.2135/cropsci2013.01.0012

Baquedano, F.J., Castillo, F.J., 2007. Drought tolerance in the Mediterranean species Quercus coccifera, Quercus ilex, Pinus halepensis, and Juniperus phoenicea. Photosynthetica 45, 229. https://doi.org/10.1007/s11099-007-0037-x

Baret, F., Guyot, G., 1991. Potentials and limits of vegetation indices for LAI and APAR assessment. Remote Sensing of Environment 35, 161–173. https://doi.org/10.1016/0034-4257(91)90009-U

Barnes, J.D., Balaguer, L., Manrique, E., Elvira, S., Davison, A.W., 1992. A reappraisal of the use of DMSO for the extraction and determination of chlorophylls a and b in lichens and higher plants. Environmental and Experimental Botany 32, 85–100. https://doi.org/10.1016/0098-8472(92)90034-Y

Bayat, B., van der Tol, C., Verhoef, W., 2016. Remote Sensing of Grass Response to Drought Stress Using Spectroscopic Techniques and Canopy Reflectance Model Inversion. Remote Sensing 8, 557. https://doi.org/10.3390/rs8070557

Beck, P.S.A., Juday, G.P., Alix, C., Barber, V.A., Winslow, S.E., Sousa, E.E., Heiser, P., Herriges, J.D., Goetz, S.J., 2011. Changes in forest productivity across Alaska consistent with biome shift. Ecology Letters 14, 373–379. https://doi.org/10.1111/j.1461-0248.2011.01598.x

Berjón, A.J., Cachorro, V.E., Zarco-Tejada, P.J., de Frutos, A., 2013. Retrieval of biophysical vegetation parameters using simultaneous inversion of high resolution remote sensing imagery constrained by a vegetation index. Precision Agric 14, 541–557. https://doi.org/10.1007/s11119-013-9315-8

Blackburn, G.A., 1998. Spectral indices for estimating photosynthetic pigment concentrations: A test using senescent tree leaves. International Journal of Remote Sensing 19, 657–675. https://doi.org/10.1080/014311698215919

Bogdanovich, E., Perez-Priego, O., El-Madany, T.S., Guderle, M., Pacheco-Labrador, J., Levick, S.R., Moreno, G., Carrara, A., Pilar Martín, M., Migliavacca, M., 2021. Using terrestrial laser scanning for characterizing tree structural parameters and their changes under different management in a Mediterranean open woodland. Forest Ecology and Management 486, 118945. https://doi.org/10.1016/j.foreco.2021.118945

Breiman, L., 2001. Random Forests. Machine Learning 45, 5–32. https://doi.org/10.1023/A:1010933404324

Brilli, L., Chiesi, M., Maselli, F., Moriondo, M., Gioli, B., Toscano, P., Zaldei, A., Bindi, M., 2013. Simulation of olive grove gross primary production by the combination of ground and multi-sensor satellite data. International Journal of Applied Earth Observation and Geoinformation 23, 29–36. https://doi.org/10.1016/j.jag.2012.11.006

Broge, N.H., Leblanc, E., 2001. Comparing prediction power and stability of broadband and hyperspectral vegetation indices for estimation of green leaf area index and canopy chlorophyll density. Remote Sensing of Environment 76, 156–172. https://doi.org/10.1016/S0034-4257(00)00197-8

Burgess, T.I., Scott, J.K., Mcdougall, K.L., Stukely, M.J.C., Crane, C., Dunstan, W.A., Brigg, F., Andjic, V., White, D., Rudman, T., Arentz, F., Ota, N., Hardy, G.E.S.J., 2017. Current and projected global distribution of Phytophthora cinnamomi, one of the world's worst plant pathogens. Global Change Biology 23, 1661–1674. https://doi.org/10.1111/gcb.13492

Bye, I.J., North, P.R.J., Los, S.O., Kljun, N., Rosette, J.A.B., Hopkinson, C., Chasmer, L., Mahoney, C., 2017. Estimating forest canopy parameters from satellite waveform LiDAR by inversion of the FLIGHT three-dimensional radiative transfer model. Remote Sensing of Environment 188, 177–189. https://doi.org/10.1016/j.rse.2016.10.048

Calderón, R., Navas-Cortés, J.A., Zarco-Tejada, P.J., 2015. Early Detection and Quantification of Verticillium Wilt in Olive Using Hyperspectral and Thermal Imagery over Large Areas. Remote Sensing 7, 5584–5610. https://doi.org/10.3390/rs70505584

Camarero, J.J., Gazol, A., Sangüesa-Barreda, G., Oliva, J., Vicente-Serrano, S.M., 2015. To die or not to die: early warnings of tree dieback in response to a severe drought. J Ecol 103, 44–57. https://doi.org/10.1111/1365-2745.12295

Camarero, J.J., Olano, J.M., Arroyo Alfaro, S.J., Fernández-Marín, B., Becerril, J.M., García-Plazaola, J.I., 2012. Photoprotection mechanisms in Quercus ilex under contrasting climatic conditions. Flora - Morphology, Distribution, Functional Ecology of Plants 207, 557–564. https://doi.org/10.1016/j.flora.2012.06.003

Camino, C., González-Dugo, V., Hernández, P., Sillero, J.C., Zarco-Tejada, P.J., 2018. Improved nitrogen retrievals with airborne-derived fluorescence and plant traits quantified from VNIR-SWIR hyperspectral imagery in the context of precision agriculture. International Journal of Applied Earth Observation and Geoinformation 70, 105–117. https://doi.org/10.1016/j.jag.2018.04.013

Camino, C., Gonzalez-Dugo, V., Hernandez, P., Zarco-Tejada, P.J., 2019. Radiative transfer Vcmax estimation from hyperspectral imagery and

SIF retrievals to assess photosynthetic performance in rainfed and irrigated plant phenotyping trials. Remote Sensing of Environment 231, 111186. https://doi.org/10.1016/j.rse.2019.05.005

Carter, G.A., 1994. Ratios of leaf reflectances in narrow wavebands as indicators of plant stress. International Journal of Remote Sensing 15, 697–703. https://doi.org/10.1080/01431169408954109

Carvajal-Yepes, M., Cardwell, K., Nelson, A., Garrett, K.A., Giovani, B., Saunders, D.G.O., Kamoun, S., Legg, J.P., Verdier, V., Lessel, J., Neher, R.A., Day, R., Pardey, P., Gullino, M.L., Records, A.R., Bextine, B., Leach, J.E., Staiger, S., Tohme, J., 2019. A global surveillance system for crop diseases. Science 364, 1237–1239. https://doi.org/10.1126/science.aaw1572

Castillo, J.A.A., Apan, A.A., Maraseni, T.N., Salmo, S.G., 2017. Estimation and mapping of above-ground biomass of mangrove forests and their replacement land uses in the Philippines using Sentinel imagery. ISPRS Journal of Photogrammetry and Remote Sensing 134, 70–85. https://doi.org/10.1016/j.isprsjprs.2017.10.016

Castrignano, A., Buttafuoco, G., Khosla, R., Mouazen, A., Moshou, D., Naud, O. (Eds.), 2020. Agricultural internet of things and decision support for precision smart farming, 1st ed. Elsevier, Cambridge.

Ceccato, P., Flasse, S., Tarantola, S., Jacquemoud, S., Grégoire, J.-M., 2001. Detecting vegetation leaf water content using reflectance in the optical domain. Remote Sensing of Environment 77, 22–33. https://doi.org/10.1016/S0034-4257(01)00191-2

Celesti, M., Biriukova, K., Campbell, P.K.E., Cesana, I., Cogliati, S., Damm, A., Drusch, M., Julitta, T., Middleton, E., Migliavacca, M., Miglietta, F., Panigada, C., Rascher, U., Rossini, M., Schuettemeyer, D., Tagliabue, G., van der Tol, C., Verrelst, J., Yang, P., Colombo, R., 2019. Exploring continuous time series of vegetation hyperspectral reflectance and solar-induced fluorescence through radiative transfer model inversion. Presented at the AGU Fall Meeting 2019, AGU.

Cendrero-Mateo, M.P., Moran, M.S., Papuga, S.A., Thorp, K.R., Alonso, L., Moreno, J., Ponce-Campos, G., Rascher, U., Wang, G., 2016. Plant chlorophyll fluorescence: active and passive measurements at canopy and leaf scales with different nitrogen treatments. J Exp Bot 67, 275–286. https://doi.org/10.1093/jxb/erv456

Chappelle, E.W., Kim, M.S., McMurtrey, J.E., 1992. Ratio analysis of reflectance spectra (RARS): An algorithm for the remote estimation of the concentrations of chlorophyll A, chlorophyll B, and carotenoids in soybean leaves. Remote Sensing of Environment 39, 239–247. https://doi.org/10.1016/0034-4257(92)90089-3

Chen, H., Liu, X., Ding, C., Huang, F., 2018. Phenology-Based Residual Trend Analysis of MODIS-NDVI Time Series for Assessing Human-Induced Land Degradation. Sensors 18, 3676. https://doi.org/10.3390/s18113676

Chen, J.M., 1996. Evaluation of Vegetation Indices and a Modified Simple Ratio for Boreal Applications. Canadian Journal of Remote Sensing 22, 229–242. https://doi.org/10.1080/07038992.1996.10855178

Chen, P., Haboudane, D., Tremblay, N., Wang, J., Vigneault, P., Li, B., 2010. New spectral indicator assessing the efficiency of crop nitrogen treatment in corn and wheat. Remote Sensing of Environment 114, 1987–1997. https://doi.org/10.1016/j.rse.2010.04.006

Cicchetti, D.V., Sparrow, S.A., 1981. Developing criteria for establishing interrater reliability of specific items: Applications to assessment of adaptive behavior. American Journal of Mental Deficiency 86, 127–137.

Cleveland, W.S., Grosse, E., Shyu, W.M., 1992. Local regression models. Statistical models in S 2, 309–376.

Colangelo, M., Camarero, J.J., Borghetti, M., Gentilesca, T., Oliva, J., Redondo, M.-A., Ripullone, F., 2018. Drought and Phytophthora Are Associated With the Decline of Oak Species in Southern Italy. Front. Plant Sci. 9. https://doi.org/10.3389/fpls.2018.01595

Combal, B., Baret, F., Weiss, M., Trubuil, A., Macé, D., Pragnère, A., Myneni, R., Knyazikhin, Y., Wang, L., 2003. Retrieval of canopy biophysical variables from bidirectional reflectance: Using prior information to solve the ill-posed inverse problem. Remote Sensing of Environment 84, 1–15. https://doi.org/10.1016/S0034-4257(02)00035-4

Commission Implementing Decision (EU) 2018/927 of 27 June 2018 amending Implementing Decision (EU) 2015/789 as regards measures to prevent the introduction into and the spread within the Union of Xylella fastidiosa (Wells et al.) (notified under document C(2018) 3972), 2018. , OJ L.

Consejería de Medio Ambiente y Ordenación del Territorio, 2018. Manual para el establecimiento y la evaluación de las parcelas de la Red Andaluza de Seguimiento de Daños sobre Ecosistemas Forestales: Red SEDA y Red de PINSAPO. Junta de Andalucía.

Cunniffe, N.J., Cobb, R.C., Meentemeyer, R.K., Rizzo, D.M., Gilligan, C.A., 2016. Modeling when, where, and how to manage a forest epidemic, motivated by sudden oak death in California. PNAS 113, 5640–5645. https://doi.org/10.1073/pnas.1602153113

Damm, A., Guanter, L., Paul-Limoges, E., van der Tol, C., Hueni, A., Buchmann, N., Eugster, W., Ammann, C., Schaepman, M.E., 2015. Far-red sun-induced chlorophyll fluorescence shows ecosystem-specific relationships to gross primary production: An assessment based on observational and modeling approaches. Remote Sensing of Environment 166, 91–105. https://doi.org/10.1016/j.rse.2015.06.004

Dash, J., Curran, P.J., 2007. Evaluation of the MERIS terrestrial chlorophyll index (MTCI). Advances in Space Research 39, 100–104. https://doi.org/10.1016/j.asr.2006.02.034

Datt, B., 1998. Remote Sensing of Chlorophyll a, Chlorophyll b, Chlorophyll a+b, and Total Carotenoid Content in Eucalyptus Leaves. Remote Sensing of Environment 66, 111–121. https://doi.org/10.1016/S0034-4257(98)00046-7

Dechant, B., Ryu, Y., Badgley, G., Zeng, Y., Berry, J.A., Zhang, Y., Goulas, Y., Li, Z., Zhang, Q., Kang, M., Li, J., Moya, I., 2020. Canopy structure explains the relationship between photosynthesis and sun-induced chlorophyll fluorescence in crops. Remote Sensing of Environment 241, 111733. https://doi.org/10.1016/j.rse.2020.111733

Delegido, J., Verrelst, J., Alonso, L., Moreno, J., 2011. Evaluation of Sentinel-2 Red-Edge Bands for Empirical Estimation of Green LAI and Chlorophyll Content. Sensors 11, 7063–7081. https://doi.org/10.3390/s110707063

Dormann, C.F., Elith, J., Bacher, S., Buchmann, C., Carl, G., Carré, G., Marquéz, J.R.G., Gruber, B., Lafourcade, B., Leitão, P.J., Münkemüller, T., McClean, C., Osborne, P.E., Reineking, B., Schröder, B., Skidmore, A.K., Zurell, D., Lautenbach, S., 2013. Collinearity: a review of methods to deal with it and a simulation study evaluating their performance. Ecography 36, 27–46. https://doi.org/10.1111/j.1600-0587.2012.07348.x

Duveiller, G., Filipponi, F., Walther, S., Köhler, P., Frankenberg, C., Guanter, L., Cescatti, A., 2020. A spatially downscaled sun-induced fluorescence global product for enhanced monitoring of vegetation productivity. Earth System Science Data 12, 1101–1116. https://doi.org/10.5194/essd-12-1101-2020

EFSA, 2018. Updated pest categorisation of Xylella fastidiosa. EFSA Journal 16, e05357. https://doi.org/10.2903/j.efsa.2018.5357

Eichhorn, J., Roskams, P., Potočić, N., Timmermann, V., Ferretti, M., Mues, V., Szepesi, A., Durrant, D., Seletković, I., Schroeck, H.-W., Nevalnien, S., Filippo Bussotti, García, P., Wulff, S., 2017. Part IV: Visual assessment of crown condition and damaging agents., in: UNECE ICP Forests Programme Co-ordinating Centre. Manual on methods and criteria for harmonized sampling, assessment, monitoring and analysis of the effects of air pollution on forests. Thünen Institute of Forest Ecosystems, Eberswalde, Germany, p. 54.

Ennos, R.A., 2015. Resilience of forests to pathogens: an evolutionary ecology perspective. Forestry (Lond) 88, 41–52. https://doi.org/10.1093/forestry/cpu048

EPPO, 2019. First report of Xylella fastidiosa in Israel. EPPO Reporting Service no. 6, Global Database [WWW Document]. URL https://gd.eppo.int/reporting/article-6551 (accessed 9.16.19).

Eriksson, H.M., Eklundh, L., Kuusk, A., Nilson, T., 2006. Impact of understory vegetation on forest canopy reflectance and remotely sensed LAI estimates. Remote Sensing of Environment 103, 408–418. https://doi.org/10.1016/j.rse.2006.04.005

Fang, X., Zhu, Q., Ren, L., Chen, H., Wang, K., Peng, C., 2018. Large-scale detection of vegetation dynamics and their potential drivers using MODIS images and BFAST: A case study in Quebec, Canada. Remote Sensing of Environment 206, 391–402. https://doi.org/10.1016/j.rse.2017.11.017

Feret, J.-B., François, C., Asner, G.P., Gitelson, A.A., Martin, R.E., Bidel, L.P.R., Ustin, S.L., le Maire, G., Jacquemoud, S., 2008. PROSPECT-4 and 5: Advances in the leaf optical properties model separating photosynthetic pigments. Remote Sensing of Environment 112, 3030–3043. https://doi.org/10.1016/j.rse.2008.02.012

Feret, J.-B., Gitelson, A., Noble, S.D., Jacquemoud, S., 2017. PROSPECT-D: Towards modeling leaf optical properties through a complete

lifecycle. Remote Sensing of Environment 193, 204–215. https://doi.org/10.1016/j.rse.2017.03.004

Fernández i Marti, A., Romero-Rodríguez, C., Navarro-Cerrillo, R.M., Abril, N., Jorrín-Novo, J.V., Dodd, R.S., 2018. Population Genetic Diversity of Quercus ilex subsp. ballota (Desf.) Samp. Reveals Divergence in Recent and Evolutionary Migration Rates in the Spanish Dehesas. Forests 9, 337. https://doi.org/10.3390/f9060337

Ferwerda, J.G., Skidmore, A.K., Mutanga, O., 2005. Nitrogen detection with hyperspectral normalized ratio indices across multiple plant species. International Journal of Remote Sensing 26, 4083–4095. https://doi.org/10.1080/01431160500181044

Forkuor, G., Dimobe, K., Serme, I., Tondoh, J.E., 2018. Landsat-8 vs. Sentinel-2: examining the added value of sentinel-2's red-edge bands to land-use and land-cover mapping in Burkina Faso. GIScience & Remote Sensing 55, 331–354. https://doi.org/10.1080/15481603.2017.1370169

Forzieri, G., Girardello, M., Ceccherini, G., Spinoni, J., Feyen, L., Hartmann, H., Beck, P.S.A., Camps-Valls, G., Chirici, G., Mauri, A., Cescatti, A., 2021. Emergent vulnerability to climate-driven disturbances in European forests. Nature Communications 12, 1081. https://doi.org/10.1038/s41467-021-21399-7

Frampton, W.J., Dash, J., Watmough, G.R., Milton, E.J., 2013. Evaluating the capabilities of Sentinel-2 for quantitative estimation of biophysical variables in vegetation. ISPRS Journal of Photogrammetry and Remote Sensing 82, 83–92. https://doi.org/10.1016/j.isprsjprs.2013.04.007

Frankenberg, C., Fisher, J.B., Worden, J., Badgley, G., Saatchi, S.S., Lee, J.-E., Toon, G.C., Butz, A., Jung, M., Kuze, A., Yokota, T., 2011. New global observations of the terrestrial carbon cycle from GOSAT: Patterns of plant fluorescence with gross primary productivity. Geophys. Res. Lett. 38, L17706. https://doi.org/10.1029/2011GL048738

Früchtenicht, E., Klein, N., Brüggemann, W., 2018. Response of Quercus robur and two potential climate change winners – Quercus pubescens and Quercus ilex – to two years summer drought in a semi-controlled competition study: II — Photosynthetic efficiency. Environmental and Experimental Botany, Experiments with trees: from seedlings to

ecosystems 152, 118–127. https://doi.org/10.1016/j.envexpbot.2018.03.019

Fuente, B. de la, Saura, S., Beck, P.S.A., 2018. Predicting the spread of an invasive tree pest: The pine wood nematode in Southern Europe. Journal of Applied Ecology 55, 2374–2385. https://doi.org/10.1111/1365-2664.13177

Gamon, J.A., Peñuelas, J., Field, C.B., 1992. A narrow-waveband spectral index that tracks diurnal changes in photosynthetic efficiency. Remote Sensing of Environment 41, 35–44. https://doi.org/10.1016/0034-4257(92)90059-S

Gamon, J.A., Surfus, J.S., 1999. Assessing leaf pigment content and activity with a reflectometer. New Phytologist 143, 105–117. https://doi.org/10.1046/j.1469-8137.1999.00424.x

Gao, B., 1996. NDWI—A normalized difference water index for remote sensing of vegetation liquid water from space. Remote Sensing of Environment 58, 257–266. https://doi.org/10.1016/S0034-4257(96)00067-3

Garrity, S.R., Eitel, J.U.H., Vierling, L.A., 2011. Disentangling the relationships between plant pigments and the photochemical reflectance index reveals a new approach for remote estimation of carotenoid content. Remote Sensing of Environment 115, 628–635. https://doi.org/10.1016/j.rse.2010.10.007

Gastellu-Etchegorry, J., Lauret, N., Yin, T., Landier, L., Kallel, A., Malenovský, Z., Bitar, A.A., Aval, J., Benhmida, S., Qi, J., Medjdoub, G., Guilleux, J., Chavanon, E., Cook, B., Morton, D., Chrysoulakis, N., Mitraka, Z., 2017. DART: Recent Advances in Remote Sensing Data Modeling With Atmosphere, Polarization, and Chlorophyll Fluorescence. IEEE Journal of Selected Topics in Applied Earth Observations and Remote Sensing 10, 2640–2649. https://doi.org/10.1109/JSTARS.2017.2685528

Gastellu-Etchegorry, J.P., Demarez, V., Pinel, V., Zagolski, F., 1996. Modeling radiative transfer in heterogeneous 3-D vegetation canopies. Remote Sensing of Environment 58, 131–156. https://doi.org/10.1016/0034-4257(95)00253-7

Gigović, L., Pourghasemi, H.R., Drobnjak, S., Bai, S., 2019. Testing a New Ensemble Model Based on SVM and Random Forest in Forest Fire

Susceptibility Assessment and Its Mapping in Serbia's Tara National Park. Forests 10, 408. https://doi.org/10.3390/f10050408

Gillespie, T.W., Ostermann-Kelm, S., Dong, C., Willis, K.S., Okin, G.S., MacDonald, G.M., 2018. Monitoring changes of NDVI in protected areas of southern California. Ecological Indicators 88, 485–494. https://doi.org/10.1016/j.ecolind.2018.01.031

Girelli, C.R., Coco, L.D., Scortichini, M., Petriccione, M., Zampella, L., Mastrobuoni, F., Cesari, G., Bertaccini, A., D'Amico, G., Contaldo, N., Migoni, D., Fanizzi, F.P., 2017. Xylella fastidiosa and olive quick decline syndrome (CoDiRO) in Salento (southern Italy): a chemometric 1H NMR-based preliminary study on Ogliarola salentina and Cellina di Nardò cultivars. Chem. Biol. Technol. Agric. 4, 25. https://doi.org/10.1186/s40538-017-0107-7

Gitelson, A.A., Merzlyak, M., Zur, Y., Stark, R., Gritz, U., 2001. Non-destructive and remote sensing techniques for estimation of vegetation status. Papers in Natural Resources.

Gitelson, A.A., Gritz, Y., Merzlyak, M.N., 2003. Relationships between leaf chlorophyll content and spectral reflectance and algorithms for non-destructive chlorophyll assessment in higher plant leaves. Journal of Plant Physiology 160, 271–282. https://doi.org/10.1078/0176-1617-00887

Gitelson, A.A., Kaufman, Y.J., Merzlyak, M.N., 1996. Use of a green channel in remote sensing of global vegetation from EOS-MODIS. Remote Sensing of Environment 58, 289–298. https://doi.org/10.1016/S0034-4257(96)00072-7

Gitelson, A.A., Keydan, G.P., Merzlyak, M.N., 2006. Three-band model for noninvasive estimation of chlorophyll, carotenoids, and anthocyanin contents in higher plant leaves. Geophys. Res. Lett. 33, L11402. https://doi.org/10.1029/2006GL026457

Gitelson, A.A., Merzlyak, M.N., 1996. Signature Analysis of Leaf Reflectance Spectra: Algorithm Development for Remote Sensing of Chlorophyll. Journal of Plant Physiology 148, 494–500. https://doi.org/10.1016/S0176-1617(96)80284-7

Gitelson, A.A., Yacobi, Y.Z., Schalles, J.E., Rundquist, D.C., Han, L., Stark, R., Etzion, D., 2000. Remote Estimation of Phytoplankton Density in Productive Waters. Arch. HydrobioI. Spec. Issues Advanc. Limnol. Limnology and Lake Management 2000+ 55, 121–136.

Gitelson, A.A., Zur, Y., Chivkunova, O.B., Merzlyak, M.N., 2002. Assessing Carotenoid Content in Plant Leaves with Reflectance Spectroscopy. Photochemistry and Photobiology 75, 272–281. https://doi.org/10.1562/0031-8655(2002)0750272ACCIPL2.0.CO2

Gnyp, M.L., Bareth, G., Li, F., Lenz-Wiedemann, V.I.S., Koppe, W., Miao, Y., Hennig, S.D., Jia, L., Laudien, R., Chen, X., Zhang, F., 2014. Development and implementation of a multiscale biomass model using hyperspectral vegetation indices for winter wheat in the North China Plain. International Journal of Applied Earth Observation and Geoinformation 33, 232–242. https://doi.org/10.1016/j.jag.2014.05.006

Gómez Calero, J.A., Zarco-Tejada, P.J., García-Morillo, J., Gama, J., Soriano, M.A., 2011. Determining biophysical parameters for olive trees using CASI-airborne and QuickBird-satellite imagery. https://doi.org/10.2134/agronj2010.0449

Gonzalez-Cascon, M. del R., Jiménez, L.S., Fillola, I.V., Santafe, M.M., 2017. Aqueous-acetone extraction improves the drawbacks of using dimethylsulfoxide as solvent for photometric pigment quantification in Quercus ilex leaves. Forest systems 26, 5.

Gonzalez-Cascon, R., Martin, M.P., 2018. Protocol for pigment content quantification in herbaceous covers: sampling and analysis. Life Sciences Protocol Repository: PROTOCOLS.IO. https://doi.org/10.17504/protocols.io.qs6dwhe

Gonzalez-Dugo, V., Zarco-Tejada, P.J., Fereres, E., 2014. Applicability and limitations of using the crop water stress index as an indicator of water deficits in citrus orchards. Agricultural and Forest Meteorology 198–199, 94–104. https://doi.org/10.1016/j.agrformet.2014.08.003

Gonzalez-Dugo, V., Zarco-Tejada, P.J., Intrigliolo, D.S., Ramírez-Cuesta, J.-M., 2020. Normalization of the crop water stress index to assess the within-field spatial variability of water stress sensitivity. Precision Agric. https://doi.org/10.1007/s11119-020-09768-6

Govaerts, Y.M., Verstraete, M.M., 1998. Raytran: a Monte Carlo ray-tracing model to compute light scattering in three-dimensional heterogeneous media. IEEE Transactions on Geoscience and Remote Sensing 36, 493–505. https://doi.org/10.1109/36.662732

Gualtieri, A.G., Chettri, S., Cromp, R., Johnson, L., 1999. Support Vector Machine Classifiers as Applied to AVIRIS Data [WWW Document].

URL /paper/Support-Vector-Machine-Classifiers-as-Applied-to-Gualtieri-Chettri/83e3788925a7a78bcc89a4540c8808f8e2b7acb0 (accessed 11.16.20).

Guanter, L., Frankenberg, C., Dudhia, A., Lewis, P.E., Gómez-Dans, J., Kuze, A., Suto, H., Grainger, R.G., 2012. Retrieval and global assessment of terrestrial chlorophyll fluorescence from GOSAT space measurements. Remote Sensing of Environment 121, 236–251. https://doi.org/10.1016/j.rse.2012.02.006

Gueymard, C., 1995. SMARTS2: a simple model of the atmospheric radiative transfer of sunshine: algorithms and performance assessment. Florida Solar Energy Center Cocoa, FL.

Gueymard, C.A., 2001. Parameterized transmittance model for direct beam and circumsolar spectral irradiance. Solar Energy 71, 325–346. https://doi.org/10.1016/S0038-092X(01)00054-8

Guillen-Climent, M.L., Zarco-Tejada, P.J., Berni, J.A.J., North, P.R.J., Villalobos, F.J., 2012. Mapping radiation interception in row-structured orchards using 3D simulation and high-resolution airborne imagery acquired from a UAV. Precision Agric 13, 473–500. https://doi.org/10.1007/s11119-012-9263-8

Haboudane, D., Miller, J.R., Pattey, E., Zarco-Tejada, P.J., Strachan, I.B., 2004. Hyperspectral vegetation indices and novel algorithms for predicting green LAI of crop canopies: Modeling and validation in the context of precision agriculture. Remote Sensing of Environment 90, 337–352. https://doi.org/10.1016/j.rse.2003.12.013

Haboudane, D., Miller, J.R., Tremblay, N., Zarco-Tejada, P.J., Dextraze, L., 2002. Integrated narrow-band vegetation indices for prediction of crop chlorophyll content for application to precision agriculture. Remote Sensing of Environment 81, 416–426. https://doi.org/10.1016/S0034-4257(02)00018-4

Haboudane, D., Tremblay, N., Miller, J.R., Vigneault, P., 2008. Remote Estimation of Crop Chlorophyll Content Using Spectral Indices Derived From Hyperspectral Data. IEEE Transactions on Geoscience and Remote Sensing 46, 423–437. https://doi.org/10.1109/TGRS.2007.904836

Hanan, N.P., Hill, M.J., 2012. Savannas in a Changing Earth System. The NASA Terrestrial Ecology Tree-Grass Project (Commissioned White

Paper submitted to NASA Terrestrial Ecology Program). South Dakota State University and The University of North Dakota.

Hay, S.I., Tatem, A.J., Graham, A.J., Goetz, S.J., Rogers, D.J., 2006. Global environmental data for mapping infectious disease distribution. Adv. Parasitol. 62, 37–77. https://doi.org/10.1016/S0065-308X(05)62002-7

Haynes, W., 2013. Bonferroni Correction, in: Encyclopedia of Systems Biology. Springer, New York, NY, pp. 154–154. https://doi.org/10.1007/978-1-4419-9863-7_1213

Hernández-Clemente, R., Hornero, A., Mottus, M., Penuelas, J., González-Dugo, V., Jiménez, J.C., Suárez, L., Alonso, L., Zarco-Tejada, P.J., 2019. Early Diagnosis of Vegetation Health From High-Resolution Hyperspectral and Thermal Imagery: Lessons Learned From Empirical Relationships and Radiative Transfer Modelling. Current Forestry Reports 5, 169–183. https://doi.org/10.1007/s40725-019-00096-1

Hernández-Clemente, R., Navarro-Cerrillo, R.M., Ramírez, F.J.R., Hornero, A., Zarco-Tejada, P.J., 2014. A Novel Methodology to Estimate Single-Tree Biophysical Parameters from 3D Digital Imagery Compared to Aerial Laser Scanner Data. Remote Sensing 6, 11627–11648. https://doi.org/10.3390/rs61111627

Hernández-Clemente, R., Navarro-Cerrillo, R.M., Suárez, L., Morales, F., Zarco-Tejada, P.J., 2011. Assessing structural effects on PRI for stress detection in conifer forests. Remote Sensing of Environment 115, 2360–2375. https://doi.org/10.1016/j.rse.2011.04.036

Hernandez-Clemente, R., Navarro-Cerrillo, R.M., Zarco-Tejada, P.J., 2014. Deriving Predictive Relationships of Carotenoid Content at the Canopy Level in a Conifer Forest Using Hyperspectral Imagery and Model Simulation. IEEE Transactions on Geoscience and Remote Sensing 52, 5206–5217. https://doi.org/10.1109/TGRS.2013.2287304

Hernández-Clemente, R., Navarro-Cerrillo, R.M., Zarco-Tejada, P.J., 2012. Carotenoid content estimation in a heterogeneous conifer forest using narrow-band indices and PROSPECT+DART simulations. Remote Sensing of Environment 127, 298–315. https://doi.org/10.1016/j.rse.2012.09.014

Hernández-Clemente, R., North, P.R.J., Hornero, A., Zarco-Tejada, P.J., 2017. Assessing the effects of forest health on sun-induced chlorophyll fluorescence using the FluorFLIGHT 3-D radiative transfer model to

account for forest structure. Remote Sensing of Environment 193, 165–179. https://doi.org/10.1016/j.rse.2017.02.012

Herrmann, I., Karnieli, A., Bonfil, D.J., Cohen, Y., Alchanatis, V., 2010. SWIR-based spectral indices for assessing nitrogen content in potato fields. International Journal of Remote Sensing 31, 5127–5143. https://doi.org/10.1080/01431160903283892

Herrmann, I., Pimstein, A., Karnieli, A., Cohen, Y., Alchanatis, V., Bonfil, D.J., 2011. LAI assessment of wheat and potato crops by VENμS and Sentinel-2 bands. Remote Sensing of Environment 115, 2141–2151. https://doi.org/10.1016/j.rse.2011.04.018

Hill, M.J., 2013. Vegetation index suites as indicators of vegetation state in grassland and savanna: An analysis with simulated SENTINEL 2 data for a North American transect. Remote Sensing of Environment 137, 94–111. https://doi.org/10.1016/j.rse.2013.06.004

Holben, B.N., Eck, T.F., Slutsker, I., Tanré, D., Buis, J.P., Setzer, A., Vermote, E., Reagan, J.A., Kaufman, Y.J., Nakajima, T., Lavenu, F., Jankowiak, I., Smirnov, A., 1998. AERONET—A Federated Instrument Network and Data Archive for Aerosol Characterization. Remote Sensing of Environment 66, 1–16. https://doi.org/10.1016/S0034-4257(98)00031-5

Homolová, L., Malenovský, Z., Clevers, J.G.P.W., García-Santos, G., Schaepman, M.E., 2013. Review of optical-based remote sensing for plant trait mapping. Ecological Complexity 15, 1–16. https://doi.org/10.1016/j.ecocom.2013.06.003

Hornero, A., Hernández-Clemente, R., North, P.R.J., Beck, P.S.A., Boscia, D., Navas-Cortes, J.A., Zarco-Tejada, P.J., 2020. Monitoring the incidence of Xylella fastidiosa infection in olive orchards using ground-based evaluations, airborne imaging spectroscopy and Sentinel-2 time series through 3-D radiative transfer modelling. Remote Sensing of Environment 236, 111480. https://doi.org/10.1016/j.rse.2019.111480

Hornero, A., North, P.R.J., Zarco-Tejada, P.J., Rascher, U., Martín, M.P., Migliavacca, M., Hernandez-Clemente, R., 2021. Assessing the contribution of understory sun-induced chlorophyll fluorescence through 3-D radiative transfer modelling and field data. Remote Sensing of Environment 253, 112195. https://doi.org/10.1016/j.rse.2020.112195

Horsfall, J.G., Cowling, E.B., 1978. Pathometry: the measurement of plant disease. Plant Disease: an Advanced Treatise.

Huete, A., Didan, K., Miura, T., Rodriguez, E.P., Gao, X., Ferreira, L.G., 2002. Overview of the radiometric and biophysical performance of the MODIS vegetation indices. Remote Sensing of Environment, The Moderate Resolution Imaging Spectroradiometer (MODIS): a new generation of Land Surface Monitoring 83, 195–213. https://doi.org/10.1016/S0034-4257(02)00096-2

Huete, A., Justice, C., Liu, H., 1994. Development of vegetation and soil indices for MODIS-EOS. Remote Sensing of Environment 49, 224–234. https://doi.org/10.1016/0034-4257(94)90018-3

Huete, A.R., 1988. A soil-adjusted vegetation index (SAVI). Remote Sensing of Environment 25, 295–309. https://doi.org/10.1016/0034-4257(88)90106-X

Huete, A.R., Jackson, R.D., Post, D.F., 1985. Spectral response of a plant canopy with different soil backgrounds. Remote Sensing of Environment 17, 37–53. https://doi.org/10.1016/0034-4257(85)90111-7

Hutchings, M., John, E., Stewart, A., 2000. The Ecological Consequences of Environmental Heterogeneity: 40th Symposium of the British Ecological Society.

InnovaPuglia Spa - Servizio Territorio e Ambiente, 2013. Uso del Suolo [WWW Document]. URL http://www.dataset.puglia.it/dataset/uso-del-suolo-2011-uds (accessed 9.2.18).

Jacquemoud, S., Baret, F., 1990. PROSPECT: A model of leaf optical properties spectra. Remote Sensing of Environment 34, 75–91. https://doi.org/10.1016/0034-4257(90)90100-Z

James, G., Witten, D., Hastie, T., Tibshirani, R., 2013. Classification, in: James, G., Witten, D., Hastie, T., Tibshirani, R. (Eds.), An Introduction to Statistical Learning: With Applications in R, Springer Texts in Statistics. Springer, New York, NY, pp. 127–173. https://doi.org/10.1007/978-1-4614-7138-7_4

Joiner, J., Yoshida, Y., Vasilkov, A.P., Schaefer, K., Jung, M., Guanter, L., Zhang, Y., Garrity, S., Middleton, E.M., Huemmrich, K.F., Gu, L., Belelli Marchesini, L., 2014. The seasonal cycle of satellite chlorophyll fluorescence observations and its relationship to vegetation phenology and ecosystem atmosphere carbon exchange. Remote Sensing of Environment 152, 375–391. https://doi.org/10.1016/j.rse.2014.06.022

Joiner, J., Yoshida, Y., Vasilkov, A.P., Yoshida, Y., Corp, L.A., Middleton, E.M., 2011. First observations of global and seasonal terrestrial

chlorophyll fluorescence from space. Biogeosciences 8, 637–651. https://doi.org/10.5194/bg-8-637-2011

Jordan, C.F., 1969. Derivation of Leaf-Area Index from Quality of Light on the Forest Floor. Ecology 50, 663–666. https://doi.org/10.2307/1936256

Jung, T., Blaschke, H., Osswald, W., 2000. Involvement of soilborne *Phytophthora* species in Central European oak decline and the effect of site factors on the disease. Plant Pathology 49, 706–718. https://doi.org/10.1046/j.1365-3059.2000.00521.x

Kallel, A., 2020. FluLCVRT: Reflectance and fluorescence of leaf and canopy modeling based on Monte Carlo vector radiative transfer simulation. Journal of Quantitative Spectroscopy and Radiative Transfer 253, 107183. https://doi.org/10.1016/j.jqsrt.2020.107183

Karnieli, A., Kaufman, Y.J., Remer, L., Wald, A., 2001. AFRI — aerosol free vegetation index. Remote Sensing of Environment 77, 10–21. https://doi.org/10.1016/S0034-4257(01)00190-0

Kattenborn, T., Fassnacht, F.E., Pierce, S., Lopatin, J., Grime, J.P., Schmidtlein, S., 2017. Linking plant strategies and plant traits derived by radiative transfer modelling. J Veg Sci 28, 717–727. https://doi.org/10.1111/jvs.12525

Kattge, J., Díaz, S., Lavorel, S., Prentice, I.C., Leadley, P., Bönisch, G., Garnier, E., Westoby, M., Reich, P.B., Wright, I.J., Cornelissen, J.H.C., Violle, C., Harrison, S.P., Bodegom, P.M.V., Reichstein, M., Enquist, B.J., Soudzilovskaia, N.A., Ackerly, D.D., Anand, M., Atkin, O., Bahn, M., Baker, T.R., Baldocchi, D., Bekker, R., Blanco, C.C., Blonder, B., Bond, W.J., Bradstock, R., Bunker, D.E., Casanoves, F., Cavender-Bares, J., Chambers, J.Q., Iii, F.S.C., Chave, J., Coomes, D., Cornwell, W.K., Craine, J.M., Dobrin, B.H., Duarte, L., Durka, W., Elser, J., Esser, G., Estiarte, M., Fagan, W.F., Fang, J., Fernández-Méndez, F., Fidelis, A., Finegan, B., Flores, O., Ford, H., Frank, D., Freschet, G.T., Fyllas, N.M., Gallagher, R.V., Green, W.A., Gutierrez, A.G., Hickler, T., Higgins, S.I., Hodgson, J.G., Jalili, A., Jansen, S., Joly, C.A., Kerkhoff, A.J., Kirkup, D., Kitajima, K., Kleyer, M., Klotz, S., Knops, J.M.H., Kramer, K., Kühn, I., Kurokawa, H., Laughlin, D., Lee, T.D., Leishman, M., Lens, F., Lenz, T., Lewis, S.L., Lloyd, J., Llusià, J., Louault, F., Ma, S., Mahecha, M.D., Manning, P., Massad, T., Medlyn, B.E., Messier, J., Moles, A.T.,

Müller, S.C., Nadrowski, K., Naeem, S., Niinemets, Ü., Nöllert, S., Nüske, A., Ogaya, R., Oleksyn, J., Onipchenko, V.G., Onoda, Y., Ordoñez, J., Overbeck, G., Ozinga, W.A., Patiño, S., Paula, S., Pausas, J.G., Peñuelas, J., Phillips, O.L., Pillar, V., Poorter, H., Poorter, L., Poschlod, P., Prinzing, A., Proulx, R., Rammig, A., Reinsch, S., Reu, B., Sack, L., Salgado-Negret, B., Sardans, J., Shiodera, S., Shipley, B., Siefert, A., Sosinski, E., Soussana, J.-F., Swaine, E., Swenson, N., Thompson, K., Thornton, P., Waldram, M., Weiher, E., White, M., White, S., Wright, S.J., Yguel, B., Zaehle, S., Zanne, A.E., Wirth, C., 2011. TRY – a global database of plant traits. Global Change Biology 17, 2905–2935. https://doi.org/10.1111/j.1365-2486.2011.02451.x

Kaufman, Y.J., Tanre, D., 1992. Atmospherically resistant vegetation index (ARVI) for EOS-MODIS. IEEE Transactions on Geoscience and Remote Sensing 30, 261–270. https://doi.org/10.1109/36.134076

Kobayashi, H., Ryu, Y., Baldocchi, D.D., Welles, J.M., Norman, J.M., 2013. On the correct estimation of gap fraction: How to remove scattered radiation in gap fraction measurements? Agricultural and Forest Meteorology 174–175, 170–183. https://doi.org/10.1016/j.agrformet.2013.02.013

Köhler, P., Frankenberg, C., Magney, T., Guanter, L., Joanna, J., Landgraf, J., 2018. Global Retrievals of Solar-Induced Chlorophyll Fluorescence With TROPOMI: First Results and Intersensor Comparison to OCO-2. Geophysical Research Letters 45. https://doi.org/10.1029/2018GL079031

Koller, S., Holland, V., Brüggemann, W., 2013. Effects of drought stress on the evergreen Quercus ilex L., the deciduous Q. robur L. and their hybrid Q. × turneri Willd. Photosynthetica 51, 574–582. https://doi.org/10.1007/s11099-013-0058-6

Korhonen, L., Korpela, I., Heiskanen, J., Maltamo, M., 2011. Airborne discrete-return LIDAR data in the estimation of vertical canopy cover, angular canopy closure and leaf area index. Remote Sensing of Environment 115, 1065–1080. https://doi.org/10.1016/j.rse.2010.12.011

Kötz, B., Schaepman, M., Morsdorf, F., Bowyer, P., Itten, K., Allgöwer, B., 2004. Radiative transfer modeling within a heterogeneous canopy for estimation of forest fire fuel properties. Remote Sensing of

Environment, Forest Fire Prevention and Assessment 92, 332–344. https://doi.org/10.1016/j.rse.2004.05.015

Kursa, M.B., Rudnicki, W.R., 2010. Feature Selection with the Boruta Package. Journal of Statistical Software 36, 1–13. https://doi.org/10.18637/jss.v036.i11

Lange, M., Dechant, B., Rebmann, C., Vohland, M., Cuntz, M., Doktor, D., 2017. Validating MODIS and Sentinel-2 NDVI Products at a Temperate Deciduous Forest Site Using Two Independent Ground-Based Sensors, in: Sensors.

Lee, J., Rennaker, C., Wrolstad, R.E., 2008. Correlation of two anthocyanin quantification methods: HPLC and spectrophotometric methods. Food Chemistry 110, 782–786. https://doi.org/10.1016/j.foodchem.2008.03.010

Lewis, P., 1999. Three-dimensional plant modelling for remote sensing simulation studies using the Botanical Plant Modelling System. Agronomie 19, 185–210. https://doi.org/10.1051/agro:19990302

Li, X., Xiao, J., He, B., Arain, M.A., Beringer, J., Desai, A.R., Emmel, C., Hollinger, D.Y., Krasnova, A., Mammarella, I., Noe, S.M., Ortiz, P.S., Rey-Sanchez, A.C., Rocha, A.V., Varlagin, A., 2018. Solar-induced chlorophyll fluorescence is strongly correlated with terrestrial photosynthesis for a wide variety of biomes: First global analysis based on OCO-2 and flux tower observations. Global Change Biology 24, 3990–4008. https://doi.org/10.1111/gcb.14297

Liaw, A., Wiener, M., 2002. Classification and Regression by randomForest. R News 2, 18–22.

Lichtenthaler, H.K., 1996. Vegetation Stress: an Introduction to the Stress Concept in Plants. Journal of Plant Physiology 148, 4–14. https://doi.org/10.1016/S0176-1617(96)80287-2

Lin, S., Li, J., Liu, Q., Huete, A., Li, L., 2018. Effects of Forest Canopy Vertical Stratification on the Estimation of Gross Primary Production by Remote Sensing. Remote Sensing 10, 1329. https://doi.org/10.3390/rs10091329

Liu, L., Liu, X., Hu, J., 2015. Effects of spectral resolution and SNR on the vegetation solar-induced fluorescence retrieval using FLD-based methods at canopy level. European Journal of Remote Sensing 48, 743–762. https://doi.org/10.5721/EuJRS20154841

Liu, P., Choo, K.-K.R., Wang, L., Huang, F., 2017. SVM or deep learning? A comparative study on remote sensing image classification. Soft Comput 21, 7053–7065. https://doi.org/10.1007/s00500-016-2247-2

Liu, W., Atherton, J., Mõttus, M., Gastellu-Etchegorry, J.-P., Malenovský, Z., Raumonen, P., Åkerblom, M., Mäkipää, R., Porcar-Castell, A., 2019. Simulating solar-induced chlorophyll fluorescence in a boreal forest stand reconstructed from terrestrial laser scanning measurements. Remote Sensing of Environment 232, 111274. https://doi.org/10.1016/j.rse.2019.111274

Liu, W., Luo, S., Lu, X., Atherton, J., Gastellu-Etchegorry, J.-P., 2020. Simulation-Based Evaluation of the Estimation Methods of Far-Red Solar-Induced Chlorophyll Fluorescence Escape Probability in Discontinuous Forest Canopies. Remote Sensing 12, 3962. https://doi.org/10.3390/rs12233962

Liu, X., Liu, L., 2015. Improving Chlorophyll Fluorescence Retrieval Using Reflectance Reconstruction Based on Principal Components Analysis. IEEE Geoscience and Remote Sensing Letters 12, 1645–1649. https://doi.org/10.1109/LGRS.2015.2417857

Liu, X., Liu, L., 2014. Assessing Band Sensitivity to Atmospheric Radiation Transfer for Space-Based Retrieval of Solar-Induced Chlorophyll Fluorescence. Remote Sensing 6, 10656–10675. https://doi.org/10.3390/rs61110656

Liu, Y., Cheng, T., Zhu, Y., Tian, Y., Cao, W., Yao, X., Wang, N., 2016. Comparative analysis of vegetation indices, non-parametric and physical retrieval methods for monitoring nitrogen in wheat using UAV-based multispectral imagery, in: 2016 IEEE International Geoscience and Remote Sensing Symposium (IGARSS). Presented at the 2016 IEEE International Geoscience and Remote Sensing Symposium (IGARSS), pp. 7362–7365. https://doi.org/10.1109/IGARSS.2016.7730920

López-López, M., Calderón, R., González-Dugo, V., Zarco-Tejada, P.J., Fereres, E., 2016. Early Detection and Quantification of Almond Red Leaf Blotch Using High-Resolution Hyperspectral and Thermal Imagery. Remote Sensing 8, 276. https://doi.org/10.3390/rs8040276

Lu, Xinchen, Cheng, X., Li, X., Tang, J., 2018. Opportunities and challenges of applications of satellite-derived sun-induced fluorescence at

relatively high spatial resolution. Science of The Total Environment 619–620, 649–653. https://doi.org/10.1016/j.scitotenv.2017.11.158

Lu, Xiaoliang, Liu, Z., Zhou, Y., Liu, Y., An, S., Tang, J., 2018. Comparison of Phenology Estimated from Reflectance-Based Indices and Solar-Induced Chlorophyll Fluorescence (SIF) Observations in a Temperate Forest Using GPP-Based Phenology as the Standard. Remote Sensing 10, 932. https://doi.org/10.3390/rs10060932

Luvisi, A., Aprile, A., Sabella, E., Vergine, M., Nicolì, F., Nutricati, E., Miceli, A., Negro, C., Bellis, L.D., 2017. Xylella fastidiosa subsp. pauca (CoDiRO strain) infection in four olive (Olea europaea L.) cultivars: profile of phenolic compounds in leaves and progression of leaf scorch symptoms. Phytopathologia Mediterranea 56, 259-273–273. https://doi.org/10.14601/Phytopathol_Mediterr-20578

Macpherson, M.F., Kleczkowski, A., Healey, J.R., Quine, C.P., Hanley, N., 2017. The effects of invasive pests and pathogens on strategies for forest diversification. Ecol Modell 350, 87–99. https://doi.org/10.1016/j.ecolmodel.2017.02.003

Mahajan, G.R., Sahoo, R.N., Pandey, R.N., Gupta, V.K., Kumar, D., 2014. Using hyperspectral remote sensing techniques to monitor nitrogen, phosphorus, sulphur and potassium in wheat (Triticum aestivum L.). Precision Agric 15, 499–522. https://doi.org/10.1007/s11119-014-9348-7

Mahlein, A.-K., Rumpf, T., Welke, P., Dehne, H.-W., Plümer, L., Steiner, U., Oerke, E.-C., 2013. Development of spectral indices for detecting and identifying plant diseases. Remote Sensing of Environment 128, 21–30. https://doi.org/10.1016/j.rse.2012.09.019

Maier, S.W., Günther, K.P., Stellmes, M., 2003. Sun-Induced Fluorescence: A New Tool for Precision Farming. Digital Imaging and Spectral Techniques: Applications to Precision Agriculture and Crop Physiology asaspecialpubli, 209–222. https://doi.org/10.2134/asaspecpub66.c16

Malenovský, Z., Homolová, L., Lukeš, P., Buddenbaum, H., Verrelst, J., Alonso, L., Schaepman, M.E., Lauret, N., Gastellu-Etchegorry, J.-P., 2019. Variability and Uncertainty Challenges in Scaling Imaging Spectroscopy Retrievals and Validations from Leaves Up to Vegetation Canopies. Surv Geophys 40, 631–656. https://doi.org/10.1007/s10712-019-09534-y

Malthus, T.J., Andrieu, B., Danson, F.M., Jaggard, K.W., Steven, M.D., 1993. Candidate high spectral resolution infrared indices for crop cover. Remote Sensing of Environment 46, 204–212. https://doi.org/10.1016/0034-4257(93)90095-F

Manion, P.D., Lachance, D., 1992. Forest Decline Concepts. APS Press.

Markiet, V., Mõttus, M., 2020. Estimation of boreal forest floor reflectance from airborne hyperspectral data of coniferous forests. Remote Sensing of Environment 249, 112018. https://doi.org/10.1016/j.rse.2020.112018

Markiet, V., Perheentupa, V., Mõttus, M., Hernández-Clemente, R., 2016. Usability of multiangular imaging spectroscopy data for analysis of vegetation canopy shadow fraction in boreal forest, in: Mapping, Monitoring & Modelling of Vegetation Characteristics Using Earth Observation. Presented at the EGU General Assembly Conference Abstracts, Ask, M. et al., Vienna, Austria., p. 14399.

Martín, A., Zarco-Tejada, P.J., González, M.R., Berjón, A., 2007. Using Hyperspectral Remote Sensing to map grape quality in "Tempranillo" Vineyards affected by Iron deficiency Chlorosis.

Mazzoni, M., Meroni, M., Fortunato, C., Colombo, R., Verhoef, W., 2012. Retrieval of maize canopy fluorescence and reflectance by spectral fitting in the O2–A absorption band. Remote Sensing of Environment 124, 72–82. https://doi.org/10.1016/j.rse.2012.04.025

Meggio, F., Zarco-Tejada, P.J., Miller, J.R., Martín, A., González, M.R., Berjón, A., 2008. Row Orientation and Viewing Geometry Effects on Row-structured Crops for Chlorophyll Content Estimation.

Melendo-Vega, J.R., Martín, M.P., Pacheco-Labrador, J., González-Cascón, R., Moreno, G., Pérez, F., Migliavacca, M., García, M., North, P., Riaño, D., 2018. Improving the Performance of 3-D Radiative Transfer Model FLIGHT to Simulate Optical Properties of a Tree-Grass Ecosystem. Remote Sensing 10, 2061. https://doi.org/10.3390/rs10122061

Mendiguren, G., Pilar Martín, M., Nieto, H., Pacheco-Labrador, J., Jurdao, S., 2015. Seasonal variation in grass water content estimated from proximal sensing and MODIS time series in a Mediterranean Fluxnet site. Biogeosciences 12, 5523–5535. https://doi.org/10.5194/bg-12-5523-2015

Meng, R., Dennison, P.E., Zhao, F., Shendryk, I., Rickert, A., Hanavan, R.P., Cook, B.D., Serbin, S.P., 2018. Mapping canopy defoliation by herbivorous insects at the individual tree level using bi-temporal airborne imaging spectroscopy and LiDAR measurements. Remote Sensing of Environment 215, 170–183. https://doi.org/10.1016/j.rse.2018.06.008

Meroni, M., Busetto, L., Colombo, R., Guanter, L., Moreno, J., Verhoef, W., 2010. Performance of Spectral Fitting Methods for vegetation fluorescence quantification. Remote Sensing of Environment 114, 363–374. https://doi.org/10.1016/j.rse.2009.09.010

Merzlyak, M.N., Gitelson, A.A., Chivkunova, O.B., Rakitin, V.YU., 1999. Non-destructive optical detection of pigment changes during leaf senescence and fruit ripening. Physiologia Plantarum 106, 135–141. https://doi.org/10.1034/j.1399-3054.1999.106119.x

Migliavacca, M., Perez-Priego, O., Rossini, M., El-Madany, T.S., Moreno, G., van der Tol, C., Rascher, U., Berninger, A., Bessenbacher, V., Burkart, A., Carrara, A., Fava, F., Guan, J.-H., Hammer, T.W., Henkel, K., Juarez-Alcalde, E., Julitta, T., Kolle, O., Martín, M.P., Musavi, T., Pacheco-Labrador, J., Pérez-Burgueño, A., Wutzler, T., Zaehle, S., Reichstein, M., 2017. Plant functional traits and canopy structure control the relationship between photosynthetic CO2 uptake and far-red sun-induced fluorescence in a Mediterranean grassland under different nutrient availability. New Phytologist 214, 1078–1091. https://doi.org/10.1111/nph.14437

Mohammed, G.H., Colombo, R., Middleton, E.M., Rascher, U., van der Tol, C., Nedbal, L., Goulas, Y., Pérez-Priego, O., Damm, A., Meroni, M., Joiner, J., Cogliati, S., Verhoef, W., Malenovský, Z., Gastellu-Etchegorry, J.-P., Miller, J.R., Guanter, L., Moreno, J., Moya, I., Berry, J.A., Frankenberg, C., Zarco-Tejada, P.J., 2019. Remote sensing of solar-induced chlorophyll fluorescence (SIF) in vegetation: 50 years of progress. Remote Sensing of Environment 231, 111177. https://doi.org/10.1016/j.rse.2019.04.030

Montandon, L.M., 2009. The impact of soil properties on soil NDVI and the quantification of the green vegetation fraction (Ph.D.). University of Colorado at Boulder, United States -- Colorado.

Montesano, P.M., Rosette, J., Sun, G., North, P., Nelson, R.F., Dubayah, R.O., Ranson, K.J., Kharuk, V., 2015. The uncertainty of biomass

estimates from modeled ICESat-2 returns across a boreal forest gradient. Remote Sensing of Environment 158, 95–109. https://doi.org/10.1016/j.rse.2014.10.029

Moralejo, E., García-Muñoz, J.A., Descals, E., 2009. Susceptibility of Iberian trees to Phytophthora ramorum and P. cinnamomi. Plant Pathology 58, 271–283. https://doi.org/10.1111/j.1365-3059.2008.01956.x

Mura, M., Bottalico, F., Giannetti, F., Bertani, R., Giannini, R., Mancini, M., Orlandini, S., Travaglini, D., Chirici, G., 2018. Exploiting the capabilities of the Sentinel-2 multi spectral instrument for predicting growing stock volume in forest ecosystems. International Journal of Applied Earth Observation and Geoinformation 66, 126–134. https://doi.org/10.1016/j.jag.2017.11.013

Murray, J.R., Hackett, W.P., 1991. Dihydroflavonol Reductase Activity in Relation to Differential Anthocyanin Accumulation in Juvenile and Mature Phase Hedera helix L. Plant Physiol 97, 343–351. https://doi.org/10.1104/pp.97.1.343

Myneni, R.B., Marshak, A., Knyazikhin, Y., Asrar, G., 1991. Discrete Ordinates Method for Photon Transport in Leaf Canopies, in: Photon-Vegetation Interactions. Springer, Berlin, Heidelberg, pp. 45–109. https://doi.org/10.1007/978-3-642-75389-3_3

Navarro-Cerrillo, R.M., Ruiz Gómez, F.J., Cabrera-Puerto, R.J., Sánchez-Cuesta, R., Palacios Rodriguez, G., Quero Pérez, J.L., 2018. Growth and physiological sapling responses of eleven Quercus ilex ecotypes under identical environmental conditions. Forest Ecology and Management 415–416, 58–69. https://doi.org/10.1016/j.foreco.2018.01.004

Niblack, W., 1986. An Introduction to Digital Image Processing, First English Edition edition. ed. Prentice Hall, Englewood Cliffs, N.J.

Noori, O., Panda, S.S., 2016. Site-specific management of common olive: Remote sensing, geospatial, and advanced image processing applications. Computers and Electronics in Agriculture 127, 680–689. https://doi.org/10.1016/j.compag.2016.07.031

North, P.R.J., 1996. Three-dimensional forest light interaction model using a Monte Carlo method. IEEE Transactions on Geoscience and Remote Sensing 34, 946–956. https://doi.org/10.1109/36.508411

North, P.R.J., Rosette, J.A.B., Suárez, J.C., Los, S.O., 2010. A Monte Carlo radiative transfer model of satellite waveform LiDAR. International

Journal of Remote Sensing 31, 1343–1358. https://doi.org/10.1080/01431160903380664

Nutter, F.W., Esker, P.D., Netto, R.A.C., 2006. Disease Assessment Concepts and the Advancements Made in Improving the Accuracy and Precision of Plant Disease Data. Eur J Plant Pathol 115, 95–103. https://doi.org/10.1007/s10658-005-1230-z

Pal, M., 2005. Random forest classifier for remote sensing classification. International Journal of Remote Sensing 26, 217–222. https://doi.org/10.1080/01431160412331269698

Pandey, P., Irulappan, V., Bagavathiannan, M.V., Senthil-Kumar, M., 2017. Impact of Combined Abiotic and Biotic Stresses on Plant Growth and Avenues for Crop Improvement by Exploiting Physio-morphological Traits. Front. Plant Sci. 8. https://doi.org/10.3389/fpls.2017.00537

Pareek, A., Dhankher, O.P., Foyer, C.H., 2020. Mitigating the impact of climate change on plant productivity and ecosystem sustainability. Journal of Experimental Botany 71, 451–456. https://doi.org/10.1093/jxb/erz518

Park Williams, A., Allen, C.D., Macalady, A.K., Griffin, D., Woodhouse, C.A., Meko, D.M., Swetnam, T.W., Rauscher, S.A., Seager, R., Grissino-Mayer, H.D., Dean, J.S., Cook, E.R., Gangodagamage, C., Cai, M., McDowell, N.G., 2013. Temperature as a potent driver of regional forest drought stress and tree mortality. Nature Climate Change 3, 292–297. https://doi.org/10.1038/nclimate1693

Paruelo, J.M., Piñeiro, G., Escribano, P., Oyonarte, C., Alcaraz, D., Cabello, J., 2005. Temporal and spatial patterns of ecosystem functioning in protected arid areas in southeastern Spain. Applied Vegetation Science 8, 93–102. https://doi.org/10.1111/j.1654-109X.2005.tb00633.x

Pearson, R.L., Miller, L.D., 1972. Remote Mapping of Standing Crop Biomass for Estimation of the Productivity of the Shortgrass Prairie. Presented at the Remote Sensing of Environment, VIII, p. 1355.

Pedrós, R., Goulas, Y., Jacquemoud, S., Louis, J., Moya, I., 2010. FluorMODleaf: A new leaf fluorescence emission model based on the PROSPECT model. Remote Sensing of Environment 114, 155–167. https://doi.org/10.1016/j.rse.2009.08.019

Peltzer, D.A., Köchy, M., 2001. Competitive Effects of Grasses and Woody Plants in Mixed-Grass Prairie. Journal of Ecology 89, 519–527.

Penuelas, J., Frederic, B., Filella, I., 1995. Semi-Empirical Indices to Assess Carotenoids/Chlorophyll-a Ratio from Leaf Spectral Reflectance.

Pimstein, A., Karnieli, A., Bansal, S.K., Bonfil, D.J., 2011. Exploring remotely sensed technologies for monitoring wheat potassium and phosphorus using field spectroscopy. Field Crops Research 121, 125–135. https://doi.org/10.1016/j.fcr.2010.12.001

Pinty, B., Verstraete, M.M., 1992. GEMI: a non-linear index to monitor global vegetation from satellites. Vegetatio 101, 15–20. https://doi.org/10.1007/BF00031911

Pisek, J., Lang, M., Kuusk, J., 2015. A note on suitable viewing configuration for retrieval of forest understory reflectance from multi-angle remote sensing data. Remote Sensing of Environment 156, 242–246. https://doi.org/10.1016/j.rse.2014.09.033

Plascyk, J.A., 1975. The MK II Fraunhofer Line Discriminator (FLD-II) for Airborne and Orbital Remote Sensing of Solar-Stimulated Luminescence. OE, OPEGAR 14, 144339. https://doi.org/10.1117/12.7971842

Poblete, T., Camino, C., Beck, P.S.A., Hornero, A., Kattenborn, T., Saponari, M., Boscia, D., Navas-Cortes, J.A., Zarco-Tejada, P.J., 2020. Detection of Xylella fastidiosa infection symptoms with airborne multispectral and thermal imagery: Assessing bandset reduction performance from hyperspectral analysis. ISPRS Journal of Photogrammetry and Remote Sensing 162, 27–40. https://doi.org/10.1016/j.isprsjprs.2020.02.010

Qi, J., Chehbouni, A., Huete, A.R., Kerr, Y.H., Sorooshian, S., 1994. A modified soil adjusted vegetation index. Remote Sensing of Environment 48, 119–126. https://doi.org/10.1016/0034-4257(94)90134-1

Qiu, B., Chen, J.M., Ju, W., Zhang, Q., Zhang, Y., 2019. Simulating emission and scattering of solar-induced chlorophyll fluorescence at far-red band in global vegetation with different canopy structures. Remote Sensing of Environment 233, 111373. https://doi.org/10.1016/j.rse.2019.111373

Rahimzadeh-Bajgiran, P., Weiskittel, A.R., Kneeshaw, D., MacLean, D.A., 2018. Detection of Annual Spruce Budworm Defoliation and Severity Classification Using Landsat Imagery. Forests 9, 357. https://doi.org/10.3390/f9060357

Rascher, U., Alonso, L., Burkart, A., Cilia, C., Cogliati, S., Colombo, R., Damm, A., Drusch, M., Guanter, L., Hanus, J., Hyvärinen, T., Julitta, T., Jussila, J., Kataja, K., Kokkalis, P., Kraft, S., Kraska, T., Matveeva, M., Moreno, J., Muller, O., Panigada, C., Pikl, M., Pinto, F., Prey, L., Pude, R., Rossini, M., Schickling, A., Schurr, U., Schüttemeyer, D., Verrelst, J., Zemek, F., 2015. Sun-induced fluorescence - a new probe of photosynthesis: First maps from the imaging spectrometer HyPlant. Glob Chang Biol 21, 4673–4684. https://doi.org/10.1111/gcb.13017

REDIAM, Junta de Andalucía, 2021. Andalusian Environmental Information Network (REDIAM). Regional Ministry website. Junta de Andalucía [WWW Document]. URL http://www.juntadeandalucia.es/medioambiente/site/rediam (accessed 1.9.21).

Richards, J.A., Jia, X., 1999. Remote Sensing Digital Image Analysis: An Introduction, 3rd ed. Springer-Verlag, Berlin Heidelberg. https://doi.org/10.1007/978-3-662-03978-6

Richardson, A.J., Wiegand, C.L., 1977. Distinguishing vegetation from soil background information. [by gray mapping of Landsat MSS data]. Photogrammetric Engineering and Remote Sensing.

Richter, R., Wang, X., Bachmann, M., Schläpfer, D., 2011. Correction of cirrus effects in sentinel-2 type of imagery. International Journal of Remote Sensing 32, 2931–2941. https://doi.org/10.1080/01431161.2010.520346

Rivera, J.P., Verrelst, J., Gómez-Dans, J., Muñoz-Marí, J., Moreno, J., Camps-Valls, G., 2015. An Emulator Toolbox to Approximate Radiative Transfer Models with Statistical Learning. Remote Sensing 7, 9347–9370. https://doi.org/10.3390/rs70709347

Roberts, O., Bunting, P., Hardy, A., McInerney, D., 2020. Sensitivity Analysis of the DART Model for Forest Mensuration with Airborne Laser Scanning. Remote Sensing 12, 247. https://doi.org/10.3390/rs12020247

Rocha, A.D., Groen, T.A., Skidmore, A.K., 2019. Spatially-explicit modelling with support of hyperspectral data can improve prediction of plant traits. Remote Sensing of Environment 231, 111200. https://doi.org/10.1016/j.rse.2019.05.019

Romero, J.M., Cordon, G.B., Lagorio, M.G., 2020. Re-absorption and scattering of chlorophyll fluorescence in canopies: A revised approach.

Remote Sensing of Environment 246, 111860. https://doi.org/10.1016/j.rse.2020.111860

Romero, J.M., Cordon, G.B., Lagorio, M.G., 2018. Modeling re-absorption of fluorescence from the leaf to the canopy level. Remote Sensing of Environment 204, 138–146. https://doi.org/10.1016/j.rse.2017.10.035

Romero, M.A., González, M., Serrano, M.S., Sánchez, M.E., 2019. Trunk injection of fosetyl-aluminium controls the root disease caused by Phytophthora cinnamomi on Quercus ilex woodlands. Annals of Applied Biology 174, 313–318. https://doi.org/10.1111/aab.12503

Rondeaux, G., Steven, M., Baret, F., 1996. Optimization of soil-adjusted vegetation indices. Remote Sensing of Environment 55, 95–107. https://doi.org/10.1016/0034-4257(95)00186-7

Roujean, J.-L., Breon, F.-M., 1995. Estimating PAR absorbed by vegetation from bidirectional reflectance measurements. Remote Sensing of Environment 51, 375–384. https://doi.org/10.1016/0034-4257(94)00114-3

Rouse, J.W., Jr., Haas, R.H., Schell, J.A., Deering, D.W., 1974. Monitoring Vegetation Systems in the Great Plains with Erts. NASA Special Publication 351, 309.

Ruiz Gómez, F.J., Pérez-de-Luque, A., Sánchez-Cuesta, R., Quero, J.L., Navarro Cerrillo, R.M., 2018. Differences in the Response to Acute Drought and Phytophthora cinnamomi Rands Infection in Quercus ilex L. Seedlings. Forests 9, 634. https://doi.org/10.3390/f9100634

Ruiz-Gómez, F.J., Navarro-Cerrillo, R.M., Oβwald, W., Vannini, A., Morales-Rodriguez, C., 2019. Assessment of functional and structural changes of soil fungal and oomycete communities in holm oak declined dehesas through metabarcoding analysis. Scientific Reports 9, 5315. https://doi.org/10.1038/s41598-019-41804-y

San, B.T., Süzen, M.L., 2011. Evaluation of cross-track illumination in EO-1 Hyperion imagery for lithological mapping. International Journal of Remote Sensing 32, 7873–7889. https://doi.org/10.1080/01431161.2010.532175

Saponari, M., Boscia, D., Altamura, G., Loconsole, G., Zicca, S., D'Attoma, G., Morelli, M., Palmisano, F., Saponari, A., Tavano, D., Savino, V.N., Dongiovanni, C., Martelli, G.P., 2017. Isolation and pathogenicity of Xylella fastidiosa associated to the olive quick decline

syndrome in southern Italy. Scientific Reports 7, 17723. https://doi.org/10.1038/s41598-017-17957-z

Sauvola, J., Pietikäinen, M., 2000. Pietikainen, M.: Adaptive Document Image Binarization. Pattern Recognition 33, 225-236. https://doi.org/10.1016/S0031-3203(99)00055-2

Savary, S., Willocquet, L., Pethybridge, S.J., Esker, P., McRoberts, N., Nelson, A., 2019. The global burden of pathogens and pests on major food crops. Nature Ecology & Evolution 3, 430–439. https://doi.org/10.1038/s41559-018-0793-y

Scholkopf, B., Kah-Kay Sung, Burges, C.J.C., Girosi, F., Niyogi, P., Poggio, T., Vapnik, V., 1997. Comparing support vector machines with Gaussian kernels to radial basis function classifiers. IEEE Transactions on Signal Processing 45, 2758–2765. https://doi.org/10.1109/78.650102

Seem, R.C., 1984. Disease Incidence and Severity Relationships. Annual Review of Phytopathology 22, 133–150. https://doi.org/10.1146/annurev.py.22.090184.001025

Seidl, R., Klonner, G., Rammer, W., Essl, F., Moreno, A., Neumann, M., Dullinger, S., 2018. Invasive alien pests threaten the carbon stored in Europe's forests. Nature Communications 9, 1626. https://doi.org/10.1038/s41467-018-04096-w

Serrano, L., Peñuelas, J., Ustin, S.L., 2002. Remote sensing of nitrogen and lignin in Mediterranean vegetation from AVIRIS data: Decomposing biochemical from structural signals. Remote Sensing of Environment 81, 355–364. https://doi.org/10.1016/S0034-4257(02)00011-1

Shearer, B.L., Crane, C.E., Cochrane, A., 2004. Quantification of the susceptibility of the native flora of the South-West Botanical Province, Western Australia, to Phytophthora cinnamomi. Aust. J. Bot. 52, 435–443. https://doi.org/10.1071/bt03131

Sibbett, G.S., Ferguson, L., 2005. Olive Production Manual. UCANR Publications.

Siegmann, B., Alonso, L., Celesti, M., Cogliati, S., Colombo, R., Damm, A., Douglas, S., Guanter, L., Hanuš, J., Kataja, K., Kraska, T., Matveeva, M., Moreno, J., Muller, O., Pikl, M., Pinto, F., Quirós Vargas, J., Rademske, P., Rodriguez-Morene, F., Sabater, N., Schickling, A., Schüttemeyer, D., Zemek, F., Rascher, U., 2019. The High-Performance Airborne Imaging Spectrometer HyPlant—From Raw Images

to Top-of-Canopy Reflectance and Fluorescence Products: Introduction of an Automatized Processing Chain. Remote Sensing 11, 2760. https://doi.org/10.3390/rs11232760

Sims, D.A., Gamon, J.A., 2002. Relationships between leaf pigment content and spectral reflectance across a wide range of species, leaf structures and developmental stages. Remote Sensing of Environment 81, 337–354. https://doi.org/10.1016/S0034-4257(02)00010-X

Sisterson, M.S., Thammiraju, S.R., Lynn-Patterson, K., Groves, R.L., Daane, K.M., 2010. Epidemiology of Diseases Caused by Xylella fastidiosa in California: Evaluation of Alfalfa as a Source of Vectors and Inocula. Plant Disease 94, 827–834. https://doi.org/10.1094/PDIS-94-7-0827

Steele, M.R., Gitelson, A.A., Rundquist, D.C., Merzlyak, M.N., 2009. Nondestructive Estimation of Anthocyanin Content in Grapevine Leaves. Am J Enol Vitic. 60, 87–92.

Stoy, P.C., El-Madany, T.S., Fisher, J.B., Gentine, P., Gerken, T., Good, S.P., Klosterhalfen, A., Liu, S., Miralles, D.G., Perez-Priego, O., Rigden, A.J., Skaggs, T.H., Wohlfahrt, G., Anderson, R.G., Coenders-Gerrits, A.M.J., Jung, M., Maes, W.H., Mammarella, I., Mauder, M., Migliavacca, M., Nelson, J.A., Poyatos, R., Reichstein, M., Scott, R.L., Wolf, S., 2019. Reviews and syntheses: Turning the challenges of partitioning ecosystem evaporation and transpiration into opportunities. Biogeosciences 16, 3747–3775. https://doi.org/10.5194/bg-16-3747-2019

Strang, G., Nguyen, T., 1996. Wavelets and Filter Banks. SIAM.

Strona, G., Carstens, C.J., Beck, P.S.A., 2017. Network analysis reveals why Xylella fastidiosa will persist in Europe. Scientific Reports 7, 71. https://doi.org/10.1038/s41598-017-00077-z

Sturrock, R.N., Frankel, S.J., Brown, A.V., Hennon, P.E., Kliejunas, J.T., Lewis, K.J., Worrall, J.J., Woods, A.J., 2011. Climate change and forest diseases. Plant Pathology 60, 133–149. https://doi.org/10.1111/j.1365-3059.2010.02406.x

Suarez, L., González-Dugo, V., Camino, C., Hornero, A., Zarco-Tejada, P.J., 2021. Physical model inversion of the green spectral region to track assimilation rate in almond trees with an airborne nano-hyperspectral imager. Remote Sensing of Environment 252, 112147. https://doi.org/10.1016/j.rse.2020.112147

Sun, Y., Frankenberg, C., Jung, M., Joiner, J., Guanter, L., Köhler, P., Magney, T., 2018. Overview of Solar-Induced chlorophyll Fluorescence (SIF) from the Orbiting Carbon Observatory-2: Retrieval, cross-mission comparison, and global monitoring for GPP. Remote Sensing of Environment 209, 808–823.

Sun, Y., Frankenberg, C., Wood, J.D., Schimel, D.S., Jung, M., Guanter, L., Drewry, D.T., Verma, M., Porcar-Castell, A., Griffis, T.J., Gu, L., Magney, T.S., Köhler, P., Evans, B., Yuen, K., 2017. OCO-2 advances photosynthesis observation from space via solar-induced chlorophyll fluorescence. Science 358. https://doi.org/10.1126/science.aam5747

Tagliabue, G., Panigada, C., Dechant, B., Baret, F., Cogliati, S., Colombo, R., Migliavacca, M., Rademske, P., Schickling, A., Schüttemeyer, D., Verrelst, J., Rascher, U., Ryu, Y., Rossini, M., 2019. Exploring the spatial relationship between airborne-derived red and far-red sun-induced fluorescence and process-based GPP estimates in a forest ecosystem. Remote Sensing of Environment 231, 111272. https://doi.org/10.1016/j.rse.2019.111272

Thompson, R.L., Goel, N.S., 1998. Two models for rapidly calculating bidirectional reflectance of complex vegetation scenes: Photon spread (PS) model and statistical photon spread (SPS) model. Remote Sensing Reviews 16, 157–207. https://doi.org/10.1080/02757259809532351

Tou, J.T., Tou, T.-C., Gonzalez, R.C., 1974. Pattern Recognition Principles. Addison-Wesley Publishing Company.

Trumbore, S., Brando, P., Hartmann, H., 2015. Forest health and global change. Science 349, 814–818. https://doi.org/10.1126/science.aac6759

Verhoef, W., 1984. Light scattering by leaf layers with application to canopy reflectance modeling: The SAIL model. Remote Sensing of Environment 16, 125–141. https://doi.org/10.1016/0034-4257(84)90057-9

Verrelst, J., Malenovský, Z., van der Tol, C., Camps-Valls, G., Gastellu-Etchegorry, J.-P., Lewis, P., North, P., Moreno, J., 2018. Quantifying Vegetation Biophysical Variables from Imaging Spectroscopy Data: A Review on Retrieval Methods. Surv Geophys 1–41. https://doi.org/10.1007/s10712-018-9478-y

Verrelst, J., Rivera, J.P., van der Tol, C., Magnani, F., Mohammed, G., Moreno, J., 2015a. Global sensitivity analysis of the SCOPE model:

What drives simulated canopy-leaving sun-induced fluorescence? Remote Sensing of Environment 166, 8–21. https://doi.org/10.1016/j.rse.2015.06.002

Verrelst, J., Rivera, J.P., Veroustraete, F., Muñoz-Marí, J., Clevers, J.G.P.W., Camps-Valls, G., Moreno, J., 2015b. Experimental Sentinel-2 LAI estimation using parametric, non-parametric and physical retrieval methods - A comparison. ISPRS Journal of Photogrammetry and Remote Sensing 108, 260–272. https://doi.org/10.1016/j.isprsjprs.2015.04.013

Vilfan, N., van der Tol, C., Muller, O., Rascher, U., Verhoef, W., 2016. Fluspect-B: A model for leaf fluorescence, reflectance and transmittance spectra. https://doi.org/10.1016/j.rse.2016.09.017

Vilfan, N., van der Tol, C., Yang, P., Wyber, R., Malenovský, Z., Robinson, S.A., Verhoef, W., 2018. Extending Fluspect to simulate xanthophyll driven leaf reflectance dynamics. Remote Sensing of Environment 211, 345–356. https://doi.org/10.1016/j.rse.2018.04.012

Violle, C., Navas, M.-L., Vile, D., Kazakou, E., Fortunel, C., Hummel, I., Garnier, E., 2007. Let the concept of trait be functional! Oikos 116, 882–892. https://doi.org/10.1111/j.0030-1299.2007.15559.x

Vogelmann, T.C., 1993. Plant Tissue Optics. Annu. Rev. Plant. Physiol. Plant. Mol. Biol. 44, 231–251. https://doi.org/10.1146/annurev.pp.44.060193.001311

Wagner, F.H., Ferreira, M.P., Sanchez, A., Hirye, M.C.M., Zortea, M., Gloor, E., Phillips, O.L., de Souza Filho, C.R., Shimabukuro, Y.E., Aragão, L.E.O.C., 2018. Individual tree crown delineation in a highly diverse tropical forest using very high resolution satellite images. ISPRS Journal of Photogrammetry and Remote Sensing, SI: Latin America Issue 145, 362–377. https://doi.org/10.1016/j.isprsjprs.2018.09.013

White, S.M., Bullock, J.M., Hooftman, D.A.P., Chapman, D.S., 2017. Modelling the spread and control of Xylella fastidiosa in the early stages of invasion in Apulia, Italy. Biol Invasions 19, 1825–1837. https://doi.org/10.1007/s10530-017-1393-5

Whyte, A., Ferentinos, K.P., Petropoulos, G.P., 2018. A new synergistic approach for monitoring wetlands using Sentinels -1 and 2 data with object-based machine learning algorithms. Environmental Modelling & Software 104, 40–54. https://doi.org/10.1016/j.envsoft.2018.01.023

Widlowski, J.-L., Lavergne, T., Pinty, B., Verstraete, M., Gobron, N., 2006. Rayspread: A Virtual Laboratory for Rapid BRF Simulations Over 3-D Plant Canopies, in: Graziani, F. (Ed.), Computational Methods in Transport, Lecture Notes in Computational Science and Engineering. Springer Berlin Heidelberg, pp. 211–231.

Widlowski, J.-L., Pinty, B., Lopatka, M., Atzberger, C., Buzica, D., Chelle, M., Disney, M., Gastellu-Etchegorry, J.-P., Gerboles, M., Gobron, N., Grau, E., Huang, H., Kallel, A., Kobayashi, H., Lewis, P.E., Qin, W., Schlerf, M., Stuckens, J., Xie, D., 2013. The fourth radiation transfer model intercomparison (RAMI-IV): Proficiency testing of canopy reflectance models with ISO-13528. Journal of Geophysical Research: Atmospheres 118, 6869–6890. https://doi.org/10.1002/jgrd.50497

Widlowski, J.-L., Robustelli, M., Disney, M., Gastellu-Etchegorry, J.-P., Lavergne, T., Lewis, P., North, P.R.J., Pinty, B., Thompson, R., Verstraete, M.M., 2008. The RAMI On-line Model Checker (ROMC): A web-based benchmarking facility for canopy reflectance models. Remote Sensing of Environment 112, 1144–1150. https://doi.org/10.1016/j.rse.2007.07.016

Widlowski, J.-L., Taberner, M., Pinty, B., Bruniquel-Pinel, V., Disney, M., Fernandes, R., Gastellu-Etchegorry, J.-P., Gobron, N., Kuusk, A., Lavergne, T., Leblanc, S., Lewis, P.E., Martin, E., Mõttus, M., North, P.R.J., Qin, W., Robustelli, M., Rochdi, N., Ruiloba, R., Soler, C., Thompson, R., Verhoef, W., Verstraete, M.M., Xie, D., 2007. Third Radiation Transfer Model Intercomparison (RAMI) exercise: Documenting progress in canopy reflectance models. Journal of Geophysical Research: Atmospheres 112. https://doi.org/10.1029/2006JD007821

Wu, G., Guan, K., Jiang, C., Peng, B., Kimm, H., Chen, M., Yang, X., Wang, S., Suyker, A.E., Bernacchi, C.J., Moore, C.E., Zeng, Y., Berry, J.A., Cendrero-Mateo, M.P., 2020. Radiance-based NIRv as a proxy for GPP of corn and soybean. Environ. Res. Lett. 15, 034009. https://doi.org/10.1088/1748-9326/ab65cc

Wu, H., Li, Z.-L., 2009. Scale Issues in Remote Sensing: A Review on Analysis, Processing and Modeling. Sensors (Basel) 9, 1768–1793. https://doi.org/10.3390/s90301768

Yáñez-Rausell, L., Malenovský, Z., Rautiainen, M., Clevers, J.G.P.W., Lukeš, P., Hanuš, J., Schaepman, M.E., 2015. Estimation of Spruce

Needle-Leaf Chlorophyll Content Based on DART and PARAS Canopy Reflectance Models. IEEE Journal of Selected Topics in Applied Earth Observations and Remote Sensing 8, 1534–1544. https://doi.org/10.1109/JSTARS.2015.2400418

Yang, P., van der Tol, C., 2018. Linking canopy scattering of far-red sun-induced chlorophyll fluorescence with reflectance. Remote Sensing of Environment 209, 456–467. https://doi.org/10.1016/j.rse.2018.02.029

Yang, W., Kobayashi, H., Suzuki, R., Nasahara, K.N., 2014. A Simple Method for Retrieving Understory NDVI in Sparse Needleleaf Forests in Alaska Using MODIS BRDF Data. Remote Sensing 6, 11936–11955. https://doi.org/10.3390/rs61211936

Yao, X., Zhu, Y., Tian, Y., Feng, W., Cao, W., 2010. Exploring hyperspectral bands and estimation indices for leaf nitrogen accumulation in wheat. International Journal of Applied Earth Observation and Geoinformation 12, 89–100. https://doi.org/10.1016/j.jag.2009.11.008

Yu, W., Li, J., Liu, Q., Zeng, Y., Zhao, J., Xu, B., Yin, G., 2018. Global Land Cover Heterogeneity Characteristics at Moderate Resolution for Mixed Pixel Modeling and Inversion. Remote Sensing 10, 856. https://doi.org/10.3390/rs10060856

Zarco-Tejada, P.J., Berjón, A., López-Lozano, R., Miller, J.R., Martín, P., Cachorro, V., González, M.R., de Frutos, A., 2005. Assessing vineyard condition with hyperspectral indices: Leaf and canopy reflectance simulation in a row-structured discontinuous canopy. Remote Sensing of Environment 99, 271–287. https://doi.org/10.1016/j.rse.2005.09.002

Zarco-Tejada, P.J., Camino, C., Beck, P.S.A., Calderon, R., Hornero, A., Hernández-Clemente, R., Kattenborn, T., Montes-Borrego, M., Susca, L., Morelli, M., Gonzalez-Dugo, V., North, P.R.J., Landa, B.B., Boscia, D., Saponari, M., Navas-Cortes, J.A., 2018a. Previsual symptoms of Xylella fastidiosa infection revealed in spectral plant-trait alterations. Nature Plants. https://doi.org/10.1038/s41477-018-0189-7

Zarco-Tejada, P.J., González-Dugo, M.V., Fereres, E., 2016. Seasonal stability of chlorophyll fluorescence quantified from airborne hyperspectral imagery as an indicator of net photosynthesis in the context of precision agriculture. Remote Sensing of Environment 179, 89–103. https://doi.org/10.1016/j.rse.2016.03.024

Zarco-Tejada, P.J., González-Dugo, V., Berni, J.A.J., 2012. Fluorescence, temperature and narrow-band indices acquired from a UAV platform for water stress detection using a micro-hyperspectral imager and a thermal camera. Remote Sensing of Environment, Remote Sensing of Urban Environments 117, 322–337. https://doi.org/10.1016/j.rse.2011.10.007

Zarco-Tejada, P.J., Hornero, A., Beck, P.S.A., Kattenborn, T., Kempeneers, P., Hernández-Clemente, R., 2019. Chlorophyll content estimation in an open-canopy conifer forest with Sentinel-2A and hyperspectral imagery in the context of forest decline. Remote Sensing of Environment 223, 320–335. https://doi.org/10.1016/j.rse.2019.01.031

Zarco-Tejada, P.J., Hornero, A., Hernández-Clemente, R., Beck, P.S.A., 2018b. Understanding the temporal dimension of the red-edge spectral region for forest decline detection using high-resolution hyperspectral and Sentinel-2a imagery. ISPRS Journal of Photogrammetry and Remote Sensing 137, 134–148. https://doi.org/10.1016/j.isprsjprs.2018.01.017

Zarco-Tejada, P.J., Miller, J.R., Mohammed, G.H., Noland, T.L., 2000. Chlorophyll Fluorescence Effects on Vegetation Apparent Reflectance: I. Leaf-Level Measurements and Model Simulation. Remote Sensing of Environment 74, 582–595. https://doi.org/10.1016/S0034-4257(00)00148-6

Zarco-Tejada, P.J., Miller, J.R., Mohammed, G.H., Noland, T.L., Sampson, P.H., 2001. Estimation of chlorophyll fluorescence under natural illumination from hyperspectral data. International Journal of Applied Earth Observation and Geoinformation 3, 321–327. https://doi.org/10.1016/S0303-2434(01)85039-X

Zarco-Tejada, P.J., Morales, A., Testi, L., Villalobos, F.J., 2013a. Spatio-temporal patterns of chlorophyll fluorescence and physiological and structural indices acquired from hyperspectral imagery as compared with carbon fluxes measured with eddy covariance. Remote Sensing of Environment 133, 102–115. https://doi.org/10.1016/j.rse.2013.02.003

Zarco-Tejada, P.J., Suárez, L., González-Dugo, V., 2013b. Spatial Resolution Effects on Chlorophyll Fluorescence Retrieval in a Heterogeneous Canopy Using Hyperspectral Imagery and Radiative Transfer

Simulation. IEEE Geoscience and Remote Sensing Letters 10, 937–941. https://doi.org/10.1109/LGRS.2013.2252877

Zarco-Tejada, P.J., Ustin, S.L., Whiting, M.L., 2005. Temporal and Spatial Relationships between Within-Field Yield Variability in Cotton and High-Spatial Hyperspectral Remote Sensing Imagery. Agronomy Journal 97, 641–653. https://doi.org/10.2134/agronj2003.0257

Zeng, Y., Badgley, G., Chen, M., Li, J., Anderegg, L.D.L., Kornfeld, A., Liu, Q., Xu, B., Yang, B., Yan, K., Berry, J.A., 2020. A radiative transfer model for solar induced fluorescence using spectral invariants theory. Remote Sensing of Environment 240, 111678. https://doi.org/10.1016/j.rse.2020.111678

Zeng, Y., Badgley, G., Dechant, B., Ryu, Y., Chen, M., Berry, J.A., 2019. A practical approach for estimating the escape ratio of near-infrared solar-induced chlorophyll fluorescence. Remote Sensing of Environment 232, 111209. https://doi.org/10.1016/j.rse.2019.05.028

Zhang, Y., Chen, J.M., Miller, J.R., Noland, T.L., 2008. Leaf chlorophyll content retrieval from airborne hyperspectral remote sensing imagery. Remote Sensing of Environment 112, 3234–3247. https://doi.org/10.1016/j.rse.2008.04.005

Zhao, F., Dai, X., Verhoef, W., Guo, Y., van der Tol, C., Li, Y., Huang, Y., 2016. FluorWPS: A Monte Carlo ray-tracing model to compute sun-induced chlorophyll fluorescence of three-dimensional canopy. Remote Sensing of Environment 187, 385–399. https://doi.org/10.1016/j.rse.2016.10.036

Zurita-Milla, R., Laurent, V.C.E., van Gijsel, J.A.E., 2015. Visualizing the ill-posedness of the inversion of a canopy radiative transfer model: A case study for Sentinel-2. International Journal of Applied Earth Observation and Geoinformation, Special Issue on “Advances in remote sensing of vegetation function and traits” 43, 7–18. https://doi.org/10.1016/j.jag.2015.02.003